Universidade Federal de São Carlos
Centro de Ciências Exatas e de Tecnologia

Departamento de Física
Programa de Pós-Graduação em Física
Grupo de Supercondutividade e Magnetismo - GSM

Quantitative magneto-optical imaging in bi-layered and in nanoscaled wedge-shaped superconducting thin films

Imageamento magneto-ótico quantitativo em filmes finos supercondutores bicamada e com gradiente nanométrico de espessura

Lincoln Brum Leite Gusmão Pinheiro

São Carlos, São Paulo, Brasil
2019

Universidade Federal de São Carlos
Centro de Ciências Exatas e de Tecnologia

Departamento de Física
Programa de Pós-Graduação em Física
Grupo de Supercondutividade e Magnetismo - GSM

Quantitative magneto-optical imaging in bi-layered and in nanoscaled wedge-shaped superconducting thin films

Imageamento magneto-ótico quantitativo em filmes finos supercondutores bicamada e com gradiente nanométrico de espessura

Tese de Doutorado apresentada ao Programa de Pós-Graduação em Física da Universidade Federal de São Carlos, como parte dos requisitos para a obtenção do título de Doutor em Ciências, Área de Concentração Física.

Ph.D. candidate (Doutorando):
Lincoln Brum Leite Gusmão Pinheiro
Advisor (Orientador):
Prof. Dr. Wilson A. Ortiz
Co-advisor (Co-orientador):
Prof. Dr. Maycon Motta
Supervisor abroad (Supervisor no exterior):
Prof. Dr. Alejandro V. Silhanek

São Carlos, São Paulo, Brasil
2019

UNIVERSIDADE FEDERAL DE SÃO CARLOS

Centro de Ciências Exatas e de Tecnologia
Programa de Pós-Graduação em Física

Folha de Aprovação

Assinaturas dos membros da comissão examinadora que avaliou e aprovou a Defesa de Tese de Doutorado do candidato Lincoln Brum Leite Gusmão Pinheiro, realizada em 11/12/2019:

Prof. Dr. Wilson Aires Ortiz
UFSCar

Prof. Dr. Maycon Motta
UFSCar

Prof. Dr. Alejandro Vladimiro Silhanek
ULg

Prof. Dr. Edson Sardella
UNESP

Prof. Dr. Rafael Zadorosny
UNESP

Prof. Dr. Fabio Luis Zabotto
UFSCar

Certifico que a defesa realizou-se com a participação à distância do(s) membro(s) Alejandro Vladimiro Silhanek e, depois das arguições e deliberações realizadas, o(s) participante(s) à distância está(ao) de acordo com o conteúdo do parecer da banca examinadora redigido neste relatório de defesa.

Prof. Dr. Wilson Aires Ortiz

À minha esposa Dayana a ao nosso filho, Vicente.

Aknowledgements

Agradecimentos

O sentimento de gratidão é algo especialmente bom e importante em todas as culturas. Talvez por isso seja um elemento presente em tantas religiões e sistemas filosóficos. Nas próximas linhas, pretendo registrar os nomes de algumas das muitas pessoas e instituições que fizeram parte da minha trajetória para conclusão da presente tese. Em maior ou menor grau, todos, de alguma forma, tem sua parcela de contribuição - e consequentemente, meu sentimento de gratidão. Em especial, gostaria de agradecer:

Ao Professor Wilson Aires Ortiz, pela orientação da presente tese. Incluo nessa orientação a atenção, o acolhimento, os ensinamentos e a confiança desde o início, quando eu ainda não morava em São Carlos. Isso tudo foi essencial para o meu desenvolvimento pessoal e científico. Muito brigado, Professor!

Ao Professor Maycon Motta, por todo o apoio pessoal e científico desde os primeiros dias e os primeiros passos no laboratório, quando ambos ainda não éramos professores em São Carlos, até a conclusão da tese, já como co-orientador deste trabalho. Muito obrigado, Maycon!

I would like to thank Prof. Alejandro Silhaneck, for supporting my internship at the research group for Experimental Physics of Nanostructured Materials, Université de Liège, in 2015-2016. The high level of the scientific discussions, the planning and the daily-life of science in your group were of great value to my academic career, and inspire my plans to the future. Thank you very much, Alejandro.

Agradeço a todos os membros da banca examinadora, por aceitarem a tarefa de avaliar esse trabalho e por participarem desta etapa final da minha formação científica.

Ao CNPq, pelo suporte financeiro para realização do doutorado sanduíche junto ao grupo do Prof. Alejandro Silhanek, na Université de Liège, Bélgica, no período entre 2015-2016, pelo programa Ciência sem Fronteiras, dentro do projeto bi-lateral liderado pelo Professor Wilson Aires Ortiz.

Ao Instituto Federal de São Paulo, pelo afastamento para capacitação que me permitiu dedicação exclusiva à pesquisa científica durante os últimos 3 anos.

Aos colegas e amigos do Instituto Federal do Rio Grande do Sul, Daniel Pires Nunes, Vinícius Michelin, Josiele S. Michelin, Flávia Garcez, Júlio Faitão, Sérgio W. Viana, Celso Dors, Enildo M. de Oliveira, Alisson D. C. Souza, Airton Bortoluzzi, Luiz Gustavo Barbosa, Vinicius Karlinski, João Rogério M. Pereira, Luciano A. Kempski, Julio C. dos Santos e José Antônio Sala, pelo inesquecível apoio enquanto eu realizava as disciplinas na Universidade de São Paulo como aluno especial em 2013.

A todos os membros do Grupo de Supercondutividade e Magnetismo: ao Prof. Fabiano Colauto, por todo o apoio para o imageamento magneto-ótico e valorosos conselhos; ao Prof. Paulo Cesar Camargo, pelas frutíferas conversas sobre ciência e a complexidade dos

sistemas; ao Professor Adilson J. A. de Oliveira, por reforçar a importância da divulgação da ciência; e ao Prof. Alexandre Gualdi pelas divertidas discussões. Ao Claudio Raffa, pelo apoio técnico em tantos afazeres e pelas importantes discussões sobre a fabricação das dezenas de componentes dedicados à evaporadora. Aos colegas pela longa convivência e paciência, nominalmente: Leo, Lázaro, Fernanda Barbosa, Maria Helena, Alberto, Hugo, José Carlos, Korllvary, Danusa, Pascotto, Marlon, David, Ítalo, Elijah e Otávio. Obrigado, gente!

Agradeço em especial aos Professores Wilson Ortiz, Maycon Motta e Fabiano Colauto, e também aos colegas Claudio Raffa, Marlon Cuadros, Danusa do Carmo, Otávio Abreu Pedroso e ao Elijah Anertey Abbey, pelas incotáveis horas de trabalho experimental no LPA, no LTFD (criado por nós durante esse período :-), e nos longos períodos de dedicação aos experimentos no SQUID e na Magneto-Ótica, tanto na minha condição de aprendiz quanto na de usuário. Obrigado pela companhia e por tudo que me ensinaram.

Aos companheiros Araldo Luiz Isaias de Moraes, Claudio Raffa, Luis Roberto Contri Lopes e Otávio Abreu Pedroso por terem contribuído enormemente nos desafios de se fazer um equipamento científico com qualidade e poucos recursos financeiros. Foi desafiador, mas está funcionando.

Ao José Francisco Domeneghetti, pela paciência com as minhas deficiências em física e por me ajudar a saná-las a tempo de passar no EUF e conseguir começar o doutorado na UFSCar. Ao Vinicius M. Lenart, Yuri A. Opata, João Frederico e Adriane Leal que, ainda na UEPG, também me apoiaram nas questões fundamentais da física. Ao Wescley Tiago Batista de Sousa, que mantém viva a amizade desde os tempos da UEPG no laboratório do Prof. Alcione, até os dias de hoje, no apoio durante a redação da tese como pesquisador no Karlsruher Institut für Technologie.

A todos os meus colegas do Instituto Federal de São Paulo, campus São Carlos, que deram o imprescindível apoio para o período de doutorado sanduíche (2015-2016), o qual demandou os três meses de licença-capacitação do primeiro quinquênio de serviço público federal. Agradeço também pelo apoio durante os dois primeiros anos de doutorado, nos quais eu trabalhava em tempo integral no IFSP e fazia o doutorado como era possível. Obrigado a todos.

Ao Ivens Meyer, pelos primeiros passos práticos nos bastidores da aeronáutica, pela paciência e sábios conselhos, e aos colegas que me deram todo o apoio de que precisei: Arnaldo Morelli, Bruno Opini, Daniela Terenzi, Érico Bruschi, Eduardo L. de Godoi, F. Benini, José Antônio G. Croce, José Nilson Gasparini, Luiz Carlos Veltrone, Maria Claudia Pizzi, Marcos V. F. Ribeiro, Mateus M. de Souza, Natanel Pereira, Paulo Vanucci, Ricardo A. Angélico, Ricardo Arai, Rodrigo Lemes, Rivelli da Silva Pinto, Thiago Cicogna e Wellington Mattos. Obrigado!

Aos professores do Departamento de Física da UFSCar, em especial ao Prof. Adenilson

José Chiquito, que não só fez nossas primeiras amostras de Pb ainda em 2016, como nos deu todo o apoio necessário para a elaboração do projeto da evaporadora, sua construção e seu uso. À Prof.ª Yara Galvão Gobato e ao Prof. Vivaldo Leiria Campo Junior pelos importantes questionamentos para a qualificação do projeto de pesquisa e pelo incentivo à carreira científica na física. Ao Prof. Mauro M. Doria, da UFRJ, pelos exemplos e conselhos desde os primórdios da minha trajetória na supercondutividade.

Fortunately, this thesis would not be possible without the support of people and institutions from abroad. The sample production and part of their characterization were possible because of the work from Carlo Ferdeghini, Cristina Bernini, Emilio Bellingeri, Joris Van De Vondel, M. Caputo, C. Cirillo, C. Attanasio, and R. B.G. Kramer. Thank you very much for your kind support. Moreover, I would like to thank Prof. Tom Henning Johansen for fruitful discussions at the GSM and for providing the MO indicators.

I would like to thank Prof. Jan Bogaert and the Maison Nord-Sud support team, from Gembloux Agro-Bio Tech, for welcoming us to Gembloux during our months at ULg.

I also would like to thank Prof. Ngoc Duy Nguyen (Université de Liège), Prof. Yannick Klein and Prof. Andrea Gauzzi (Université Pierre-et-Marie-Curie), and Prof. Joris Van De Vondel (Katholieke Universiteit Leuven) for the technical visits to their laboratories and helpful explanations about their work. The visits inspired me, and I am sure it will inspire my students soon.

I would like to thank Prof. Bertrand Dutoit, from École polytechnique fédérale de Lausanne (EPFL), for his kind reception and support for my application in the HTS Modelling Summer School 2016. It changed the way I see the applied superconductivity, for better.

Je voudrais remercier tous mes collègues du laboratoire à l'Université de Liège : Jérémy Brisbois, Xavier Baumans, Obaïd Adami, Jonathan Avila, Gorky Shaw, Joseph Lombardo, João Resende et plus tard, Sylvain Blanco Alvarez. Vous avez rendu mes journées à Liège très joyeuses et amusantes. Merci beaucoup !

J'aimerais aussi remercier mes amis Jérémy Brisbois et Elodie Herens pour tous les bons moments à tous les endroits que nous avons nous rencontrer. Merci beacoup !

Além dos amigos e colegas dessa trajetória também devo relembrar outros importantes pesquisadores, amigos e colegas que contribuíram para minha formação: Professores Luis Maurício Resende, Magda G. Leite, Davi Fusão, Irapuan Santos, Fabio Edenei Mainginski, Sandra Tramontin, José Maia, José R. Okida e Nadia Veronique Jourda Kovaleski. Tive ainda o prazer de ser colega de trabalho dos mesmos na UTFPR, há 10 anos. Aos Professores Alcione R. Jurelo, Pedro Rodrigues Jr., Luiz Américo, Rosângela M. Costa e Paulo Pureur Neto, pelos primeiros passos na supercondutividade. Aos Professores do Departamento de Física da UEPG, Sandro Ely de Souza Pinto, Antonio Marcos Batista, José Francisco Serbena e Gelson Biscaia de Souza, por acreditarem que eu poderia fazer algo

de bom na física.

Registro também o adorável apoio de Tillmann Buttschardt, Jan R. K. Lehmann, Sarah Schaack, Andrey Borges, Erina and Isao Mizota, Monika Lechner, Rodrigo Q. de Albuquerque e suas famílias, com os quais tivemos a oportunidade de conviver e compartilhar bons momentos durante a redação desta tese. Muito obrigado!

Aos queridos amigos Daniel e Rosário, Lizi e Ricardo, e Fernanda e Andrea, que sempre emanaram incentivo e apoio, em todas as oportunidades.

Aos meus pais Luiz e Lindalva (hoje avós) pelo incentivo à busca pelo conhecimento desde sempre, pelo amor e pela oportunidade da vida. Aos meus avós, do interior de São Paulo e do Paraná, pelo acolhimento caloroso e sadias conversas. Às minhas irmãs por compartilharmos as bases da vida. A Joanna, minha sogra, pelo carinho e apoio sempre presente. Meu muito obrigado a todos!

À Dayana Almeida, minha amada companheira, que compartilha comigo, há tantos anos, sonhos, projetos e vidas. Ao nosso filho Vicente, pelas alegrias profundas e inexplicáveis que trouxe às nossas vidas. Vocês são e sempre foram, certamente, a melhor parte dos meus dias.

List of Figures

List of Tables

List of abbreviations and acronyms

AC	Alternate Current.
DC	Direct Current.
EPNM	research group for Experimental Physics of Nanostructured Materials, ULg.
FC	Field Cooling.
GL	Ginzburg-Landau theory.
GSM	Grupo de Supercondutividade e Magnetismo.
HT	Applied field (H) vs. Temperature (T).
IFSP	Instituto Federal de Educação, Ciência e Tecnologia de São Paulo.
J_C	Critical current density.
MBE	Molecular Bean Epitaxy.
MO	Magneto-Optical.
MOI	Magneto-Optical Imaging.
MOL	Magneto-Optical Layer.
T_C	Critical temperature.
TM	Thermomagnetic.
TMI	Thermomagnetic instability.
ULg	Université de Liège.
UFSCar	Universidade Federal de São Carlos.
YBCO	$YBa_2Cu_3O_{7-\delta}$.
ZFC	Zero Field Cooling.

Contents

Abstract

Vortex matter in superconductors has been the focus of research of both theoretical and experimental groups around the world. When developing superconducting devices patterned on thin films one should bear in mind that flux avalanches might occur for some materials at a certain range of applied fields and temperatures. For example, technological applications of NbN thin films may be threatened by the occurrence of magnetic flux avalanches of thermomagnetic origin appearing in a large portion of the superconducting phase. This work deals, in parallel, with two distinct superconducting thin film systems by the technique of quantitative magneto-optical imaging: A bi-layered specimen composed by overlapped layers of Nb and NbN and wedge-shaped superconducting thin films of V_3Si and Pb. AC susceptibility and DC magnetometry were used to characterize both the single and multiple-layer films. Magneto-optical imaging reveals interesting features of the dendritic flux avalanches in the bi-layer system, including halo-like patterns around them, and crossing avalanches. The wedge-shaped systems opened a new way to tune the critical current in the film and allowed us to study the resulting changes in the flux penetration patterns along the film. The observation of flux avalanches reported here implies that, as usual, attention to this feature must be given when films with variable thickness and bi-layers are envisaged for possible applications.

Keywords: superconductivity, flux avalanches, superconducting bi-layer, wedge-shaped thin films, thermal evaporation.

Resumo

A Matéria de Vórtices em supercondutores tem sido foco de pesquisas de grupos teóricos e experimentais em todo o mundo. Ao desenvolver dispositivos supercondutores litografados usando filmes finos, deve-se ter em mente que avalanches de fluxo podem ocorrer para alguns materiais em uma determinada janela de campos e temperaturas aplicados. Por exemplo, aplicações tecnológicas de filmes finos de NbN podem ser ameaçadas pela ocorrência de avalanches de fluxo magnético de origem termomagnética que aparecem em grande parte da fase supercondutora. Este trabalho trata, paralelamente, de dois sistemas distintos de filmes finos supercondutores analizados pela técnica de imageamento magneto-óptico quantitativo: uma amostra de duas camadas de Nb e NbN e filmes finos supercondutores de V_3Si e Pb em forma de cunha. Susceptibilidade AC e magnetometria DC foram utilizadas para caracterizar os filmes. O imagemanto de fluxo magnético revela características interessantes das avalanches de fluxo dendrítico no sistema de duas camadas, incluindo padrões do tipo halo em seu entorno e cruzamento de dendritos. Os sistemas em forma de cunha abriram uma nova maneira de sintonizar a corrente crítica no filme e analisar suas consequências na distribuição de fluxo dentro do filme supercondutor. A observação das avalanches de fluxo nestes dois sistemas implica que deve-se dar atenção às características aqui descritas quando a espessura variável dos filmes ou bicamadas são planejadas para possíveis aplicações.

Palavras-chave: supercondutividade, avalanches de fluxo, bicamada supercondutora, filmes finos em forma de cunha, evaporação térmica.

1 Introduction

From the early days of superconductivity - discovered by Heike Kamerlingh Onnes in 1911 - to the prediction and experimental observation of the Josephson effect, in the 1960's, decades of experimental work were necessary to fulfill the surprising list of superconducting properties. Fascinating applications based on these properties are always coming to light, proposed and realized by scientists and engineers. Nowadays, superconductors are present in strong magnets for medical imaging, particle accelerators, and aircraft electrical engines, as well as in the heart of quantum computers. These applications allow one to state that the superconductor technology is one of the bases for the development of science.

Some of these promising technologies, such as magnetic field sensors and qubits, are based on thin films. During their deposition, the thickness uniformity is an important issue, but not easily solvable. In this context we address the question: how does the thickness variation affect the superconducting properties of thin films? Furthermore, overlays of superconductors are in the core of Josephson-junction architectures, but there is still a gap in literature on the magneto-optical imaging of such bi-layered systems.

The present work deals with the study of bi-layered thin film superconductors and nanoscaled wedge-shaped superconducting thin films; both addressed by quantitative magneto-optical imaging. After a historical review in Chapter 2, this thesis shows in its 3^{rd} chapter the experimental methods and the materials studied. In Chapter 4 we show in detail a numerical method for quantitative magneto-optics and apply it to the study of two different superconducting thin films, in order to highlight some critical issues related to the use of magneto-optical imaging when the sample is a superconductor. Chapter 5 is

a whole new application of such numerical method, associated with to DC magnetometry and AC susceptometry to investigate a superconducting bi-layer made out of Nb and NbN. Concerning the wedge-shaped thin films, Chapter 6 deals with the study of flux avalanches in an anisotropic V_3Si thin film, identified, after our characterization, as a wedge-shaped sample whose thickness variation was not part of the original plan of the sample makers. In Chapter 7, we present the preparation process and the quantitative magneto-optical imaging for nanoscaled wedge-shaped superconducting thin films of Pb, discussing some newly found aspects of the physics of these systems. The final remarks and perspectives are summarized in Chapter 8. Some useful information from parallel works during the PhD period are organized in the Appendix. Moreover, there is a list of publications related to this thesis and, finally, the bibliography which we used as a base for our discussions.

2 Historical review and state of the art

2.1 The superconducting state

The superconducting state appears below the critical temperature (T_c), and the first discovered superconducting materials required the liquid helium technology, due to the extremely low temperatures needed to go below T_c in such specimens. Figure 1 (a) reproduces the historical graph of the sudden disappearance of Hg, published by Heike Kammerlingh Onnes in 1911 [1], where T_c can be easily identified. Panel (b) of the same figure shows a recent result about the resistivity of a single element (Bi-III), published in the Science Advances Journal more than 100 years after the first one, in April 2018 [2] .

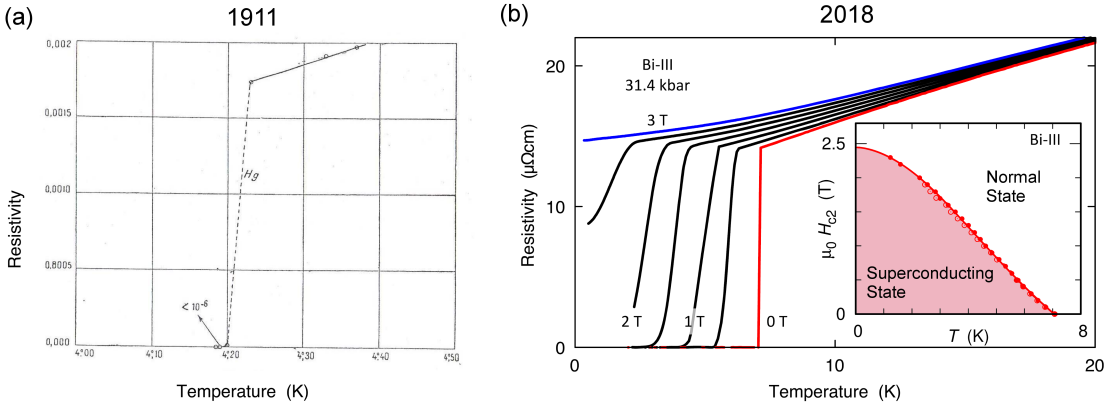

Figure 1: (a) Resistivity versus temperature for a specimen of pure Hg, the first known superconductor, with a T_c of 4.2 K. (b) Resistivity versus temperature measurement for the high pressure phase of bismuth (Bi-III), stable in 3.14 GPa, for increasing applied magnetic field up to 3 T. Adapted from [1] and [2].

In the last 3 decades, students all around the world probably heard about high-temperature superconductors (HTS), after the seminal work by Bednorz & Müller [3] and

by Chu et al. [4] - materials whose T_C could be above the liquid nitrogen temperature[1]. Despite the enormous expectations of a room temperature superconductor, to the best of our knowledge, the human-kind was not able (yet) to produce such a fantastic material. The more recent expectation about room temperature superconductivity relies on hydrogen-based materials at high pressures, such as the hydrogen sulfide (H_3S) [5], whose $T_C = 203$ K (-70 °C) at 90 GPa, and LaH_{10}, for which $T_C = 260$ K at 180-200 GPa [6], the highest temperature so far.

The magnetic field also plays an important role in the behavior of the superconductors. Above the critical magnetic field (H_c), the superconducting state no longer exists, and the materials undergo a transition to the normal state. This dependence is illustrated in the inset of Figure 1 (b), where the diagram shows two distinct regions for the Bi-III: Below $H_c(T)$ the material is in the superconducting state (magenta region in the diagram), while for fields greater than $H_c(T)$ the material is in the normal state (white region in the diagram). The field dependence of the normal-superconductor transition can also be recognized in the effect of the applied magnetic field on the resistivity measurements of the panel (b). There are two definitions for the critical field: H_{c1}, above which the superconductor is no longer a perfect diamagnet; and H_{c2}, that corresponds to the extinction of the superconducting state. The experimental points in the inset of Figure 1 (b) are for H_{c2}. More details about these definitions are given in the next section. Another remarkable property of the superconducting state is a discontinuity in the specific heat at $T = T_c$. Figure 2 shows measurements of the electronic specific heat of elemental Ga as a function of temperature.

[1] My first contact with superconductivity was at the high school when the physics teacher told us a little bit about the fantastic possibilities of the high-temperature superconductors.

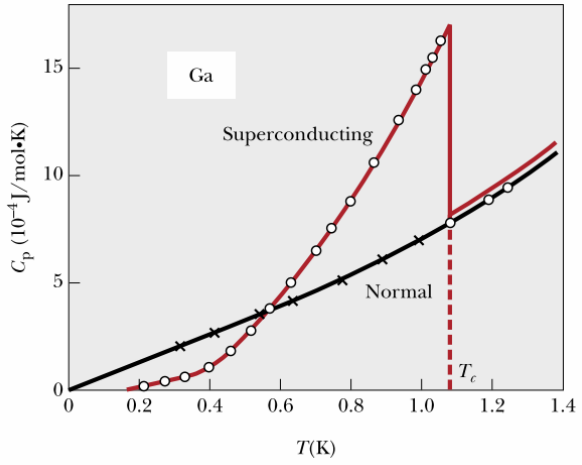

Figure 2: Electronic specific heat *vs* temperature for superconducting Ga in zero applied magnetic field, as a red line, and normal gallium in a magnetic field of 0.020-T, in a black line. Adapted from [7].

All these fascinating properties of the superconducting metals fit quite well in the "*Theory of Superconductivity*" proposed by J. Bardeen, L. Cooper, and R. Schrieffer in 1957 [8, 9] - the **BSC theory**. All the authors were already dealing with the challenge of explaining how the superconductivity takes place but was the idea of Cooper about bounding electron pairs in a degenerate Fermi gas [10] that led them to the whole theory. The so-called **Cooper pairs**, pairs of electrons whose bounding state is mediated by phonons play the role of the charge carriers in the superconducting state.

A few years after the BSC theory, B. D. Josephson published an intriguing paper whose title is self-explained: "*possible new effects in superconductive tunneling*" [11]. The Josephson effect, as we call the tunneling phenomena in superconductors, is the base of modern magnetometers sensors, the Superconducting Quantum Interference Devices (SQUID), and also is paving the way through quantum computing [12].

Even before a theory that explains the superconductivity from a microscopic point of view, Ginzburg and Landau had already described the superconducting state in an advantageous form, using the Landau theory of second order phase transitions.

2.2 The Ginzburg-Landau theory

2.2.1 Introduction

One of the key consequences of this Ginzburg-Landau theory (GL) is the definition of two characteristic lengths of the superconductors: the coherence length, ξ_0 and penetration depth, λ. Nevertheless, the concept behind these two defining parameters of the superconducting state was already in use years before the GL formalism came to light.

In the early 1930's the two remarkable properties of the superconductors were already known - the zero resistivity and the perfect diamagnetism - this last one is the so-called Meissner effect, after W. Meissner and R. Ochsenfeld [13], who reported experimental observations of perfect diamagnetism that were not simply the diamagnetic response of a perfect conductor [14]. This last feature of the superconductors was subject of the London brothers efforts [15], in which they propose:

$$\vec{E} = \frac{\partial}{\partial t}\left(\frac{m}{n_s e^2}\vec{J}\right) \tag{2.1}$$

and,

$$\vec{\nabla} \times \vec{J} = -\frac{n_s e^2}{m}\vec{B} \tag{2.2}$$

as a constitutive relation to the Maxwell equations. In Equations 2.1 and 2.2, m is the mass of the charge carrier (called superelectron at that time), n_s is the density of charge carriers in the superconducting state, $\vec{E}$ is the electric field, $\vec{J}$ is current density, and $\vec{B}$ is the magnetic flux density. In the superconducting state, n_s goes to its upper limit (accounting all the charge carriers), and one can introduce the London penetration depth $\lambda_L(0)$ to explain the non-abrupt penetration of magnetic flux into the superconductor, as shown in Equation 2.3, adapted from reference [14] for a unidimensional approximation.

$$\vec{B}(x) = \vec{B}_0 \cdot e^{\frac{-x}{\lambda_L(0)}} \tag{2.3}$$

In this equation, x is a coordinate that points towards the interior of the sample, $\vec{B}(x)$ is the magnetic field as a function of x, $\vec{B}_0$ is the outer value of $\vec{B}$, and λ_L is the London penetration depth. This parameter can also be written as

$$\lambda_L(0) = \sqrt{\frac{m^* c^2}{4\pi n_s e^{*2}}}, \tag{2.4}$$

where m^* and e^* are the mass and the charge of the super-electron and n_s the volumetric density of superelectrons[2].

At the beginning of the twentieth century, physical theories and scientific propositions did not spread as fast as nowadays. From the United Kingdom, in early 1950, Pippard described what we call currently as the Pippard coherence length [16], at the same time that, from Russia, Ginzburg and Landau proposed a theory for superconductivity [17] in which a coherence length has a meaning closely related to the one proposed by Pippard. Although Pippard used the variable ξ only in the paper published in 1953 [18], at the end of 1950, he already submitted the basic ideas that would lead him to the definition of ξ [16]. In both descriptions, ξ is related to the density of the charge carriers in the superconducting state.

2.2.2 The GL equations

The GL equations are two coupled differential equations that are derived from the expansion of the free-energy density in powers of a complex order parameter that carry information of the superconductor state. Such an order parameter is the pseudo wavefunction $\psi(\vec{r})$, whose meaning is linked to the superconducting state by assuming that

$$|\psi(\vec{r})|^2 = n_s(\vec{r}). \tag{2.5}$$

[2]The London brothers used the two-fluid model to describe the superconducting state, i.e., below T_c there are two distinct electronic carriers, the normal electrons, and the superelectrons.

Also, one should define the order parameter as

$$\psi(\vec{r}) = |\psi(\vec{r})|e^{-\phi(\vec{r})}, \tag{2.6}$$

setting $\phi(\vec{r})$ as a phase factor. Once the normal-superconductor transition is a second-order one (in absence of magnetic field) , this complex order parameter must be zero in the normal state (disordered state) and real in the superconducting state (ordered state). Assuming that $\psi(\vec{r})$ varies slowly in space and is small, this theory starts expanding the free-energy density in the superconducting state f_s as

$$f_s = f_n + \alpha|\psi(\vec{r})|^2 + \frac{\beta}{2}|\psi(\vec{r})|^4 + \frac{1}{2m^*}\left|\left(\frac{\hbar}{i}\vec{\nabla} - \frac{e^*}{c}\vec{A}\psi\right)\right|^2 + \frac{h^2}{8}\pi. \tag{2.7}$$

In Equation 2.7, f_n is the free-energy density of the normal state, $\alpha(T)$ and β are phenomenalogical constants, $\vec{A}$ is the magnetic vector-potential, and c is the speed of light in vacuum. By minimizing this equation with respect to $\vec{A}$ and to $\psi(\vec{r})$, two distinct but coupled differential equations are obtained:

$$\alpha\psi + \beta|\psi(\vec{r})|^2\psi + \frac{1}{2m^*}\left(\frac{\hbar}{i}\vec{\nabla} - \frac{e^*}{c}\vec{A}\right)^2\psi = 0 \tag{2.8}$$

and

$$\vec{J} = \frac{e^*}{m^*}|\psi(\vec{r})|^2\left(\hbar\vec{\nabla}\phi - \frac{e^*}{c}\vec{A}\right) \tag{2.9}$$

An interesting aspect of these equations is that, for a constant $|\psi|$, Equation 2.9 can be reduced to the second London equation (Equation 2.2).

To write these equations in a dimensionless form, one has defined the distance in which ψ varies considerably, the coherence length ξ, and the penetration depth λ, whose meaning is the same as in the London model. Both parameters can be written as

$$\xi = \left(\frac{\hbar^2}{m^*|\alpha|}\right), \tag{2.10}$$

and

$$\lambda = \sqrt{\frac{m^*\beta}{e^{*2}|\alpha|}}, \tag{2.11}$$

In this framework it is also important to define the thermodynamic critical field ($H_C(T)$),

$$H_C(T) = \frac{\phi_0}{2\sqrt{2}\pi\xi(T)\lambda(T)}, \tag{2.12}$$

where $\phi_0 = \frac{hc}{2e} \approx 2.068 \times 10^{-7}$ G·cm^2 is the magnetic flux quantum, h in the Planck constant, c the speed of the light, and e the electron charge. The critical current density J_C is defined as the one whose self-field, i.e., the field produced by the current, is equal to H_C in the superconducting surface.

One can also define the dimensionless parameter κ,

$$\kappa = \frac{\lambda}{\xi}, \tag{2.13}$$

which is used to delimit the border between type-I and type-II superconductors - the topic of the next section.

2.2.3 The dirty limit for λ and ξ

In the framework of the GL theory, one can also account for the effects of impurities on the characteristic lengths λ and ξ, by means of the mean free path l_e. Additionally, one need to call upon the BCS description of the coherence length, nominally,

$$\xi_0 = 0.18\frac{\hbar v_F}{k_B T_C}, \tag{2.14}$$

where $\hbar$ is the Planck constant divided by 2π, v_F is the Fermi velocity, and k_B is the Boltzman constant. Basically, for materials produced in ordinary conditions, $l_e \ll \xi_0$, what is called the *dirty limit*. So, in the dirty limit, the characteristic parameters for the

superconducting state are given by [19, 20]:

$$\xi(T) = 0.855\sqrt{\xi_0 l_e}\left(1 - \frac{T}{T_C}\right)^{-1/2} \tag{2.15}$$

$$\lambda(T) = 0.64\lambda_L(0)\sqrt{\frac{\xi_0}{l_e}}\left(1 - \frac{T}{T_C}\right)^{-1/2}, \tag{2.16}$$

where $\lambda_L(0)$ is the penetration depth at zero Kelvin, obtained by the London theory.

2.2.4 Type-I superconductors and the intermediate state

Materials whose λ to ξ ratio is smaller then $\frac{1}{\sqrt{2}}$ are called type-I superconductors. Beyond the simplistic explanation that this kind of material either is superconducting or is in the normal state, the materials of this category offer an amazing phenomenon called the intermediate state. One of the greatest triumphs of the GL theory was to explain the occurrence of the intermediate state, which can be ascribed directly to the demagnetizing factor N. Figure 3 shows, schematically, a magnetization curve for a typical type-I bulk superconductor with demagnetizing factor $N \approx 0$ (a), and for $N \neq 0$ in panel (c), in which the intermediate state takes place. The inset in both panels (a) and (b) illustrates the direction of the applied magnetic field H in the samples and their shapes.

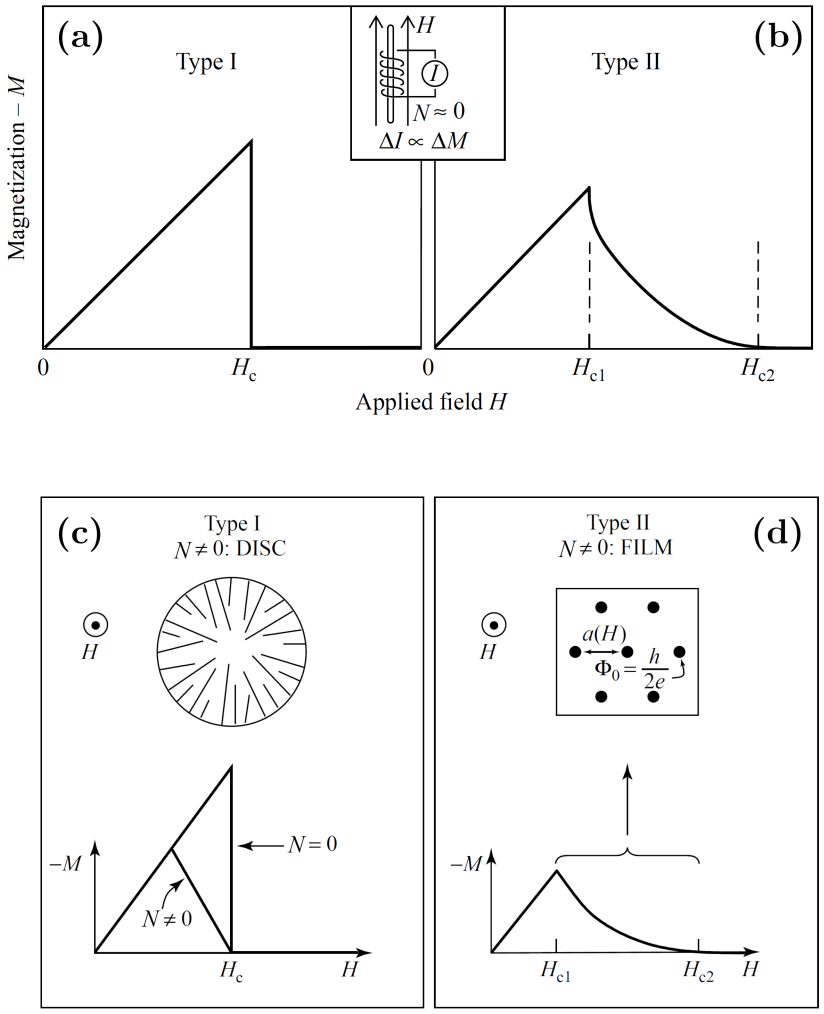

Figure 3: Scheme of a superconductor-normal transition with demagnetization factor $N = 0$ for type-I (a) and type-II (b) superconductors. The inset shows the needle-shaped sample whose main axis is parallel to the applied field H. For a type-I material in a disk shape (c) and a type-II thin film, the transition is broader. Adapted from [21].

In Figure 4 one can appreciate an experimental magnetization curve of a sample of pure Sn with spheroidal shape. There is no identifiable hysteresis in the magnetization loop, although it presents the intermediate state, indicated by the small deviation from a vertical decrease of the curve in the second and fourth quadrants.

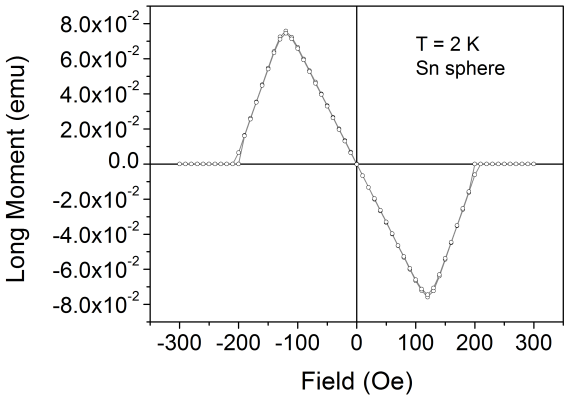

Figure 4: Magnetization versus applied magnetic field for a superconducting sphere made out of pure tin. The sample preparation and the magnetization measurements were carried out at the GSM group.

The intermediate state is not only a broad transition from the superconducting to the normal state. It is a complex and multi-factorial phenomenon of strongly correlated systems that is better comprehended if one considers its topology. The direct observation of the domain structure of the intermediate state was extensively studied by Prozorov *et al.* [22, 23, 24], using magneto-optical imaging. Figure 5 shows a phase diagram of a superconducting bulk Pb disk. Prozorov and coauthors [22] regarded the dynamics of the domain walls in the intermediate state, describing it as a kind of froth, what they called the suprafroth. This suprafroth has its cells delimited by the superconducting domains of the material, while the inner part of the cell is a normal metal with magnetic flux inside. Their dynamics are the same for soap foams in panels (b) and (c). Even food production can receive benefits from the advance of science on this subject, once the froth structure is common in food preparation [see panel (d)].

Nevertheless, the froth structure in superconductors has a particular issue not easily achieved in gas bubbles - the Lorentz force between the supercurrents and the flux inside each normal cell of the intermediate state. For low fields but already on the intermediate state, the cells are also called tubes, due to its circular cross-section, as can be seen in top-right inset of Figure 5(a).

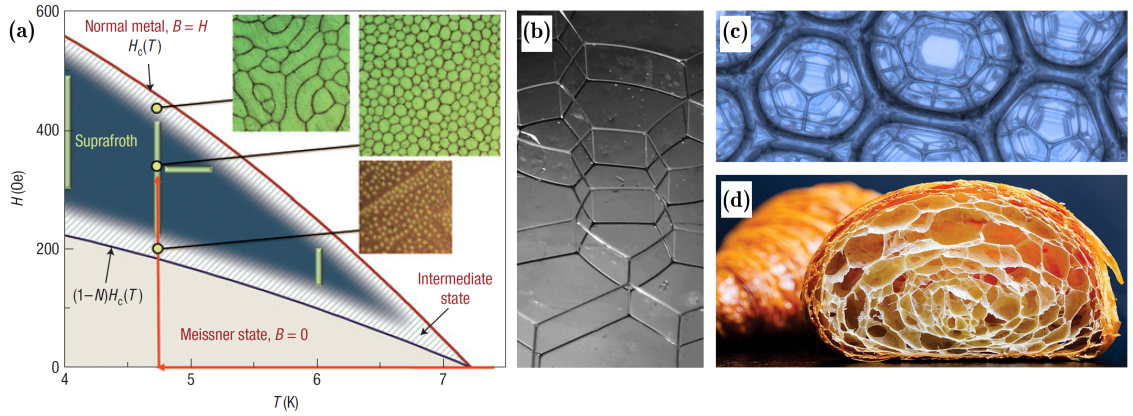

Figure 5: Foams in nature and superconductors. (a) Type-I superconductor Pb phase diagram; (b) quasi-2D froth structure of soap foam inside of flat glass slides. (c) A photograph of the Weaire–Phelan foam fabricated at Trinity College, Dublin, using soap in a vessel with a special projected design (Courtesy from Ruggero Gabbrielli to Physics Today); (d) Froth structure of a *croissant au beurre*, showing the universal application of these studies. Adapted from [22, 25, 26, 27].

Figure 6 shows magneto-optical (MO) images of a Pb single crystal in a disk shape, for different ramp-up speeds of the applied magnetic field H [23], after a zero-field cooling (ZFC) procedure, at $T < T_C$. The authors showed that increasing the field faster leads to the columnar domain structure described by Landau, but this columnar structure is a track of the movement of the tubes due to the Lorentz force [23].

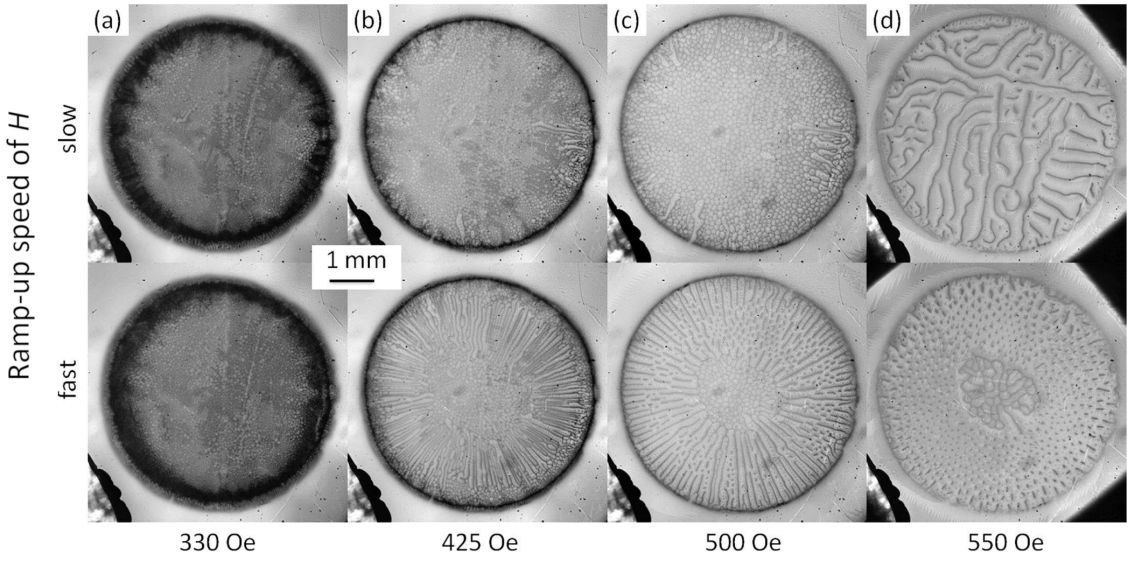

Figure 6: Magneto-optical images of type-I sample of lead, after ZFC for different fields: (a) 330 Oe, (b) 425 Oe, (c) 500 Oe, and (d) 550 Oe. Each panel shows the sample in a slow ramp-up speed of H (top) and at fast ramp-up speed (bottom). Adapted from [23].

2.2.5 The type-II superconductors and the mixed state

2.2.5.1 The superconducting vortex

Type-II superconductors are those materials whose λ to ξ ratio is greater then $\frac{1}{\sqrt{2}}$. In this case, the flux inside the superconductor is admitted but not in the shape of whole normal regions as in the intermediate state, but in very small regions allowing only one single quantum of flux in it. In type-II superconductors, regardless of the value of the demagnetizing factor, the transition from the superconducting to the normal state in the presence of an external magnetic field will always show the mixed state, where the quantized flux filaments inside the superconductors are called vortices. Figure 3(b) shows a magnetization curve as a function of the applied field H for a type-II superconductor, where both the critical fields H_{C1} and H_{C2} are indicated. The mixed state will take place when $H_{C1} < H < H_{C2}$. The vortex arrangement inside the superconductor is illustrated on the inset of Figure 3(d).

The vortex structure is better described using both the coherence length and the penetration depth, introduced earlier in this chapter. While ξ represents the radius of the normal state region into the sample, i.e., the vortex core, λ represents the distance across the superconducting region where the supercurrents are flowing to keep the magnetic flux inside the normal core, as illustrated in Figure 7.

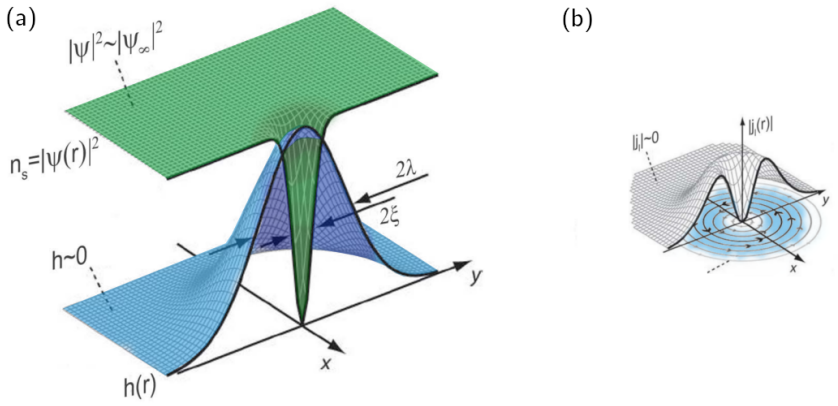

Figure 7: Schematic illustration of a vortex in a type-II superconductor. (a) Magnetic flux distribution around the vortex core, illustrating the meaning of λ; the coherence length ξ measured as a radial distance of the vortex core. (b) The superconducting currents around the center of the vortex as a function of the radial distance r. Adapted from [].

Abrikosov predicted the vortex existence and its properties in his remarkable paper in 1957 [28]. He also anticipated an intrinsic and important characteristic of the superconducting vortices: their natural repulsion against each other, which is responsible for their hexagonal arrangement in the superconductor, as shown in Figure 3 (d). When $\kappa > \frac{1}{\sqrt{2}}$, the energetic balance between the normal and superconducting phases makes the normal cores to carry as few field as possible, in such a way that the flux inside the normal core is one flux quantum.

2.3 Pinning and the critical state models

2.3.1 Pinning

The first quadrant of a magnetization loop of a type-II superconductor, i.e., its virgin curve, is explained by means of a gradual entrance of vortices into the sample. The magnetic field inside each vortex decreases the overall magnetization of the specimen. Nevertheless, a complete loop of a typical superconducting sample shows a remarkable hysteretic behavior, as shown in Figure 8 for a Nb cube taken at 2 K after a ZFC.

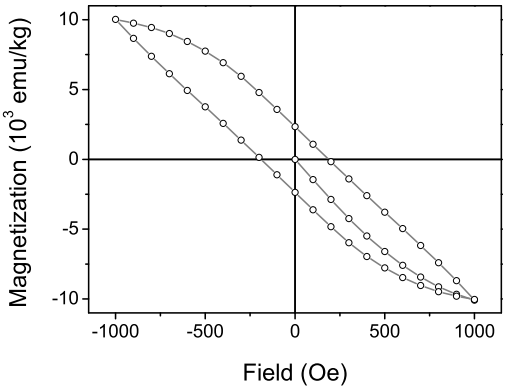

Figure 8: Magnetization loop for a Nb cube ($3 \times 3 \times 3$ mm^3) at T = 2 K, after a zero field cooling (ZFC) procedure. Data courtesy by Prof. Maycon Motta, UFSCar.

One can start the discussion about such a hysteretic behavior by the Lorentz force ($\vec{F}_L$), written as

$$\vec{F}_L = \vec{J} \times \vec{B} = \vec{J} \times n\phi_0\hat{z}, \tag{2.17}$$

where $\vec{J}$ is the total current density, n is the number of vortices, and $\hat{z}$ a unity vector pointing the z direction (parallel to H). The motion of the vortex system at a velocity $\vec{v}$ gives rise to an electric field $\vec{E} = \vec{B} \times \vec{v}$, parallel to $\vec{J}$. The power dissipation due to this electrical field would make superconductors useless for power transport applications. Real samples always show some potential wells that can trap the vortex once it gets there. Inclusions of other materials, grain boundaries, or even crystallographic defects can act as **pinning centers** for the superconducting vortex. If $\vec{v} = 0$, there will be no electrical field and hence, no dissipation.

In this framework, one can describe a pinning force F_p that should be equal to F_L to assure the dissipationless condition in the superconductor. The pinning force is what defines J_C in a practical superconductor, and can be written as

$$F_p = J_C B \tag{2.18}$$

One should keep in mind that this is not the depairing current density (J_d), the

one that destroys the Cooper pair. Taking into account other contributions to the free energy (surface barriers and losses of the vortex motion), in practice, we have $J_C < J_d$. For example, Hunt [29] measured $J_C = 5.26 \cdot 10^7$ A/cm^2 for a 47 nm thick Pb film, while the depairing current density for lead is estimated in the range of 10^8 –10^9 A/cm^2 [30].

2.3.2 The Bean critical state model

An interestingly successful model to describe and predict the properties of type-II superconductors is the one proposed by C. Bean [31, 32] . One can summarize it assuming that, for a bulk sample, the shielding current always equals to J_c wherever it is necessary; the magnetic flux gradient is constant towards the sample center (which differs from the London approach shown in Figure **??**), and where there is no current, there is no field. Figure 9 clarify these aspects.

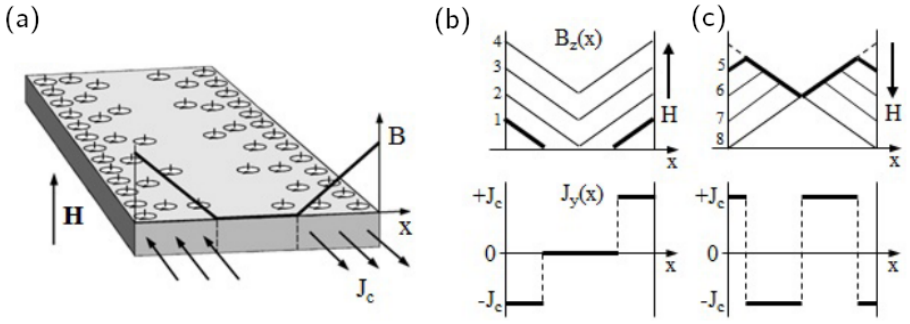

Figure 9: Critical state, following the Bean model, for bulk samples. (a) J_C, magnetic field B and vortex distribution in a bulk superconductor at $T < T_C$. (b) Field (top) and current density (bottom) profiles for increasing field after a ZFC procedure, and (c) field (top) and current density (bottom) profiles for decreasing field after reaching the maximum H. Adapted from [33] and [32].

The Bean model describes very well the overall sample response in bulk superconductors. Nevertheless, for thin films, the demagnetization factor plays an important role, and even when one applies H only perpendicularly to the film plane, there will always be an in-plane component of the field. The modifications in the Bean model to suits the thin films are explained in the next section.

2.4 Superconducting thin films

2.4.1 History

Let us state a superconducting *thin* film as a film whose thickness is comparable to its coherence length at $T = 0$, ξ_0. The first article on superconducting thin film, to the best of our knowledge, was published by Shalnikov in 1938 [34]. The author reported experimental results on resistivity measurements carried out on films of Sn and Pb deposited on top of glass surfaces at 4.2 K and whose thickness lied between 2 and 5 nm for both metals. The measurements were done *in situ*, inside a high vacuum chamber, using four platinum electrodes. At that time, the scientific community did not expect to achieve a type-II behavior on superconducting thin films - this explains why Shalnikov look so surprised describing that the critical field of his thin films was higher than those of the bulk samples. Unfortunately, he did not mention the size of these glass slides, so the values of the critical current i_C can not be precisely used to calculate J_C of his films.

2.4.2 2D superconductors?

An important remark is that superconducting thin films are not 2D superconductors. As an example, thin films of lead - whose thickness should lie close to 30 nm (ξ_0 for Pb) - are still 3D if we consider the Pb cell parameter as 0.49 nm. Two-dimensional thin films of lead shown superconductivity modulated by quantum size effects, as described by Guo *et al.* [35]. The authors deposited Pb films with few atomic layers in MBE facility, and measured the critical temperature *in situ*, using transport measurements. Their findings are summarized in Figure 10. The authors observed quantum oscillation in both the critical temperature and in the density of states close to T_C, as a function of the monolayers of Pb.

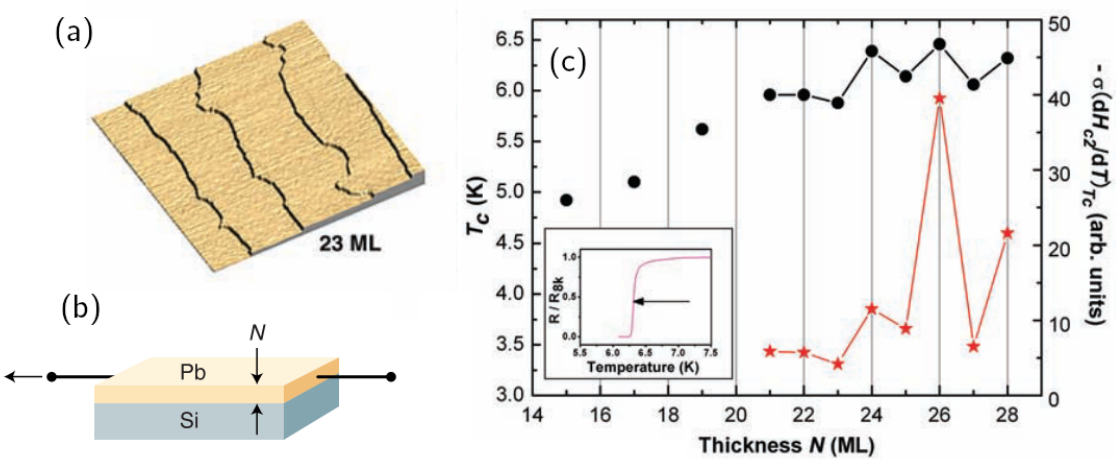

Figure 10: (a) Scanning tunneling microscope image (2×2 μm^2) of 23 monolayers (ML) of Pb. (b) Schematic representation of the transport measurement, where the number of monolayers (N) is indicated, and the lead current are represented by black arrows. (c) Quantum oscillations on the critical temperature of thin films of Pb (black line and y-left scale) as a function of the film thickness. Also, the density of states $N(E_F) \propto -\sigma(dH_{c2}/dT)_{T_C}$ is the red curve and y-right scale. The inset indicates which point in the the resistivity *vs* temperature curve was used to measure T_C. Adapted from [35].

2.4.3 Type-II films of a type-I material

Dolan and Silcox, in 1973 [36], published a remarkable paper on the threshold of the type-I response of thin films, using bitter decoration to access single-vortex resolution in films made out of lead and tin with various thicknesses. The authors claim a critical thickness of 250 nm for Pb and 180 nm for Sn, which are smaller than measurements made by critical-field data (900 nm for Pb and 520 nm for Sn) by the same authors. An essential feature of this study is the level of defects in the film - the higher the pinning, the easier the film will behave like a typical type-II superconductor.

For films whose thickness is smaller than the London penetration depth ($d << \lambda$), one can define an effective penetration depth Λ, after Pearl [37]:

$$\Lambda(T) \approx \frac{2[\lambda(T)]^2}{d}, \tag{2.19}$$

Using this effective penetration depth to calculate κ, the thinner the film, the more "type-II" it will be.

2.4.4 The Bean model for thin films

The demagnetization factor for thin films is close to the unity in the out-of-plane axis (z) and small for the in-plane coordinates (x and y) [38], in such a way that an externally applied field H_z is deformed in the vicinity of a superconductor, leading to tangential components H_x and H_y. These tangential fields also have opposite directions when comparing the top and the bottom surfaces of the film, as schematically shows Figure 11. There is a strong variation of $H_x(z)$ along the sample thickness d, which contributes to the Lorentz force.

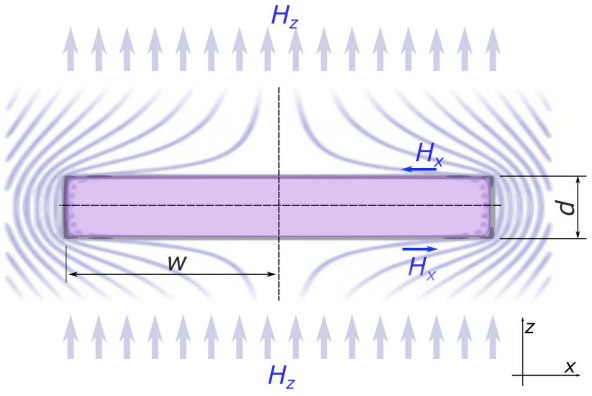

Figure 11: Schematic representation of the tangential fields due to the high demagnetization factor of a thin film. The y axis is pointing along the page plan. This schematic representation is for an infinitely long sample in the y direction. Adapted from [39].

Assuming an infinite sample in the y axis (pointing into the plan of this page), with its thickness $d << w$, or at least $d < \lambda < \Lambda << w$ for thin films, one can write the $B_z(x)$ for a situation where the applied magnetic field is increased from zero after a ZFC as follows [40, 41]:

$$B_z(x) = \begin{cases} 0 & |x| < a \\ H_p \ \text{atanh}\left(\frac{w}{|x|}\sqrt{\frac{x^2-a^2}{w^2-a^2}}\right) & a < |x| < w \\ H_p \ \text{atanh}\left(\frac{|x|}{w}\sqrt{\frac{w^2-a^2}{x^2-a^2}}\right) & |x| > w \end{cases} \tag{2.20}$$

where the quantities and coordinates are defined in Figure 11, and a is the coordinate of

the flux front, defined by

$$a = \frac{w}{\cosh(\frac{H}{H_p})}, \tag{2.21}$$

and H_p, the characteristic field for the full penetration into a thin disk is given by

$$H_p = \frac{J_C d}{\pi}. \tag{2.22}$$

In this context, the current density will be

$$J_y(x) = \begin{cases} \frac{2J_C}{\pi} \text{atanh}\left(\frac{x}{w}\sqrt{\frac{w^2-a^2}{a^2-x^2}}\right) & |x| < a \\ J_C \frac{x}{|x|} & a < |x| < w \end{cases} \tag{2.23}$$

Zeldov *et al.* [41] used these equations to plot the graphs in Figure 12, for the magnetic field B and the current density J. Panels (a) and (b) show the results for a superconducting slab, while panels (c) and (d) for a thin film. Panel (e) shows the representation of these geometries.

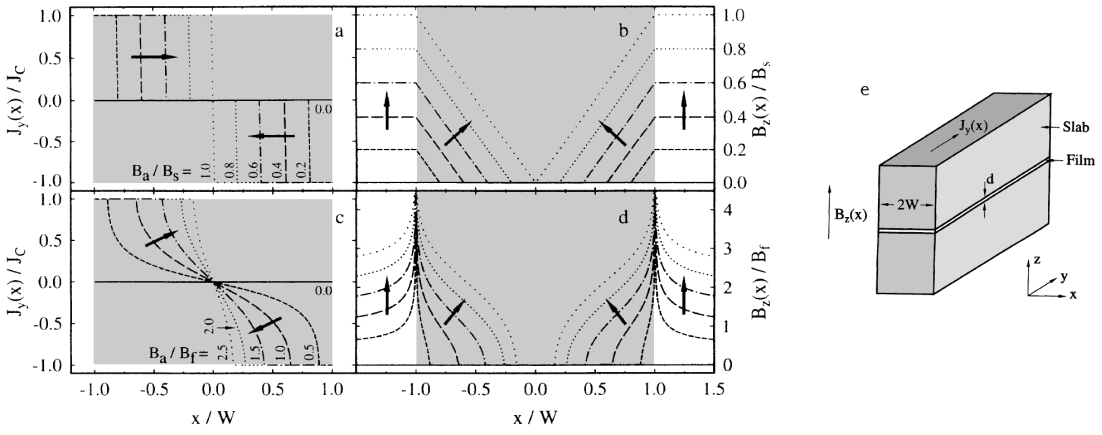

Figure 12: Calculated current density and critical-state behavior of the internal field as one increases the applied field, at $T < T_C$, after a ZFC; (a) and (b) are for a thick slab, while (c) and (d) are for a thin film. Arrows indicate the profiles as the applied field is increased. (e) Schematic representation of the samples. Adapted from [41].

These calculations are valid for the whole material extension, except a small region λ in the film edges [41]. The intensity of the magnetic field at the edge of the

sample is surprisingly higher than the applied field by an amount of [41]:

$$H_{edge} \approx \sqrt{\frac{w}{d}} H_z \tag{2.24}$$

The strong demagnetization effect also shows significant consequences if one decreases the applied field after letting some flux trapped in the film, as illustrates the theoretical results in Figure 13. A remarking aspect of those results is the negative values at the edges of the superconductor even when the decreasing applied field is still positive, as one can see in panel (d), the dashed line 0.5 B_a/B_f.

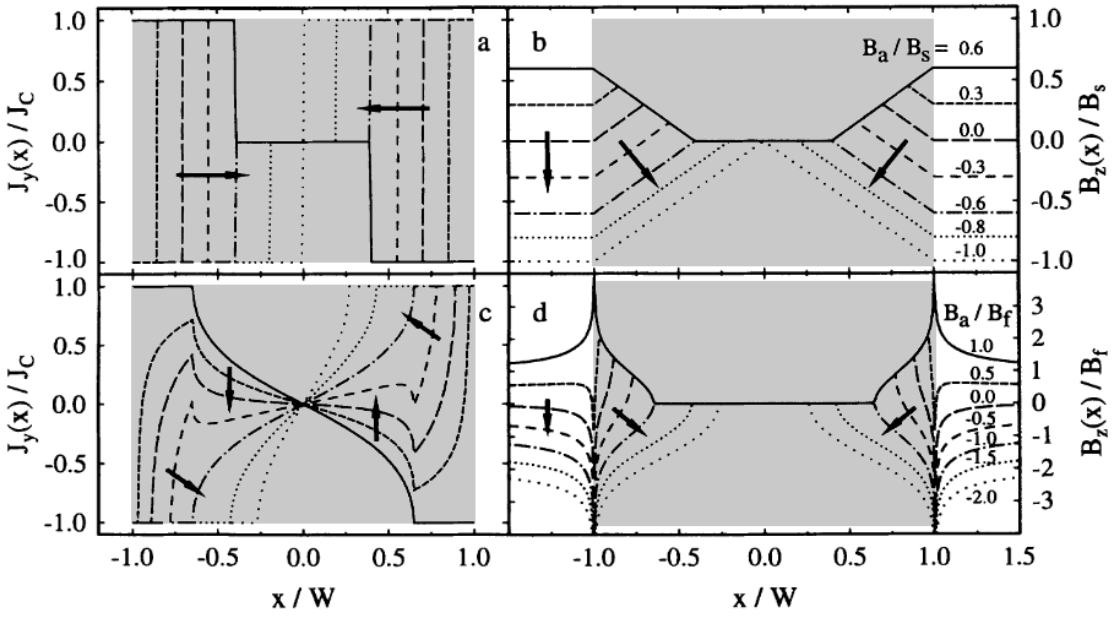

Figure 13: Calculated current density and critical-state behavior of the internal field as one decreases the applied field for a sample initially at a partial penetrated state; (a) and (b) are for a thick slab, while (c) and (d) are for a thin film. Arrows indicate the profiles as the applied field is increased. Adapted from [41].

The Bean model for thin films describes very well the experimental results from magneto-optical imaging, such as the one selected in Figure 14, for a $YBa_2Cu_3O_{7-\delta}$ type-II superconducting strip at $T = 10$ K and $\mu_0 H = 40$ mT applied perpendicularly to the film plane, after a zero-field cooling (ZFC).

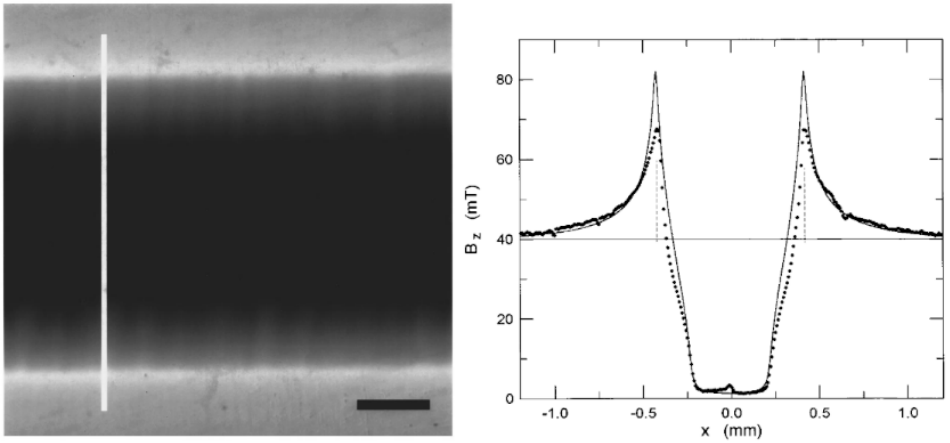

Figure 14: Magneto-optical image of a YBCO strip, 300 nm thick and 0.8 mm wide, and 5 mm long (The black bar in the bottom is 0.2 mm long). The vertical white bar indicates where the cross-section B profile at right was taken. The continuous line is the calculated profile for that situation, whereas the scatter points are the measured values from the image. The dashed lines indicate the film edges. Adapted from [42].

The critical state, as described by these models for thin films, has even more interesting characteristics if one regards not only a fraction of the sample, but pays attention to the whole system. In 1994, Schuster *et al.* [43] described the discontinuity-lines (d-lines) as a natural consequence of the shielding current flow in a finite sample. D-lines are these highlighted lines starting at the sample corners and ending at the flux front meeting region, as one can see in Figure 15 (a). An explanation for its occurrence is illustrated in panel (b) for a superconducting film in a strip-shape, with current curving abruptly towards the left direction. The big red $\odot$ symbol is a region equally distant from the curving current lines. That spot is so more shielded than all the other $\odot$ symbols. A chain of regions more shielded than its neighbors is the origin of the d-line.

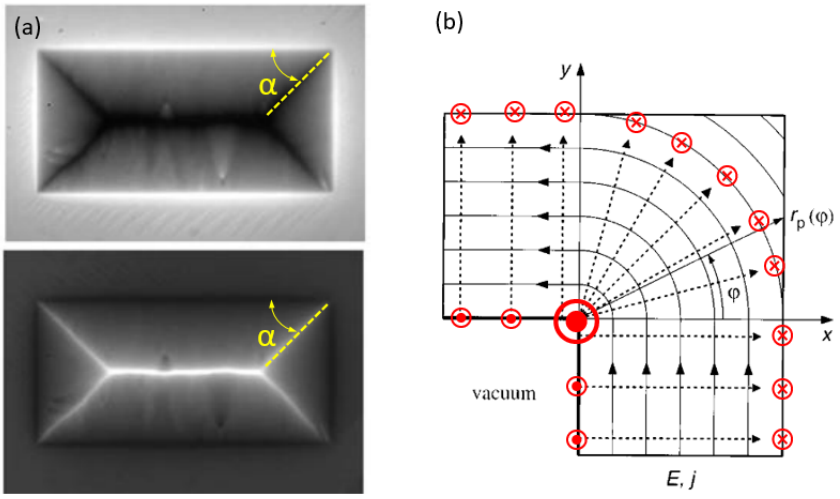

Figure 15: Discontinuity-lines (d-lines) definition. (a) Magneto-optical images of a YBCO rectangular-shaped thin film, in the full penetration state after ZFC (top) and at the remnant state (bottom). (b) Schematic representation of current lines changing its direction in a curved strip, in such a way that the red point ⊙ is shielded by all the current lines in the curve, whereas all the other points surrounding the strip are less affected. Adapted from [44] and [45].

Albrecht *et al.* [46] also use the d-lines angle as a measurement of the J_C anisotropy in thin films, as presented in Figure 16. In their paper, the authors use the Bean model for thin films to write the relation

$$\frac{J_{C1}}{J_{C2}} = \tan\alpha, \tag{2.25}$$

for a sample whose edges are perpendicular to each other. If $\alpha < 45°$, J_{C2} is larger than J_{C1}. Nevertheless, for $\alpha > 45°$, J_{C1} is higher. This is useful for anisotropic films, such as the one in Figure 16, in which there is an anisotropy induced by a patterning in the substrate, prior to the film deposition.

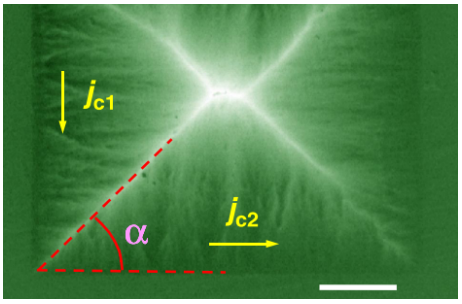

Figure 16: MO image of the remanent state in an anisotropic MgB_2 film at 12 K (the white bar at the bottom is 1 mm long). The angle α indicates the orientation of the d-line. Adapted from [46].

The Bean model is not able to describe some practical situations. For certain values of temperature and applied magnetic field, there may be thermomagnetic instabilities and consequently flux avalanches, a scenario that cannot be accounted for by any critical state model.

2.5 Flux avalanches in thin films

Once called vortex avalanches, these intriguing phenomena in superconductors have been intensively studied in the last 50 years, if one sets as a starting point the work by de Gennes *et al.* in 1966 [47]. Figure 17 shows a magnetic moment *vs* applied magnetic field curve for a Pb thin film, where the flux jumps produce a saw-like curve, which is today seen as a typical signature of flux avalanches. This sudden change in the superconductor magnetization is not only a purely magnetic effect, but it also depends on the thermal properties of the material.

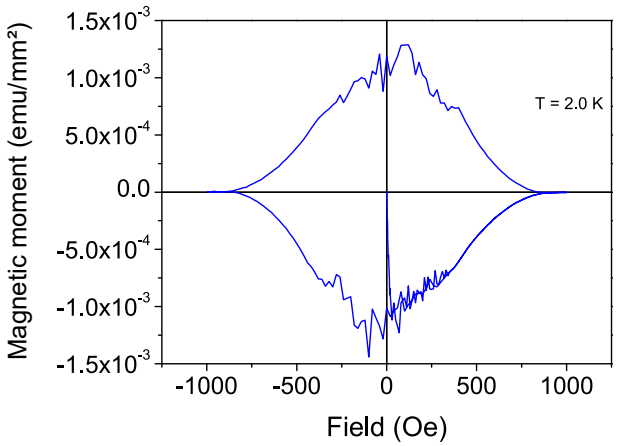

Figure 17: Magnetic moment *vs* applied magnetic field for a 100 nm thick Pb film, covered by a Ge layer, at $T = 2$ K. The noisy behavior is ascribed to flux avalanches in the superconductor.

Figure 18 (a) shows a magneto-optical image of a superconducting MoSi film that was invaded by a dendritic flux avalanche after a ZFC procedure followed by a field increase. The velocity of flux avalanches rushing into the sample is orders of magnitude higher than the speed of sound in the same materials. In general, the crack-like structure of the branches resembles that of mechanical cracks, with a tangible advantage: one can erase them by setting the temperature of the sample above T_C and starting the experiment again. In Figure 18(b), there are three different magneto-optical images of a V_3Si sample in the same value of the applied field and temperature taken in three different runs, each one with a basic color (red, green, and blue), after a ZFC. They are combined in the image at the bottom to show another important property of flux avalanches: their occurrence is stochastic.

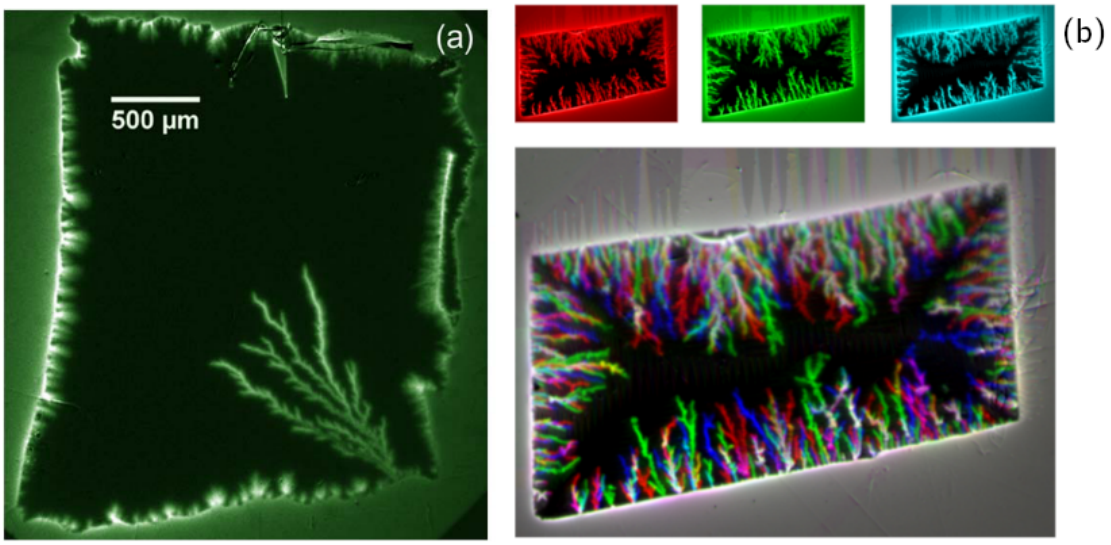

Figure 18: MO image of a MoSi film after ZFC followed by a field increase (a), same procedure for a V_3Si thin film is shown in panel (b). Three different experiments are shown simultaneously at the bottom, and only the white color features are the same for the three experiments.

2.5.1 Flux avalanches avoid each other

One of the first statements that flux avalanches avoid each other is in Ref. [48] while describing the dendritic flux patterns in MgB_2 films. Figure 19 summarizes their findings showing a sequence of MO images, after a ZFC procedure down to T= 3 K and increasing the field up to 180 Oe. Avalanches are not so branched in such conditions, and all their branches seem to avoid each other during their way through the sample (c). Panels (d) and (e) focus on the substantial direction change of one single branch.

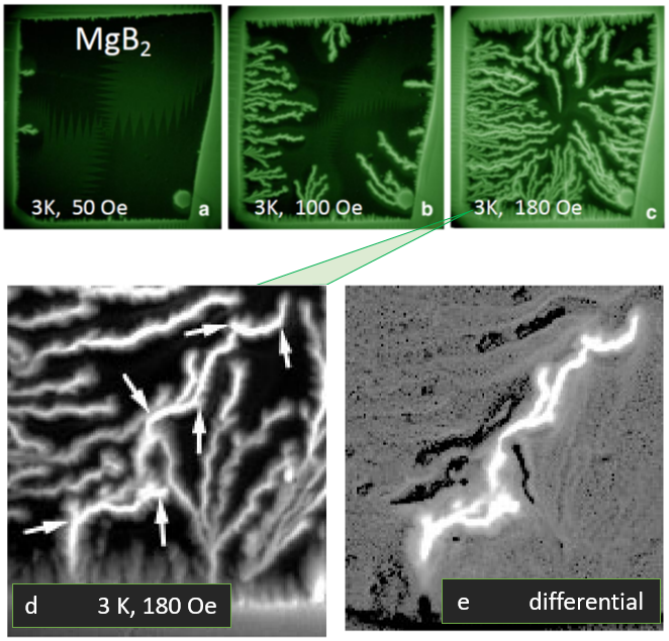

Figure 19: Example of flux avalanches avoiding each other. From (a) to (c), increasing field at constant temperature after a ZFC procedure. (d) Zooming in the last dendrite, indicating the points where it changed its growth direction. (e) Differential image of the image used in (d). Adapted from [48].

2.5.2 Anti-avalanches

Antiflux avalanches or simply anti-avalanches occur when we are decreasing the applied magnetic field in a superconducting film after keeping some flux trapped inside the sample. Some authors [41] describe that the reversal of the shielding currents at the borders of the sample produces a source of antiflux even while the applied magnetic field is still on the positive side. In Magneto-Optical experiments, they usually are seen in the opposite color of the "conventional" flux avalanches. The first remark on antiflux avalanches is their higher threshold temperature, ascribed to the extra heat released due to vortex-antivortex annihilation. In a HT diagram, the antiflux avalanches occupy an instability area larger than the corresponding area for flux avalanches [49].

The annihilation zone

Following the description given by Frello *et al.* [50], the annihilation zone is a boundary of zero flux density dividing the regions of flux and antiflux, that coexist due to the application of a moderate reverse field in a sample which already had flux

trapped by pinning. This terminology has been used to describe the contour of antiflux avalanches in some works, as summarized in Figure 20. Panel (a) shows a MO image of a $NbBa_2Cu_3O_{6+x}$ single crystal after a ZFC down to $T = 78$ K, and the application of 1000 Oe and -750 Oe, subsequently, and then removing the applied field and letting the sample in the remnant state. Panels (b) and (c) show dendrites of anti-flux in which the annihilation zone is in black.

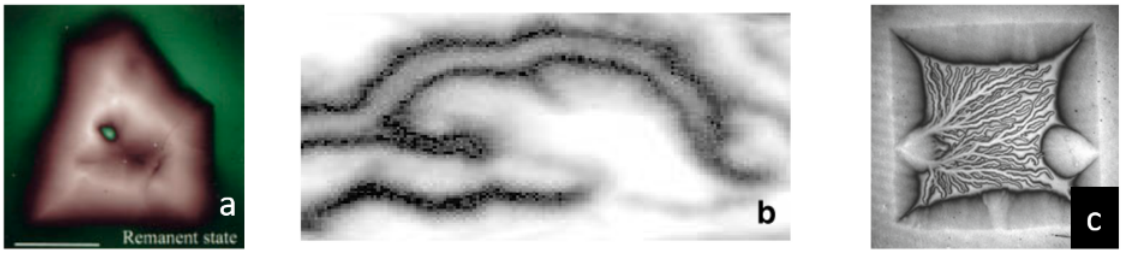

Figure 20: A few existing examples of MO images where the authors describe an annihilation zone: (a) A $NbBa_2Cu_3O_{6+x}$ single crystal [50] at $T = 78$ K in remanent state (green is for positive fields, and red for negative fields), (b) a MgB_2 thin film [48], and (c) an YBCO thin film [51]. In all panels, the annihilation zone is indicated in black.

2.5.3 The thermomagnetic model

The most successful model to describe both the finger-like and the dendritic flux avalanches in superconductors is the thermomagnetic (TM) model. This model does not depend explicitly on the basic superconducting parameters (such as λ and ξ), but its relation to the superconducting material comes from a nonlinear current-voltage power law that describes very well the type-II superconducting behavior [52],

$$\vec{E} = \frac{\rho_0}{d}\left(\frac{j}{j_c}\right)^{n-1}\vec{j}, \tag{2.26}$$

where $\vec{j}$ is the sheet current, whose relation with the current density is $\vec{j} \cdot d = \vec{J}$. Also, $j = |\vec{j}|$, ρ_0 is the resistivity constant, and n is the creep exponent. In this context, the TM model can be written for a superconducting thin film (H perpendicular to the film surface), deposited on a substrate that is its only non-negligible heat exchanger, based on

the heat diffusion equation, the Ampère law, and the Faraday law:

$$c\frac{\partial T}{\partial t} = \kappa_0 \nabla^2 T - \frac{h_0(T - T_0)}{d} + \frac{\vec{j} \cdot \vec{E}}{d}, \tag{2.27}$$

$$\vec{\nabla} \times \vec{B} = \mu_0 \vec{J}, \tag{2.28}$$

$$\vec{\nabla} \times \vec{E} = -\frac{\partial \vec{B}}{\partial t}, \tag{2.29}$$

where c is the superconductor heat capacity, κ_0 is the thermal conductivity, d is the film thickness, h_0 is the coefficient for heat transfer to the substrate, T_0 the substrate temperature, and T the film temperature. The TM model suits the well-established idea that the avalanche triggering is due to a thermomagnetic instability (TMI) - that is why one needs to know the heat diffusion dynamics in the films, which is obtained by solving the above four equations together. In a general form, one can state that a TMI will occur when the magnetic flux diffusion (D_m) is higher than the heat diffusion (D_t) [53], which can be summarized by the dimensionless parameter τ:

$$\tau = \frac{D_t}{D_m} = \mu_0 \frac{\kappa_0 \sigma}{c}, \tag{2.30}$$

where σ is the electrical conductivity. The TMI occurs for $\tau \ll 1$, i.e., if the magnetic diffusion is much larger than the heat diffusion, when there is no time for the heat to spread out in the superconducting material, and so even the motion of small quantities of flux (that releases heat) can trigger flux avalanches, which will grow following the positive feedback displayed in Figure 21.

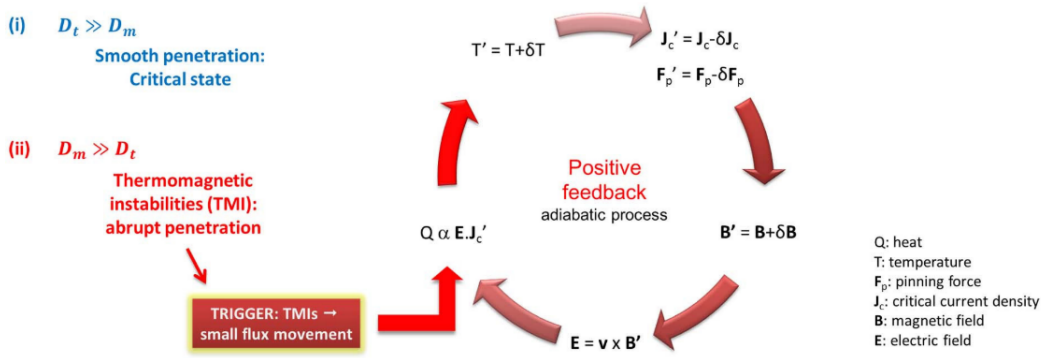

Figure 21: Schematic diagram of a positive feedback cycle leading to flux avalanches. Kindly yielded by Prof. M. Motta, adapted from [54].

When $\tau \gg 1$, the TM model also describes well the flux distribution in the superconducting film, which occurs as a smooth flux penetration. Once all superconducting parameters seem to be, somehow, functions of T and H, so are those used in the TM model. The TM model also predicts the existence of a threshold flux penetration depth (ℓ^*) - a value for the flux penetration from which the flux avalanches take place in the sample. For a long strip ($2w$ width) one can write [55]:

$$\ell^* = \frac{\pi}{2}\sqrt{\frac{\kappa T^*}{EJ_C}}\left(1 - \sqrt{\frac{2h_0 T^*}{ndEJ_c}}\right)^{-1}, \tag{2.31}$$

So, ℓ^* is a **function of** J_C (and a lot of other parameters). In Equation 2.31, T^* has the meaning of

$$T^* = -\left(\frac{d\ln J_C}{dT}\right)^{-1} \tag{2.32}$$

If there is a ℓ^* and ℓ is a function of H for a given temperature T, one can also identify the threshold magnetic fields (H^{th}):

$$H^{th} = \frac{J_C d}{\pi}\text{arccosh}\left(\frac{w}{w-\ell^*}\right), \tag{2.33}$$

and the upper H_2^{th}, which occurs when $\ell^* = w$. Another useful tool coming from the TM model is the discussion of the avalanche triggering using an H-J_C diagram, as shown in

Figure 22(a) for the same sample shown in Figure 16 [46]. Panel (b) shows that, if J_C is small enough, as when the temperature is close to T_C, no matter the intensity of the applied field, the superconductor will not enter in the TM instability zone. On the other hand, as it is shown in (c), for higher values of J_C, small variations of the critical current density will result in a similar H_1^{th}. As we will discuss in Chapters 6 and 7, for samples in which J_C is expected to vary, one also expects to detect J_C variation by identifying different values of H^{th} at higher temperatures.

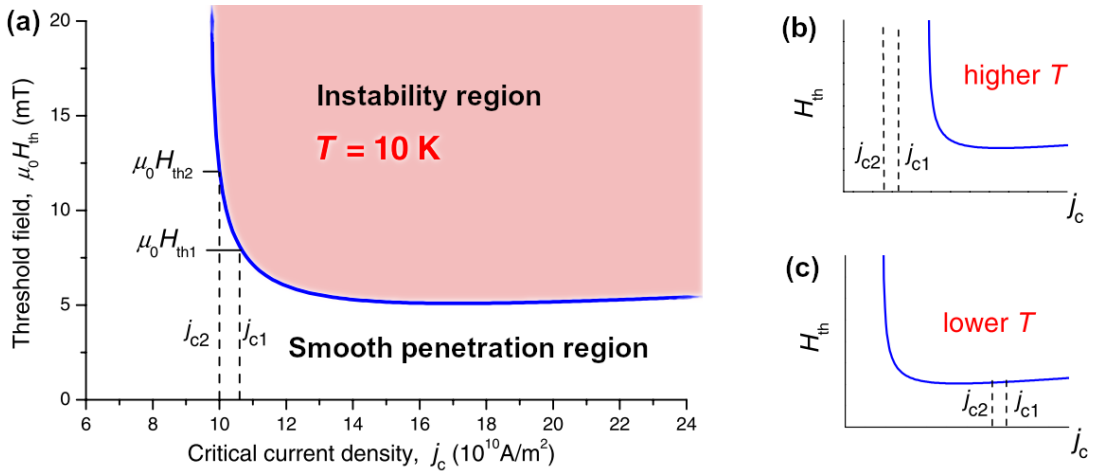

Figure 22: (a) H-J_C diagram showing the threshold field for the dendritic TMI as a function of J_C, calculated using the Equations 2.31 and 2.33. (b) Diagram for higher temperatures (close to T_C). (c) Diagram for lower temperatures. Adapted from [46].

2.5.4 Flux avalanche simulations using the TM model

The use of the TM model to describe flux avalanches not only suits surprisingly well the experimental data as it allows one to access some information unachievable by experimental means. The new information the simulations revel is the temporal evolution of the thermal component and the electric field component of this dynamics. Figure 23 shows these numerical simulations for a dendrite in its first 52 ns of existence, considering the maps of flux density (a), current density (b), temperature (c), and electric field (d). Figure 23 also compares a numerical simulation using the TM model (e) with a magneto-optical experiment (f) in samples with identical geometry and in similar conditions of magnetic history, field, and temperature.

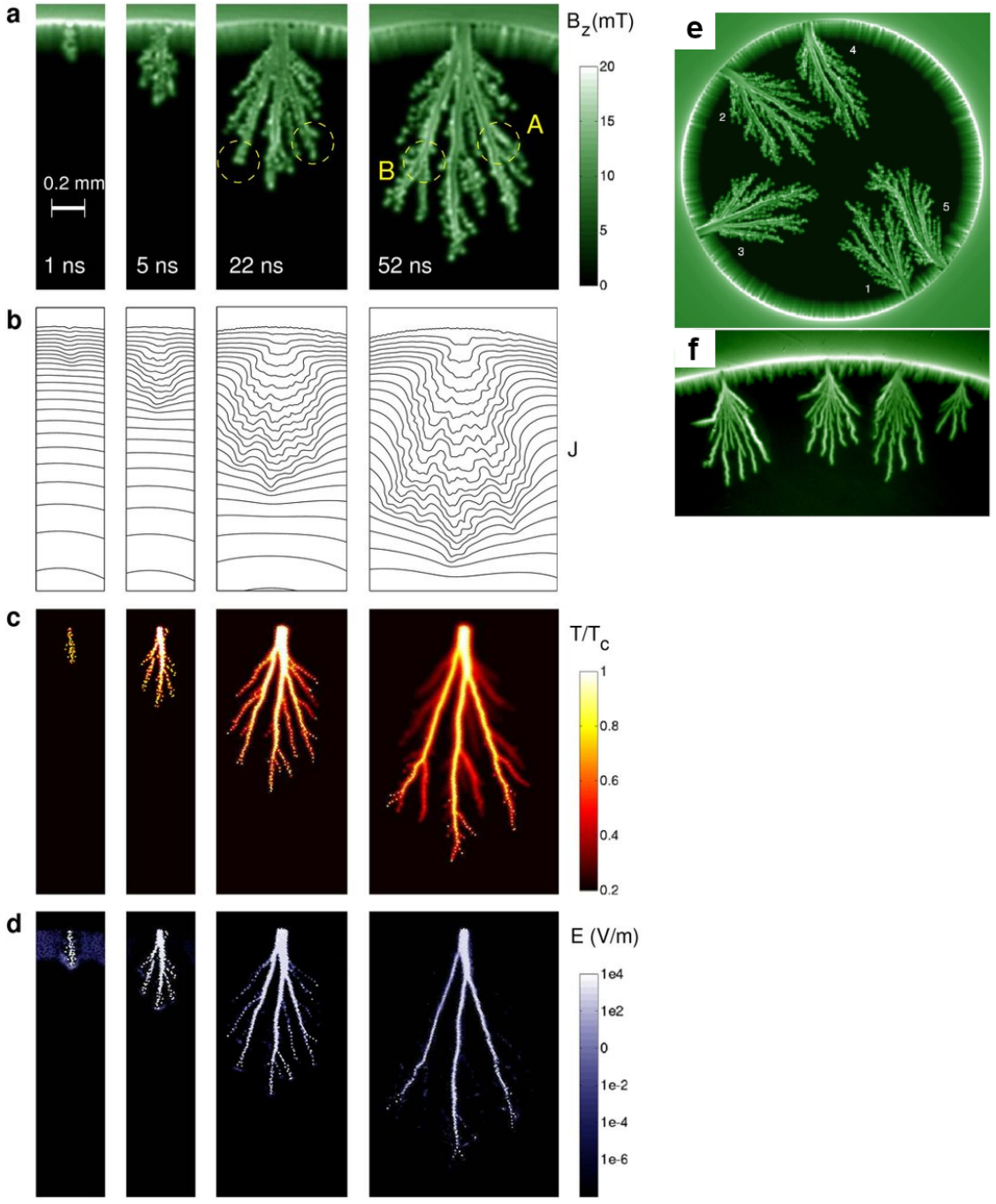

Figure 23: Distributions of the magnetic flux density B_z (a), the induced sheet current J (b), the temperature T (c) , and the electrical field E (d), after nucleation of the thermo-electromagnetic instability in different frames, indicated in planel (a). (e) Simulated superconducting disk after five flux avalanches occurred in the sequence indicated by the numbers as the applied field was increased from zero to $\mu_0 H_a = 8.5$ mT, to be compared with the magneto-optical image of the flux density in a superconducting MgB_2 film cooled down to 6 K and then exposed to an applied field of 3.8 mT (f). Adapted from [56].

Row (a) of Figure 23 shows the evolution of the magnetic flux B_z of a flux avalanche. In the first frame, the magnetic pressure at the sample edge can be seen as

the brightest region. As the avalanches rush into the sample, the magnetic pressure at the sample edge decreases. Row (b) shows the deviations of the current lines due to the dendritic structure, while (c) shows the local temperature evolution. The latter is rather important because it allows one to label the phenomena as flux avalanches instead of vortex avalanches, once the core of the structure reaches $T > T_C$ for a few moments, which allows one to state that what enters into the sample during this short period of time is not quantized vortices, but continuous flux. The large electric field E in the locations of high temperature, shown in row (d), is compatible with the electrical resistance of the film in the ohmic state. The simulated flux avalanches have all the properties that one expects from a thermally driven avalanche: it heats (even above T_C) the material along their paths and shows a supersonic flux propagation.

2.5.5 Beyond the thermally driven flux avalanches

Different from what one can obtain from the TM model, not all the flux avalanches are thermally driven, i.e., occurs adiabatically. A recent work [57] shows that there are also dynamically driven flux avalanches, i.e., avalanches dominated by thermal diffusion ($D_m \ll D_t$), which makes it an isotropic process. The authors performed tens of thousands of magneto-optical measurements of the same sample by developing and using a flat lithographed heater very close to the sample (in this case, a rectangular Nb thin film), as illustrated in Figure 24 (a) and (b). By placing the same heating structure on the other side of the sample and using it as a thermometer, they could detect how the heat released from the heater affects the sample, and they were able to repeat the experiments enough to perform a reliable statistical analysis of these stochastic events. By defining a parameter $\epsilon = L/W$ to characterize the avalanche geometry (L is the avalanche length, and W is its width), the authors describe that when thermal diffusion dominates the avalanche shape, the dynamically driven regime leads to round-shaped avalanches ($\epsilon > 1$). On the other hand, the strong magnetic flux gradient leads to an elongated avalanche when the magnetic diffusion is higher than the thermal diffusion, and this is what makes flux avalanches thin and extended towards the sample center.

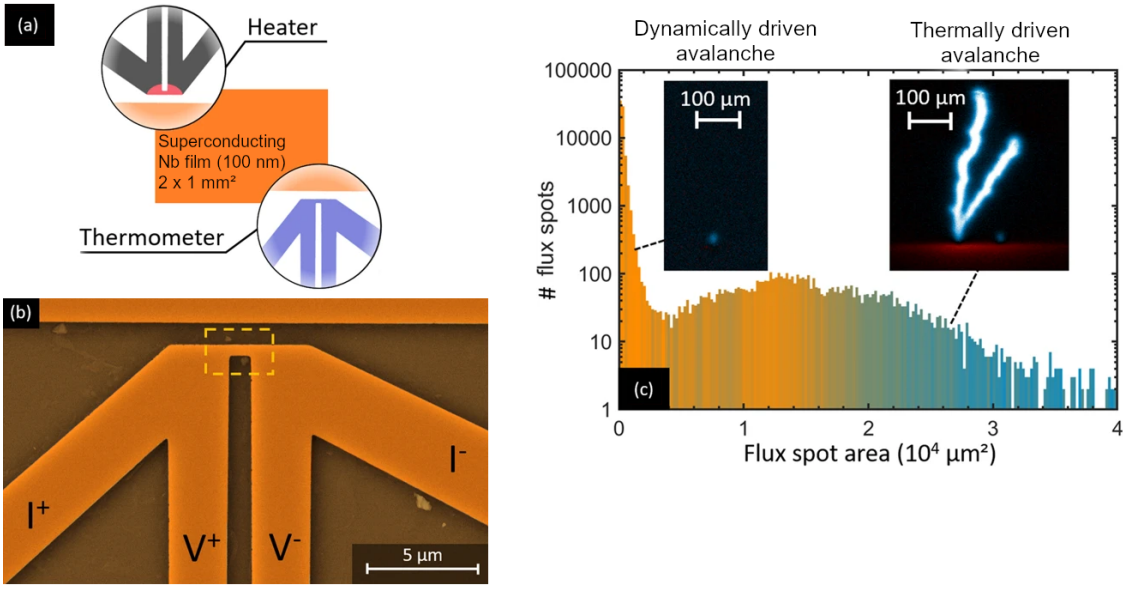

Figure 24: (a) Schematic representation of the experimental layout of the rectangular Nb film, the nano-heater, and the thermometer. (b) Zoomup in the nano-heater design made by SEM. (c) Histogram of the number of flux spots (avalanches) as a function of the flux spot area for 79726 recorded events. The color scale in the histogram refers to the mean-field to trigger the avalanche: blue is for $H = 24.75$ Oe, and orange is for 17.75 Oe. Adapted from [57].

2.6 Guiding flux avalanches

Why does a flux avalanche always rush into the sample center? Is there any way to deviate or guide the growth direction of the flux avalanches? The answers to these questions are organized in the following subsections.

2.6.1 Hybrid systems

As one discussed in the previous section, the elongated shape of the thermally driven flux avalanches is due to the strong flux gradient from the sample edges to its center. With this concept in mind, several works have been trying to guide flux avalanches, including some cases with some additional sources of the magnetic field. Brisbois *et al.* [58] have shown that an in-plane magnetized film on top of the superconducting layer can change the flux avalanche propagation direction as illustrates Figure 25. For a given magnetization orientation (a), the smooth penetration is shown in panels (b) and (c),

while the avalanche regime is in panel (d). The same can be seen in the bottom row of images [(e)-(h)], where the avalanche branches from panels (d) and (h) are clearly affected by the previous magnetization direction of the magnetic layer, shown in (a) and (e).

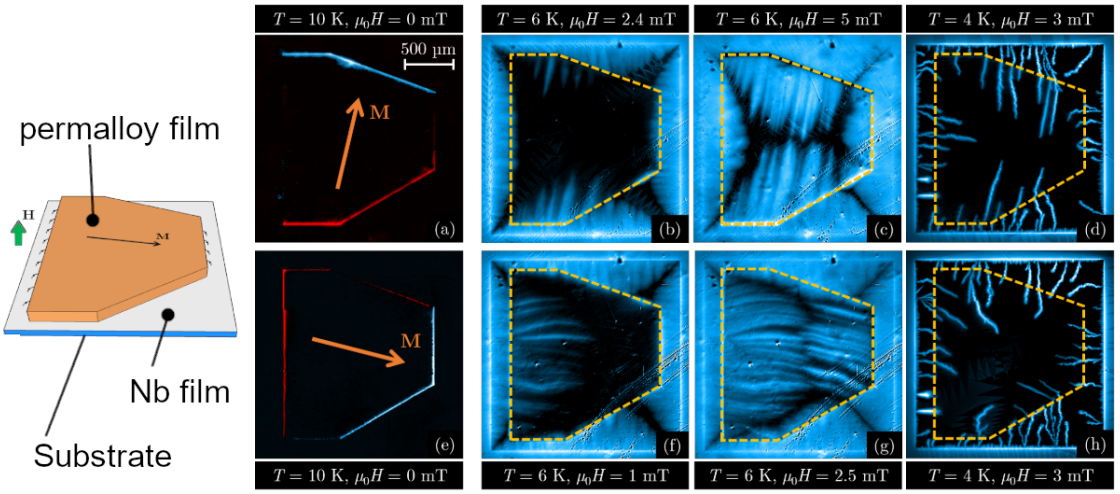

Figure 25: At left, schematic view of the hybrid sample, a Si substrate with a 100 nm thick Nb layer on top of it. A permalloy layer is deposited above the Nb film. Panels (a) through (h) show magneto-optical images of the system, with a color scale that is black for zero field, blue for fields pointing out of the page (positive), and red for field pointing into the page plan (negative field). All the images were done after a ZFC, and both temperature and applied field are shown for each panel. Adapted from [58].

2.6.2 In-plane external magnetic field

Another way to change the avalanche propagation direction is the application of an in-plane external magnetic field (H_{xy}). Carmo *et al.* [59] applied $H_{xy} = 965$ Oe in different directions, as shown in Figure 26. Yellow arrows indicate the direction of the in-plane H_{xy} (except in panel (a) where $H_{xy} = 0$). The prime panels (a') through (e') shows the smooth penetration regime, where the asymmetry in J_C can be readily seen by the d-line angles - J_C is higher in the direction parallel to H_{xy}. In panels (b) and (c), one can easily identify that the edges with higher J_C show more numerous avalanches. Despite the sample shows no appreciable change in the critical state when H_{xy} is aligned to the sample diagonal [(d') and (e')], the growth direction of the flux avalanches is always perpendicular to the higher J_C direction.

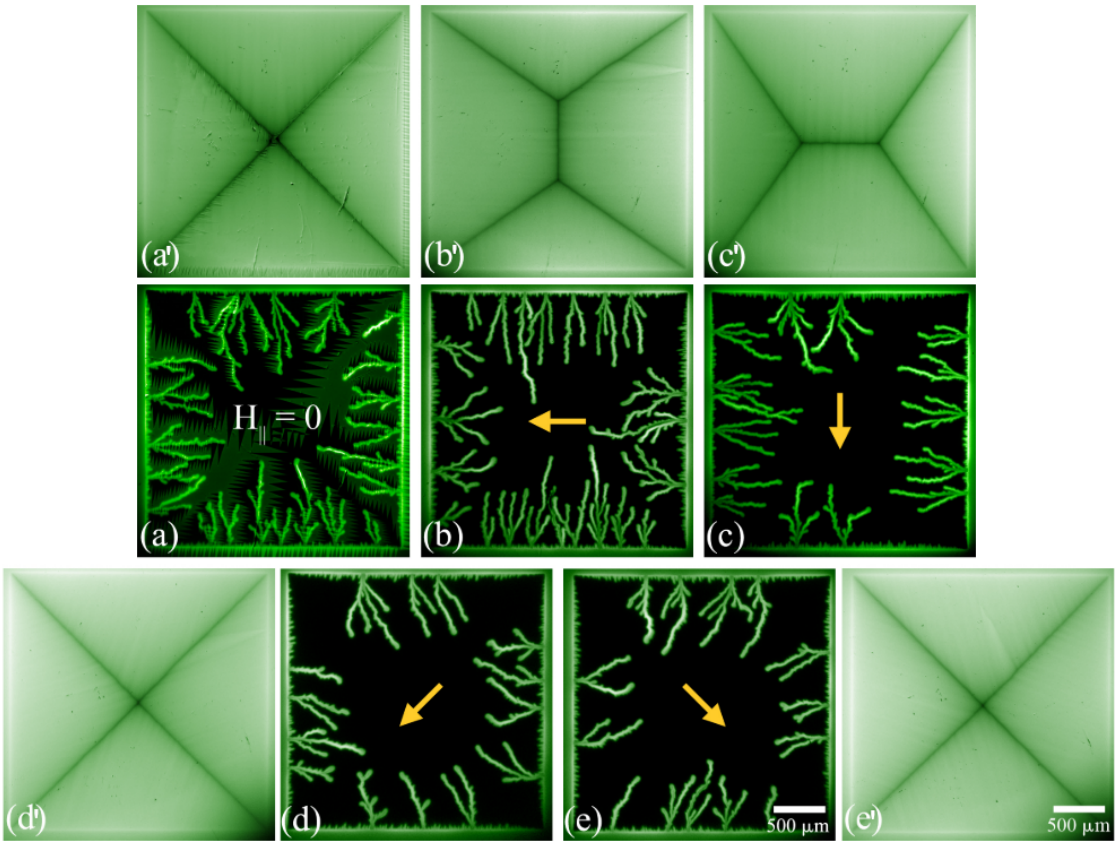

Figure 26: Magneto-optical images of a Nb thin film with an in-plane magnetic field applied in different directions. The panels (a) through (e) show the avalanche regime for each one of them, in a perpendicular field of $H_z = 33$ Oe at $T = 3.2$ K, while the panels (a') throw (e') shows the smooth full penetration state for its counterpart in avalanche regime, but in a higher field, $H_z = 220$ Oe and temperature, $T = 6$ K. Adapted from [59].

2.6.3 Patterning with artificial defects

The artificial pinning created by patterning small antidots in a superconducting film also affects the growth of flux avalanches. Figure 27 shows a MoGe thin film patterned with squares 0.4×0.4 μm^2 (antidots), whose centers are 1.5 μm apart from each other. The avalanche shape in such samples is called *Christmas tree*-like structure, due to its peculiar propagation: the main trunk is perpendicular to the edge of the sample and the secondary branches occur at 45 degrees. Basically, this fantastic shape is due to the current-crowding effect at the corners of the square antidots [60].

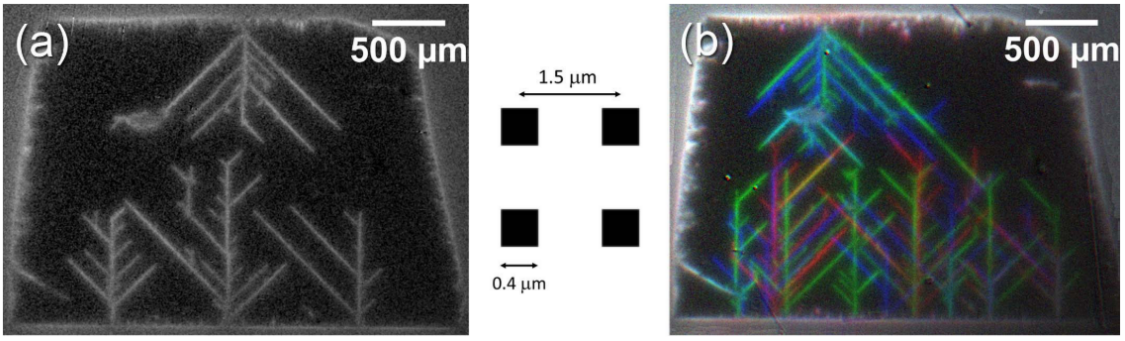

Figure 27: Magneto-optical images of MoGe thin film at $T = 4.5$ K and $H = 1$ Oe applied perpendicular to film (a). Superimposing similar experiments ran three times one has the image in (b), where images corresponding to different runs were artificially colored red, green and blue. Adapted from [61].

2.7 Superconducting thin film with varying J_C

All the concepts presented earlier allow one to appreciate better the work from Lu *et al.* [62], in which they simulated a superconducting thin film numerically with three different values of J_C in different regions of the same film. Figure 28 summarizes their main findings related to one of the subjects of this thesis. Panel (a) shows the film geometry and the value of J_C for each constitutive stripe of the film. Panels (b) and (c) show the magnetic flux distribution in the film at $T < T_C$ and increasing field from the virgin state at different temperatures. In the first image of panel (b), one can appreciate the smooth flux penetration, deeper in the lower J_C slab at the left, and smaller in the higher J_C slab at the right. In this simulation, the discontinuity vertical line at the borders, where J_C suddenly changes, seems to act like a defect and trigger avalanches. In the row of images (c), one can identify the difference of the avalanches of the two extremity edges, in size and number: the lower J_C shows less and bigger avalanches, while the high J_C edge shows more and smaller avalanches.

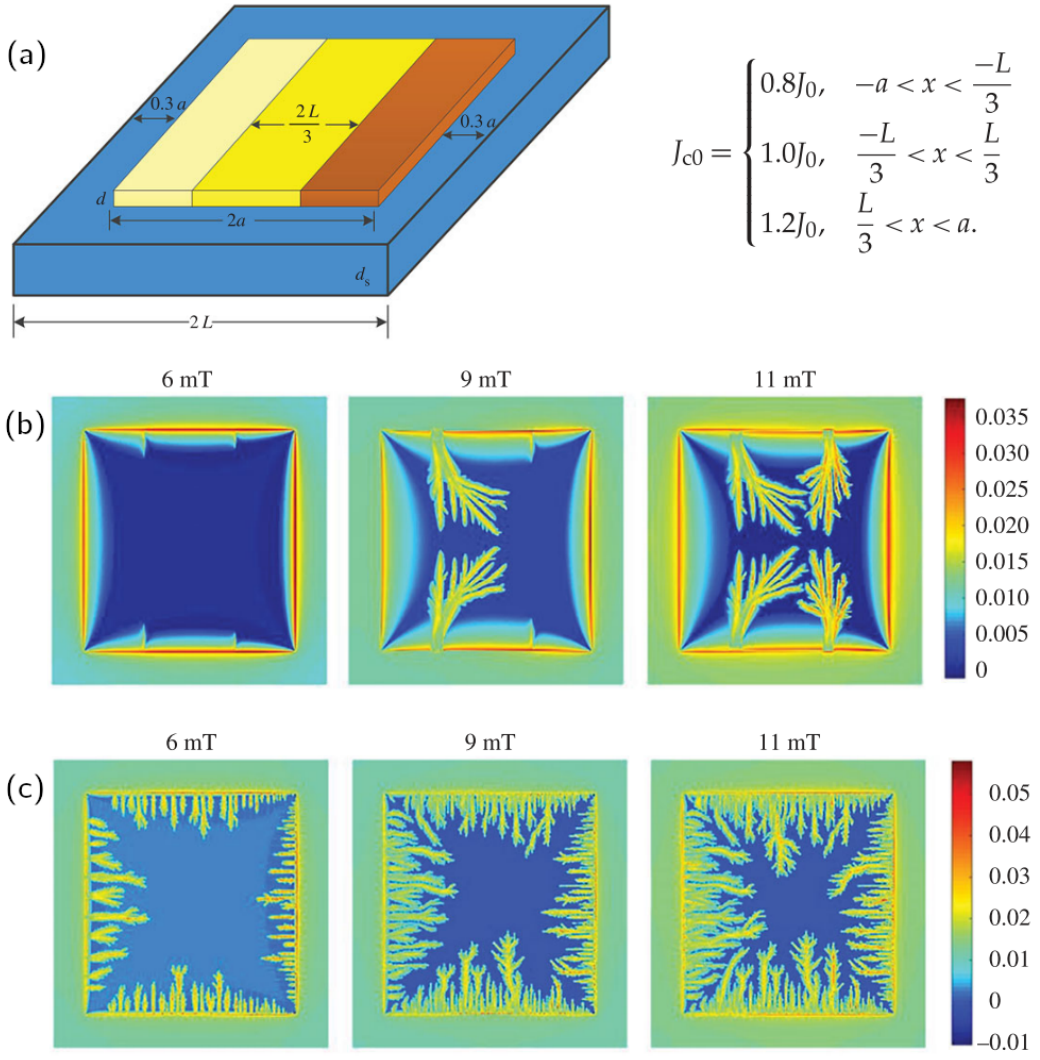

Figure 28: (a) Schematic representation of the sample and the J_C for each slab of the sample. In the two rows at the bottom, B_z maps of the sample for increasing fields after a ZFC, at $T = 0.5T_C$ (b) and $T = 0.25T_C$ (c). Adapted from [62].

2.8 Bi-layered superconducting films

We will adopt the term "bi-layered" to refer to a sample made out of two layers of superconducting films, even when there is an insulating layer separating the superconducting films, or when there are non-superconducting covering layers. The study of the effects of superposing two different superconductors begun in the 1960 decade, by two distinct groups: Giaever & Megerle, while studying tunneling phenomena, in 1961 [63]; and Hauser & Theuerer, aiming to investigate the interference of the superconducting state

from one layer on the other one, by measuring T_C as a function of the lead film thickness, deposited on the top of aluminum films [64]. At that time, they had the first experimental evidence that the resistive behavior in superconductors in certain conditions of temperature, applied field, and current were due to vortex motion, also by Giaver [65, 66]. Figure 29 (a)-(d) illustrates the circuit and the main results of those works.

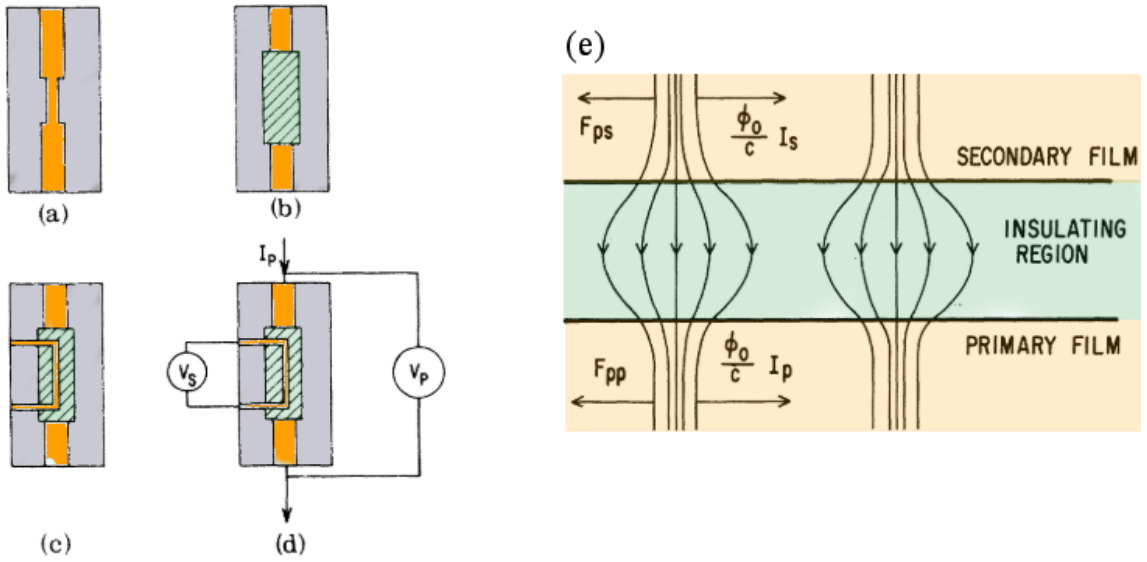

Figure 29: The Giaver circuit - if one creates magnetic flux in one layer by passing a DC current through it, one will create vortices in this layer. The extension of these vortices can generate vortices in the other layer. Adapted from [65, 66].

The two Sn circuits are insulated from each other by a thin SiO_2 layer. The larger circuit, called primary, is used to drive a current. So, below T_C, when a small DC current is driven through the primary, one was able to measure a potential difference in the secondary. Panel (e) shows a schematic explanation for this response: Both superconductors remain coupled if the insulating layer is as small as the vortex inter-distances. The authors used a voltage low enough to avoid tunneling effects, so there is no electric coupling between the two films, only the magnetic coupling. Once there is no transient electric field effect due to the constant current in the primary, the voltage in the secondary may be ascribed to the vortex movement.

At the end of the sixties, there was also a superconducting data storage device using superimposed films, created and patented by Lacroix [67], where the bit of information is stored as a persistent superconducting loop in a sandwich of three different

superconducting films.

The superimposed films can also affect the avalanche regime. Recently, Tamegai *et al.* studied the critical states and thermomagnetic instabilities in three-dimensional nanostructured superconductors [68], i.e., stacks of unconnected Nb strips, insulated from each other by SiO_2, as illustrated in Figure 30. The MO images from panels (a) through (e) reveal Nb stripes with width and thickness of 20 um and 300 nm, respectively. Each layer is insulated from the others by a 300 nm thick SiO_2 layer. In that work it was shown that flux avalanches can start in one layer and end at another.

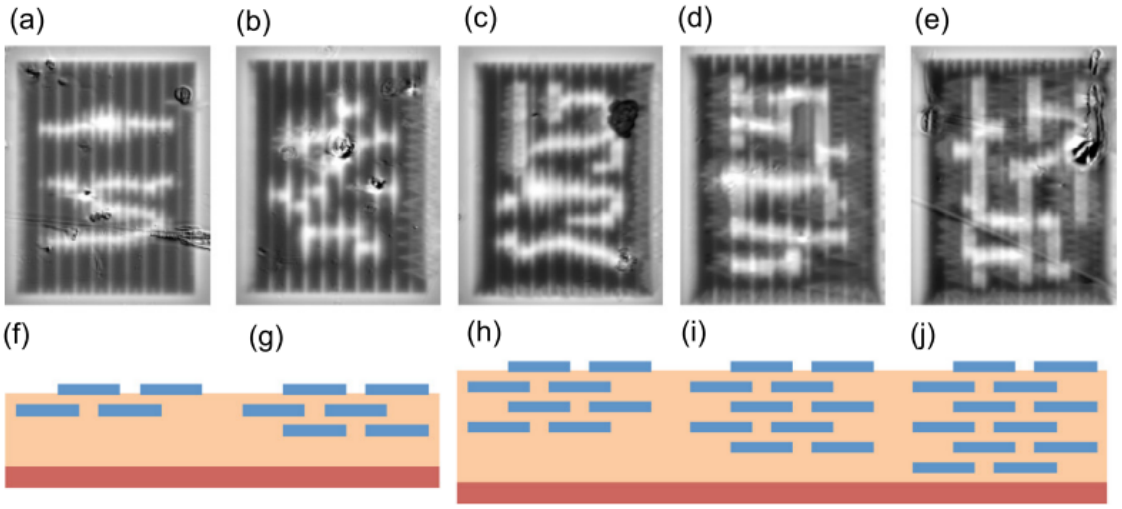

Figure 30: Magneto-Optical images of flux avalanches at $T = 5$ K in shifted strip arrays with different numbers of layers (a) 2-layers (70 Oe), (b) 3-layers (100 Oe), (c) 4-layers (130 Oe), (d) 5-layers (160 Oe), and (e) 6-layers (170 Oe). Schematic Cross section of shifted strip arrays with (f) 2-layer, (g) 3-layer, (h) 4-layer, (i) 5-layer, and (j) 6-layer. The avalanches start in one strip, and end after crossing some other strips. Adapted from [68].

2.9 The proximity effect

When a superconductor and a normal metal are close enough, ξ_0 is usually taken as a dimension scale to define proximity, the Cooper pairs from the superconductor can affect the electronic state of the neighbor material, i.e., they still are bounded in the vicinity of the interface between these two materials. This phenomenon usually decreases the critical temperature of the superconductor but makes part of the normal metal to

be also in the superconducting state. It is called the proximity effect. The first paper on such subject was written by R. Holm & W. Meissner[3] [69] *Messungen mit Hilfe von flüssigem Helium XIII: kontakfwiderstand zwischen Supraleitern und Nichtsupraleitern*, in a free translation, "Measurements using liquid helium XIII: Contact resistance between superconductors and non-superconductors." The proximity effect can take place in a superconducting bi-layer made out of two different superconductors. In this case, the critical temperature of this system should be between the T_c of both superconductors and, if thin films compose the system, the bi-layer material should behave like one single superconductor, once there is only one single superconducting state (from the superconductor with higher T_c).

2.10 Nanoscaled wedge-shaped thin films

The wedge-shape in thin films, i.e., a sample of variable thickness, is usually not desired, and it is described as a drawback of the techniques that produce them [70]. Nevertheless, nanoscale wedge-shape thin films are essential in the discovery of new compounds and the improvement of their properties [71, 72], as illustrated in Figure 31. Panel (a) shows a side view of a substrate (silicon wafer, for instance) with a shadow mask on top of it. This substrate receives a non-uniform deposition of two materials, indicated in green and red. The green material has its maximum thickness on the left of panel (b), while the maximum thickness of the red material is on the right side. At the bottom part of panel (b) there is a cross-section view showing the composition profile of each sample. Figure 31(c) shows the element diffusion to produce the atomically mixed film.

[3]The same author who discovered the perfect diamagnetism of the superconducting state.

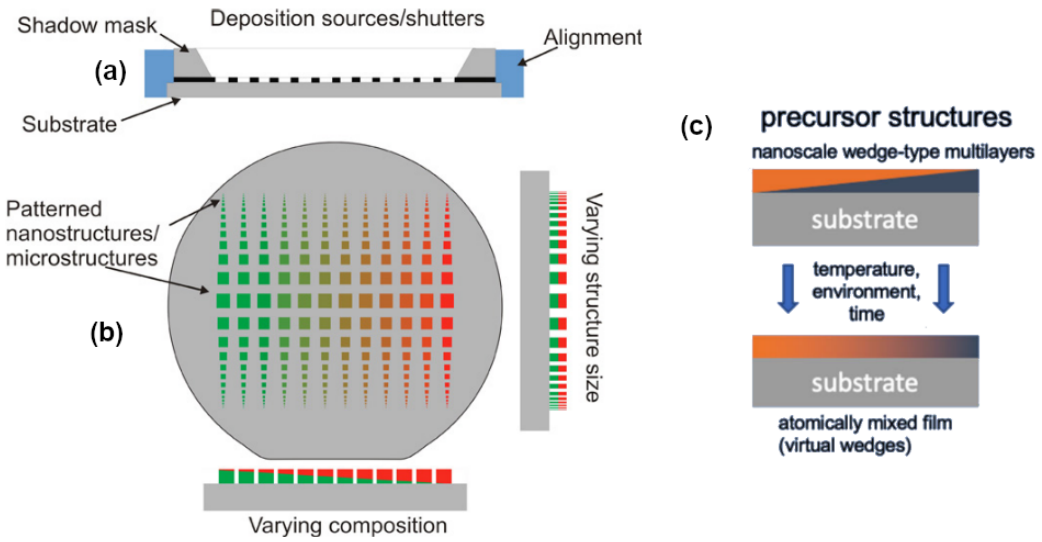

Figure 31: (a) Lateral view of a substrate-holder mounted with a shadow-mask; (b) three orthogonal views of a standard silicon substrate in which two wedge-shaped depositions were performed in opposite directions, and (c) schematic thickness profile and its application on the discovery of new materials using combinatorial synthesis and high-throughput characterization of thin-film materials libraries. Adapted from [71, 72].

Wedge-shaped thin films are also a key-feature in novel heterostructured devices such as gas sensors [73], briefed in Figure 32. Panel (a) shows a cross-section of the device profile, where the wedge-shape of the Mg is highlighted. Panels (b) and (c) describe the expectations and the positive experimental results of this system.

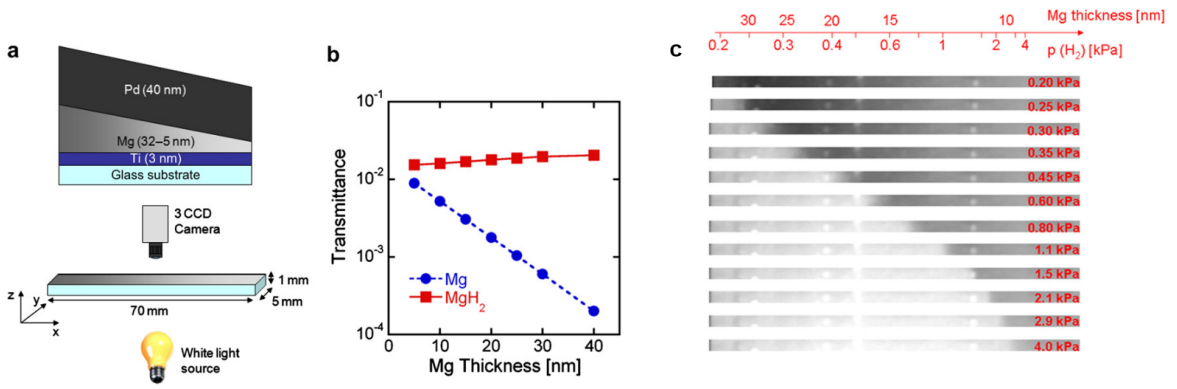

Figure 32: (a) A wedge-shaped thin film of Mg, with varying thickness along the x direction, deposited on a glass substrate $70 \times 5 \times 1$ mm^3. The Mg wedge is sandwiched between a Ti-adhesion layer 3 nm thick and a Pd-cap layer 40 nm thick. (b) Simulation of the optical transmittance of pure Mg and after the magnesium hydrogenation. (c) Sample snapshots taken at different times while increasing the H_2 partial pressure from 12 to 4000 Pa. The Mg thickness, along with the sample and the corresponding loading pressure is reported on top. Adapted from [73].

Nanoscale wedge-shape thin films have a modulated thickness, varying continuously from a maximum to a minimum - or even zero - thickness value. The processing of such wedge-shaped geometry is not a standardized domain. The methods reported to get a linear variation of the layer thickness can be separated into two categories, according to the gradient extension:

- **Linear and long-range gradient**: one can change both the position of the substrate or the source in order to enlarge the non-uniform deposition region of the substrate [73] (i); one can select specifically the borders of the substrate to achieve non-uniform thickness [74, 75], usually with a non-rotating substrate-holder (ii); Ludwig [76] described a method using a turntable and fixed shutters, by moving the substrate through the sputtering plasma (iii). A drawback of (i) and (ii) is the lack of control on the thickness gradient, i.e., the thickness variation is usually very smooth, as we explain in more details in Chapter 6. The method (iii) relies on a more sophisticated mechanical system, not necessarily available for all the deposition systems.

- **Non-linear and short-range gradient**: Such as those using a bi-layer resist shadow mask and rf-sputtering deposition [77], in which variation length is a few microns.

2.10.1 Wedge-shaped superconducting systems

Thickness homogeneity is a crucial parameter for thin film-based devices. Commercial evaporation facilities are prepared to keep the distance between the substrate and the vapor source in a safe range - usually from 10 to 20 inches - which allows few squared centimeters for standard sizes on silicon wafer substrates. Within this context, variation in the thickness is undesirable, and usually, the border of the wafer is left away.

This subject has been the theme of some theoretical and numerical works but focused on mesoscopic superconductors [78, 79, 80]. In these three works, there is no explicit thickness dependence of J_C, once they deal with superconductors whose $\kappa >> 1/\sqrt{2}$. More recently, Gladilin *et al.* [81] simulated a wedge of a type-I superconductor, in the limits at which the film would show some type-II behavior concerning the quantization of flux; nevertheless, they did not discuss the J_C variation. In their simulations, samples whose thickness decreases in one direction were studied numerically using the time-dependent Ginzburg-Landau approach. Figure 33 shows the sample model and some of the calculated results. The thick sample border is a type-I superconductor; nevertheless, the thinnest border was selected to behave as a type-II, just being thin enough. In summary, their results showed that this thickness gradient modulates the vorticity of each fluxoid - starting as a fluxon (ϕ_0) in the type-II border. If one applies an electrical current, as the film gets thicker and λ decreases, the vortices began to melt, although, collectively, they still behave as an array of vortices. The authors also studied a thick sample of lead (5 μm thick) using scanning hall probe microscopy to check the numerical results about the existence of vortices even in a typical type-I superconductor. Still, the vorticity is larger than one in this case.

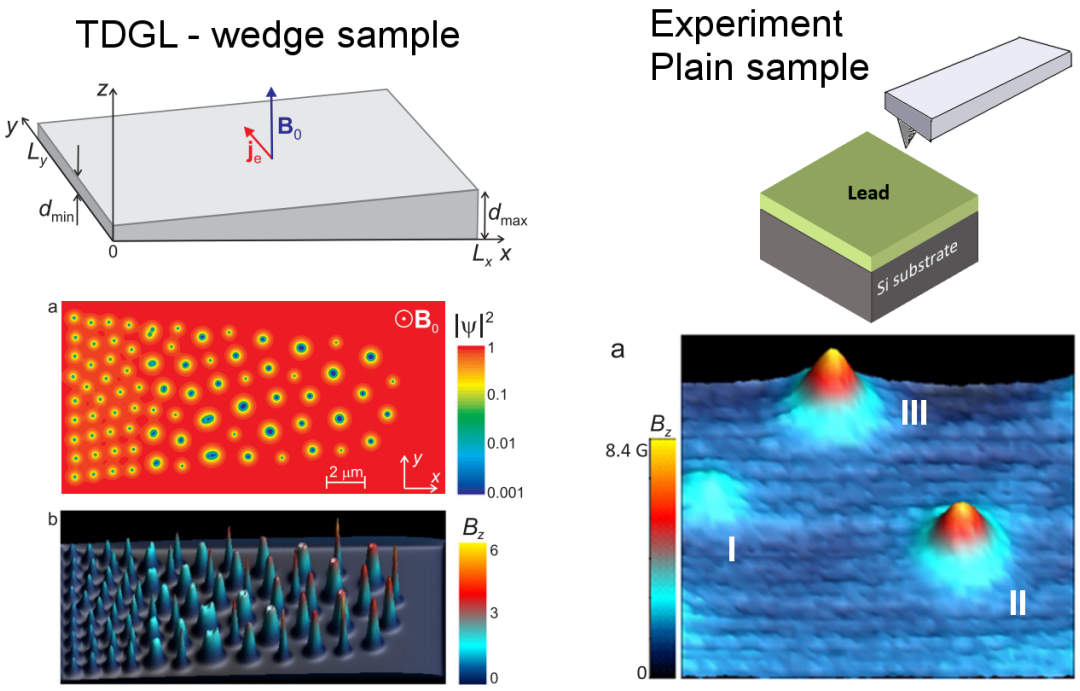

Figure 33: On top-left, the wedge-shaped film of a type-I superconductor, in the threshold between geometrical-driven type-I and type-II superconductivity used in the simulation. At the bottom left, the numerical results showing the increase in the vorticity as one looks towards the thicker part of the sample. The right column of images is for a plain film of Pb, 5 μm thick (illustrated on top), and the results from the scanning Hall probe, in which there are more than one flux quanta in each vortex. Adapted from [81].

To the best of our knowledge, experimental results of a nanoscaled wedge-shaped superconducting thin film were not reported on the literature. To deal with such a challenging task, we developed a dedicated chamber and internal apparatus, of which a brief description is one of the sections of the next chapter.

3 Experimental Methods & Materials

The present thesis deals with different kinds of superconducting materials and several experimental methods. This chapter describes the materials used to make the thin films, the different deposition techniques, and all the characterization techniques employed to conduct this study.

3.1 Superconducting thin films

A schematic representation of all the crystal structures studied in this thesis is shown in Figure 34. All images have the same scale to favor the comparison. The data used to draw these images were taken at the COD open database [82].[1]

[1]The crystallographic data about each phase were obtained from:

α-Sn & β-Sn - Oehl et al. In situ X-ray diffraction study on the formation of a-Sn in nanocrystalline Sn-based electrodes for lithium-ion batteries. CrystEngComm, 2015, 17, 8500.

Pb - Fortes, A. D. et al. Phase behaviour and thermoelastic properties of perdeuterated ammonia hydrate and ice polymorphs from 0 to 2GPa. Journal of Applied Crystallography, 2009, 42, 846-866.

Nb Schimmel, G. H. et al. Hydrogen Cycling of Niobium and Vanadium Catalyzed Nanostructured Magnesium Journal of the American Chemical Society, 2005, 127, 14348-14354.

NbN - Yen, C.M.; Toth, L.E.; Shy, Y.M.; Anderson, D.E.; Rosner, L.G. Superconducting Hc-Jc and Tc measurements in the Nb-Ni-N, Nb-Hf-N, and Nb-V-N ternary systems Journal of Applied Physics, 1967, 38, 2268-2271.

V_3Si - Wallbaum, H J; Ueber das Vanadiumsilicid, V_3Si, Zeitschrift fuer Metallkunde, 1939, 31, 362-362.

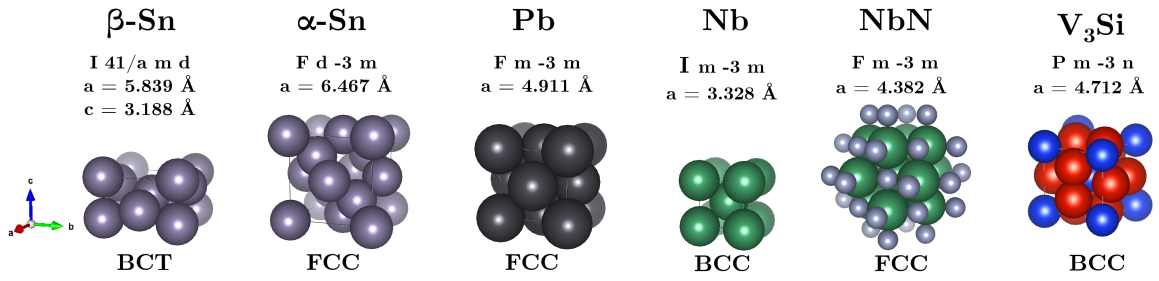

Figure 34: Crystal structures of the materials investigated here. Below the label of each composition there is the space group and the lattice parameters. The lattice symmetry is indicated below the images: BCT for body-centered tetragonal, FCC for face-centered cubic, and BCC for body-centered cubic. These illustrations were made using the VESTA3 software [83].

3.1.1 Tin - Sn

Also one of the first known superconductors, tin has two allotropic structures: α-Sn and β-Sn. The metallic phase is β-Sn, the so-called white tin. This ductile metal is a typical type-I superconductor in the bulk geometry and its critical temperature is 3.7 K [38]. Its tetragonal phase (β-Sn) is stable at room temperature, but below 13.2 °C it will slowly undergo to the α-Sn. Also known as the gray tin, α-Sn is not metallic - it is mechanically fragile and better classified as a semiconductor [84]. Recently, the α-Sn covalent structure was found to be a topological Dirac semimetal under strain and a topological insulator under stress [85]. In bulk and film forms α-Sn is not a superconductor. Nevertheless, Liao *et al.* [86] have shown that for few atomic layers of Sn deposited on top of a Bi_2Te_3 substrate, α-Sn is a superconductor whose T_c varies from 1 to 3 K, depending on the number of Sn layers (up to 20 in the Ref. [86]). Tin is also present in the 20^{th} century superconductor technology in the alloy Nb_3Sn, widely spread in commercial superconducting magnets all over the world.

3.1.2 Lead - Pb

Lead was one of the firsts known superconductors, also discovered by H. K. Onnes in 1913. This FCC heavy metal has $T_c = 7.2$ K and has the benefit of being

easily achievable in thin film shape, once it can be deposited using conventional thermal evaporation. In the bulk form, its experimental value of the penetration depth $\lambda_0 = 39 - 59$ nm [87, 88], $\kappa = 0.48$ [38]. For a 47 nm thick film, $J_C(0) = 5.26 \cdot 10^7$ A/cm^2 [29]. Although this metal has been used by the mankind for thousands of years, Pb is widely known for its toxic effects on life, and there are efforts for substituting it in its large scale applications, like paints in the past and car batteries nowadays. Nevertheless, the research of superconductivity and vortex matter can take advantage of Pb, in a safe and environmentally responsible way, by separating the etching waste material and following safety protocols, as is done for all the materials in this work.

3.1.3 Niobium - Nb

The element number 41 in the periodic table [89], niobium became famous by their critical role in steel industry, where small additions suffice to enhance the mechanical properties of structural steels [90]. Also, niobium shows a remarkable mechanical strength at high temperatures, which makes it as an important element for high performance aircraft propulsion systems [91]. In addition, Brazil has the largest world reserves of Nb ore.

Niobium is the elemental superconductor with the highest $T_c = 9.1$ K [14]. Once Nb has a very high melting temperature (and even higher boiling temperature) the usual solution to grow thin films are high energy film deposition techniques, like sputtering or laser ablation. Nb is present in state of art superconducting coils for medical applications in Magnetic Resonance Imaging (MRI) machines and particle accelerators, like the Large Hadron Collider (LHC), at CERN.

3.1.4 Niobium Nitride - NbN

This binary compound has a critical temperature $T_c = 16$ K and shows a higher critical field (≈ 44 T as a bulk [92]) than pure Nb, what makes it more suitable for superconducting technological applications [93], such as hot-electron bolometers [94], high-

frequency superconducting circuits [95, 96], single-photon detectors [97], and qubits for quantum computers [98]. Regarded from the [111] axis [99], the rock-salt structure of NbN ($a = 4.39$ Å) is formed by alternating planes of nitrogen and niobium. The occurrence of dendritic flux avalanches were already reported in this system [100], which, due to its high T_c exhibits flux avalanches in a large window of fields and temperatures. NbN films are often produced by reactive sputtering, and so were the samples used in this work.

3.1.5 Vanadium silicide - V_3Si

A member of the A15 family, which includes Nb_3Sn and Nb_3Ti, the V_3Si compound was reported to be a superconductor in 1954 [101] (bulk), with $T_c = 16.7$ K at ambient pressure [102, 103]. As a single crystal, it exhibits a highly anisotropic critical current [104] and shows a low-temperature martensitic phase transition, from cubic at room temperature to tetragonal below 30 K [105, 106]. This material also has interesting properties in the normal state, where it has been used in resistive switching memory devices [107, 108]. V_3Si has received attention recently due to the global interest in possible two-band superconductors - where ultra high-quality samples shaped as thin films are mandatory [109, 110, 111].

3.2 Thermal Evaporator Development

The ability to produce superconducting thin films matches the need for good quality samples to study Vortex Matter. So far, this lack of facilities to produce our films has been circumvented by the maintenance of good and long-lasting partnerships with some sample-making groups around the world. In 2016, Prof. Maycon Motta, Prof. Wilson Ortiz, and I recognized some interesting research concerning Pb films, such as the possibility of making wedge-shaped thin films or new patterning geometries for antidots. Prof. Joris van de Vondel, from the Catholic University of Leuven, Belgium, enjoyed the proposal and produced a batch of Pb films, including a wedge-shaped sample of Pb. The samples produced by Prof. Van de Vondel were used in Chapters 4 (Figure 56) and 7

(Figure 75). Nevertheless, these samples were not enough to fulfill our questions about this subject, and we kept employing efforts to develop a dedicated thermal evaporator facility to produce films in quantity and in the shape we need for this project. The "dedicated" information is important once Pb is a metal with a low melting point, and so it can become a contaminant for further depositions of different materials.

The roots of our project rely on some equipment seen in technical visits to the labs from Prof. Ngoc Duy Nguyen, at ULg, Belgium, and Prof. Adenilson Chiquito, at UFSCar, Brazil. Both not just explained details about their equipment but also offered support for us to build our own. Figure 35 shows a schematic illustration of a generic thermal evaporator, while Figure 36 shows a photograph of the system.

An important remark is that the first (but not only) reason to develop this chamber was to be able to produce nanoscaled wedge-shaped superconducting thin films. From first scratch to final commissioning and then to the successful preparation of the first wedge-shaped Pb film, the process took three years for design, construction, modifications and adaptions. More details about the E01 (as we labeled this chamber) are organized in Appendix A.

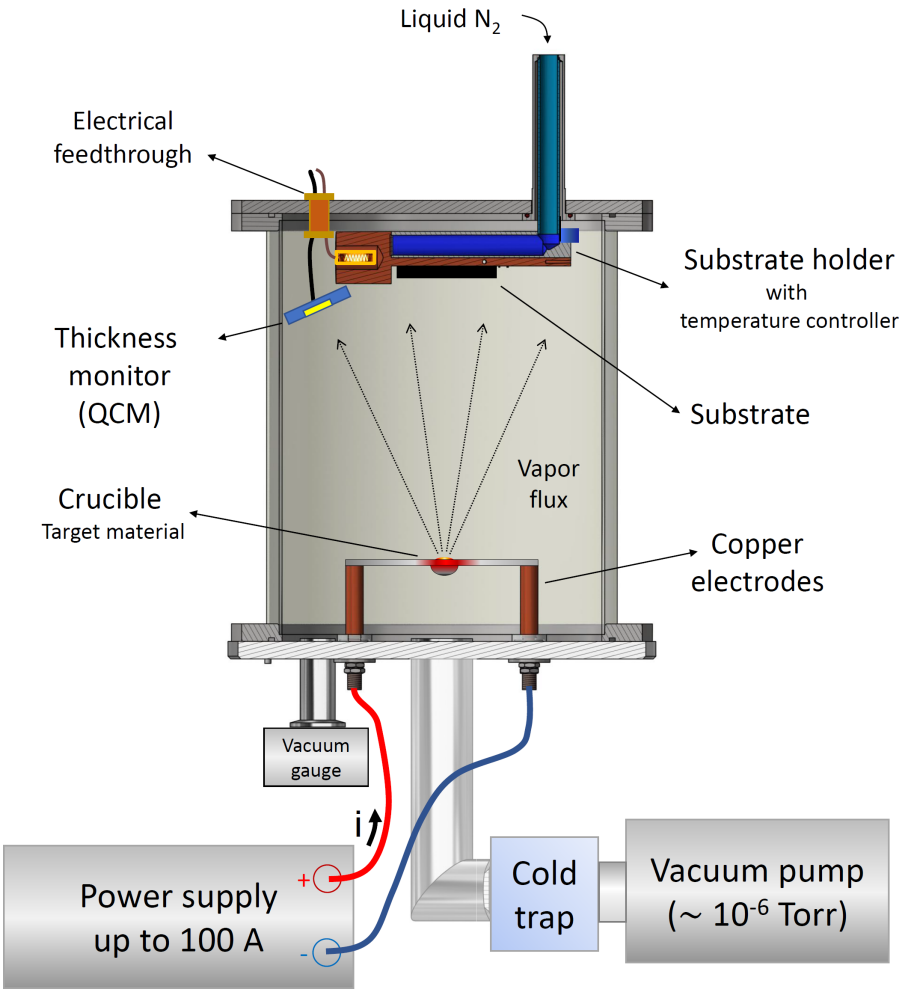

Figure 35: Thermal evaporator general scheme. The external structure of the vacuum chamber is made of stainless steel and it allows one to achieve pressures down to $2 \cdot 10^{-7}$ torr using rubber seals.

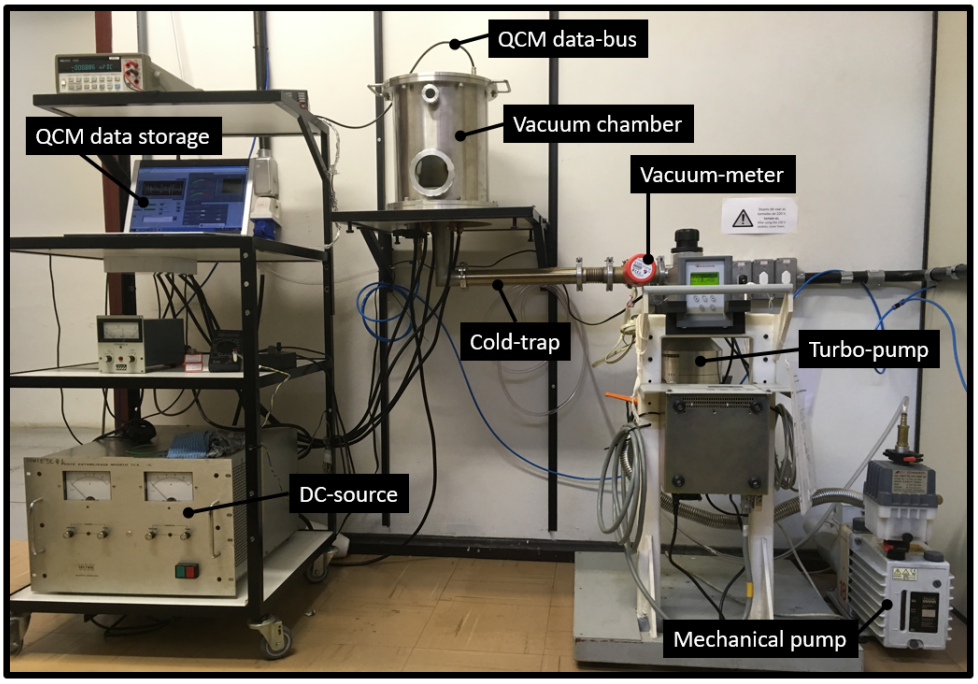

Figure 36: Photograph of the GSM evaporator facility to produce metallic thin films, called E01. The main components are labeled and indicated in the picture. QCM stands for Quartz-Crystal Microbalance, used as a thickness monitor.

3.3 Films deposition - thermal evaporation

3.3.1 Chamber setup

This section regards the samples produced in the evaporator developed in GSM. Among the parameters which can be adjusted for each deposition we can focus on:

- **The relative position and the distance between the substrate and the crucible** - the relative position between the source and the substrates reflects the expected thickness uniformity over the substrate surface, and are also important parameters to avoid unwanted non-uniform heating on the substrate holder due to radiation coming from the hot material source (specially for Ge and Sn deposition in this chamber). One also needs these distances to estimate the film thickness by weighing the crucibles before and after evaporation.

- **Substrate holder for low temperature deposition** - To avoid granularity which

can be created during the film deposition, care should be taken with the substrate temperature during the deposition process.

- **Chamber pressure during deposition** - the lower the pressure, the better the chemical homogeneity and the crystallographic uniformity, due to the larger mean free path of the atom in the vapor flux from the crucible to the substrate.

- **Oxygen getter** - Once PbO is not a superconductor, the partial oxygen pressure inside the chamber during deposition is a key aspect of the process. We did not measure this quantity directly, but we trap remaining oxygen by depositing Al or Ti on the chamber walls before the superconducting film deposition. For this, one needs a shutter (or a shield around the Al crucible) to protect the substrate.

- **Deposition rate** - also to avoid granularity in the samples one should use a constant deposition rate during the film growth. It is mandatory to use a shutter to protect the substrates while the evaporation begins then the current through the crucible is adjusted to stabilize its temperature and, therefore, its deposition rate. This is also the subject of the next subsection.

3.3.2 Temperature for metallic evaporation

This technique heats its crucibles using the Joule effect. Furthermore, the temperature needed to evaporate the metals used in this work depends on the chamber pressure and the element to be grown. Table 1 shows the evaporation temperature of Al, Ge, Pb, and Sn at reduced pressure.

Table 1: Evaporation temperatures of some metals at ambient and reduced pressures. Adapted from [112].

Element	**Melting point (°C)**	**Evaporation temperature (°C)**		
		10^{-8} torr	10^{-6} torr	10^{-4} torr
Al	660	677	821	1010
Ge	937	812	957	1167
Pb	328	342	427	497
Sn	232	682	807	997

3.3.3 Thickness monitor - Quartz Crystal Microbalance

The Quartz Crystal Microbalance (QCM) is one of the key parts of the film deposition, once it allows us to monitor the deposition rate during the process, as well as the final thickness of the films. For the samples produced in GSM, we used a homemade QCM based on the open-source project Open-QCM (https://openqcm.com/). The adaptation of the Open-QCM project to our needs was done mainly by the undergrad Physics Engineering student Otávio Abreu Pedroso, who worked especially in the electronic assembly and in a data-acquisition software. Using this software and LabView, we were able not only to record the raw data but also to correct the thickness of the films based on the QCM temperature and the geometric considerations, once the sample holder used was static. Figure 37 shows a picture of the QCM developed in GSM.

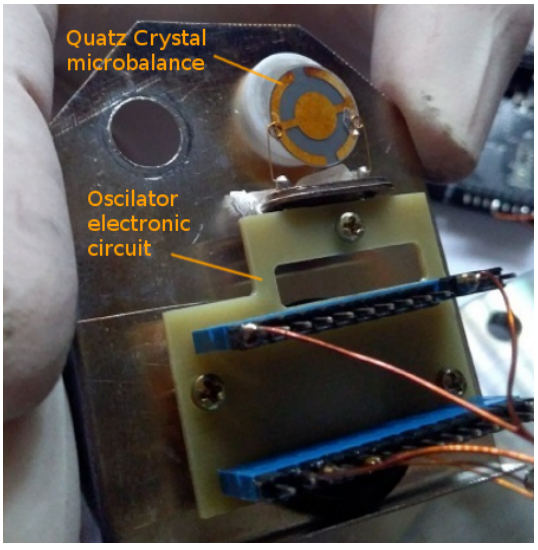

Figure 37: Photograph of the Quartz Crystal Microbalance (QCM) used in the evaporation facility at the GSM.

3.3.4 Raw materials etching

To avoid contamination during the film deposition, it is mandatory to clean the raw materials by chemical etching. For each material, one has an appropriate etching procedure, which consists of chemical solutions to oxidize and dissolute everything upon the raw material surface. We performed every etching procedure in a chemistry fume hood

located in the Sample Preparation Laboratory (*Laboratório de Preparação de Amostras*, LPA) at the GSM group in the Physics Department of UFSCar. All the etching solutions were based on the recipes used in NanOLab (UFSCar), led by Prof. Adenilson Chiquito [113]. All chemical ratios in this subsection are volumetric. The etching for the materials are described in the following list:

- **Aluminum (Al)**

  There were two different recipes used for chemical etching of aluminium, (a) a hydrofluoric acid based solution and (b) a blend of less dangerous acids:

  (a) $HF + H_2O$ (1:1)

  (b) $HNO_3 + H_3PO_4 + CH_3COOH$ (1:15:2)

  The solution (a) etches the aluminum surface in a few seconds, but its precursors are more expensive (and dangerous). Solution (b) needs one or two minutes to clean the aluminum surface, which changes its color appreciably.

- **Germanium (Ge)**

  Despite the use of a strong acid as the hydrofluoric, the solution

  $$HF + HNO_3 \text{ (1:1)},$$

  shows a slow reaction on the Ge shot surface. It took few minutes to change its surface color.

- **Lead (Pb)**

  When stored in air, lead shots shows a dark gray color and may contain not only oxidized Pb but also carbonates. To remove them, we used the solution:

  $$CH_3COOH + H_2O_2 \text{ (1:1)},$$

and we could see a fast reaction and the immediate change of the metal surface - it becomes bright and shiny. To stop the cleaning reaction, we drop the shots in the isopropyl alcohol, after diluting it three times in water.

- **Silicon substrate wafer (Si) and Sn**

  Also know as Piranha etch, the appropriate etching mixture for Sn and Si substrates is a solution of H_2SO_4 and H_2O_2, following the volumetric ratio (3:1). The prescribed protocol indicates that the hydrogen peroxide is added gently to the acid. Small quantities, such as 4 ml, were often used. Once the solution is ready, one poured the liquid on the substrates, already cleaved in the desired shape. One then waited for 30 s, while slightly moving the becker in circles. The acid solution is removed, and we diluted the remnant using distilled water, three times. Then, we removed the substrate pieces, one by one, from the beaker containing water to another one with isopropyl alcohol - the aim of this step is to avoid rings of residue left behind, as water marks, on the substrate surface. The final step is to remove the alcohol using gas flux with no water vapor, e.g., pressurized nitrogen or argon.

3.4 Film deposition techniques out of GSM - sputtering and pulsed laser deposition

3.4.1 Electron-beam physical vapor deposition

Some of the Pb films studied in this work were deposited by Prof. Joris van de Vondel in the Catholic University of Leuven (Belgium), where he used an electron-beam physical vapor deposition (e-beam) facility. In this method, an electron beam is accelerated towards a target (in this case, shots of Pb) in high vacuum (at least 10^{-5} torr), which strikes and heats the material until its evaporation (or sublimation) temperature. The main advantage of this technique is the higher temperature in the crucible (if compared to thermal evaporation).

3.4.2 DC Sputtering

In Chapter 5 (Quantitative magneto-optical imaging in Nb/NbN thin films), the samples were prepared by DC magnetron sputtering. Prof. Carmine Attanasio and coworkers from Unisa, in Salerno (Italy), provided those specimens as a request from Prof. Alejandro V. Silhanek, ULg (Belgium). This deposition technique allows one to make films not only with metals but also with ceramics. After reaching a low base pressure (usually 10^{-8} mbar), one needs to insert a small quantity of gas, such as Ar (non-reactive sputering) or a mixture of Ar and N_2 (reactive sputtering), until a pressure of $\approx 10^{-3}$ mbar. In the DC sputtering, a DC high voltage is applied between the target and the substrate, partially ionizing the remaining gas inside the chamber. The charged particles are responsible for removing the target material by successive strikes on it, and they deposit naturally on the substrate surface, as is illustrated in Figure 38.

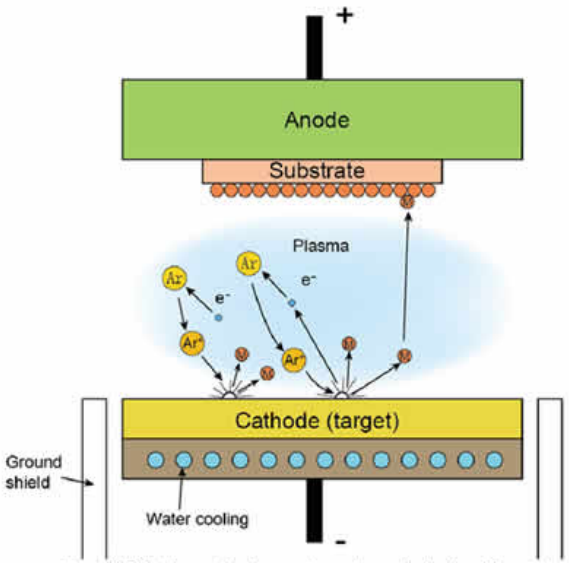

Figure 38: Schematic illustration of the DC sputtering film deposition. The substrate is electrically linked to the anode, while the target (the source of material) is in contact with the cathode. The partially ionized Ar strikes the target and releases atoms from the target to the substrate. There is usually a ground shield and a cooling system in the cathode, as well as a heating system in the substrate holder. Adapted from [114].

3.4.3 Pulsed Laser Depositon

The first wedge-shaped sample V_3Si studied in this work (Chapter 6) was made by the Pulsed Laser Deposition (PLD) technique, by Prof. Carlo Ferdeghini and coworkers, at the facilities of the SPIN Laboratory, in Genova (Italy). In his system, they use two excimer lasers and one Nd:YAG laser, coupled to two PLD systems with a multitarget carousel and an *in situ* monitoring of the growth by Reflection High-Energy Electron Diffraction (RHEED). In this technique, the target material is striked by pulses of laser in high vacuum, in order to ablate small clusters of the source material, like a plasma plume, and launch them to the substrate. PLD has the interesting feature of keeping, at least partially, the microstructure of the target material on the deposited film - which is suitable for complex system such as the high-temperature superconductor $YBa_2Cu_3O_{6+x}$ [115]. Figure 39 illustrates this feature for YBCO.

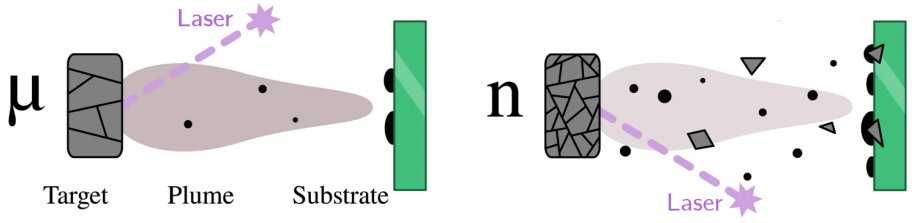

Figure 39: Schematic illustration of PLD target grain size on the growth process of the deposited film, proposed by Khan *et al.* [115]. The uniformity in the left illustration may lead one to think that microcrystalline μ-YBCO produces better films then the nanocrystalline n-YBCO (at right), but the larger fragments and the increase on the number of grain boundaries in the n-YBCO lead to a higher J_C film, due to the increase in film surface granularity when the n-YBCO is used as a target. Adapted from [115].

3.5 Characterization techniques

3.5.1 Scanning Electron Microscopy (SEM) and Energy Dispersive X-ray Spectroscopy (EDS)

The Scanning Electron Microscopy (SEM) [116] may be basically described in three steps: (1) focus an electron beam into a small spot (typically a few μm^2) in the

sample surface, usually accelerated by a voltage of the order of 10 kV focused and guided by magnetic lenses; (2) collect the intensity of electrons which are either back-scattered (BSE) or ejected from the sample, also called secondary electrons (SE); and (3), scan this spot all over the region of interest on the sample, as illustrated in Figure 40(a). Once the wavelength of the electrons collected is smaller than the wavelength of visible light, SEM allows one to achieve higher resolution than optical microscopy. Furthermore, by using a X-ray detector in the SEM facility, one can perform Energy Dispersive X-ray Spectroscopy (EDS) measurements [116], which detects the X-ray emitted by the sample after being excited by the electron beam. Since each chemical element has its own X-ray emission signature after electronic excitements, the identification of the elements is possible. Several authors [117, 118, 119] also use this technique to estimate the thickness of thin films. Figure 40 illustrates the sample-electron interaction zone, in which electrons from a beam interact with the sample, emitting back-scattered electrons, secondary electrons, and X-ray - from which the element detection and quantification is possible. An important remark is the pear-shape of the interaction zone (also described as droplet-shaped), which - for the thin films dealt with in this thesis - collects more data from the substrate than from the material under study. Also, the beam energy and the atomic weight of the elements which compose the sample also play an important role in the interaction zone size. SEM images shown in Chapter 7 were taken with a Philips XL30 FEG [120], in the Structural Characterization Laboratory (*Laboratório de Caracterização Estrutural*, LCE) - UFSCar, Brazil. SEM and EDS data in Chapter 6 were collected by a Leica Cambridge S360, equiped with the detector Oxford X-Max 20 and software Oxford AZtec 2.2(for the Energy Dispersive X-ray Analysis), in CNR Spin facilities, in Italy.

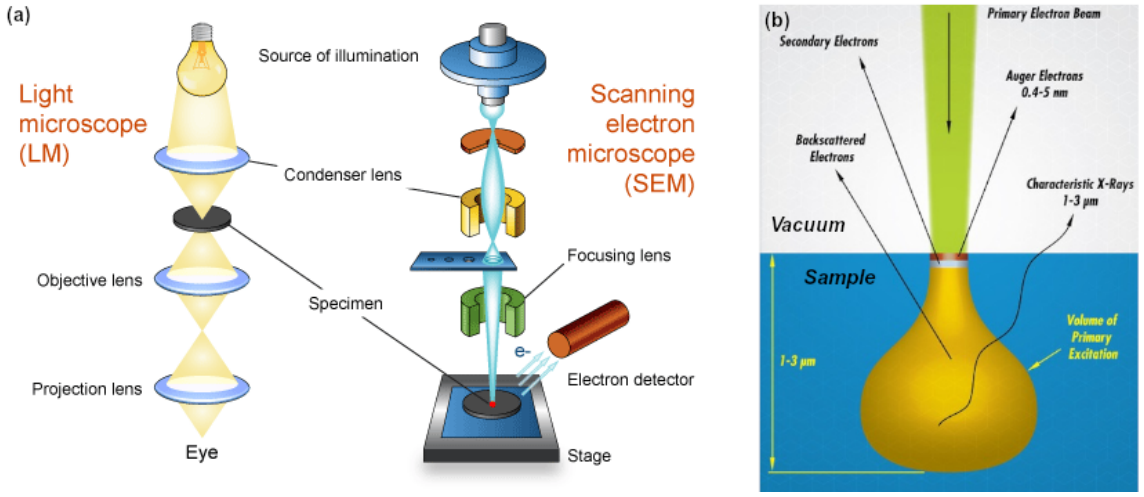

Figure 40: Comparison of the main components of (a) an optical microscope and (b) a scanning electron microscope. (c) Schematic view of the sample-electron beam interaction during a SEM experiment, in which electrons, visible light, and X-ray are produced by the intricate interaction within the specimen. Adapted from [121, 122].

3.5.2 Atomic Force Microscopy (AFM)

The Atomic Force Microscopy (AFM) is one of the most reliable techniques to investigate nano-sized samples. It is based on a very small tip at the extremity of a cantilever which scans very close to and across the surface of the sample. As the cantilever shakes, the light beam focused on it changes its angle of incidence in the detector, and this information is translated into topographic map. Figure 41 brings some pictures of the Bruker Nanoscope V AFM used in this thesis [(a) and (b)], details of the cantilever are shown in panel (c) and a scheme of the main components is presented in (d).

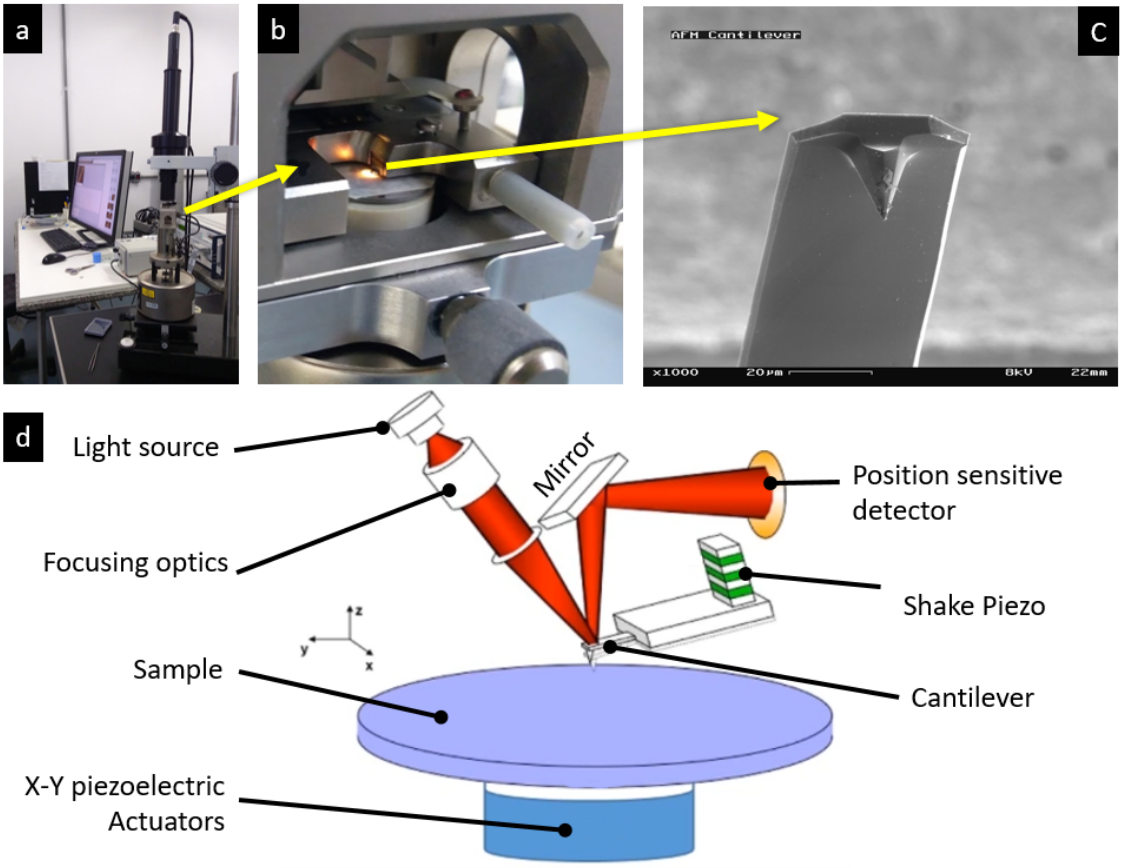

Figure 41: Photographs of the Atomic Force Microscopy of the LCE facility at UFSCar (a), and a zoomup of the working region (b). The cantilever is located in the highlighted region of panel (b), and is shown in details in panel (c). The main components in an AFM are presented in panel (d). Adapted from [123].

3.6 Magnetic measurements

The DC magnetometry has been at the core of the experimental research in superconducting materials, since the perfect diamagnetism and the existence of vortices inside the superconductor are properly revealed by this kind of measurement. In addition, AC susceptometry offers a reliable way to obtain $T_C(H)$. All the DC magnetometry and AC susceptometry measurements were caried out in a comercial MPMS 5 magnetometer from Quantum Design, in the GSM labs at UFSCar. Measurements as sensible as 10^{-6} emu are easily achievable. Such a sensitivity is due to a radio-frequency (RF) driven superconducting quantum interference device (SQUID) [124]. The temperature controller

is as precise as 0.01 K, and once the sample is in a region of stable temperature, curves of $H_{C2}(T)$ can be precisely obtained.

3.6.1 DC Magnetometry

For DC magnetic moment measurements, there is a set of coils arranged in a second-order gradiometer configuration, as shown in Figure 42 (a). This set of connected coils detects the magnetic moment of a moving sample along the z direction. The sample is mounted in a plastic straw (b) by using sewing threads and some holder, such as polymeric capsules or teflon discs. The inset in panel (a) shows what one can access when the *squid-response* data file is opened, the raw data used to calculate the magnetic moment of the sample.

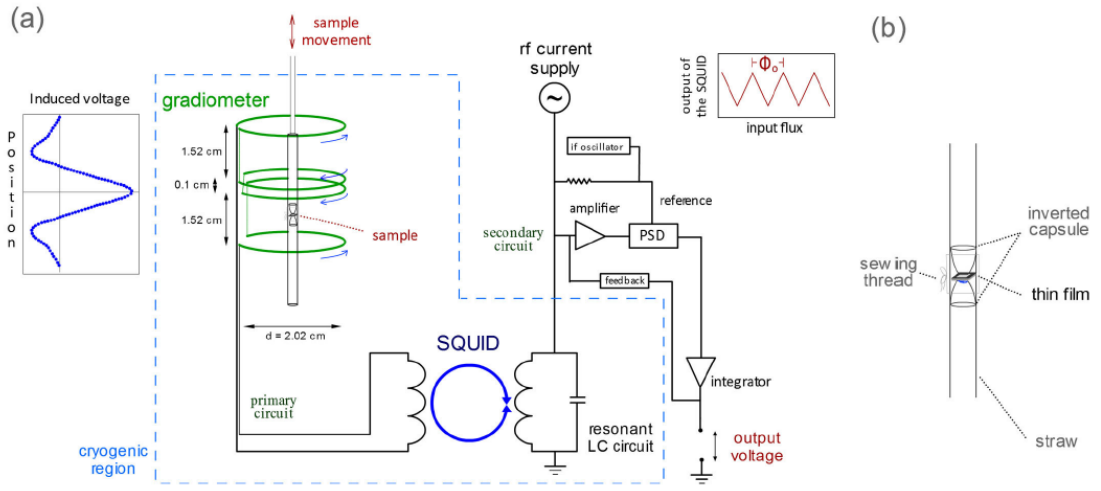

Figure 42: (a) The gradiometer schematic circuit and its coupling to the SQUID sensor. The inset shows the induced voltage as the sample is moved along the z direction. (b) Sample assembly in a plastic straw with gelatin capsules, vacuum grease, and sewing thread. Adapated from [124].

3.6.2 AC Susceptometry

All the AC susceptibility measurements were also performed in the MPMS 5 magnetometer, as illustrated in Figure 43. A Lock-in compare the AC signal from the source coil and the one coming from the detection coils. Differently from the DC magnetization measurement, the sample does not move during an AC measurement: a train

of AC pulses is used to excite the sample, which stays at rest. To eliminate background noise and existing asymmetries among the sensing coils, the measurement procedure is repeated with the sample placed in two different positions in the z axis. The MPMS 5 allows one to range the AC driver field h, i.e., the excitation field, from 0.01 to 3.8 Oe.

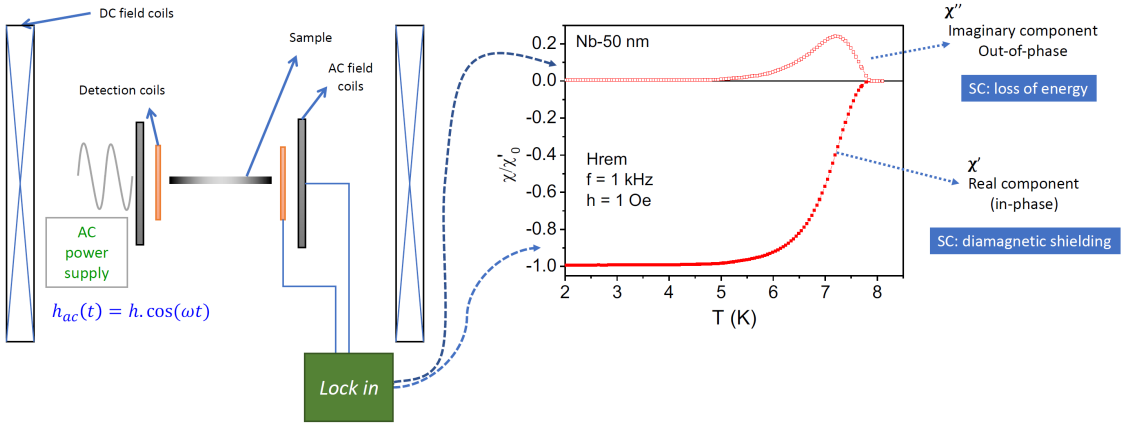

Figure 43: At the left, schematic representation of the sample space region inside the magnetometer, where one can identify the DC field coils (more external), AC field coils and detection coils. The signal from the detection coils is compared to the applied signal by a lock-in and ploted as the in-phase and the out-of-phase components of the susceptibility as a function of the temperature, for instance, in the right panel. Kindly yielded by Prof. Maycon Motta, GSM, UFSCar.

3.7 Magneto-Optical Imaging - MOI

The Magneto-Optical Imaging (MOI) is a technique that allows one to see the spatial distribution of the magnetic field through a planar surface. That is so because one uses a flat indicator film whose optical properties change as a function of the local induction field. The concept of MOI started in 1956 by the use of cerium salts as indicators, but the resolution was limited to 0.25 mm at that time [125]. Its use as a high-resolution microscopy technique began in the 1970-1980 decades and evolved side-by-side with the development of new indicators. The most important physical property of the indicator for using in MOI is its Verdet constant (V), a measurement of strength of the Faraday effect in that material, which relates the rotation of the polarized light beam and the intensity of induction field. The Verdet constant unit is $\frac{rad \cdot T}{m}$. The angular difference between the light beam initial angle and the output after crossing the Faraday-active material, α, is

given by:

$$\alpha = V \cdot B \cdot d, \tag{3.1}$$

where d is the distance inside the material that the light passes through, and $\vec{B}$ the local flux density, as illustrated in Figure 44. The Faraday-active material, also called magneto-optical layer (MOL), is one of the three constituent layers of the indicator. Panel (b) in Figure 44 shows the indicator structure used in this work, which consists of a special substrate: $Gd_3Ga_5O_{12}$ (gadolinium gallium garnet, GGG), on which one deposits the MOL, a bismuth-substituted yttrium iron garnet film (Bi:YIG) $Bi_xY_{1-x}FeO$ grown by liquid phase epitaxy. Below the MOL, a thin aluminum metallic mirror is deposited to reflect the polarized light beam used during the MOI experiment [126, 127].

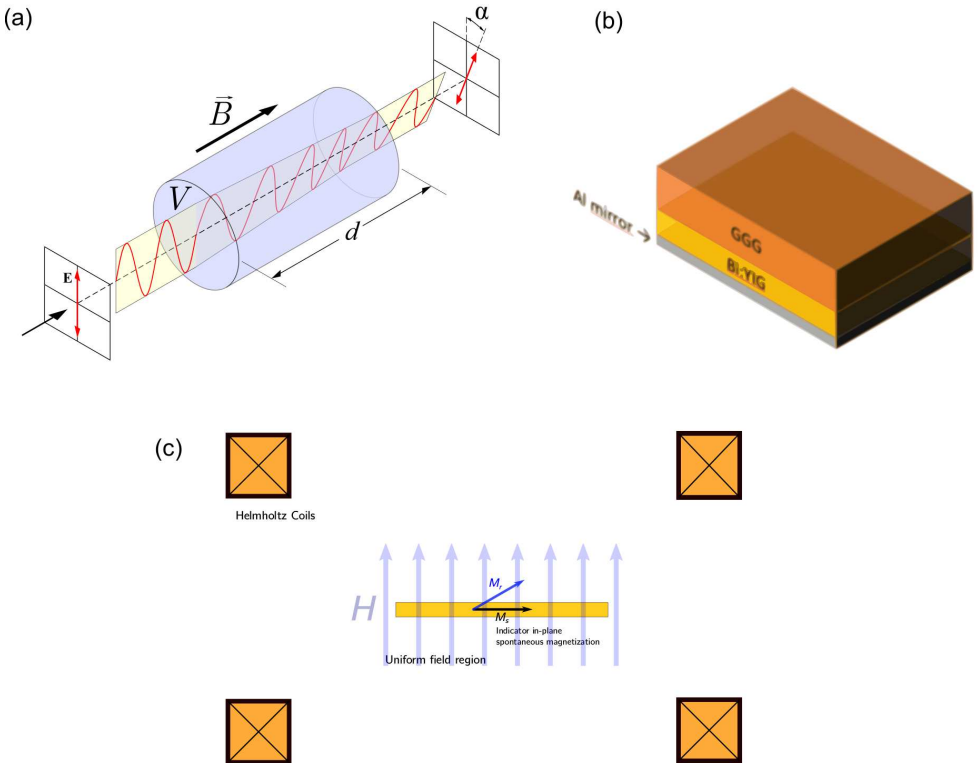

Figure 44: (a) Schematic representation of the Faraday-effect. A polarized light beam coming from the left passes trough a transparent material, with an apreciable Verdet constant V, along the distance d. The angle *alpha* is proportional to the induction field in the material, B. (b) Indicator structure. (c) The spontaneous magnetization in the MO layer used in this work is parallel to the film surface, and an out-of-plane magnetization component takes place when the indicator is subject to a perpendicular applied magnetic field (H), produced by a set of Helmholtz coils. Adapted from [61].

3.7.1 Magneto-optical imaging setup

3.7.1.1 MOI setup at UFSCar

The Magneto-Optical Imaging facility at GSM is available since 2010 and was built with financial support by Fapesp. Our system is based on the experimental setup of Prof. Tom H. Johansen at the University of Oslo. Figure 45 shows a photograph of the MOI platform in panel (a), and an illustration of its main components in panel (b).

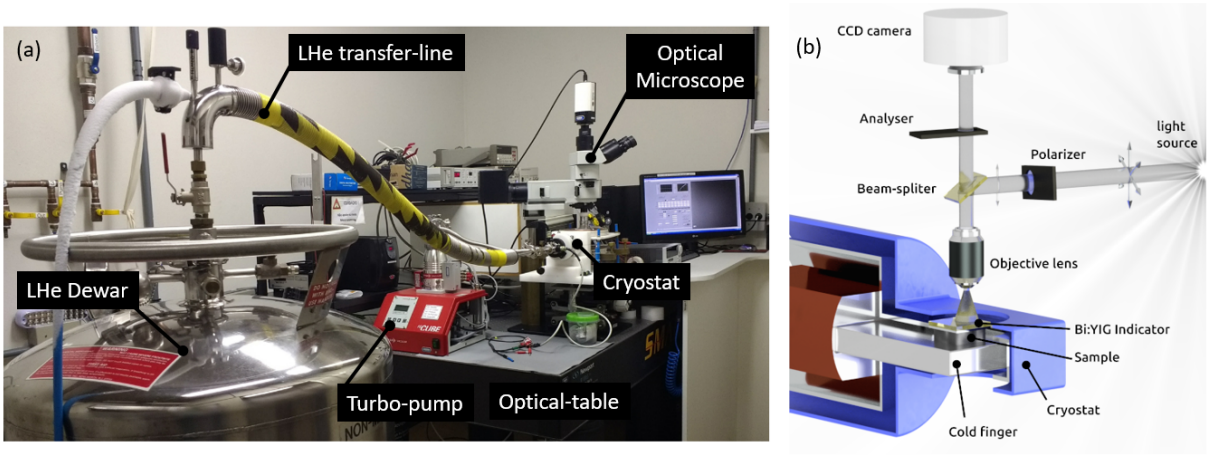

Figure 45: (a) Photograph of the MOI facility at GSM, UFSCar, Brazil. (b) Schematic illustration of the MOI experimental setup. Adapted from [128, 61].

The experiment works as follows: liquid helium (LHe) is collected from the Dewar, passes through the transfer-line and exchanges heat with the cold finger while pumping out with a Sogevac SV40B pump. The region surrounding the cold finger, inside the cryostat, was previously evacuated by another pump, a HiCube model turbo-pump from Pfeifer. A heater is installed into the cold finger and the temperature control is provided by an Oxford ITC 503S temperature controller. Three current sources can be used to generate the magnetic field: a Sorensen model SGI800X6C-1AAA, a Keithley model 6221 and an Elgar model SW1750A, which allows one to reach fields up to 150 Oe, 48 Oe and above 1 kOe, respectively. The experimental setup is also composed by a reflected beam polarization microscope model BX-RLA2, from Olympys, equipped with a 100 W halogen lamp (U-LH100H-3), a polarizer (U-PO3), an analyzer (U-AN360-3),

and an ultraviolet cut filter (U-25L42). The cryostat and the copper coil set are mounted on an x-y-z micrometer stage to focus the sample. The images are acquired by a digital camera model Retiga-4000R Fast 1394 Mono Cooled from QImaging with 4.19 megapixel (2048 x 2048 pixels) in a 12-bit digital output connected to a software developed at LabView. The microscope and the 3D positioner stage, including the cryostat and the coils, are mounted on a Newport optical table model RT equipped with active pneumatic suspension system in order to minimize noise from mechanical sources (labeled Optical-table in the photograph).

3.7.1.2 MOI setup at ULg

Part of the MO images in Chapter 4 (Figures 51, 52, and 53) were acquired in the EPNM research group at the Université de Liège, Belgium, during my internship in 2015-2016. Figure 46 describes some of the most important features of that experimental station.

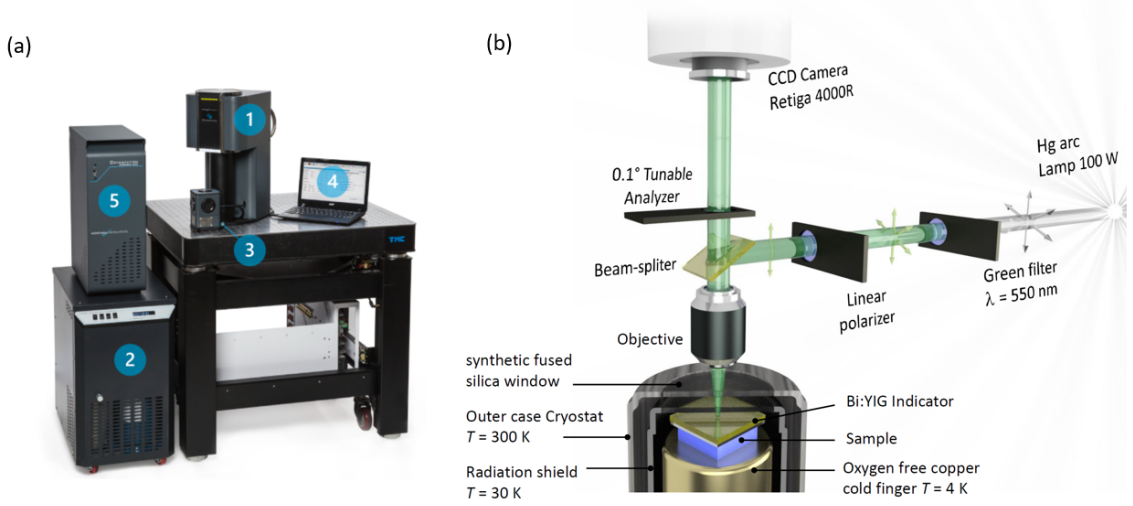

Figure 46: (a) Cooling system components of the Montana Cryostation used in ULg MOI: a closed-cycle cryogen-free cryocooler (1), a variable speed helium compressor (2), the cryostat and sample chamber (3), the laptop with user interface (4), and control unit (5) [129]. Panel (b) shows, schematically, the main components of at MOI setup. The coils to apply of the external magnetic field (not shown) are installed surrounding the sample chamber.

The ULg MOI setup is based on a modular Olympus BX-RLA2, including a source of unpolarized white light, namely, a 100W arc burner lamp (USH 103 D), a

green filter (U-25IF550, peak at $\lambda = 550$ nm), a polarizer (U-PO3), and the analyzer (AN-360). The digital camera is a CCD RETIGA-4000R, 4.2 megapixels on a 12-bit gray-scale, resulting in a 2048×2048 px^2 image. The EPNM experimental setup uses a LabView interface to control the cold-finger temperature, the applied field and the image acquisition. The image recorded is an average of 10 images, in order to reduce the noise from the background. More details about this system can be found in the thesis of J. Brisbois [58].

3.7.1.3 T_C measurements in MOI

An important and challenging feature of every MOI assembly is the thermal contact between the sample and the cold-finger, in both systems described above. The main indication of the quality of the assembly is the determination of the critical temperature of the sample. In an MOI experiment, one can measure T_C by field cooling the sample at a small field ($H = 20$ Oe, for instance), and letting the sample in the remnant state ($H = 0$) after the base temperature is stable. By increasing the temperature at a small rate, typically 0.2-0.5 K/min, the images are captured at each 0.1 K, from the base temperature to above the expected value of T_C. The T_C value is defined by the temperature in which one cannot observe the sample in the MO images anymore - above T_C, the superconducting shielding currents no longer occur, and the MOL only shows a uniform brightness all over the image. Once the thermometer of the cold-finger is a few centimeters far from the sample, and it is closer to the cold source, the temperature in the sample is usually higher than the nominal value indicated in the MO images.

4 Numerical Methods for MOI

4.1 Introduction

The critical examination of the images coming from the MOI measurements is one of the most important steps of our work in this field, despite its qualitative bias. In order to quantify the effects of the magnetic field on the samples under study, we need to aim at eliminating all possible experimental artifacts and be sure about the size of the error bar of what we intend to measure - in this case, the distribution of magnetic flux density on the surface of flat superconductors. Most of these experimental artifacts were clearly pointed out in the review paper published by Joos *et al.* [44] e.g., inhomogeneous illumination, local dependent polarization effects on the optical components, the magnetic domain structure of the MOL, sign change of the B_z component and the defects in the MOL. Even without overcoming all these limitations, the conversion (from pixel intensity to magnetic flux density) is not only possible but truly helpful. The MO images studied in this work were analyzed by using a technique jointly developed at Université de Liège, in Liège, Belgium, during an academic exchange between 2015 and 2016, within Brazil's Science without Borders Program. Although the results shown in this chapter are new and not published yet, the technique is also described in details in a previous paper [130], published in 2018, of which I am one of the co-authors.

4.2 Conversion Algorithm: from pixel intensity to magnetic flux density

4.2.1 Calibration

In order to avoid some of the above mentioned experimental difficulties, the image calibration must be done specifically for each assembly of the MOI setup, i.e, for each sample mounted on the cryostat, a new image calibration should be performed. This protocol avoids artifacts coming from defects in the MOL or scratches on the mirror. Calibrating pixel by pixel from light intensity to B_z maps, one overcomes most of the inhomogeneous illumination and the local dependent polarization effects in the optical components.

The analyzer angle

The image calibration starts even before the sample assembly, by setting the angle between the polarizer and the analyzer to achieve the magnetic field range within which one plans to run the experiment. When the analyzer and the polarizer are perfectly crossed, nothing is supposed to appear in the camera once all the polarized light is blocked. In other words, the intensity is null and the image is black. For the special case of MOI [44], the Malus's law that describes the intensity I to be captured by the camera can be written as:

$$I = I' \sin^2(\alpha + \Delta\alpha), \tag{4.1}$$

where I' is the light intensity that passed trough the polarizer, after absorption and depolarizing effects in this optical component, α is the Faraday rotation due to B_z in the MOL and $\Delta\alpha$ is the angular deviation between polarizer and analyzer. Our typical procedure at GSM is to set a standard angle $\Delta\alpha_{std}$ on the analyzer. The result of using this procedure is shown in Figure 47(a) for some selected values of $\Delta\alpha_{std}$. The images at the right of each panel were taken at room temperature and show how the indicator brightness

change as H is scanned. The applied magnetic field H for each image is indicated in its graphs at left by red dots and labels in the corresponding graph on the left.

In Figure 47(a) one can readily realize that the points a1 and a3 show approximately the same brightness (y axis). In this sense, it is impossible to associate unequivocally the brightness of the pixels to a single value of the magnetic field in the range from -150 Oe to 0. Another important remark is the position of the local minimum of these parabolic-like curve. In its vicinity, the change in the brightness response is smaller as one increases the field, and there are noise for both positive and negative fields surrouding the local minimum in this $|\Delta\alpha_{std}|$ configuration, specially for 0 to -100 Oe. The noise problem will be better discussed in the next sections.

Setting the analyzer to $-\Delta\alpha_{std}$, as shown in Figure 47(b), one gets the brightest point for a negative field and the minimum for a positive field. Again, there is a range of fields within which two different values of H correspond to approximately the same response in the indicator.

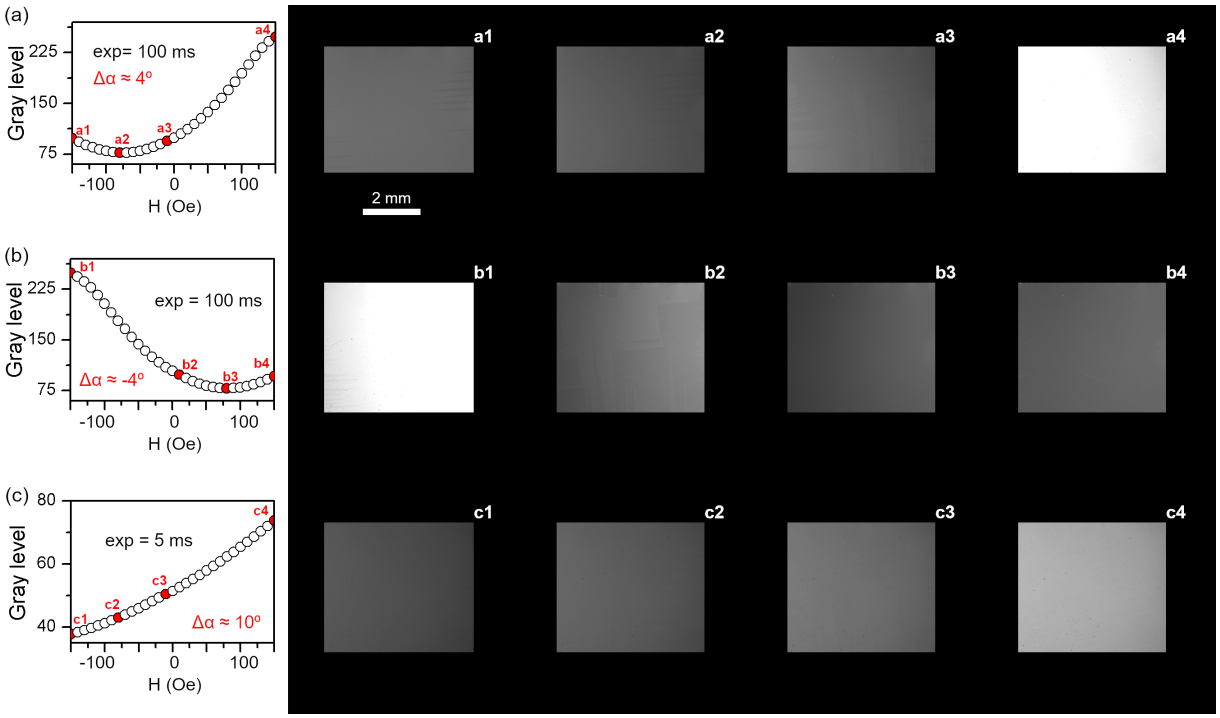

Figure 47: (a) Mean pixel intensity versus applied magnetic field for the standard angle between the analyzer and the polarizer ($\approx 4°$ clockwise). (b) The same angle, but rotated counterclockwise from the orientation of complete crossing. (c) a larger angle, $\approx 10°$, in which more light can pass through the optical system. All the pictures are shown as they were taken by the camera. The white bar below the panel a1 is the scale bar for the MO images.

Increasing $\Delta\alpha$ will allow more light to reach the camera sensor. Figure 47 (c) illustrates with MO images the situation for $\Delta\alpha \approx 10°$. The exposure time had to be severely decreased to avoid camera saturation - it changed from 100 ms, for the standard angle, to 5 ms. This is the best position for calibration once it shows only one brightness intensity ascribed to one single value of the magnetic flux density in the MO layer. The next step is to collect information on how each pixel changes its brightness as we change the applied magnetic field. Additionally, from now on we will also use the induction field B related to H by the constitutive relation $B = \mu_0 H$, once we are interested in the local induction field and how it is distributed in the MO layer.

Each pixel responds differently

Figure 48 is an important example in this subject, showing MO images for the same assembly, the same temperature but in different applied magnetic fields. Panel (a)

was taken with $H = -48$ Oe and panel (b) with $H = 48$ Oe, using the standard analyzer angle $\Delta\alpha_{std}$. In both panels, one can identify punctual defects on the MO layer, but they are more visible in panel (b). Furthermore, the scratch-like defect in the center of the images shows different influences in its neighborhood when H changes, as one can observe in the third peak of the profile in panel (b), and its counterpart in panel (a). Also, the inhomogeneous illumination aforementioned appears as an inclination of the cross-section profiles, and once both profiles are on the same scale, the discrepancy between then indicates that this also changes differently for different values of B_z. For all these reasons, the calibration made pixel by pixel is the most precise approach to make quantitative MOI on superconducting samples. All the information in the Figure 48 were collected using the ImageJ application [131].

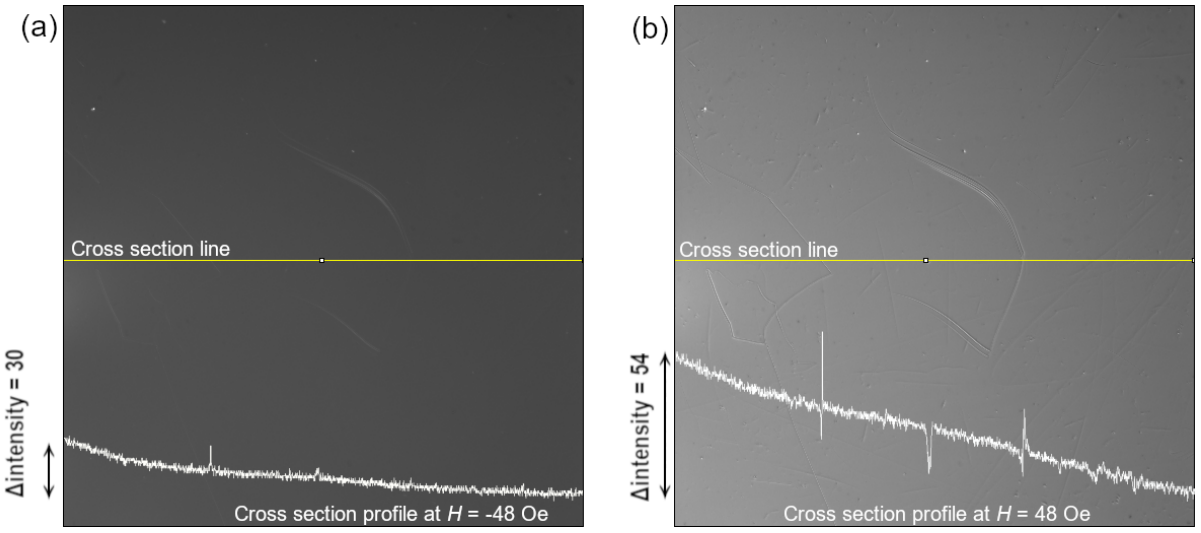

Figure 48: Examples of MO images taken at $T = 15$ K with (a) $H = -48$ Oe; (b) $H = 48$ Oe. The yellow lines in the middle of both panels indicate the position where the intensity profile graphs were taken, both curves are in the same scale.

Data acquisition for calibration

The sample assembly on the cold finger is the same as the standard protocol described in Chapter 3. The next step is to perform a scan of the applied magnetic field, just like we performed at room temperature to set the analyzer angle, but in a temperature close to the range in which the experiments are planned. This is necessary because the cold finger shrinks a few millimeters during the cooling procedure from room temperature to

the base temperature (≈ 3 K), and we usually need to change the microscope parameters (focus and xy position) to locate the sample. For superconductors, one should collect the calibration data in temperatures just above T_c, in order to get the parameters of each pixel without influence of the superconducting sample and as close as possible of the temperature range.

Data processing for calibration

The data processing for calibration can be easily done in any programming language that supports image processing, such as Python or C++. Nevertheless, this data acquisition and processing protocol was developed in the EPNM research group, specially by Prof. Alejandro Silhanek, Jérémy Brisbois and myself, in the Univesité de Liège during the sandwich period, and the group had already started the numerical analysis of the MO images in Matlab before my internship. So, all the following steps were performed in Matlab.

By stacking the collected images, one can imagine a data cube wherein the information needed for calibration are column vectors of aligned pixels, as is illustrated by the red arrow in Figure 49 (a). Using the brightness level value for each of those pixels from the column vector, one can plot them as a function of H, as shown in Figure 49 (b). We used a second order polynomial fitting to generate the colored lines. Figure 49 (b) shows only 16 different points collected at different positions on the image, to show how different the pixel behavior can be, depending on its position. For each run, the processing is carried out using all the $2048 \times 2048 = 4\ 194\ 304$ column vectors of pixels to deal with.

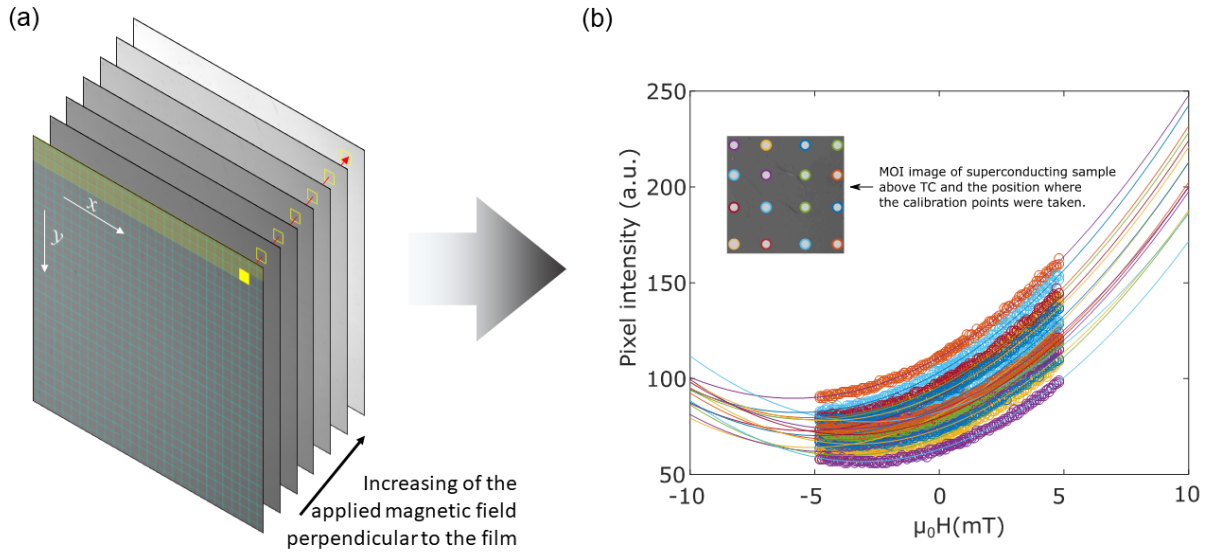

Figure 49: (a) Schematic illustration of the data cube made of a stack of images and a column vector through its pixels across different fields. The yellowish pixels on the top of the first image represent the scanned pixels til the one highlighted in yellow, to illustrated the scanning protocol. (b) A plot of the data collected as a function of H. The 16 points on the inset indicate where in the image the column vector were taken to make the parabola-like graph, where we used circles for the data and lines for the fitting. All the data were taken at T = 15 K, and applied fields ranging from $H = -48$ Oe to $H = 48$ Oe.

Based on the critical model for thin films, one can expect that the induction field B at the edge of the superconducting film is higher than $\mu_0 H$, for all the reasons described in Chapter 2. Therefore, it is important to fit a function on the collected data and not just use the data cube as a reference to check future results. The fitted function will allow one to measure fields higher than those used to calibrate the system.

So, the next step is to choose a function to fit the data. Joos *et al.* [44] describe the response of the iron garnet[1], i.e., the function for calibration of the MO layer as

[1]Similar to the one used in this work, as described in Chapter 3.

follows:

$$B_z = B_k \tan\left\{\arcsin\left[\frac{1}{CM_s}\arcsin\left(\sqrt{\frac{I(x,y)-I_1(x,y)}{I'(x,y)}}\right)+\Delta\alpha\right]\right\}, \tag{4.2}$$

where B_z is the magnetic flux density perpendicular to the sample plane, $I(x,y)$ is the light intensity on the camera sensor, $I_1(x,y)$ is the background image, and $I'(x,y)$ is the light reflected from the mirror after passing through the MOL. The physical properties of the MO layer relevant to the case are embraced by B_k, which is the anisotropy field of the MOL, C is a constant similar to the Verdet constant, M_s is the spontaneous magnetization of the ferrimagnetic film. The Equation 4.2 will be more useful if one can rewrite it to describe how the intensity $I(x,y)$ depends on B_z. By performing some algebraic operations, one finds the following expression:

$$\frac{I(x,y,B_z)-I_1(x,y,B_z)}{I'(x,y,B_z)} = \sin^2\left(CM_s\left\{\sin\left[\arctan\left(\frac{B_z}{B_k}\right)\right]-\Delta\alpha\right\}\right) \tag{4.3}$$

If one does not subtract the background information for the calibration, then $I_1(x,y,B_z)=0$, so Equation 4.3 becomes

$$I(x,y,B_z) = I'(x,y)\sin^2\left(CM_s\left\{\sin\left[\arctan\left(\frac{B_z}{B_k}\right)\right]-\Delta\alpha\right\}\right). \tag{4.4}$$

This function describes all the induction field range of the MO layer, from zero up to the indicator saturation, which is close to 10 kOe. Nevertheless, this treatment becomes somewhat simpler for small fields as those applied on our experiments (up to $H = 150$ Oe, for instance): a closer look at the data points in Figure 49(b) suggests a parabolic function, so we write:

$$I(x,y,B_z) = a(x,y)B_z^2 + b(x,y)B_z + c(x,y). \tag{4.5}$$

In such a parabola, one can name its minimum value as I_{min}, occurring at a specific field B_{min}, so that:

$$I_{min} = c(x,y) - \frac{b^2(x,y)}{4a(x,y)}, \tag{4.6}$$

$$B_{min} = -\frac{b(x,y)}{2a(x,y)} \tag{4.7}$$

This two values are specially important when one needs to calibrate data whose range lies on both sides of the minimum and when one deals with hybrid systems (such as superconductors in contact with a magnetic layer), situations where one should choose which side of the parabola to perform the calibration. The I_{min} is also used in the data collected in MOI station from ULg, where we must correct the fluctuations from the light source.

Fitting this second order polynomial equation to the range of data usually collected, the standard error for each coefficient is lower than 2 %. Each one of the column vectors has three parameters resulting from the calibration.

4.2.2 The conversion protocol

After the parameters of each pixel were calculated, one can extrapolate the calibration data to estimate a larger range of field intensity than what was initially measured. Nevertheless, converting a pixel intensity to a magnetic field value requires the inversion of the parabola. If one chooses only the positive side of the parabola, for each image $N_i(H)$ (from now on called only N_i) of a sequence of i images, taken by changing the applied field, the value of the local magnetic field B for a pixel located at coordinates (x,y) of the image is given by

$$B(x,y,N_i) = \frac{-b(x,y) + \sqrt{b^2(x,y) - 4a(x,y)\left[c(x,y) - I(x,y,N_i)\right]}}{2a(x,y)} \tag{4.8}$$

Figure 50 shows curves based on the coefficients obtained from the fitting of the parabolas in Figure 49(b), but for the Equation 4.8. This glance at the calibration curves for a number of different pixels emphasizes how important is the individual calibration to achieve the most reliable results.

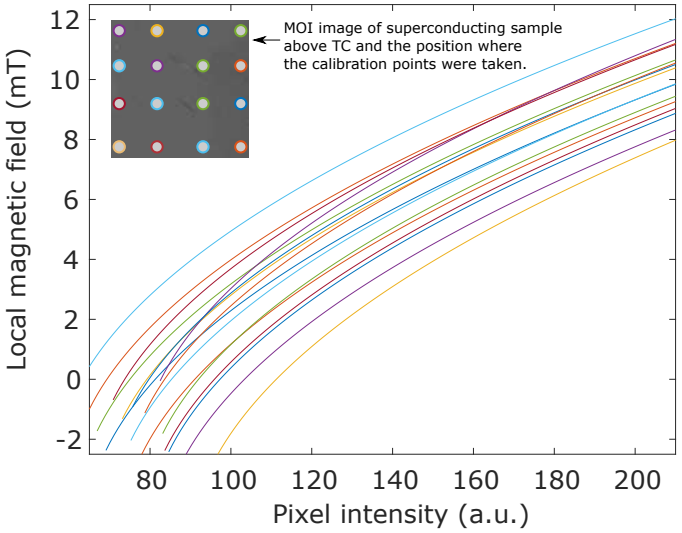

Figure 50: Positive branch of the inverted parabolas; for the same 16 points presented in Figure 49(b), whose localization is represented on the inset.

As expected, this method is unable to deal with information due to defects on the MO indicator, dust between the indicator and the sample, and grease spots. Besides that, the movement of the magnetic domain walls affects the local value of the magnetic field, so the walking wall should be followed carefully.

4.3 Quantitive MOI for the critical state

The first system we studied with the conversion algorithm was a Nb thin film, with thickness of 30 nm, lithographed as a rectangle of 400×800 μm^2, decorated with two small Co circular dots close to the edges of the larger borders. The diameters of the dots are 10 μm and 20 μm, and they were magnetized parallel to the plan of the Nb film[2]. The MO image in Figure 51(a) is the raw image taken at $T = 4$ K and $H = 10$ Oe. One

[2]These samples were studied in depth as a simple hybrid system of a magnet on top of a superconductor in the PhD thesis of Jérémy Brisbois [58].

can see the strong brightness at the borders of the sample, as expected for a high-quality Nb film in these conditions of temperature and field. The Co dots can be identified by the arrows just below the yellow cross-section line. The angle $\Delta\alpha$ was selected to allow the identification of the north and south pole of the Co dots, which is seen as a contrast from white to black within each dot. At the bottom half of the MO image, there are domain walls of the MO layer and also defects on the indicator[3]. The yellow line locates where the cross-section profile of panel (b) was measured. The profile of the raw image is in gray and it is scaled at the left y-axis. Panel (c) shows the converted image, and its B_z profile is indicated in black in panel (b).

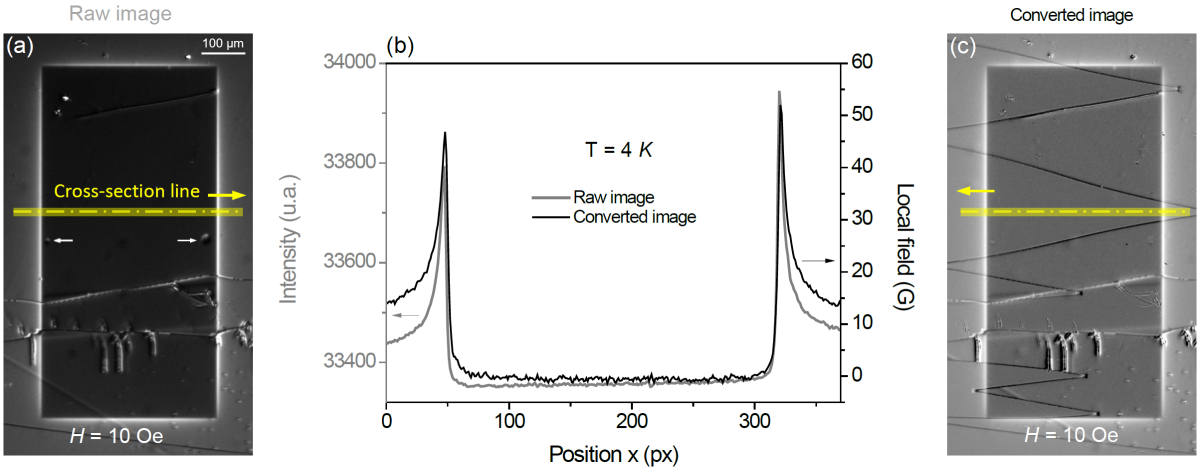

Figure 51: (a) Raw MO image of the Nb thin film taken at 4 K and 10 Oe. The yellow line indicates where the intensity profile of panel (b) [left axis] was obtained. (c) Converted image in which each pixel represents the value of B_z at that location; the field profile along the yellow line is shown in panel (b) [right axis].

The flat centered region of the profiles, which can be observed between the positions 50 px and 310 px in Figure 51(b), refers to the shielded part of the superconducting film. Nonetheless, there is a non-zero slope obtained from the raw image (gray line). This inclination is due to the inhomogeneous illumination, which is clearly corrected by the pixel-by-pixel calibration procedure (black line). It also occurs with the maximum field at the sample's border - the left hand side of the gray line-profile is more shifted down than

[3]In this assembly a pressure clip was used to decrease the distance between the indicator and the superconducting film. The mechanical stress caused by this pressure clip increases the quantity of domain walls.

the right hand side of the same curve, as well as for the peaks. The noise range amplitude around zero for this region is ±1 Oe. In panel (c) one can see a clear zigzag dark line crossing the sample that was not there in the raw image - these are domain walls which appear due to the calibration step, and will be present in all calibrated images of that MOI assembly.

Another important remark of this conversion is the effect on the magnetized dot of the calibrated image. Despite both dots are well visible in Figure 51(a), they are not visible anymore in the calibrated image, in panel (c). This aspect could be wrongly described as a drawback, but this is actually a precise confirmation of the calibration quality: the calibration tell us how each pixel response changes as it is exposed to an uniform (and externally applied) magnetic field. The fact that one can not see the dot in the calibrated image means that, for those circumstances of temperature and applied magnetic field, there was no variation on the perpendicular component of flux at the positions of the dots. In other words, flux at those positions was kept the same as at $H = 0$, even at lower temperature and higher field as compared to the calibration run taken at $T > T_C$. This is the reason why we can not identify the dots in Figure 51(c).

4.3.1 The smooth flux penetration

By using the conversion protocol described earlier, Figures 52(a) through (e) show the evolution of the flux penetration into the sample described in the previous section, in calibrated MO images. The experiment was performed at $T = 4$ K after a ZFC, increasing H from zero to 128 Oe and so decreasing to zero. Once we expect to distinguish both, positive and negative flux densities, we choose an artificial color pallet in which black is zero field, and from zero to blue-white, the positive B_z. Negative values go from black to red-yellow, as shown in Figure 53.

At the right-hand side of each MO image in Figure 52(a)-(e), there are graphs showing an average B_z profile (a')-(e') obtained along the yellow line placed at the bottom left of each image. This cross-section starts outside the sample and goes until its center, to avoid the domain wall effects on the profile - which could disturb the physical interpre-

tation. Nonetheless, as shown in Figure 51(b), the profile is expected to be symmetric. In order to visually discriminate positive from negative magnetic fields, we choose an artificial color pallet in which black is zero, positive fields appear in the black to blue-white range, whereas negative fields are seen in the black to red color interval.

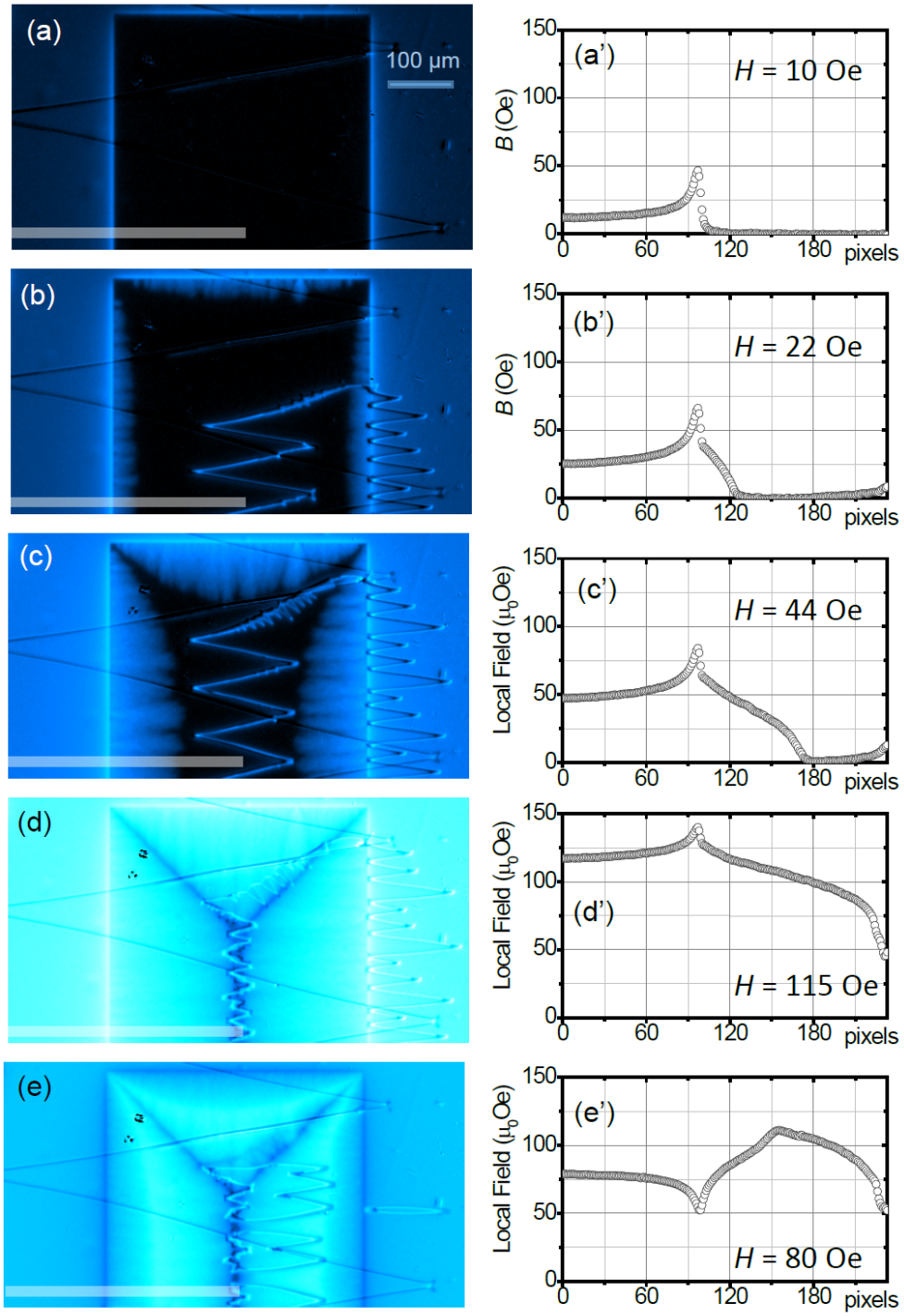

Figure 52: Calibrated magneto-optical images of a 30 nm thick rectangular Nb film, after a ZFC procedure and then under an applied DC magnetic field of (a) 10 Oe; (b) 22 Oe; (c) 44 Oe; (d) 115 Oe and finally decreasing the field down to (e) 80 Oe. The yellow line at the bottom of each image is the region over which the profile was calculated (avarage of 15 profile lines of pixels). The zigzag features in the images are magnetic domain walls in the MO indicator.

As we can see in Figure 53 (a) and (b), when decreasing the field after the full

penetration state, the magnetic flux density measured on the border of the sample is different from the applied magnetic field. In panel (b) the measured field in the edge is negative while the applied decreasing field is still in the positive branch ($H = 32$ Oe).

The critical state model predicts that, for film geometry, B_z on the border of the sample will be negative as soon as one flips the sense of the applied field, since the gradient of the external field changed its sign. In this regard, we probably do not see it in the experiment shown due to the limited resolution of the MOI technique. Not only the model but also this kind of experiment allow us to interpret that the positive flux trapped in the sample does not go out - it is annihilated by the anti-flux that enters from the border, even when the system is still under a positive field after a maximum field.

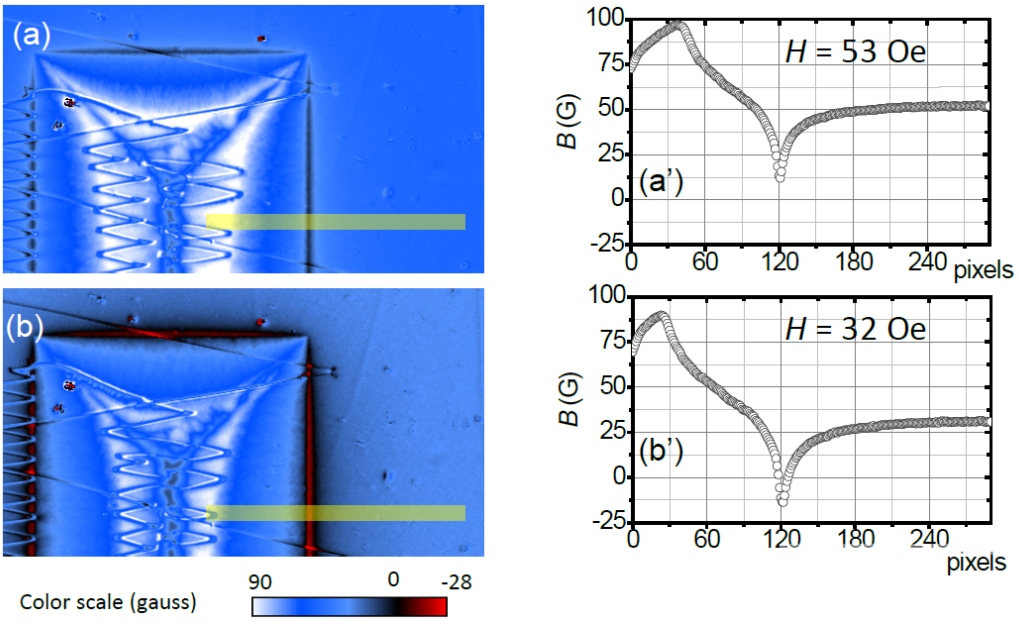

Figure 53: Calibrated magneto-optical images of a 30 nm thick rectangular Nb film, after a ZFC and after a maximum applied magnetic field of 125 Oe. The field was then decreased to (a) 53 Oe, and (b) 32 Oe. At the right-hand side of each image, (a') and (b') show B_z profiles of images (a) and (b), respectively. The yellowish bar at the bottom of each image is the region over which the profile was obtained. The zigzag features in the images come from the MO indicator.

4.3.2 The parabola artifact

When calibrations are performed without special care to the angle $\Delta\alpha$ and the field range, the results can show what we call *the parabola artifact*. It appears when

the field is decreased from a maximum value, as shown in Figure 54. From panel (a) to (e), it seems that there is a prominent and unexpected positive flux at the border of the superconducting film, which can be seen in panels (d') and (e'). From where positive flux would come from? Why does it appear only in that situation?

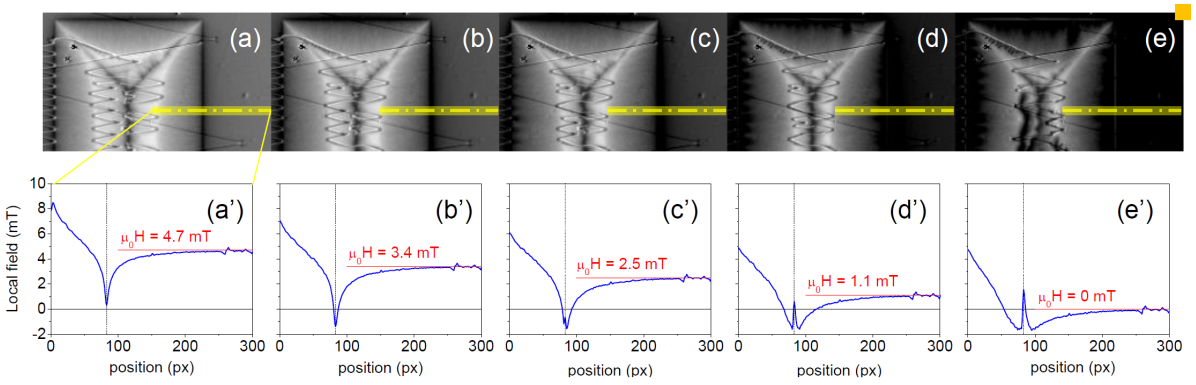

Figure 54: Calibrated Magneto-Optical images of a rectangular Nb film 30 nm thick, after a zero-field-cooling procedure and after a maximum magnetic field of 125 Oe as applied and then decreased to (a) 47 Oe, (b) 34 Oe, (c) 25 Oe, (d) 11 Oe, and (e) zero. Panels (a') to (e') show B_z profiles of the respective calibrated images.

The graphs in panels (c') to (e') show that negative field is indicated only if it does not exceed ≈ -15 Oe. The prominent positive peak in these panels starts at -1.5 Oe. The origin of this artifact is clarified by analyzing a region far from the sample, in the same set of images. The small orange square at the top right of Figure 54(e) shows a region of size 30×30 px^2 whose mean intensity was plotted as a function of the applied magnetic field and shown in Figure 55. The I_{min} and B_{min} values are indicated by dashed red line. Negative fields more intense than B_{min} will resemble the positive fields in the image, as a consequence of the angle $\Delta\alpha$ chosen in the beginning of the experiment. So, the positive field $H = 30$ Oe gives the same brightness of the negative field -47 Oe, and one can only distinguish both using the experimental context; that is why this artifact can easily be interpreted as real physics.

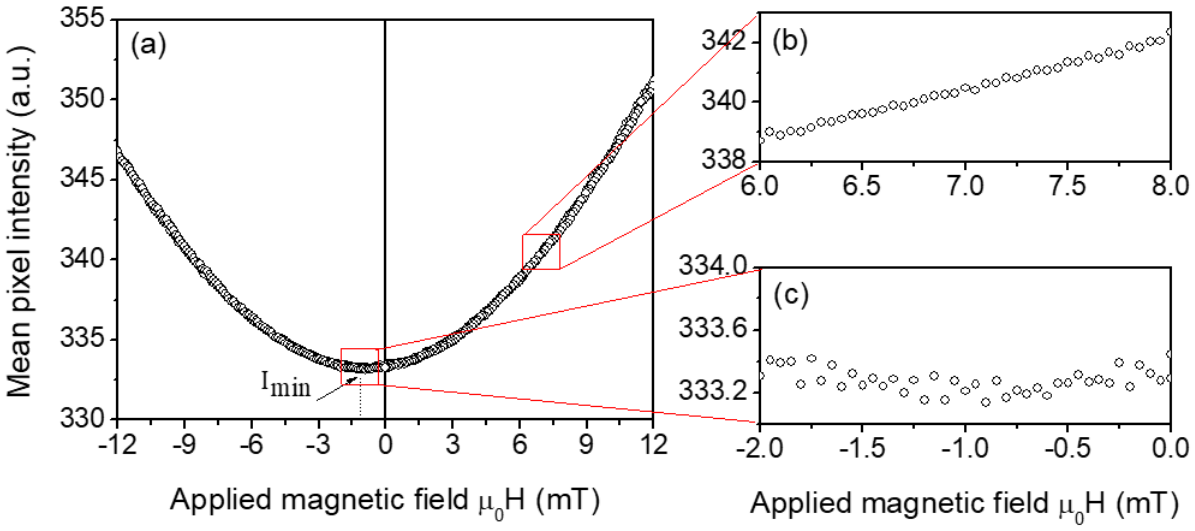

Figure 55: (a) Mean pixel intensity *vs.* applied magnetic field for a 30×30 px^2 region far from the sample, indicated by the yellow square in panel (e) of Figure 54. (b) Inset showing the noise level for regions far from the parabola minimum and (c) around the minimum.

4.4 Quantitave MOI for flux avalanches

In this section we will discuss the calibration protocol applied to a Pb thin film 100 nm thick and protected with 110 nm thick Ge layer to avoid Pb oxidization. The samples were deposited by e-beam evaporation, at the Katholieke Universiteit Leuven (KU Leuven), in Belgium, by Prof. Joris Van de Vondel. The critical temperature of the sample is 7.2 K, measured by DC magnetometry.

Figure 56 shows raw and calibrated MO images and line profiles of the Pb-Ge film described above. Panels (a) and (b) show raw images taken at $T = 4$ K after ZFC, at $H = 4$ Oe and $H = 46$ Oe, respectively. There is a strong inhomogeneous illumination in these raw MO images. The intensity profile in a light gray line, in panel (c), gives another view to the brighter region at the top right of panel (a). Panels (d) and (e) are the calibrated MO images from the images in (a) and (b). The yellow line in panel (d) indicates the region used to plot the B_z profile (black line) in panel (c). The illumination issue is basically solved by the calibration. Nonetheless, the noise from the domain walls

keeps disturbing the profile analysis.

In fact, the depression after the first peak in the black line, reading from left to right, is due to domains arrangement in the MO layer. Conceivably, the domain located at the right side of the profile is not the same used to calibrate the system, once the zero field region is shifted to the negative side of the y axis.

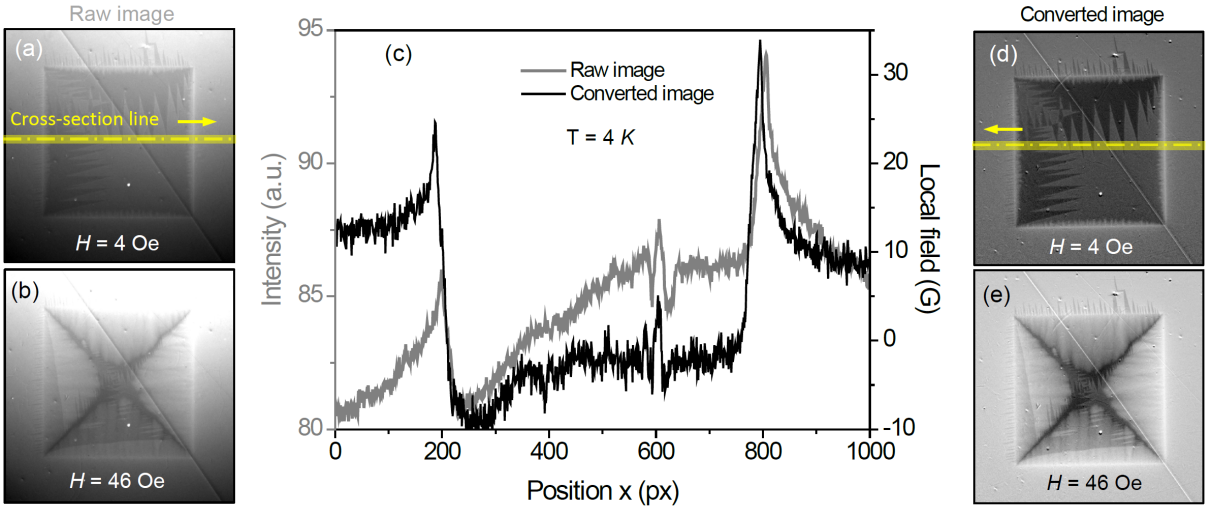

Figure 56: (a) Raw MO images of the Pb thin film and indication of the profile shown in panel (b) where the field profiles are plotted using two different scales: Intensity of the light at the left (*arbitrary units*, a.u.) and local magnetic field (B) at the right. (c) Converted MO images. For all images the temperature is 4 K, and the applied field is indicated in the image.

All aspects of Figure 56(a) are better visualized in panel (d). The MO layer defects are less visible and the inhomogeneous illumination effects are less prominent. Furthermore, the flux penetration is smooth and almost symmetrical from both edges.

This is a vivid example showing that, for a more precise MOI calibration, the magnetic domain of the MO layer should also be the same in the calibration and during the experiment. One way often used to hold the domains is to apply a low-intensity horizontal (in-plane) magnetic field to the system, as long as it does not disturb the physical system under study.

The calibration, i.e., the quantitative magneto-optics applied for studying flux avalanches clarify some tricky aspects of this abrupt phenomenon. Figure 57 shows a set

of calibrated MO images of the squared Pb-Ge film, after a ZFC and initially increasing the applied magnetic field from $H = 2$ Oe (I-A) up to 47 Oe (II-A) and then decreasing down to -47 Oe (III-E). In panel (II-A) the local field at the edges are -20 Oe despite the external applied magnetic field is still in the positive side, at 25 Oe. For the calibration used in this sample, the I_{min} value is at $B_{min} \approx -100$ Oe, so we can analyze the images without the parabola artifact in mind.

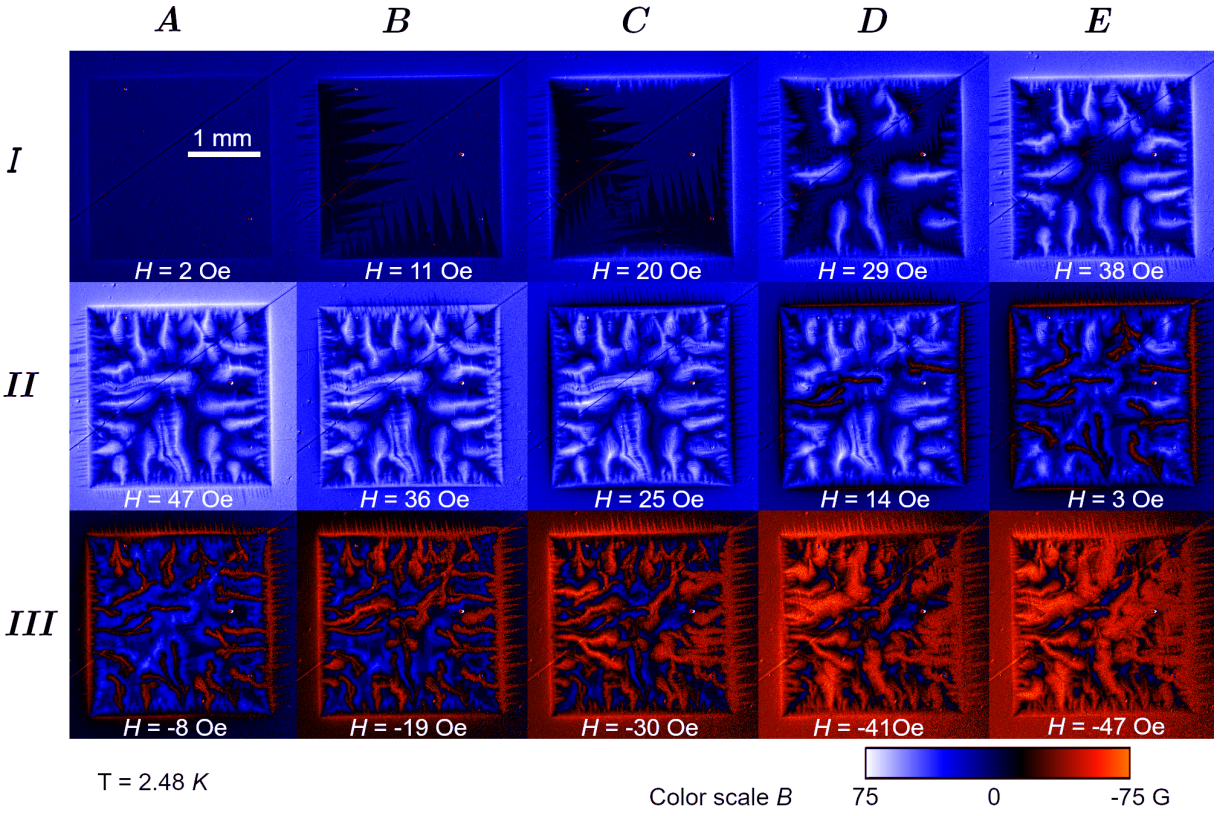

Figure 57: Flux avalanches in the Pb thin film using an artificial color scale for visualization of both negative and positive fields. All the images were captured at T= 2.48 K. The first image of the first row (I-A) starts with $H = 2$ Oe and advances to its right (I-B, I-C, ...) as the increase of H is indicated at the bottom of each panel, until the maximum of 47 Oe (II-A). In the second row is the decreasing field, down to -47 Oe (III-E).

In panel I-D ($H = 29$ Oe) of Figure 57, there are flux avalanches starting from all edges of the sample. All the avalanches have a well-defined core surrounded by a blurred region that looks like smooth flux penetration coming from the dendrite. As the applied field increases, and number of avalanches rise, they try to avoid each other, as expected. The anti-flux avalanches, starting during the decedent field on panel II-D,

seems less blurred than the positive avalanches, and most of them use at least part of the positive avalanches core as a paved way to spread out into the sample.

4.5 Conclusions

In summary, the use of numerical analysis in MO images shows important features from both the studied material, and the MOI technique itself. The protocols needed to produce quantitative MOI also prevents important artifacts in the results, making the MO analysis more reliable. Another important feature of such protocols is the possibility of studying positive and negative applied fields without mixing-up the meaning of the pixel brightness. The numerical methods for MOI allow one to make quantitative magneto-optical imaging in more complex systems, as the one studied in the next chapter: a bi-layered system composed by a thin Nb film with a NbN layer on top of it, which shows a rich and complex avalanche regime.

5 Quantitative magneto-optical imaging in Nb/NbN thin films

This chapter is based on the manuscript *Magnetic flux avalanches in Nb/NbN thin films*, submitted to the journal **Low Temperature Physics** in October 2019.

5.1 Introduction

In view of its high critical field and transition temperature, niobium nitride is a widely applied superconducting material. In this chapter, we explore the magnetic properties of single films of Nb, NbN and the hybrid system Nb/NbN. Our results indicate that the presence of Nb in the vicinity of NbN causes partial inhibition of flux avalanches, thus extending the region of smooth penetration regime in the HT-diagram, which represents a practical improvement in terms of applicability of films of this material. As discussed ahead, the hybrid system can be prepared using an *in situ* procedure during the film growth, without decreasing the upper critical field of Nb. We used AC susceptibility and DC magnetometry to characterize both single layer films, Nb and NbN, as well as the bi-layered specimen. Quantitative magneto-optical imaging was employed to map the instability regimes. We also describe interesting features of anti-avalanches, namely, a halo-like structure and crossing avalanches.

5.2 Sample preparation and methods

All samples studied here were produced by the research group led by Prof. Carmine Attanasio, at the Università degli Studi di Salerno, Italy, in 2017. To perform a comparative analysis of the magnetic flux avalanche regime, Nb and NbN single films and hybrids (Nb/NbN and Nb/I/NbN) were deposited on Si(100) substrates at room temperature in a ultra-high vacuum DC diode magnetron sputtering system with a base pressure in the low part of the 10^{-8} mbar range. The argon pressure during deposition of the Nb layer was $P_{Ar} = 2.5 \cdot 10^{-3}$ mbar, while NbN was reactively sputtered in an atmosphere of Ar and N_2, with $P_{Ar} = 2.5 \cdot 10^{-3}$ mbar and $P_{N_2} = 0.7 \cdot 10^{-3}$ mbar. The deposition rates were $r_{Nb} = 0.26$ nm/s for Nb and $r_{NbN} = 0.17$ nm/s for NbN, as measured by a QCM previously calibrated by measuring the step height of photolithographically patterned films with a Bruker DektakXT stylus profiler. Samples with different structures were deposited by keeping the thickness of the Nb and NbN individual layers constant, namely $d_{Nb} = 15$ nm and $d_{NbN} = 60$ nm. Hereafter, the single films were named Nb15 and NbN60 for Nb and NbN, respectively. Apart from the single films, both NbN/Nb bilayers and NbN/I/Nb tri-layers were realized. The I layer is an insulating barrier, mainly constituted by Nb_2O_5, obtained by thermal oxidation in air of 3 nm thick Nb layer, in order to suppress the proximity effect between the two superconducting layers.

The investigated samples, having approximately the same area of 4×4 mm^2, were characterized by AC susceptometry and DC magnetometry in a commercial MPMS 5 Quantum Design magnetometer. Magneto-optical imaging experiments were carried out in the GSM MOI facility, as described in Chapter 3. We also perfomed a numerical convertion from pixel intensity of magneto-optical images to the local magnetic flux density, mapping B_z all over the sample and its neighborhood, following the protocol reported in Chapter 4.

5.3 AC susceptibility measurements

The critical temperature of superconducting thin films is thickness dependent and usually lower than the bulk values [132]. The onset critical temperature (T_C) of the samples were determined by AC susceptibility measurements, presented in Figure 58(a), showing the following values: (6.90 ± 0.05) K for Nb15; (10.50 ± 0.05) K for the NbN60, (10.00 ± 0.05) K for the bi-layer, and a double transition for the tri-layer sample: the first at (6.00 ± 0.05) K, and the second at (4.86 ± 0.05) K. In this tri-layer sample, the critical temperature of both layers is lower than that obtained for the other samples, single ones or bi-layer. Besides that, MO imaging of the tri-layer specimen showed several scratches on the sample surface, disqualifying the specimen, which thus will not be discussed henceforth. The critical temperature for the NbN film is close to values reported in the literature for similar thicknesses [133, 134]. It is also important to mention that T_C of the single NbN layer is 0.5 K above that the bi-layer. This small depreciation of T_C is assumed here to be a consequence of growing the NbN film on top of the Nb layer already deposited on the substrate.

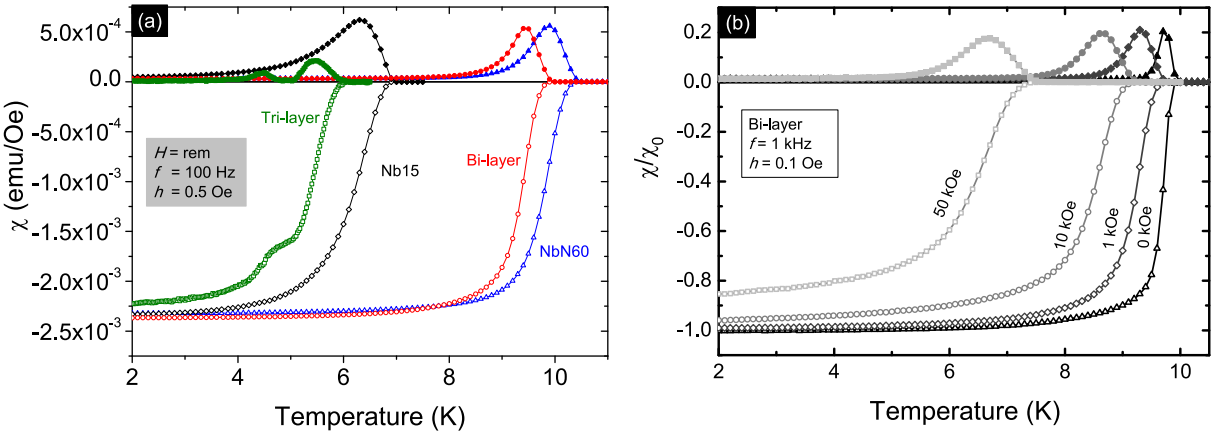

Figure 58: AC susceptibility *vs* temperature for all films investigated (a) and for different applied magnetic fields H for the bi-layer system (b). The y axis is normalized by χ_0, which is the Meissner plateau value for the in-phase component of the AC susceptibility for each sample. The frequency (f) and the amplitude (h) of the AC excitation are indicated in each panel.

The fact that we do not observe a double or a broader transition in the bi-layer as

compared to the single layer films is a relevant hint suggesting the occurrence of a highly transparent proximity effect [63] between the layers. The absence of a double transition in the bi-layer sample remains for applied magnetic fields up to $H = 50$ kOe, as shown in Figure 58(b). The proximity effect in the bi-layer specimen was suppressed by the insertion of an additional 5 nm thick Nb_2O_5 insulating layer between the superconducting films as shown in Figure 58(a).

By performing susceptibility measurements as a function of temperature for H up to 50 kOe, we determined the H_{C2} *vs* t diagram presented in Figure 59, t being the reduced temperature, $t = \frac{T}{T_c}$. We estimate the $H_{C2}(0)$ values by fitting the data to the expression $H_{C2}(t) = H_{C2}(0) \cdot (1 - t^2)$, plotted as dashed lines in the same graph. For both the Nb/NbN bi-layer and NbN60 films, $H_{C2}(0)$ is close to 110 kOe, whereas for the Nb15 film it is approximately 27 kOe. Based on the derivative of the upper critical field versus temperature near T_C, we determined the superconducting coherence lengths at 0 K ($\xi(0)$) of 10.7 nm, 4.7 nm, and 4.6 nm, for Nb15, NbN60, and the bi-layer, respectively. We did not detect flux avalanches in AC susceptibility measurements using driving fields up to 3.8 Oe, consistently with the existing literature [135, 136], since avalanches occur only at higher fields.

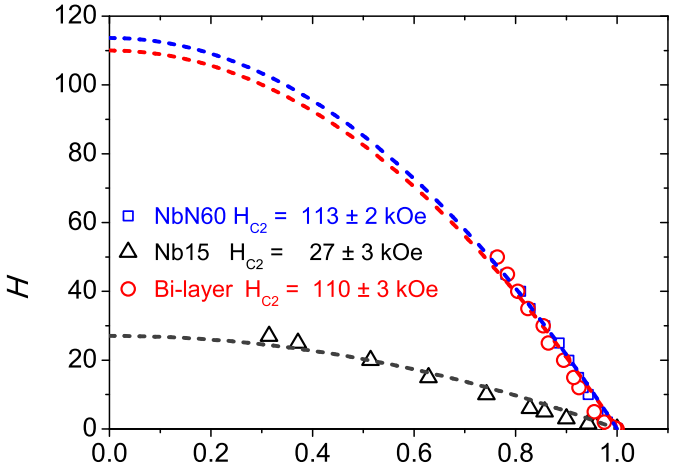

Figure 59: H_{C2} versus reduced temperature $t = T/T_c$ for Nb15, NbN60 and the Nb/NbN bi-layer, showing the extrapolated upper critical field at $T = 0$ K.

5.3.1 Flux jumps regime

In order to identify the instability regimes of these systems, we measured the DC magnetization as a function of the applied magnetic field at the same reduced temperature $t = 0.3$. The result is presented in Figure 60. The presence of magnetic flux jumps is clearly identified, for all samples as a noisy magnetic response, being particularly prominent for the NbN60 sample. Note, however, that avalanche activity is strongly suppressed by the proximitized Nb layer (bi-layer sample).

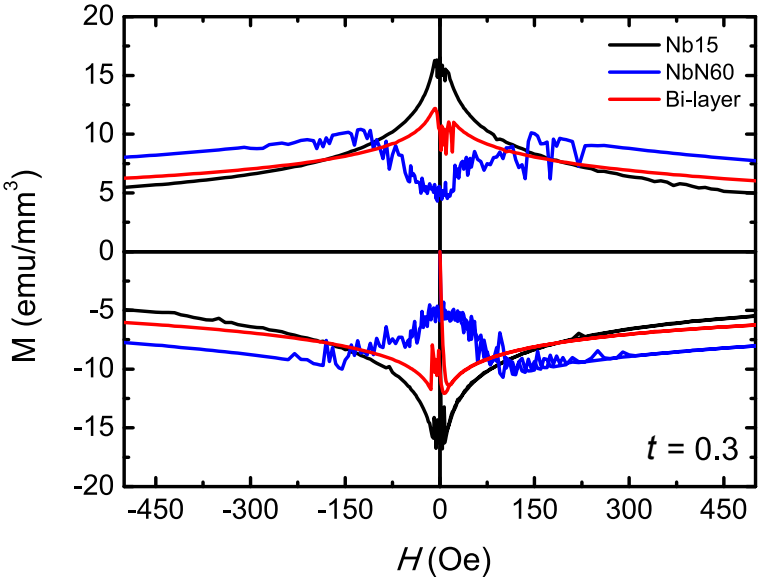

Figure 60: DC magnetization as a function of the applied magnetic field at $t = \frac{T}{T_C} = 0.3$. The noisy response at low fields observed in all samples corresponds to the occurrence of magnetic flux jumps.

The critical current density is a crucial parameter determining whether the thermomagnetic avalanches will take place [53]. For any given superconducting film, there is a threshold value of J_C below which no flux jumps take place. Based on the Bean critical state model [31, 32], one can roughly estimate J_C by the difference between the increasing and decreasing branches of the magnetization loop. This approach is acceptable in the smooth part of the magnetization loop (i.e. without flux jumps). A direct inspection of Figure 60 shows that the critical current densities are rather similar for all samples, whereas the avalanche activity in the bi-layer sample has decreased as compared to that in the NbN single layer.

5.4 Quantitative MOI for the Bi-layered system

As discussed earlier, in Chapter 4, performing quantitative magneto-optical imaging in a range including positive and negative fields requires some fine adjustments, especially to avoid experimental artifacts. Figure 61 shows the mean intensity level *vs* H of the whole MO image. The blue ellipse highlights the field range, where we will focus our efforts on the following paragraphs. At least in this field range, there is only one value of brightness for each value of the applied field H. Furthermore, the field range is far enough of the parabola minimum, and so the noise level is not too high. Taking into account these two features, one can make a convenient choice of $\Delta\alpha$ to study the critical-state penetration and the occurrence of anti-avalanches in these systems.

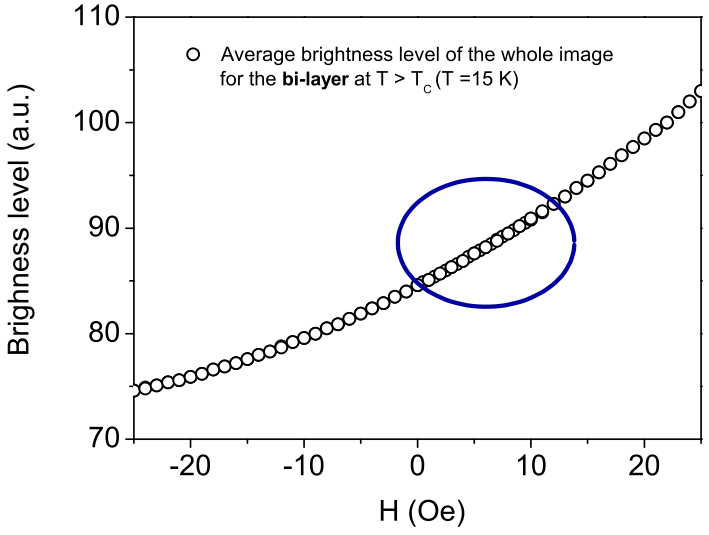

Figure 61: Mean intensity level of the whole MO image taken at $T = 15$ K (above T_C of all samples) as a function of the applied field. The field range where this Chapter is focused (close to zero) has only one single value of pixel brightness for each field.

Flux avalanches disrupting the smooth penetration after a zero field cooling procedure can be visualized in the MO images of Figure 62(a), for each of the investigated films. In all those MO images, the brighter the pixel, the higher perpendicular flux density. While large dendritic flux avalanches are observed in both NbN60 and Nb15 films, the bi-layer system exhibits much less activity, only some small finger-like avalanches occurring

from the left and right edges. By changing the temperature, magnetization loops allow one to delineate the instability region in the applied magnetic field versus reduced temperature (H-t) diagram shown in Figure 62(b). This figure presents one of the main messages of this Chapter, namely, a substantial enlargement of the stability regime, i.e., where only smooth flux penetration occurs, of the bi-layer system as compared to the bare NbN film. In other words, the bi-layer instability regime (in green) shrinks toward that of the Nb15 one (in yellow).

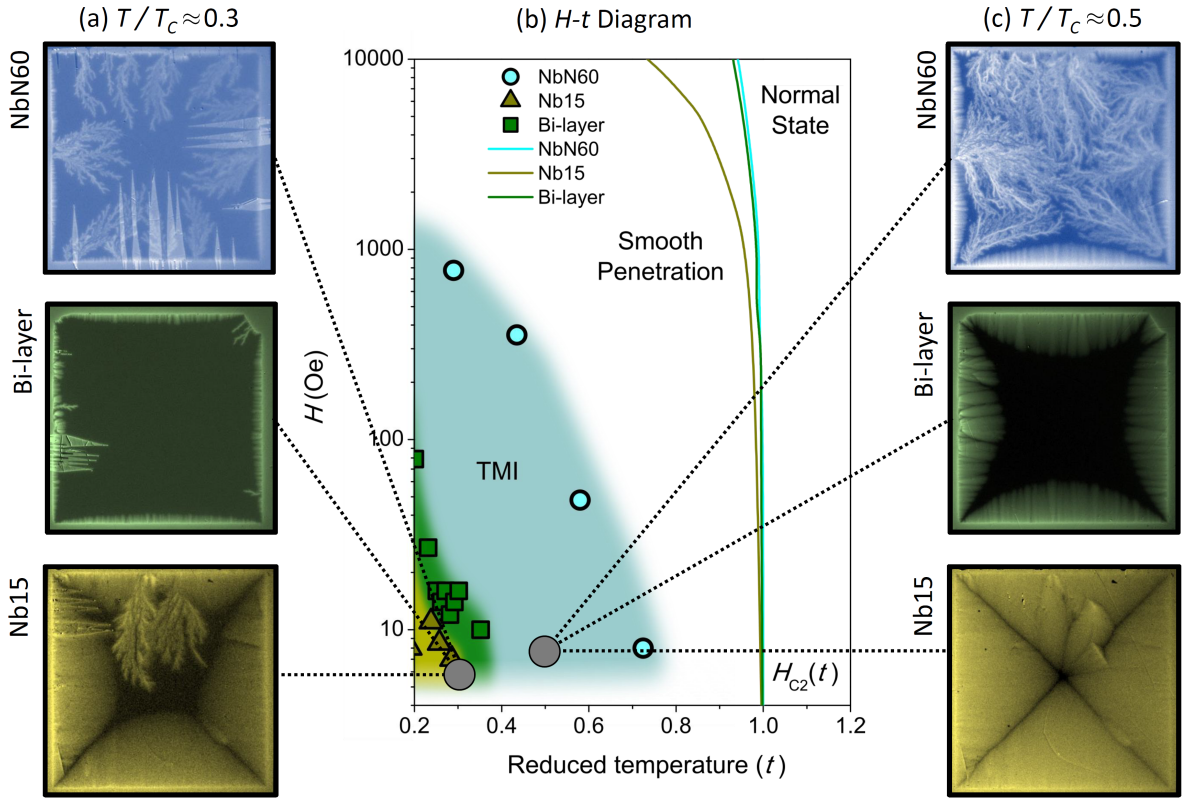

Figure 62: Column (a) shows MO images for each studied samples at $t \approx 0.3$ and $H = 4$ Oe. The zig-zag-like features in the images are related to domain walls in the indicator film. (b) H-t diagram showing the thermomagnetic instabilities regime as a function of the reduced temperature; (c) MO images taken at $t \approx 0.5$ and $H = 8.5$ Oe.

When $t \approx 0.5$, the NbN60 sample exhibits avalanches, as presented on the top MO image in Figure 62 (c). Both the bi-layer and the Nb15 films show smooth penetration, with the latter one in the fully flux penetrated state. All the flux avalanches presented in Figure 62 show positive flux only, i.e., they were created following the virgin curve of the magnetization loop by increasing the applied field from zero. By decreasing the applied

magnetic field in a superconducting film, after keeping flux trapped into the sample, negative field-polarity avalanches, or simply anti-avalanches, can occur. Anti-avalanches can show an annihilation zone [48, 51], i.e., a boundary of zero flux density separating the regions of flux and antiflux, which coexist due to the application of moderate reverse fields in a sample with flux already trapped by the pinning centers. This terminology has been used to describe the contour of anti-avalanches in the early stage of MO investigations of the abrupt flux penetration in superconducting thin films [48].

Once anti-avalanches are created by decreasing the applied magnetic field, their onset depends on the previous magnetic history of the system. Figure 63(a)-(e) presents quantitative MO images obtained at certain magnetic fields along the hysteresis loop of the NbN/Nb bilayer sample at $T = 3.5$ K. The spatial profile of the induction component $B_z(r)$ at the bottom of each image has been obtained from an average of 40 lines as shown by the translucent yellow bar in panel (a).

Figure 63(a) shows a typical critical state-like field profile for the virgin curve in a magnetization loop where the inner part of the film is still in the Meissner state (dark inner area), i.e., $B = 0$. In panel (b), the applied field reaches its maximum value ($H = 46$ Oe), and $B > 0$ at the center of the sample. The diagonal dark lines forming an X shape pattern are named discontinuity lines (d-lines), and delineate the locations where the supercurrent undergoes an abrup change of direction. Panel (c) shows the flux density landscape after decreasing H down to 14 Oe starting from its maximum value, and just before the occurrence of the first anti-avalanche in the system. The field profile in panel (c) reveals a large quantity of positive flux trapped in the sample. The first anti-avalanche (d) starts from the top left corner into the upper left d-line. This preferential track suggests that most likely this avalanche is driven by the flux-antiflux annihilation process. The magnetic profile at the bottom of panel (d) shows the recorded imprint of this anti-avalanche, and it does not change the polarity of the induction field B along its path, but strongly decreases the local field as it passes. By decreasing the applied magnetic field by 1 Oe, another anti-avalanche is triggered from the left edge, transpassing the center of the sample and then crossing the first avalanche of anti-flux. The second anti-avalanche

does not change the local field to negative values, although it decreases further the average B in the whole sample. Nevertheless, these two anti-avalanches exhibit particular features that can be better emphasized by implementing differential MOI [137], i.e. by subtracting consecutively recorded images. The result of this procedure is presented in panels (f) and (g) of Figure 63.

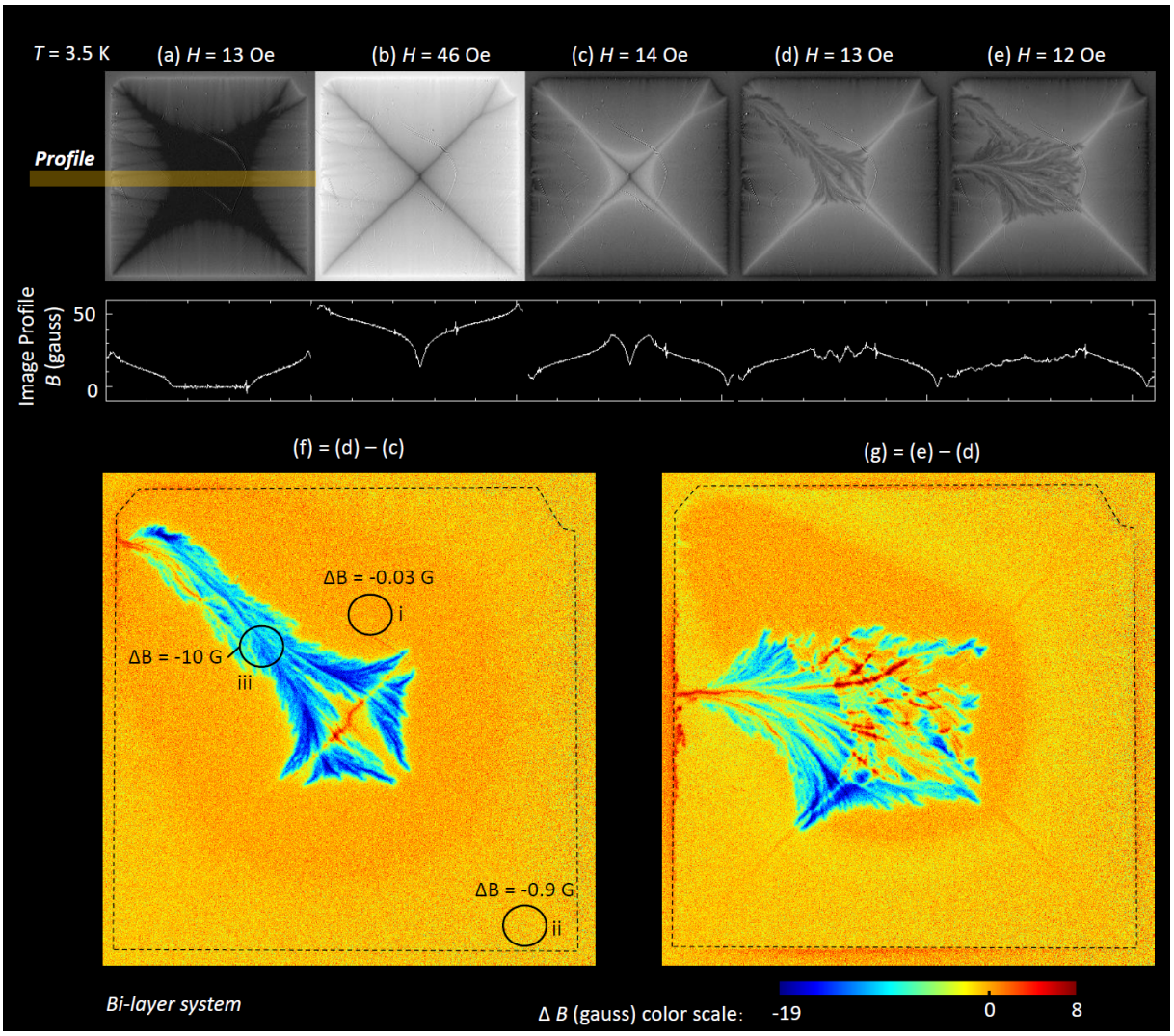

Figure 63: (a)-(e) A sequence of quantitative MO images of the bi-layer system, for different applied magnetic fields, after a ZFC procedure, at $T = 3.5\ K$. At the bottom of each panel the B_z profile is shown, averaged from 40 lines delimited by the translucid yellow bar identified in panel (a). (f) Differential image obtained by subtracting (c) from (d), which shows the first anti-avalanche and an orange halo surrounding it. The field variation ΔB is indicated by black circles, (i) inside the halo, (ii) outside the halo, and (iii) inside the avalanche. (g) Differential image between panels (e) and (d), where the second anti-avalanche crosses the first one. The color scale indicates that the trapped field increased in some regions where the avalanche branches cross each other. The dashed lines in panels (f) and (g) are indications of the sample edges.

Note that the first anti-avalanche running along the d-line runs essentially along it, with moderate lateral spread. A remarkable feature is the appearance of a halo surrounding the anti-avalanche, a feature that, to the best of our knowledge, has not been reported so far. The halo definition in the context of flux avalanches is described in the

next subsection. To describe this halo in a quantitative form, we measured the average variation of B in three circular regions with 25,000 pixels each in different regions throughout the sample. The result is marked by the black circles seen in panel (f). The circle (i), inside the halo itself, is the region where the local field decreased less ($\Delta B_i = -0.03$ G). This procedure was done in other points across the halo (not shown), to confirm this observation. Outside the halo, the circle (ii) results in $\Delta B_{ii} = -0.9$ G, and inside the avalanche (circle (iii)), the average flux density variation within this area was $\Delta B_{iii} = 16$ G $- 26$ G $= -10$ G. According to the color scale, one can see that there are regions in the anti-avalanche branches where the field variation is as high as -19 G. The differential MO image in panel (f) allows one to state that the average field in the sample decreased. The trapped flux in the system seems to lead to this unexpected halo. More details on the halo structure and its surroundings are provided in the next subsection. The halo is not a thick annihilation zone, as one can see in the B_z profile of Figure 63 (d) and (e) − there is no crossover between positive to negative flux there, and thus, no zero-field region. This halo refers to the absence of rearrangement of the flux distribution in the region around the abrupt penetration during the first anti-avalanche.

Furthermore, the sample Nb15 also shows a halo-like structure around its first anti-avalanche. Figure 64 shows MO images taken at 2.4 K at the decreasing field of 7 Oe (a), and 6 Oe (b), after reaching a maximum field of 46 Oe. In the latter, one can see the first anti-avalanche. Panel (c) is the differential image from (b) and (a), which allows one to observe a small halo around the avalanche triggered at the top edge of the sample. The red circles in panel (c) were used to count intensity of the variation among the broader gray region (circles number 1 and 4) and the lighter regions (circles number 2 and 3). The intensity of the field in the brighter regions (circles 2 and 3) is one order o magnitude larger than the other parts of the sample (circles 1 and 4). All the measurements made in the sample indicates that the flux inside this specimen changed, but in that halo where the circles 2 and 3 are placed, it changed less. It is important to mention that this is not a simple reshaping of the incoming flux front - this is a picture of how the system stabilized just after the step in the decreasing field and avalanche burst. Figure 64 also shows data

for NbN60 film, in panels (d) and (e). As one can see in the differential image of panel (f), there was no halos around anti-flux avalanches, even in the same conditions of Nb15 samples, i.e., the first anti-avalanche rushing into the critical-state-like penetrated flux.

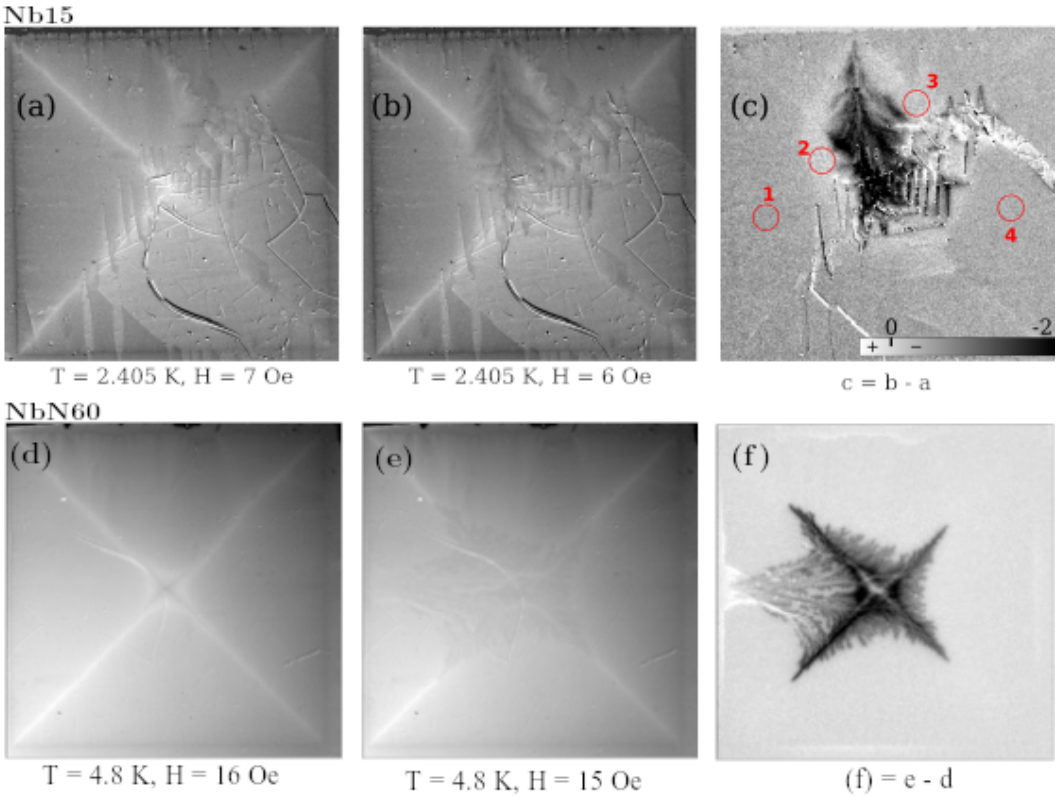

Figure 64: (a) MO image of the Nb15 sample, after a ZFC procedure down to 2.405 K and after decreasing H from 46 Oe to 7 Oe. (b) Anti-flux avalanche at H = 6 Oe. (c) the matrix difference between the anti-avalanche image and the previous image, $(c) = (b) - (a)$., where a halo can be seen around the black anti-avalanche. MO images of the NbN60 were taken at $T = 4.8$ K in decreasing fields, $H = 16$ Oe (d) and $H = 15$ Oe (e). Panel (f) is the matrix difference between the later two images.

Another intriguing aspect of the set of images shown in Figure 63 is that the second anti-avalanche crosses the first one. The color scale in Figure 63(g) allows one to highlight the fact that the branches of the first avalanche transpassed by the second one, undergo a positive variation of the local magnetic field as high as 8 G. Flux avalanches triggered during a ZFC procedure are known for avoiding each other during their propagation into the sample [48], no matter whether they are small and fingerlike or large and highly branched. However, avalanches may cross each other in descending fields because there is still positive flux where the prior anti-avalanche passed. Although the halo of the

first anti-avalanche has changed after the advent of the second avalanche, this last one does not have a halo surrounding it.

5.4.1 Halo definition

We define halo as the region of excess brightness (in our case, ΔB) surrounding the first anti-avalanche for the bi-layer system. Figure 65(a) is the same differential image presented in Figure 63(f). Panels (b), (c) and (d) are the averaged ΔB profiles for three regions of the sample, indicated by translucent gray bars. Panel (b) shows the ΔB profile passing through the avalanche trunk, where there is an intense negative variation of B ($\Delta B < 0$), as well as a smooth variation close to the sample edges (outside the halo). In (c), the halo region presents the highest brightness in the whole image ($\Delta B = 0$). Panel (d) presents a region outside the halo where ΔB is negative and constant. Therefore, the term halo is suitable to describe such a region in the framework of differential images.

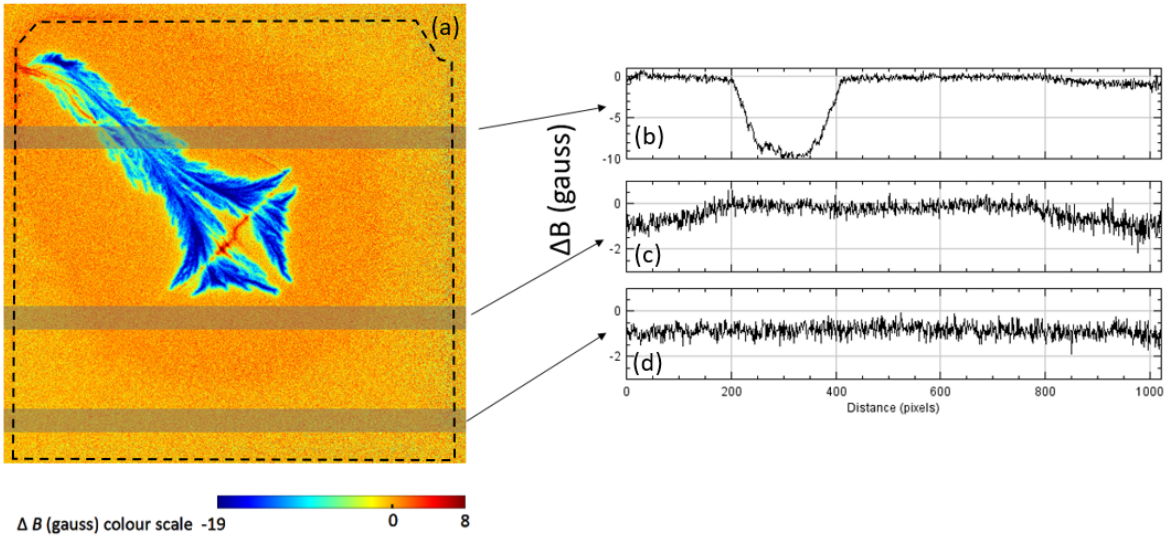

Figure 65: Description of the halo structure. (a) Differential image obtained by subtracting (d) from (c) panels of Figure 63(f). Averaged ΔB profiles taken from the translucent gray bars, passing through (b) the anti-avalanche, (c) the halo, and (d) outside the halo.

5.5 Conclusions

Quantitative MOI allowed us to unveil anti-avalanches crossing each other, as well as the lack of vortex rearrangement in a large region surrounding the first anti-avalanche. This latter effect manifests itself as a halo of nearly unperturbed magnetic flux density. Furthermore, the present study revealed that the applicability of thin films of NbN, concerning the instability regime, was improved by means of a *in situ* thin Nb layer pre-deposition, without changing its upper critical field at the same reduced temperature. The region where the avalanches take place in the field-reduced temperature diagram decreases for the hybrid system as compared to the NbN film, becoming closer to that of the Nb film. In other words, there is a suppression of the occurrence of flux avalanches in the hybrid NbN/Nb system without considerably depreciating its other properties.

6 Flux avalanches in V_3Si superconducting thin films

This Chapter is an extended version of the article *Imaging flux avalanches in V_3Si superconducting thin films*, published in 2019 [138].

6.1 Introduction

Silicides are well known used in a variety of purposes, from surface hardening of cutting tools to resistive switching memory devices [107, 108]. The superconducting phase of the vanadium(II) silicide was once called a *high temperature superconductor* in the 1970s, before the advent of the superconducting cuprates [103]. Flux jumps have been reported in single crystals of V_3Si [139, 140, 141], but until recently, no direct observation of avalanches in thin films of this superconductor had been reported. In 1954 [101] a bulk sample of the compound V_3Si was for the first time reported being a superconductor, with $T_c = 16.7$ K at atmospheric pressure [102, 103]. As a single crystal, it exhibits highly anisotropic critical current [104] and shows a low-temperature martensitic phase transition, from cubic at room temperature to tetragonal, below 30 K [105, 106]. For decades, researches discussed if this crystallographic transition was the key for the superconductivity, but both phases were found to achieve the superconducting state. V_3Si has received attention recently due to the global interest in possible two-band superconductors - where ultra high-quality samples shaped as thin films are mandatory [109, 110, 111]. There were no studies about flux avalanches in V_3Si thin films, until the paper in which this Chapter is based on [138]. Another important remark is that

the experiments on that sample were performed in 2014-2015, before implementation of quantitative magneto-optics in our group, being this the reason why the data in this Chapter was not submitted to the standard calibration procedure.

6.2 Experimental details

The sample treated here was deposited in 2008 by the group headed by Prof. Carlo Ferdeghini, in Genova, Italy, and the first publication with details of the sample deposition is Ref. [109] in our list. As summarized in Chapter 3, films deposited using the PLD technique demands one or more targets. Silicon pieces and a Vanadium ingot, both from Koch-light laboratories, were used to prepare the target by arc-melting furnace in argon, and then melted again in a induction furnace to outgas the target and ensure it was a single phase bulk. This bulk was analyzed by micrography and X-ray diffraction (XRD), which confirmed the exact stoichiometric of this new target. The V_3Si thin films were deposited on a (111)-oriented $LaAlO_3$ substrate by the PLD method, using this single stoichiometric target in ultra-high vacuum, 10^{-10} mbar. The substrate temperature during the deposition was close to 1200 °C and the background pressure lower than $5 \cdot 10^{-8}$ mbar. The laser frequency was kept constant during the deposition, 30 Hz, and the fluency was 2 J/cm^2. The thickness of the sample was measured *in situ* by a Reflection High Energy Electron Diffraction (RHEED) system. At the central part of the substrate, the films were 180 nm thick. These films were polycrystalline and had the [210] crystallographic direction perpendicular to the substrate surface, as is illustrated in Figure 66. It is important to mention that the sample studied in this Chapter was cleaved by notching the border of the substrate.

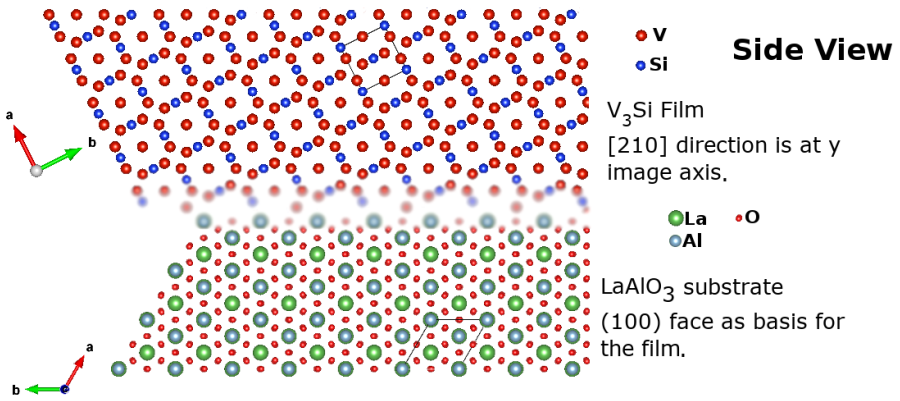

Figure 66: Schematic illustration of the crystallographic structures of both the substrate and superconducting film of V_3Si. The blurred region between the two materials is intended to represent the buffer zone.

6.3 AC and DC measurements

By using AC magnetic susceptibility measurements, as shown in Figure 67(a), we determined T_c of (14.5 ± 0.1) K as the upper bound of a broad normal-superconducting transition ($\delta T \approx 2$ K), at remnant field. In order to investigate the instability regime, which one wants to locate and, eventually, to avoid in applications, magnetization loops were performed and are summarized in Figure 67 (b) and (c). In panel (b) we compare the DC magnetization vs. applied magnetic field curves taken at three different temperatures (2 K, 7 K, and 12 K), whereas panel (c) shows a wider picture of the thermomagnetic instabilities , illustrating how the field range varies with temperature.

An interesting feature of the Figure 67 (b) is the stronger diamagnetic signal for fields from $H = 10$ Oe to $H = 1000$ Oe at 7 K as compared to 2 K. Moreover, this feature changes after the flux jumps stop (for fields higher than $H = 5000$ Oe), and the sample behaves just as one would expect from a type-II superconducting film in a critical state-like, smooth penetration regime.

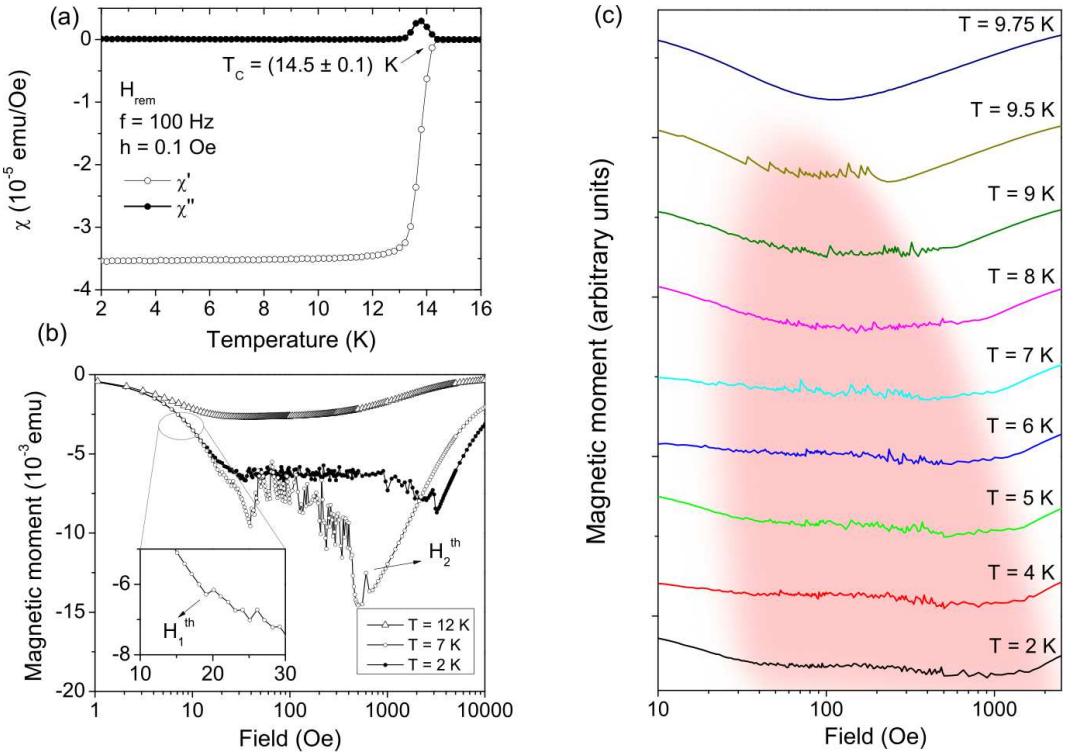

Figure 67: (a) AC susceptibility versus temperature for the V_3Si film, at remanent field (H_{rem}), showing the broad normal-superconducting transition. (b) Isothermal DC magnetization versus applied magnetic field taken at 2 K, 7 K and 12 K, for a V_3Si film. For lower temperatures and $H > 10$ Oe, the noisy behavior is the signature of flux avalanches. Inset: Lower threshold field for thermomagnetic instabilities at 7 K. (c) DC magnetization versus applied magnetic field for temperatures ranging from $T = 2$ K to $T = 9.75$ K. For ease of viewing, curves taken at different temperatures have been shifted vertically. The colored background (magenta) illustrates the region where thermomagnetic instabilities take place.

In the inset of Figure 67(b), the black arrow at left indicates the lower threshold field H_1^{th}, delimiting the beginning of the instability regime at $T = 7$ K. At higher fields, the upper threshold field H_2^{th} is indicated. A challenging part of studying flux avalanches using magnetic measurements is that, at lower temperatures, the first occurrences are too small to be identified in the magnetization curve, comparable to the background noise. Nevertheless, by analyzing the MOI results (shown in the next section) one can identify such small avalanches at lower fields, allowing for quantitative determination of the instability region, as in the illustration (magenta background) in Figure 67(c).

6.4 MOI measurements

The MOI measurements presented in this Chapter were done as described in Chapter 3. A visual summary of the MOI performed on the pristine sample is shown in Figure 68. Each column comprises images vs. applied field selected experiments at a constant temperature: $T = 2.51$ K in column (a), $T = 7.00$ K in (b), and $T = 12.0$ K in (c). Along each line, one can analyze how the sample behaves after a ZFC procedure down to the indicated temperature. Each line corresponds to a fixed applied magnetic field of $H = 10$, 20, 30 and 46 Oe.

The flux avalanches shown in column (a) are smaller, more numerous and less branched than the avalanches in column (b), as already shown by T. H. Johansen [48]. In Figure 67(c), the jumps at lower temperatures are also smaller. Furthermore, still on panel (c), avalanches at 7 K are larger and more branched. A visual confirmation of the larger jumps is shown in Figure 67(b).

Another aspect of this set of images is that the smooth flux penetration at all temperatures, notably at 12 K, exhibits a fanlike shape. This feature is known to reflect the existence of defects, either at the borders or within the film [43, 142, 143]. Evidences of a direct correlation between such flocking in the MO image and misorientations among grains has also been treated in [144].

Once the temperature is higher as one goes to the right-hand side of Figure 68, in column (b) J_c is lower than in colum (a) - this can be seen by the smooth flux front emerging from the bottom edge of the sample, which had penetrated more at $T = 7.00$ K than at $T = 2.51$ K, due to the decreasing of the shielding capability at higher temperatures. But this behavior of $J_c(T)$ is not enough to explain the anisotropic shielding effect visible in Figure 68, where the brightness level close to the sample edges shows an asymmetric decrease towards the center. The flux penetrates deeper into the sample from the bottom edge. A possible cause for the anisotropy in the fronts of penetrated flux could be a temperature gradient across the film. One important point to have in mind is that the unidirectional heat removal from the cryostat cold finger could cause a temperature

gradient across the film. Then, we have reversed the sample assembly on the cold finger, in order to check this possibility, which was ruled out by undebatable fact that exactly the same experimental results.

The crystallographic orientation of the grains could also be a possible source of the flux penetration anisotropy, since in a single crystal of V_3Si the ratio of the critical currents along different crystallographic directions can exceed 3 [104]. Nevertheless, this could only be the case for epitaxial thin films, not for a polycrystalline specimen studied here [109].

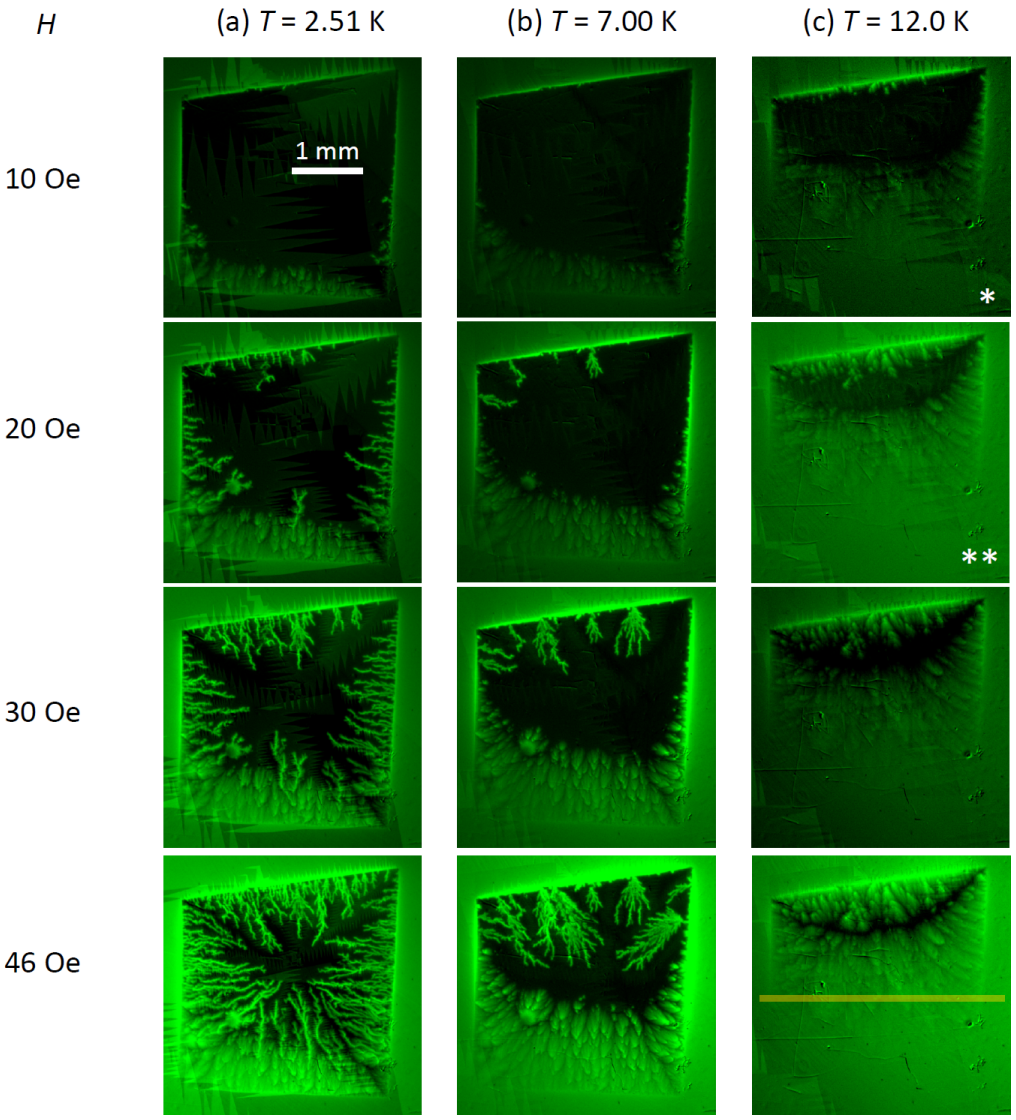

Figure 68: Magneto-optical images taken after a ZFC procedure at constant temperatures (a) $T = 2.51$ K, (b) $T = 7.00$ K, and (c) $T = 12.0$ K. The applied fields are $H = 10$ Oe, 20 Oe, 30 Oe, and 46 Oe. The * and ** marks on the top right panels, are for images whose brightness and contrast were adjusted to have a better visualization. The yellowish line in the last panel shows, approximately, the place where the sample was cleaved for the next MOI measurement, presented in the next figure.

To check the reproducibility of such inhomogeneous shielding we cleaved the pristine sample in the position indicated in the last image of the column (c) of Figure 68 and used the upper piece to a new round of MO measurements. Figure 69 shows MO images taken at $T = 2.42$ K, 7.00 K, and 12.0 K, after a ZFC procedure, for fields $H = 10$ Oe, 20 Oe, 30 Oe, and 46 Oe, applied perpendicular to the plane of the film. An important aspect of this assembly is that we adjusted the brightness and contrast of the

images at the highest field, and kept the same scale for the images at lower fields - that is why images on the first line appear darker. Looking at the first row of Figure 69, the image at higher temperature shows the lower shielding effect, just as expected once the critical current decreases for increasing temperatures.

Examining the last row of images, for an applied field $H = 46$ Oe, one can easily identify that the image at $T = 7.00$ K has a larger shielded region than that at $T = 2.42$ K. This is due to the fact the quantity of avalanches is higher at the lower temperature, and, most probably, related to what we see in the magnetization measurements in Figure 67 (b), where the curve at $T = 7.00$ K shows a stronger diamagnetic signal than that at $T = 2.42$ K. Also in this last line, the image of column (c) still shows the four borders, which is different from the correlated image of the pristine mother sample in Figure 68 (c). This can be taken as a check for consistency of the assumption that the reason for the anisotropic shielding is due to the thickness variation of J_C, which is larger at the central part of the film than at the lower border.

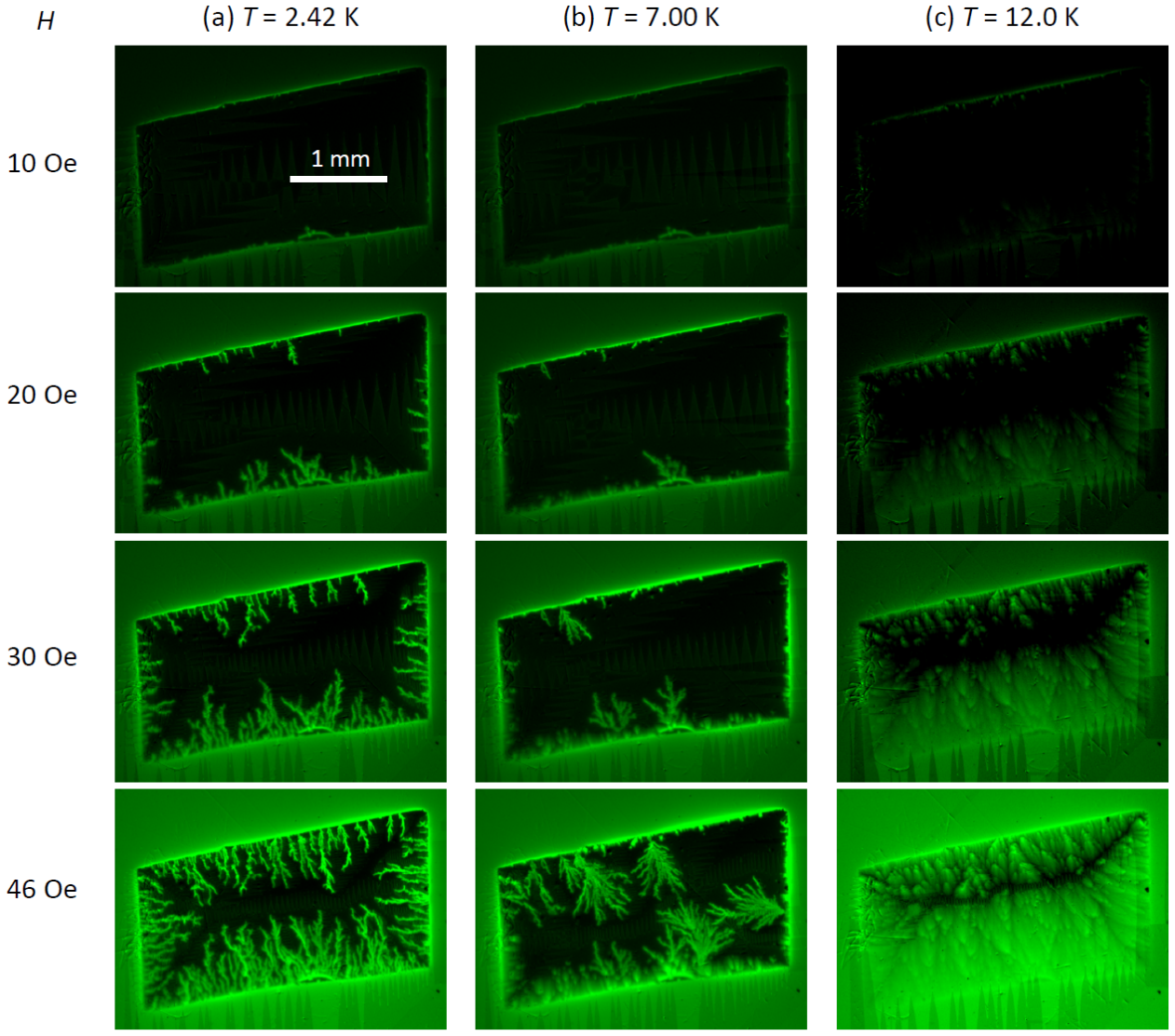

Figure 69: Magneto-optical images of the cleaved sample, taken after a ZFC procedure at constant temperatures (a) $T = 2.42$ K, (b) $T = 7.00$ K, and (c) $T = 12.0$ K.The applied fields are $H = 10$ Oe, 20 Oe, 30 Oe, and 46 Oe, as indicated on the left

.

6.5 Thickness measurement

One hypothesis that could explain the inhomogeneous flux penetration throughout the film is a non-uniform thickness. Different attempts to measure the thickness of the sample were performed, but most of them were unsuccessful. XRD low angle reflectivity gave no appreciable results probably due to the high value of roughness of the surface,

as one can observe in the SEM image in Figure 70(a). We also were not able to find a selective etching for the film and not for the substrate in order to realize a step that could be measured by AFM or other profilometry technique. The solution adopted was to perform some destructing tests on sister films by measuring for a cross section of the film by SEM. The sample was embedded into resin and prepared cross-sectional measurement of the thin film thicknesses. The problem with this approach is that the substrate ($LaAlO_3$) is very brittle and tends to fracture during the metallographic preparation. For this reason the thickness measurement was only possible in certain position along the length of the sample where the V_3Si film was intact, as is illustrated in panels (b) and (c) of Figure 70. The film thickness measurements show a trend in the direction examined in the cross section (from about 100 nm to about 60 nm). This test was in agreement with a relative indirect thickness measurements by evaluating the intensity of the Si peak in EDS measurements, which are summarized in Figure 71.

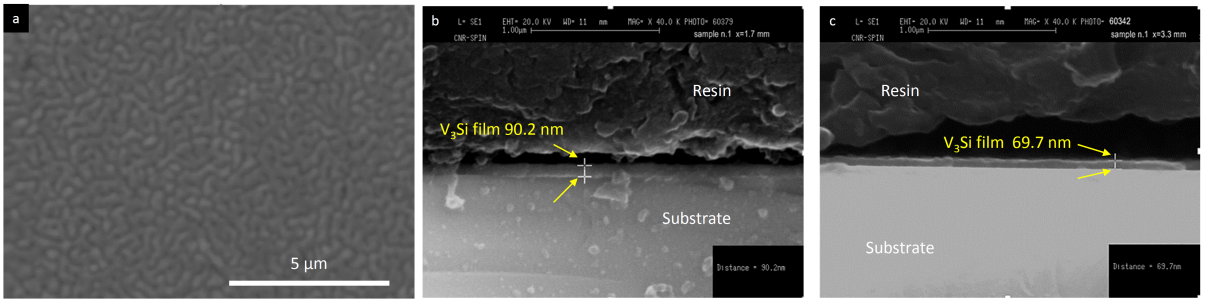

Figure 70: (a) SEM image of the V_3Si surface, where the roughness of the sample is evident. Panels (b) and (c) are examples of SEM cross-section images of the same film, but in different positions along it, showing the thickness variation.

The direct observation of thickness variation from SEM cross-section images needs to be translated, in a non-destructive way, to the sample that we performed MOI measurements. So, we made EDS measurements on sister samples, applying 8 kV to ensure that the spectrum response includes enough information coming from the substrate. The ratio between the intensity peak of Si (from the sample) and Al (from the substrate) was mapped all over the a squared sample, in a Cartesian order: starting close to the bottom-left corner of the sample, where we set the origin of a Cartesian plane, and choosing

the sample edges to be the x and y axis, the first line (in blue) of measurement was at y =0.5 mm, in which 7 EDS regions were recorded. The second (in red) and the third line (in green) were taken at y = 3 mm and y = 4.5 mm, respectively. The variation of such ratio can be ascribed to the film thickness measured directly in SEM. The calculated thickness values are shown in the vertical axis of Figure 71, as a function of the x position of each EDS measurment. The thickness variation is confirmed along both directions parallel to the sample edges, which is consistent with the observed peculiar flux penetration. The inset in Figure 71 is an example of EDS spectrum, showing the counts per second normalized the energy, as a function of the X-ray energy detected. The Al (from substrate) and Si (sample) peaks are labeled.

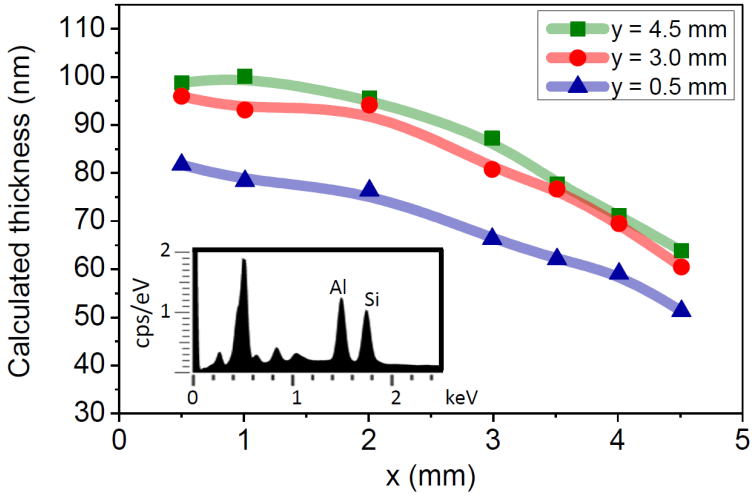

Figure 71: Calculated thickness as a function of the position on the surface of a sister sample. The inset exemplifies an EDS spectrum in which the ratio between the intensity peak of Si and Al was used to obtain the calculated thickness.

It is worth to mention that such a nanoscaled thickness variation was not made intentionally, but rather it was a consequence of the limitations of the deposition technique. When a film is deposited, a key-parameter is its uniformity. For a position away from the center of the substrate, the thickness decreases due to a small difference on the distance from the material source (or target) to the substrate. Furthermore, this tiny variation along the sample length is challenging to measure in standard equipment like AFM and confocal laser microscopy, so this indirect quantitative measurement of the film thickness using EDS suits adequately nanoscaled wedge-shaped thin films.

6.6 Conclusion

Flux avalanches of dendritic profile were observed, for the first time, in V_3Si thin films in the presence of a magnetic field applied perpendicularly to the plane of the film. Possible reasons for the anisotropic pattern of the penetrated flux front were investigated, leading to the conclusion that the cause is a non-negligible thickness gradient which, on average, amounts to 7 nm/mm. As seen in this Chapter, flux avalanches may occur in V_3Si, so that, the list of superconducting films exhibiting this behavior must be updated (see, e.g., [128] for a comprehensive inventory) and, therefore, such a characteristic must be taken into consideration when films of this A15 superconductor are envisaged for possible applications. This study also motivated us to go along with the idea of making, intentionally, nanoscaled wedge-shaped superconducting thin films - which is the focus of the next Chapter.

7 Nanoscale wedge-shaped superconducting thin films

7.1 Motivation

The intriguing non-uniform flux penetration due to a thickness variation in the V_3Si film, presented in Chapter 6, motivated the group to revisit a subject started by Prof. Maycon Motta, Dr. Jo Cuppens, and Prof. Alejandro Silhanek in Leuven in 2011: a nanoscaled wedge-shaped superconducting thin film. Ideally, this wedge-shaped sample would be a film with a well-defined geometry, having a thickness decreasing linearly down to a non-zero value at the opposite edge. The **nanoscale** term is adequate for the situation because of the difference between the maximum and minimum thicknesses would be in the nanoscale (dozens of nanometers). We intend to make a ramp, i.e., an inclined surface, whose angle is about $5 \cdot 10^{-6}$ rad (or 0.003°), considering the surface of the substrate as the reference, and extending through a few millimeters. Microscopy techniques such as atomic force, scanning electron, and confocal laser might allow us to characterize such a tiny surface inclination. Apart from the technological challenges, if we were able to produce such a wedge-shaped film, we would like to control the inclination in order to investigate the smooth and abrupt penetration regimes, and so being able to enhance the comprehension on the following questions: **(1)** *can we affect the smooth penetration regime by varying the sample thickness along one of its dimensions?* **(2)** *Will the avalanche regime be influenced by this variation?* Figure 72 presents the features we expected from a MO experiment in an ideal wedge-shaped superconducting thin film, where J_C is constant all over the sample. The illustration is organized in two columns: the left column of images

(a, c, e & g) is related to a film with uniform thickness, and the right column (b, d, f & h) to a wedge-shaped thin film. Panels (a)-(d) display the superconducting films after a ZFC procedure, at $T < T_C$ and $H_{c1} < H << H_{c2}$. Considering a critical state model, panel (a) illustrates the flux penetrated at a certain depth (ℓ) into the film, where the screening currents are J_C, and their cross-sections are represented by the reddish areas (c). Whereas ℓ is the same for all the borders in a uniform sample (a), the thinner and the thicker borders of the wedge-shaped sample (b) would present different values of ℓ at the same value of H. Charge conservation and current continuity allow one to expect the screening current i to be the same all over the film once there are neither sources nor drains in the system. So, as shown in (d), by keeping J_C constant throughout the specimen, the cross-section area of the left border should be equal to that one at the right border, and once the thickness is different, its extension is also different. Panels (e)-(h) show the samples at a higher applied field, enough to force flux to reach the center of the sample. Therefore, the MO images of the wedge-shaped V_3Si film, presented in Figure 68, seems to follow the ideia that J_C is constant (or nearlly) along the different edges.

As a consequence of what was discussed above, we expect that the d-lines should be shifted towards the thicker border (f). We also expected to detect a difference in the avalanche triggering and in their sizes, shapes, and upper limit temperatures. Differently from what one would expect for a sample whose thickness is uniform, a change in angles of the d-lines cannot be directly ascribed to an anisotropy in J_C, as the case described by Albrecht *et al.* [46], and discussed briefly in Chapter 2 of this thesis. One expects to visualize the d-line changing its direction even if J_C keeps constant all over the sample.

Unfortunately, for the V_3Si sample in Figure 68, some d-lines at the corners are not well-defined and cannot be used to evaluate the critical current density.

A somewhat lower quality of the sample, which also results in the fanlike penetration, might be the cause for a critical current smaller than it would be for a good-quality homogeneous film of the same thickness. Also important to mention is that the horizontal shift of the d-lines at the center of the sample towards the thicker edge is clearly visible and confirms the shallower penetration in the thicker region of the film. The occurrence

of avalanches also may be affected by the thickness variation even if J_C is constant. This is an additional indication that V_3Si, studied in Chapter 6, is a wedge-shaped thin film whose J_C does not vary strongly across the film.

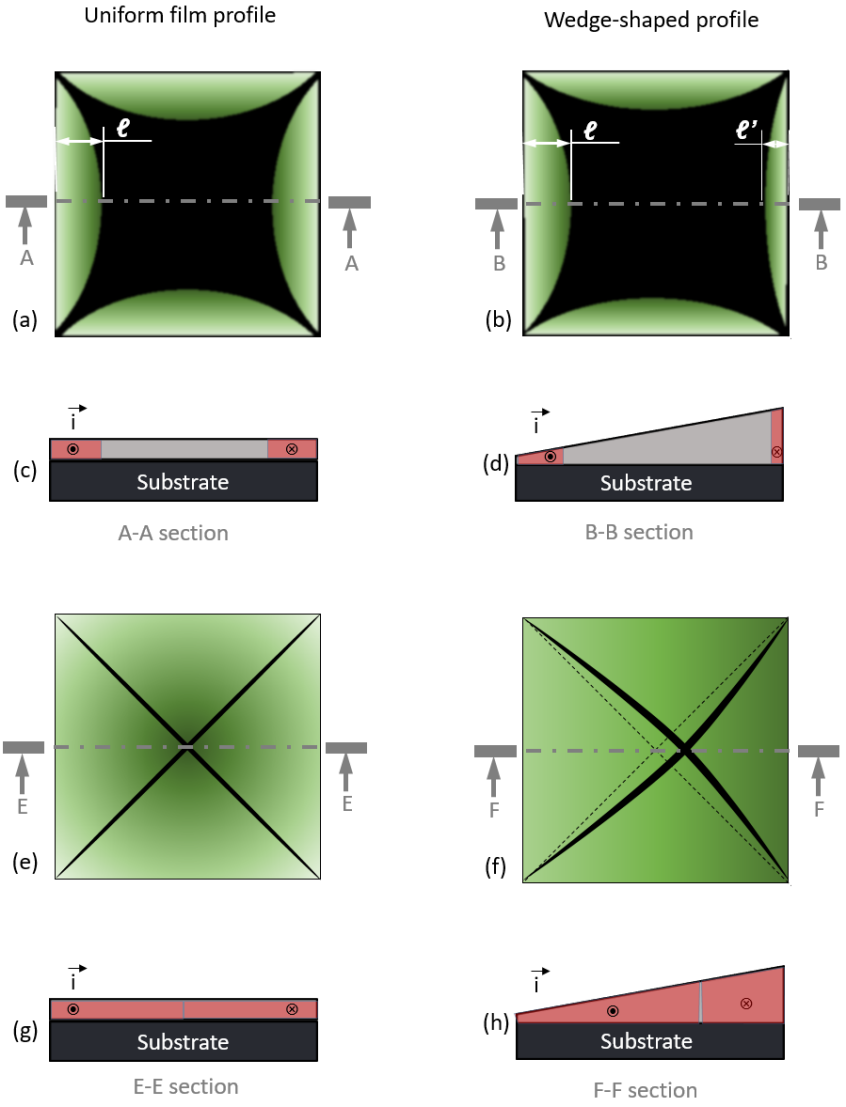

Figure 72: Schematic representation (out of scale) of uniform (a) & (c) and wedge-shaped (b) & (d) superconducting thin films at $T < T_C$, and $H_{C1} < H < H_{C2}$ perpendicular to the substrate surface, for a sample with constant J_c partially penetrated by magnetic flux. The reddish regions represent the portions of the film where the magnetic field has penetrated. Panels (c, d, g & h) are illustrations of the expected response in a MO-imaging experiment for the full penetration state at higher fields. The applied field H is larger in panels (e) and (f), where one has full penetration. The dashed diagonal lines in (h) highlight the deviation of the d-lines from the center.

For several materials, $J_C(d)$ varies inversely with the thickness, i.e., the smaller the thickness, the higher is J_C [145, 146, 147, 148, 149]. Figure 73(a) illustrates a strong

asymmetric flux penetration into a specimen whose J_C is variable along the one of the in-plane axis (x for instance), as could be also the case for a quite strong thermal gradient, for example. In panel (b), a wedge-shaped film with $J_C \propto 1/d$ is shown and the asymmetry in the flux penetration is expect to be smaller than in panel (a). In both situations, the cross-section area for the same current i is represented as being 10 times smaller on the left edges of the sample in panels (c) and (d) as compared to the right side.

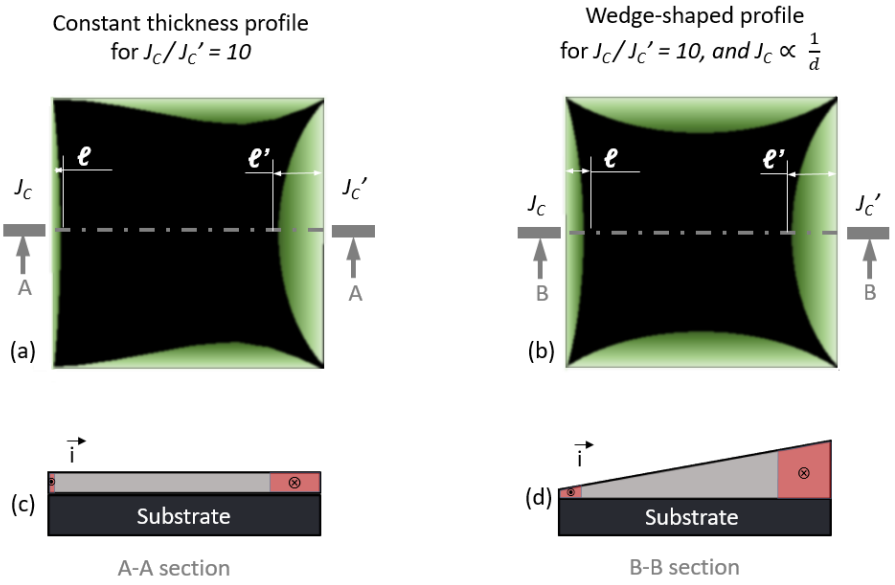

Figure 73: Schematic representation of a constant thickness film (a) & (c), with a J_C gradient from left to right. Panels (b) & (d) are for a wedge-shaped superconducting thin film whose J_C is also not constant, but is inversely proportional to the thickness. All the panels are for $T < T_C$, and $H_{C1} < H < H_{C2}$ perpendicular to the substrate surface. The reddish regions represents the portions of the film where the magnetic field has penetrated.

Back in 2011, in Leuven, Motta, Cuppens and Silhanek prepared a wedge-shaped amorphous MoGe film by moving a shutter in front of the substrate in a PLD apparatus. This film was observed in 2015, in the MOI facility at GSM. Figure 74 illustrates the experimental approach to reach the wedge-shaped sample (a), the schematic view of the film thickness (b), an optical image of the sample surface (c), and its MO images for low applied magnetic fields after a ZFC procedure, captured at 2.44 K.

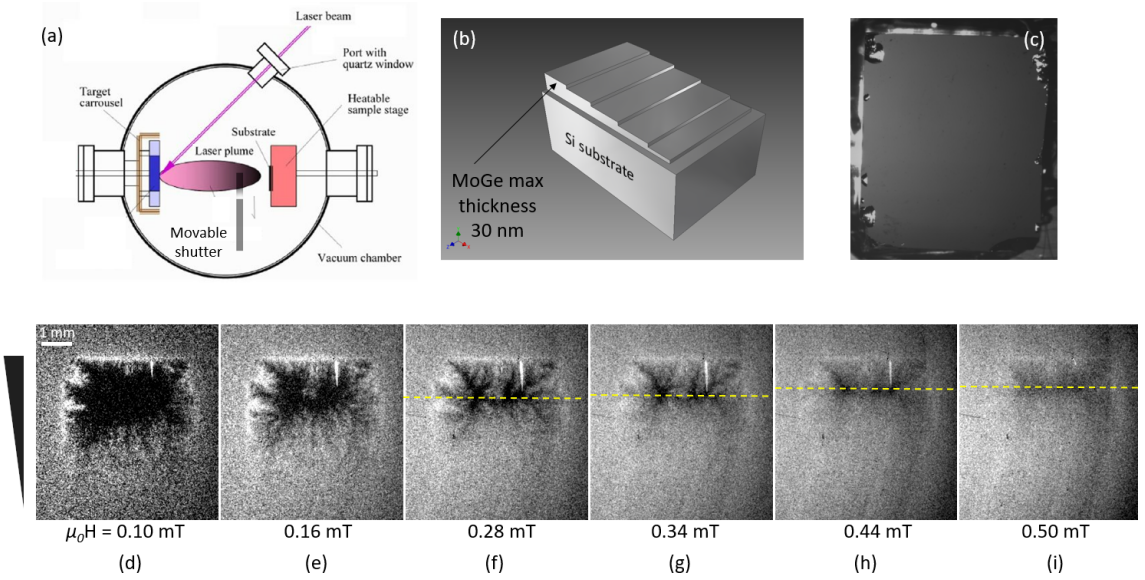

Figure 74: (a) Scheme of a vacuum chamber for pulsed laser deposition with a moving shutter to obtain a film with a staircase-like thickness. Theses steps are in the range of dozens of microns along 5 mm. (c) Optical image of the as-deposited film. Panels from (d) through (i) show magneto-optical images of the MoGe sample. The first image was substracted from the all the others, just after the ZFC procedure down to $T_{base} = 2.44\ K$. The thickness variation has its maximum at the top edge and its minimum, close to zero, at the bottom edge.

Once the critical current density of MoGe films is rather small, due to its low intrinsic pinning [61], the images are noisy, and we were not able to access the instability region using the MOI cryostat. In spite of these drawback, the MO images in Figure 74 show the expected asymmetry in the smooth flux penetration - and a clear indication that the current-carrying capacity of the bottom edge are different from the top edge. Furthermore, a remarkable feature of these images is the moving horizontal d-line, as illustrated by a yellow dashed line in panels (f) through (i),

We also carried out MOI on Pb wedge-shaped samples , protected by a Ge layer, produced by Prof. Joris von de Vondel at the Catholic Univesity of Leuven (KU-Leuven) in January 2018. He used e-beam evaporation for both elements, reaching a nominal maximum thickness of 500 nm for the Pb layer and 100 nm for the Ge protective cap. He also used the moving shutter technique to reach the wedge-shape profile. Figure 75 (a) through (d) shows MO images of this sample captured at 2.66 K and fields ranging from 4.5 Oe to 46 Oe. Once this sample has no lithographed boundaries, as one can observe

on the top view optical image of panel (e), it is not an easy task to analyze the d-lines. A remarking feature of this sample is that the d-lines continue moving even after they are established, as one can see in Figure 75 in panels (f) and (g). In these two panels, brighter regions show where the flux density increased, and the darker borders close to its d-lines shows where it decreased. Both wedge-shaped films presented so far, namely, MoGe and Pb, share an important characteristic: the thickness gradient is misaligned with the edges of the specimens.

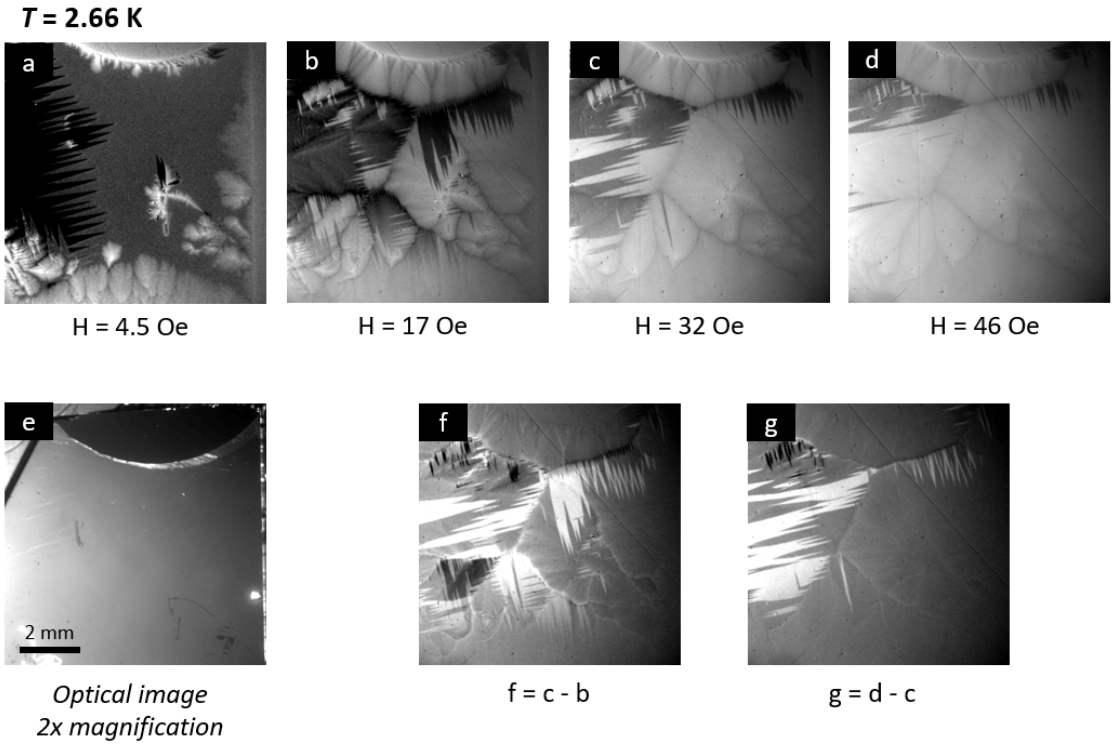

Figure 75: From (a) through (d), MO image *vs.* applied magnetic field after a ZFC procedure in a Pb-Ge wedge-shaped superconducting thin film. (e) Optical image of the sample, showing its shape and surface. (f) and (g) are matrix subtractions, where the brighter shades of gray indicate places where the B field increased, while the contrary happens at darker locations.

Despite a wedge-shaped film would interest to us being made of any material, Pb was especially suitable for this case because of the crossover between type-I and type-II superconductivity, predicted numerically for a wedge-shaped sample in Ref. [81]. In a recent work, Cadorim et al. [150] have shown that, for a mesoscopic sample, κ_c depends on its thickness d, so that a crossover from type I to type II is expected to occur as d

increases. Even if we were not able to see directly this crossover, the type-I character of bulk Pb should play an important role on how the superconducting properties of the film change with the thickness, as well as on the flux dynamics and on the occurrence and evolution of the flux avalanches.

7.2 The diffuse-shadow method to obtain wedge-shaped thin films

As described in Appendix A, we developed a high vacuum chamber ($\approx 10^{-7}$ torr) to deposit films using conventional thermal evaporation, which is based on the Joule heating, to achieve controllable conditions to grow a wedge-shaped nanoscaled superconducting thin film. We also built all the apparatus inside this chamber, such as the non-movable **d**iffuse-**s**hadow **s**hutter (dss), the thickness monitor, and the current leads for crucibles to ensure its position related to the substrate, as illustrated in Figure 76. On the left, the Pb vapor is partially blocked by the crucible shield. The dss is placed partially covering the Pb crucible, in order to take advantage of the non-punctual vapor source, as indicated by the dashed lines delineating the atom path from the Pb crucible to the substrate holder. A dark-gray color indicates the uniform and the wedge-shaped deposition region for Pb, just below the substrate-holder as well as below the dss. The position of the crucibles in relation to the shields and shutters should allow the protective Ge vapor to cover all the wedge-shaped deposition zone. Otherwise, part of the samples may degrade before its full characterization. By varying the distance between the dss and the substrate-holder, one expects to control the area of the wedge-shaped deposition zone, and thus change the thickness gradient.

Aiming to reduce the number of depositions with different shutter-to-source distances, to check the extension of the diffuse shadow on the substrate-holder, we imported the 3D representation of the deposition chamber, made in the Autodesk™ Inventor™ 2018 software [151], to Blender software [152]. We then perfomed photorealistic studies

by considering Pb source as an extended red light and Ge as a blue light, and we were able to check the regions where there should be Pb, but not Ge (blue regions), as illustrated in Figure 77 for a comb-like diffuse-shutter[1].

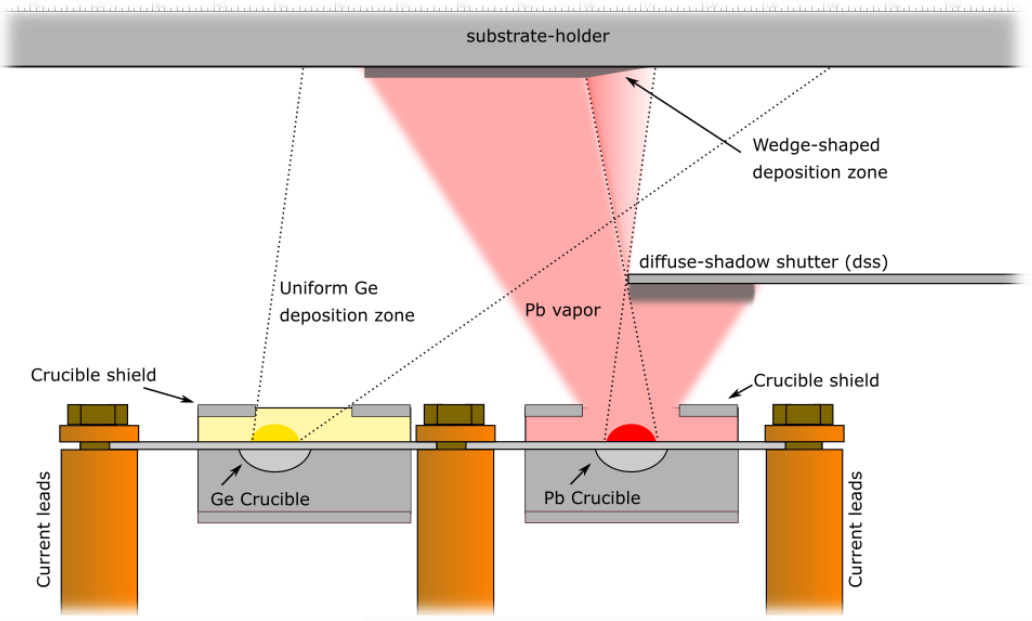

Figure 76: Schematic representation of the diffuse-shadow method to produce nanoscaled wedge-shaped thin films. Both Ge and Pb crucibles share the same negative current lead. The thickness of the deposited Pb in the dss (dark gray layer) is larger than in the substrate-holder because it is closer to the vapor source. The objects are not to scale.

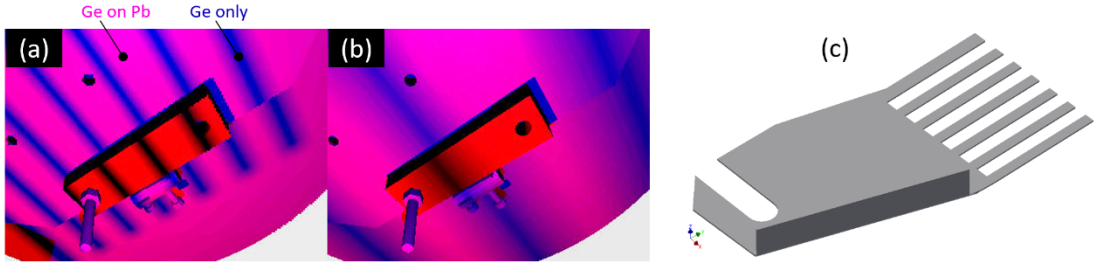

Figure 77: Simulation of a Pb-Ge deposition using a comb-like diffuse shadow shutter. The areas fully protected from the Pb source are shown in blue, and the pink region have both Pb and Ge. The shutter is closer to the substrate-holder in (a). The longer thickness gradient is expected when the shutter is closer to the crucible (b). The shape of the shutter is shown in (c), where each tooth is 4 mm wide, separated by 4 mm.

By using a first version of the dss, presented in Figure 78(a), and changing the protective layer for Al, we prepared the first successful batch of Pb deposition on a Si

[1]All the shutters with different shapes used in this work are described in the Appendix A.

substrate. The first positive results arose from a Pb film with maximum thickness of 300 nm, protected by a 20 nm thick Al layer. Two photographs of the top part of the chamber are shown in Figures 78(b) and (c), where one can see the gradient of Pb at the center part of the figure. This thickness gradient that one can see on the substrate-holder is due to the vertical part of the dss. The effect of the other two teeth in the horizontal part of the dss was too thin to be visualized by naked eyes.

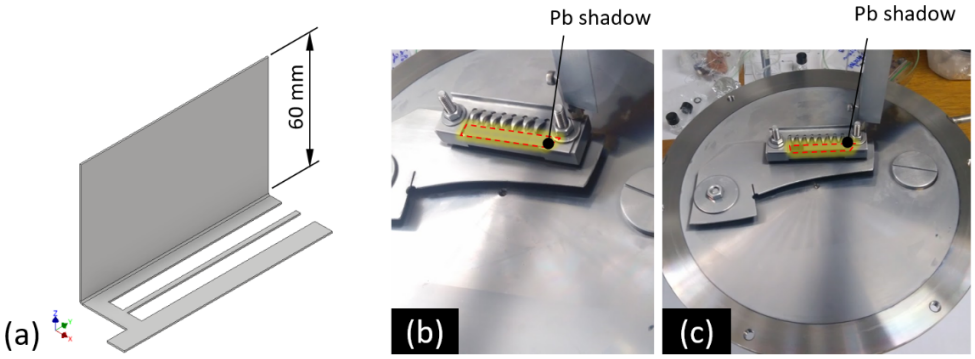

Figure 78: (a) First version of the dss. Photographs of the top part of the chamber (b) and (c), taken just after the deposition of a 300 nm thick layer of Pb and a protective layer of Al, 20 nm thick. The red dashed rectangle indicates the position of the deposited specimen.

We cleaved the sample and imaged it at 2.39 K, under a varying applied field, as shown in the left column of Figure 79. At its left edge, the thickness of the Pb film is 300 nm, and we do not observe flux avalanches starting from this thicker side.Furthermore, the avalanches do not start all over the length of the sample, but, instead, are restricted to a certain portion of the film. The right column in Figure 79 (panels g-l) shows the differential images of their counter parts in the left column (a-f). These differential images show that, simultaneously, there are big, thick and quite dendritic avalanches on the left side, and small, thin, and finger-like avalanches on the right side. The smaller the thickness, the smaller and less branched is the flux avalanche. Johansen et al. [48] have already addressed the relationship between morphology of the flux avalanches and temperature for a uniform MgB_2 film, where more branched and larger avalanches appear for temperatures close to T^*. In the case of a wedge film, T^* is thickness dependent and also changes along the sample.The morphology diversity of the flux avalanches in this

wedge-shaped sample is highlighted in Figure 80, taken at the remnant state after a field cooling procedure with 50 Oe. The critical temperature obtained from measurements in the MOI setup is 7.05 K [2].

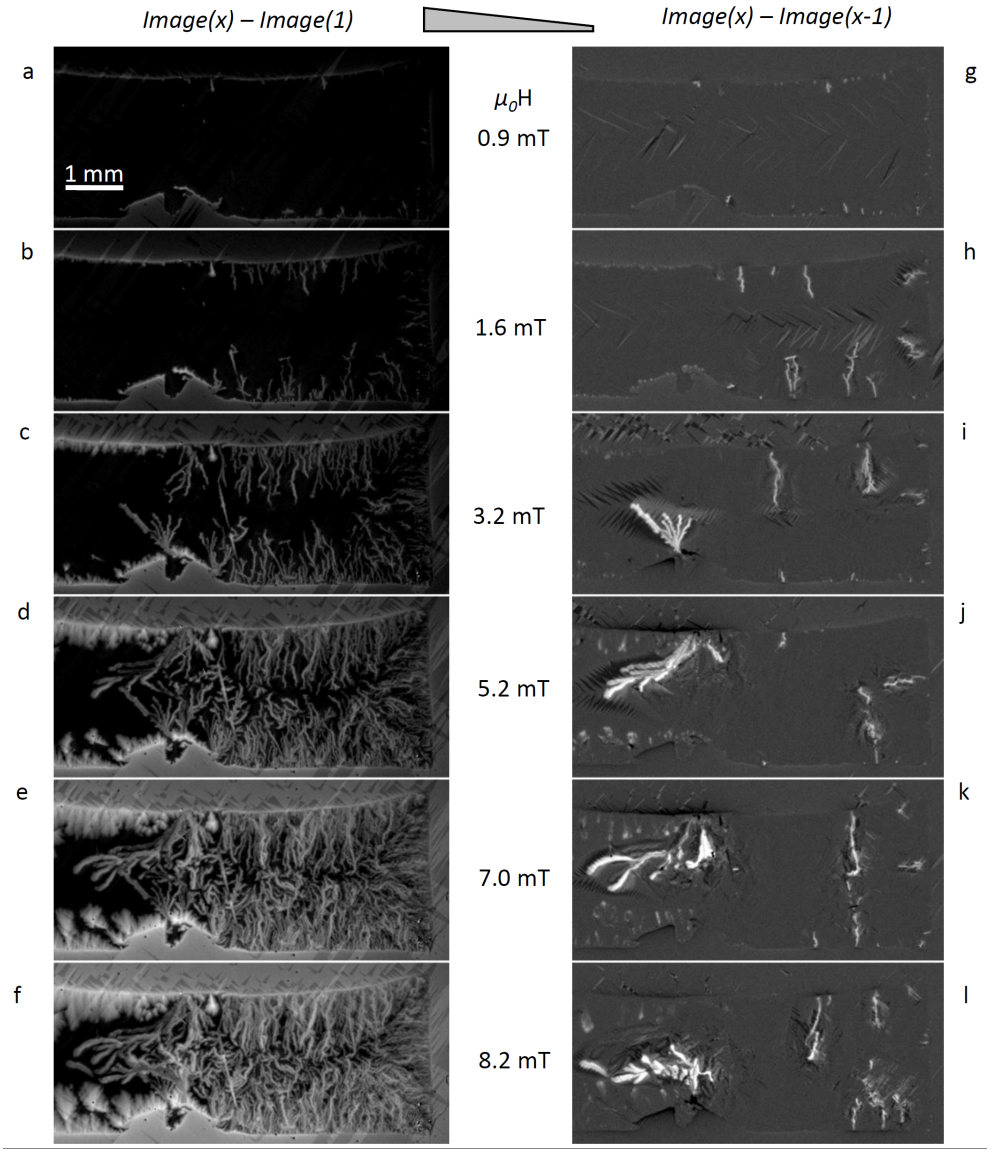

Figure 79: MO images of a cleaved sample with a wedge-shaped Pb film. The left column, from (a) through (f), shows images from which the very first was subtracted, taken after a ZFC procedure down to $T_{base} = 2.39$ K. The right column shows images at the same fields, although using the differential approach, detailed in Chapter 3. The applied magnetic field H is shown in the central column. Thickness variation is indicated by the gray wedge at the top.

[2]It is also important to mention that this value depends on several parameters, and the most important is the amount of grease used to improve the thermal contact between the sample and the cold finger. For this reason, the nominal values of temperature will be shown henceforth.

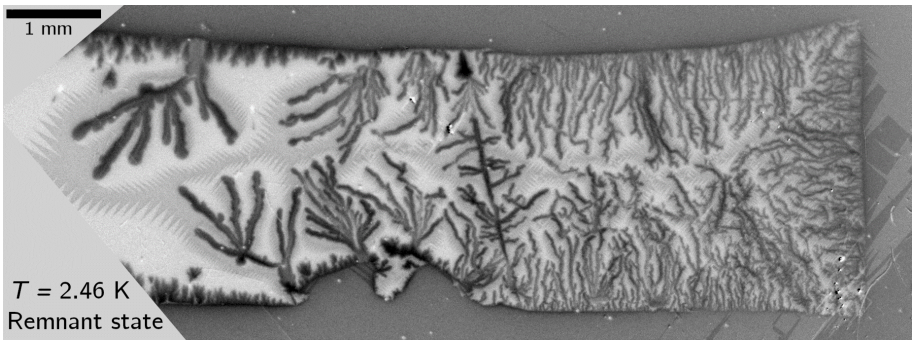

Figure 80: MO images of a wedge-shaped Pb film at 2.46 K and remnant field, after a field cooling procedure, $H_{FC} = 50$ Oe. One can clearly see the morphology diversity of the avalanches across the sample.

The ideal system to study such an interesting subject would be a superconducting film with well defined borders, and a natural solution would involve the use of lithography. However, Pb is reactive to acetone, the solvent needed in the lift-off step. The samples we prepared by using this process were damaged. The next attempt was based on shadow masks to be used during deposition, which is the subject of the next section.

7.3 Wedge-shaped samples using metallic shadow masks

One of the consequences of using shadow masks to delineate the border of the samples is illustrated in Figure 81(a). In this schematic representation, the substrate is exposed to a vapor source, and the vapor reaches the substrate everywhere except in the black region, protected by the shadow mask. In that illustration, the mask is positioned far from the substrate so that one can see its shadow. In real assemblies, although the mask is in close contact with the substrate, its thickness produces a similar effect. In the setup used in these depositions, there will be at least one edge with Pb but not Ge, and at least another one with Ge, but not Pb, as indicated in panel (b).

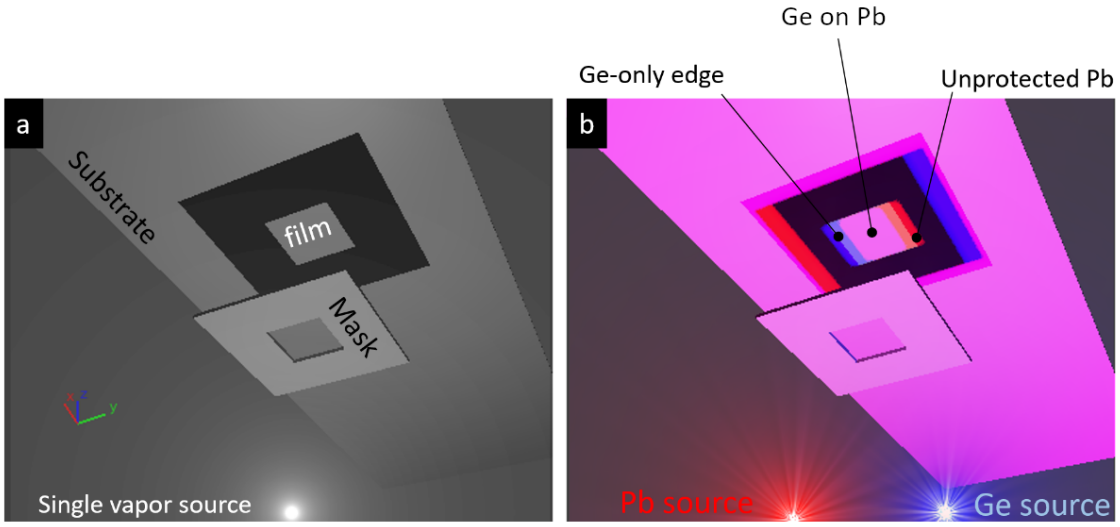

Figure 81: (a) Schematic representation of a shadow mask (or stencil mask) on a vapor deposition with a single source. The mask is far from the substrate for allowing the shadow visualization. The black region surrounding the sample is totally protected from the vapor. (b) Two different sources of materials: Pb as red and Ge as blue. The black region is protected from both vapor sources. The red regions have Pb only, and the blue regions have Ge only. All pink regions present Pb covered by Ge.

We have attempted to produce not only Pb, but also Sn samples. We tried both pure Sn and Sn with an Al cap as a protective layer. Despite we were able to detect superconducting signals in both depositions, it does not last more than a few days. In most of the papers on superconducting properties of Sn in the 1960s the samples were deposited in low temperatures and the measurements were performed *in situ*, most probably to avoid the crystallographic change between α and β tin. In view of our own results, and having in mind the available information from older studies, we decided to focus on Pb films to study the wedge-shaped superconducting thin films.

7.4 Smooth and Steep wedges

Our experimental apparatus allowed us to vary the distance between the diffuse-shutter and the substrate (h_s), so we were able to produce different thickness gradient along the films, as shown in Figure 82. Panels (a) and (b) are photographs taken just after the deposition with $h_s = 153$ mm and $h_s = 102$ mm, respectively. The diffuse shadow is not clearly visible in panel (a), and so we numbered the dss teeth (also numbered in panel

(d)). The distance h_s is illustrated in panel (c). The edges of the dss shadow in panel (a) are not well-defined, which is an indication that the Pb thickness varies smoothly, whereas the more defined edges of the dss shadow presented in panel (b) indicates a steeper variation of the Pb thickness.

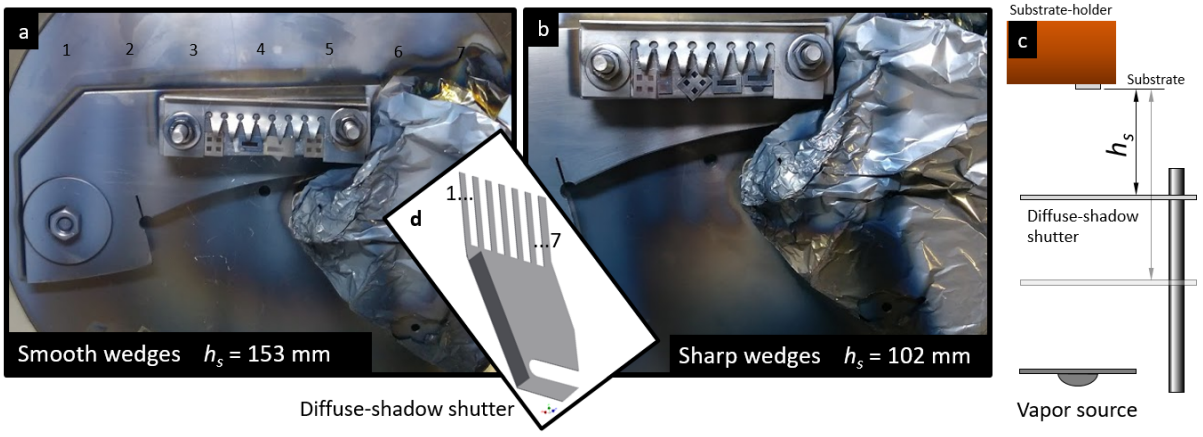

Figure 82: Photographs of the top part of chamber, containing the substrate holder and the masks, for a larger distance h_s between the dss and the substrates (a) and for the shortest distance achievable (b). To facilitate the identification of the dss shadow, the dss fingers are numbered. The meaning of h_s is sketched in (c), and in (d) the 3D CAD image of the dss.

Our incursions on smooth wedges did not produce samples with appreciable thickness variation, so all the samples shown in this Chapter belong to the steeper wedge setup just described. We will refer to the larger possible thickness as the **nominal thickness**, measured by the weighting method.

7.5 Rectangular wedge-shaped sample

7.5.1 Sample deposition and characterization

The first wedge-shaped sample intentionally made is a rectangular sample, 2×7 mm^2 and 124 nm nominal thickness. The position of the film in its substrate and the position of the substrate in the chamber during the deposition is shown in Figure 83. A sister sample of this rectangle (from the same batch) was used in DC magnetometry

and AC susceptibility measurements, from which we have determined $T_C = 7.2$ K.

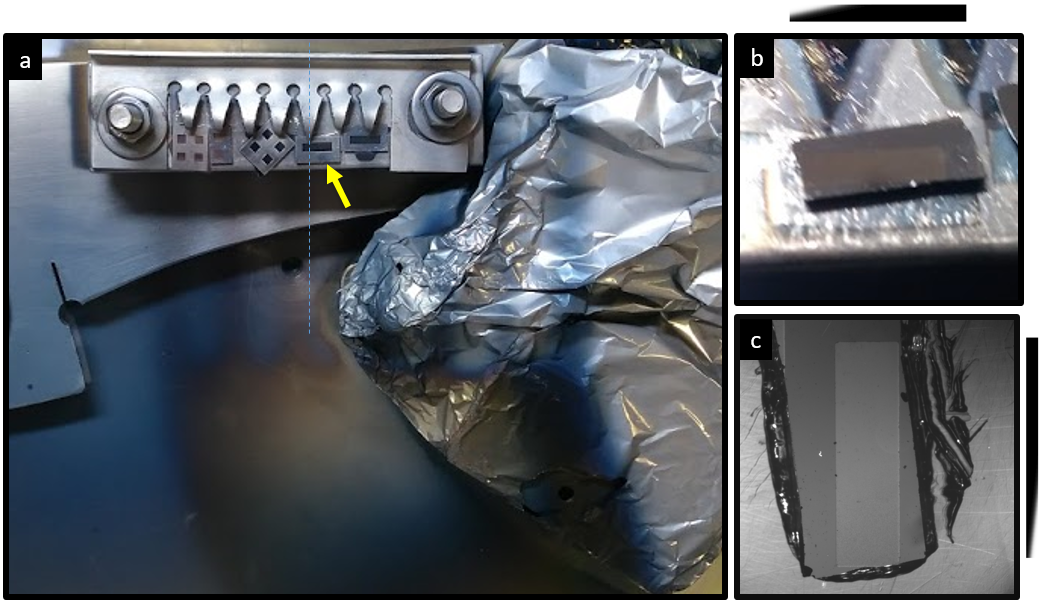

Figure 83: (a) Picture of the chamber as soon as it was opened, where the rectangular sample is indicated by a yellow arrow. The blue dashed line is a guide-to-the-eye of the center of the diffuse shadow. (b) Photograph of the rectangular sample without the shadow mask, but still in the position it was deposited. (c) the sample mounted in the MOI cold-finger, with its thinner edge pointing down. The black bars close to panels (b) and (c) indicate the wedge orientation.

Based on the sample position during the evaporation, one expects it to show a uniform thickness zone and a wedge-shaped region close to the smaller edges. After the MOI measurements, we slightly removed the film with a wood needle in 5 points along the longer edge of the rectangle, to avoid the unmatched borders, i.e., Pb only or Ge only, as discussed in section 7.3. We performed AFM measurements in these new edges (at least two measurements at each location). The raw results, i.e., the measurement of both Pb + Ge layers, are summarized in Figure 84. By discounting 20 nm of Ge determined by the weight method, one can evaluate the Pb thickness. Figure 85 shows the Pb thickness through the rectangle length, indicating the positions where the AFM measurements took place in panel (a). The real sample is shown in panel (b), whereas in panels (c) through (g) we show the AFM images of the right edge profile. The roughness of the Ge layer (the one with which the AFM tip interacts) is homogeneous all over the sample, showing grains in the nanometric scale, with lateral sizes ranging from 200 to 500 nm.

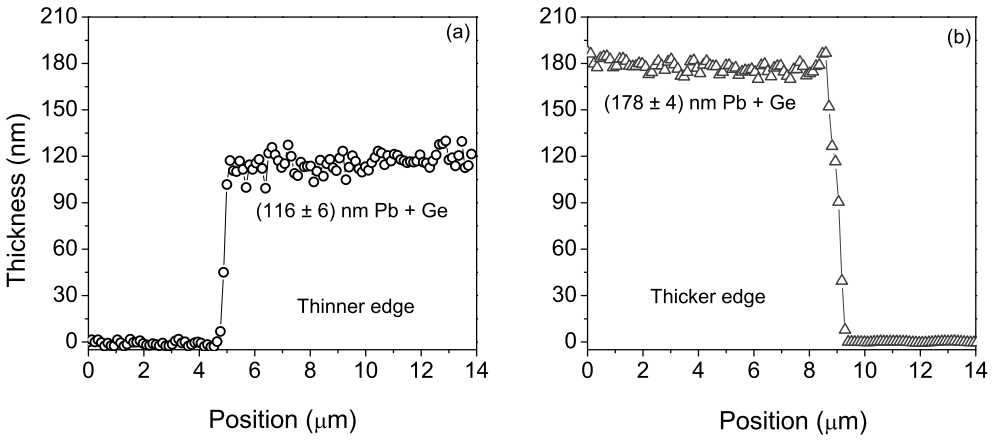

Figure 84: Thickness measurements (step mode) of the Pb + Ge layers close to the thinner edge (a) and close to the thicker edge (b) of the rectangular sample. The plateau in $y = 0$ coordinate is the Si substrate.

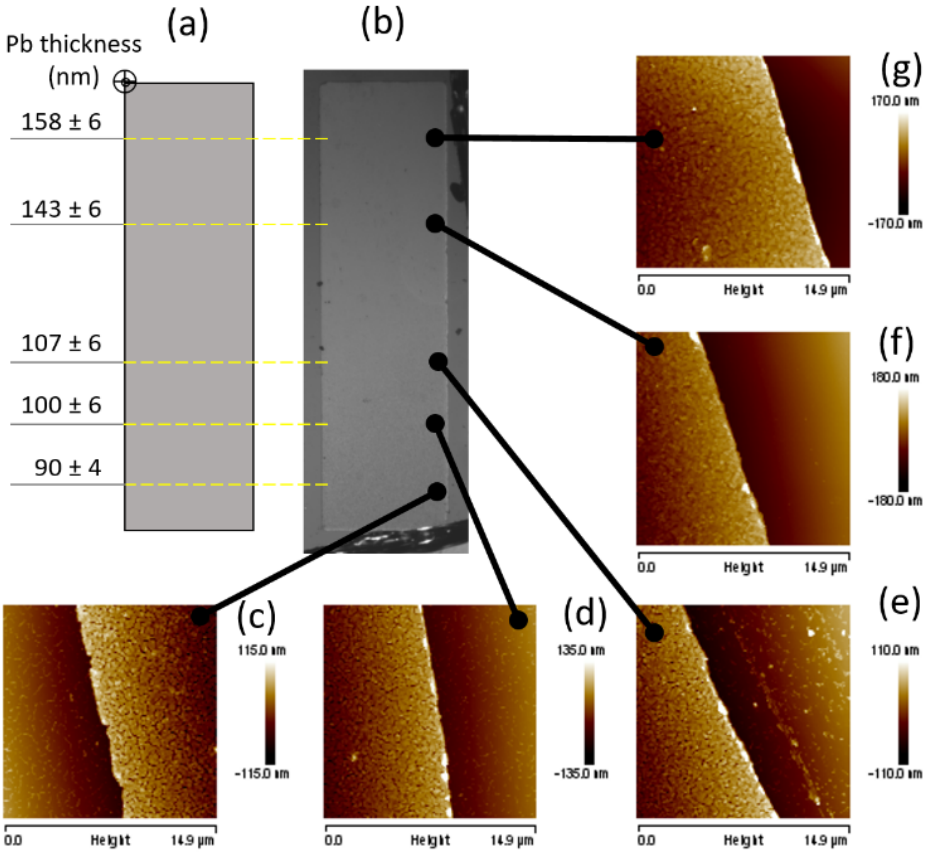

Figure 85: Values of thicknesses measured along the longer side in the retangular sample (a). (b) Optical image of the sample with the positions where the AFM images (c) through (g) were taken.

Figure 86 shows the five measurements and their respective error bars as a function of the position in the vertical axis of the sample. The two thicker values are more or

less compatible with a region of quasi-uniform thickness at left, whereas the other three points are clearly in a wedge-shaped region of the film. By performing a linear fit in these three points, one has roughly a variation of 10 nm/mm, with the minimum (extrapolated) thickness of 86 nm. Such a small variation corresponds to an inclination of $9 \cdot 10^{-6}$ degrees relative to the Si substrate.

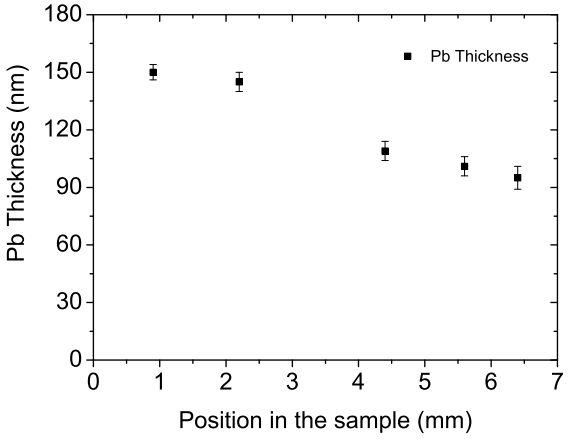

Figure 86: Thickness as a function of the position along the longer edge of the 7 mm long rectangular sample.

7.5.2 Obtaining thickness by EDS

As already discussed in Chapter 6, we used EDS to identify and quantify the elements on the same regions we performed AFM measurements to determine the film thicknesses. The results are summarized in Figure 87 and indicates where the EDS measurements were taken. Also shown is the quantity of the main three elements: Pb, Ge, and Si. As expected, the fraction of Pb decreases as the thickness decreases, and one also has a higher signal due to Si as the film becomes thinner - an indication that the electron beam interacts more with the substrates as the film thickness decreases.

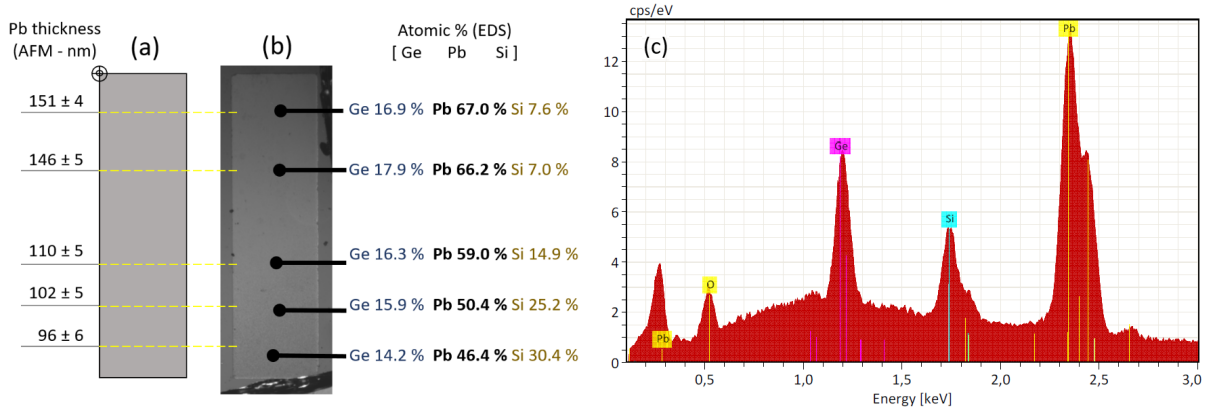

Figure 87: Thickness as a function of the position in the rectangular specimen (a), the atomic % of each one of the three main elements (Ge, Pb, and Si) (b), and an EDS spectrum obtained from the thinnest part of the rectangular sample (c). The acceleration voltage was 5 kV. The longer edge of the film is 7 mm long.

Once the Ge layer is expected to be uniform for all samples from the same batch, we used the Pb/Ge ratio and the AFM measurements of the rectangular sample to make the curve in Figure 88. A linear fit is also shown, despite its rough adjustment. Basically, one can identify that the thicker the Pb layer, the higher will be the Pb/Ge ratio, and for each 10 nm of variation in thickness, Pb/Ge ratio changes ≈ 0.1124.

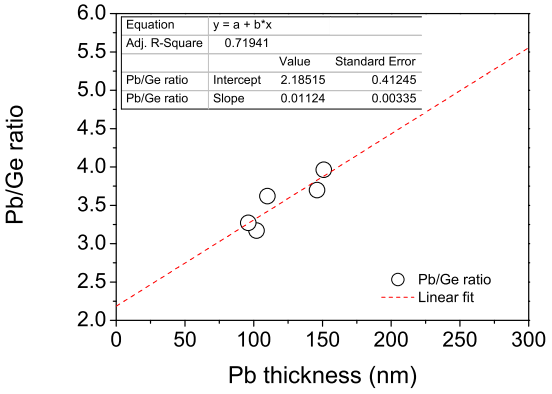

Figure 88: Pb/Ge ratio versus thickness.

7.5.3 Critical-state regime

For the rectangular gradient film, the MO images are organized in three different figures: the smooth penetration at $T = 4$ K is presented in Figures 89 and 90, while the

avalanche regime is presented in more details in the next subsection, in Figure 91. The first interesting features of this sample is the difference between the flux penetration depth at a constant applied field of what we identify as a nearly uniform thickness zone (the upper half part of the sample) and the bottom half of the film, where the gradient is steeper, as one can see in Figures 89(a) through (d).

If J_C of this Pb thin film had no dependence with the thickness, we would expect that the flux would penetrate deeper from the thinner edge than from the thicker edge. Nonetheless, this sample shows exactly the contrary: J_C depends on the thickness d, in such a way that the thinner the film, the higher J_C is, as also presented by Nb and YBCO films, for example [145, 146, 147]. The H_p value, the applied field for which the flux front reaches the center of the sample at a given thickness, is remarkably different: it is close to 20 Oe for the uniform part of the sample, and as high as 46 Oe for the thinner part. Another important aspect of the wedge is that the thickness gradient seems to be a little bit misaligned relative to the sample edges, as one can regard in panels (d) and (e). The black smudge on the left-hand side of all images is a piece of vacuum grease, which jumped from the cold finger assembly during the experiment. Fortunately, it is above the indicator and does not affect the sample response to T and H.

An interesting feature of this wedge-shape sample is presented in panels (f) through (j) of Figure 89. It shows MO images for higher applied fields. One can observe that the upper part of the images smeared out when compared to the wedge-shaped region. It is so because the upper critical field depends inversely on the film thickness [145]. H_{C2} for the nearly uniform zone is $H_{C2}^{uniform} \approx 100$ Oe (above this value we did not see that part of the sample in the MO image), while it is $H_{C2}^{wedge} > 150$ Oe. Therefore, it also reinforces the role played by the thickness variation on the superconducting properties of thin films.

In order to quantify the difference in the flux front in each region of the sample, Figure 90 shows the same MO image presented in panel (c) of the previous figure, as well as four translucent white bars at different positions where the B_z profiles were taken. The length of these bars was limited to the center of the sample to avoid the domain walls

of the indicator, clearly brighter. The profiles identified as A and B are in the nearly uniform thickness zone, whereas the C and D are in the steeper wedge. At $H = 8$ Oe and $T = 4$ K, the flux penetrated into the wedge up to 0.3 mm and 0.6-0.8 mm in the nearly uniform zone (the middle of the sample in the x direction is at $w = 1$ mm). An important remark is that the sample was placed perpendicularly to the cold-finger heat flow, in order to avoid a thermal gradient in the sample in the same axis we made the thickness gradient. The critical temperature obtained by the MOI setup is 5.1 K

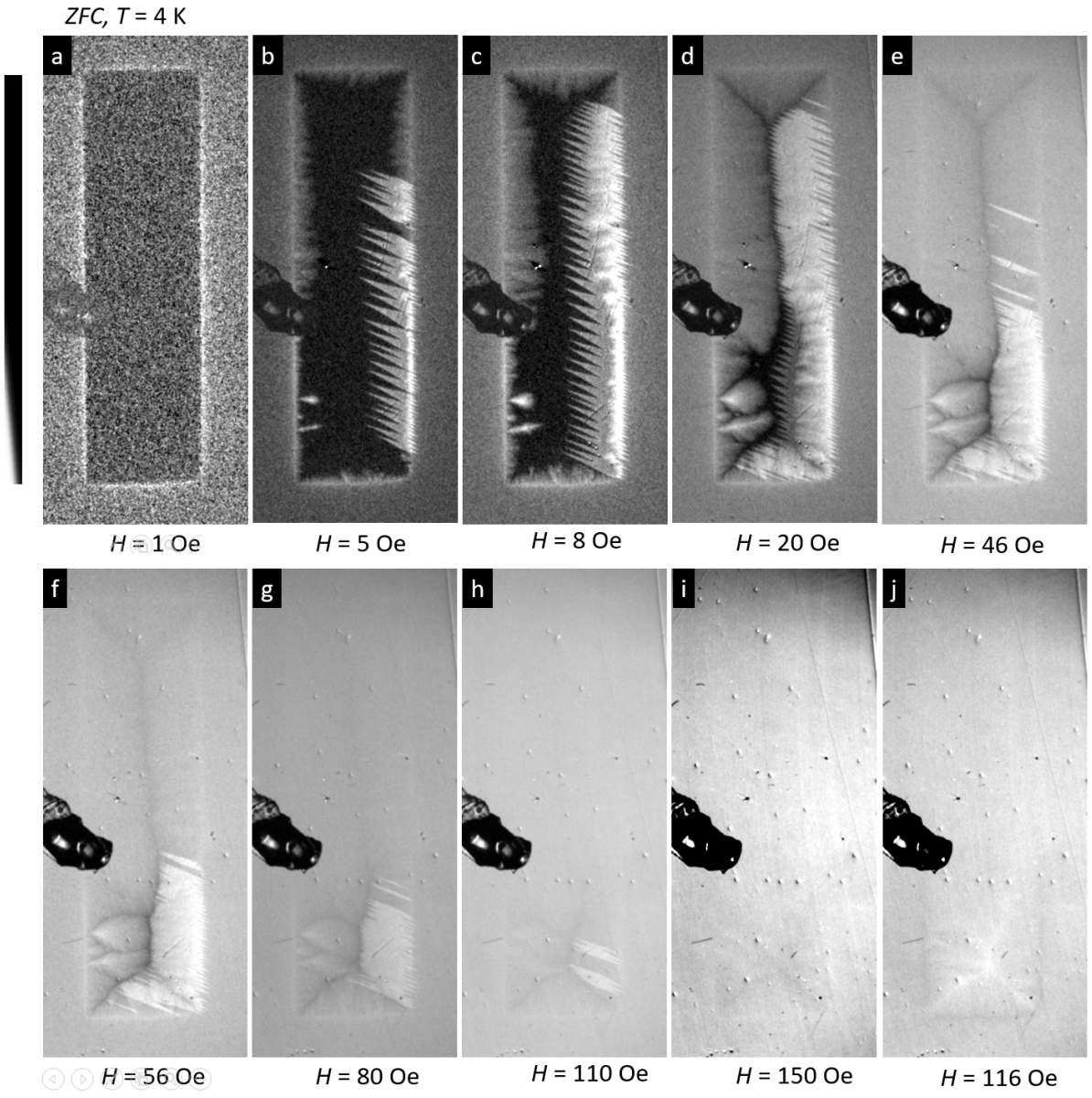

Figure 89: MO images of the smooth flux penetration for the rectangular sample, at T = 4 K, for increasing H: (a) 1 Oe, (b) 5 Oe, (c) 8 Oe, (d) 20 Oe, (e) 46 Oe, (f) 56 Oe, (g) 80 Oe, (h) 110 Oe, (i) 150 Oe; and one decreasing field (j) 116 Oe. The black vertical bar at the left side of panel (a) is a pictorial representation of the thickness variation along the wedge.

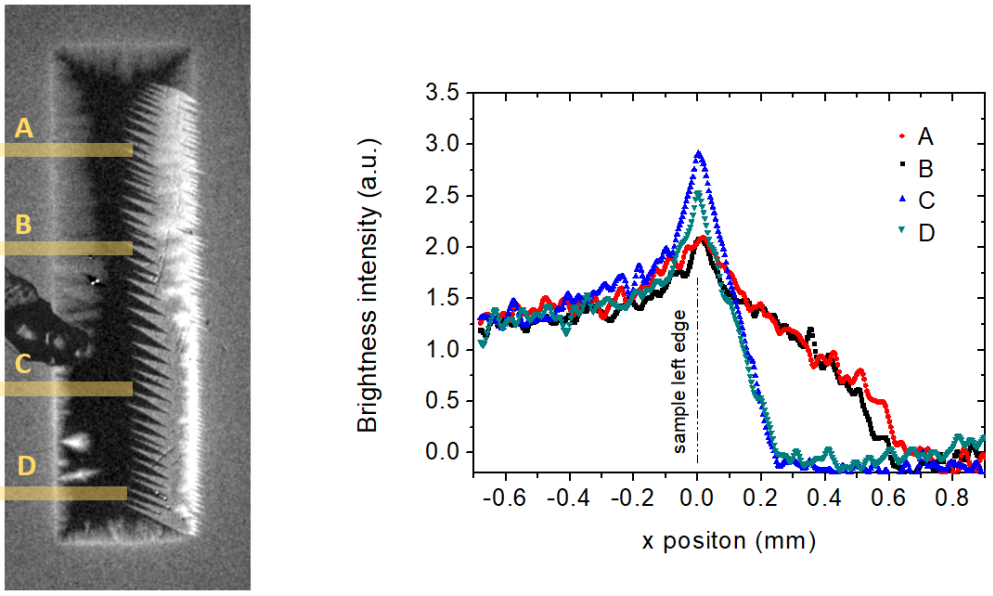

Figure 90: At left, MO image showing the flux penetration of the rectangular sample also shown in panel (c) of Figure 89, at $T = 4$ K and $H = 8$ Oe. The translucid yellow bars indicate the regions where the profiles shown in the graph on the right were taken averaging 52 pixels vertically.

The flux penetration depth can be used to estimate the critical current density for both regions of this sample. Considering the Bean model for uniform thin films, one can rewrite Equations 2.21 and 2.22 as:

$$\frac{\pi H}{\text{acosh}\left(\frac{w}{a}\right)} = J_C \cdot d \tag{7.1}$$

All the relevant information is summarized in Table 2. The product $J_C \cdot d$ is 6 times higher for the wedge zone. One must keep in mind that the wedge thickness at that point is smaller than in the uniform zone, so the critical current density is even higher there. By assuming that the uniform zone is 150 nm thick, one can estimate $J_C^{uniform} = 1.4 \cdot 10^6$ A/cm^2, whereas the thinnest edge has a thickness of ≈ 85 nm, the value can be as high as $J_C^{wedge} = 1.5 \cdot 10^7$ A/cm^2. Therefore, the critical current along the gradient can be one order of magnitude higher than in the uniform part of the sample.

Table 2: Parameters used to estimate the product $J_C(d)$ based on the Bean model for the nearly uniform region of the sample in the full penetration state for each region at 4 K.

Quantity (unit)	**Uniform**	**Wedge**
w (mm)	1	1
ℓ (mm)	0.8	0.3
a (mm)	0.2	0.7
H_p (Oe)	20	46
H_p (A/m)	1591.5	3660.6
acosh(w/a)	2.2924	0.8955
$J_C \cdot d$ (A/m)	2181	12841

7.5.4 Avalanche regime

The avalanche regime is also affected by the thickness variation. Precisely, it corroborates the previous analysis of the J_C distribution throughout the sample, where one expects to trigger more flux avalanches along the edges with higher J_C. Figure 91 shows a series of MO images at $T \ll T_C$ after a ZFC procedure and slowly increasing field H. In panel (a), the magnetic flux is around the edges of the sample, and its interior is shielded uniformly at all borders. In panel (b), one can see the first avalanches, triggered exclusively at the thinner region of the sample. The avalanche morphology is different from edge to edge, as discussed earlier, which can be better observed in panels (c) and (d), the avalanche and the critical state-like smooth penetration coexist along the lateral edges. An important feature of the avalanches in panels (d) and (e) is their size and the deviation of their ramifications toward the thicker zones, which is the same observed in that sample without well-defined edges in Figure 79.

Additionally, the flux avalanches of antiflux also present different morphologies as shown in panels (f) through (j) of Figure 91. However, huge avalanches are triggered even in the thicker regions of the sample where no positive avalanche takes place.

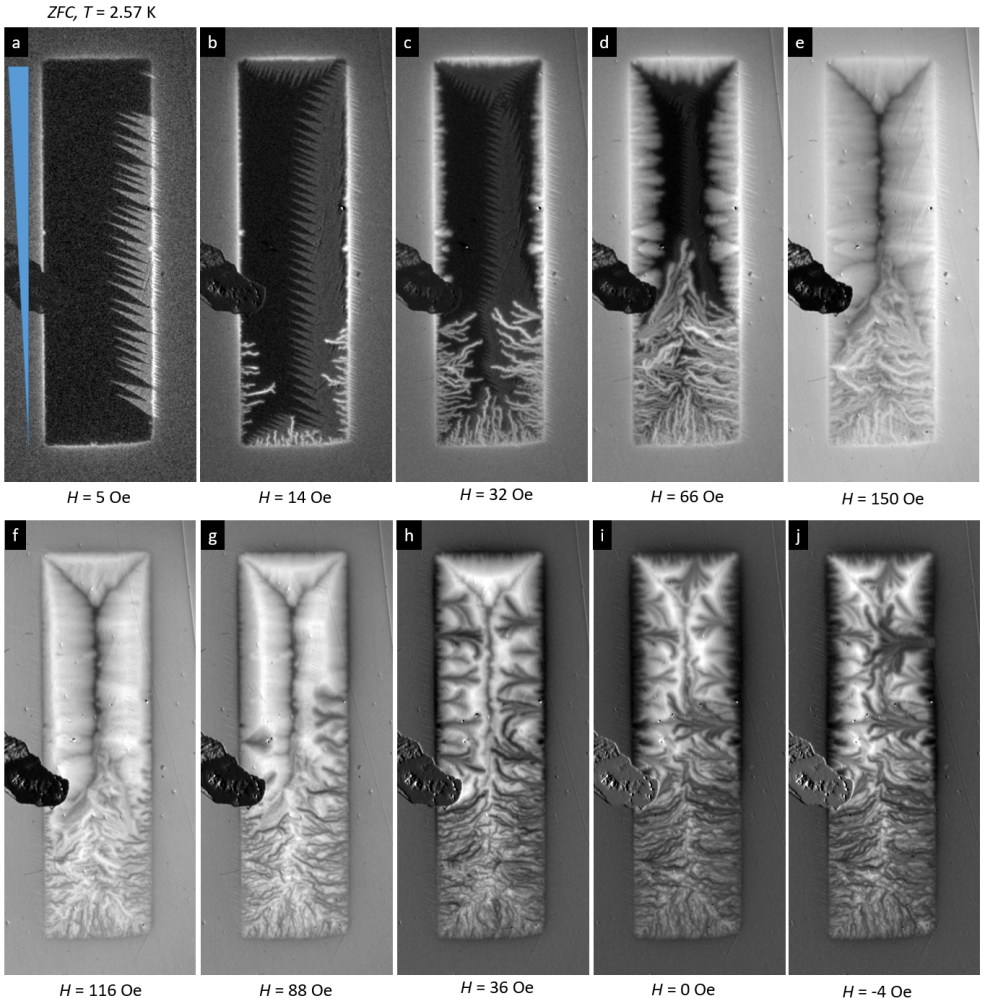

Figure 91: MO imaging after a ZFC at $T = 2.57$ K (a) $H = 5$ Oe, (b) 14 Oe, (c) 32 Oe, (d) 66 Oe, (e) 150 Oe, the maximum field. Images taken for decreasing fields are shown for (f) $H = 116$ Oe, (g) 88 Oe, (h) 36 Oe, (i) zero, and (j) -4 Oe. The thicker edge is at the top of the image, and the thinner on the bottom, as indicated by the triangle in panel (a). The black smudge in the left of all images is a piece of vacuum grease released from the assembly during the cooling process. The sample area is $\approx 2 \times 7$ mm^2.

In Section 2.6, we discussed a few methods that one uses to guide flux avalanches. Nevertheless, it seems that the deviations observed in the wedge-shaped Pb films presented in this Chapter do not fit in none of the aforementioned methods of guiding avalanches. When the sample has no avalanches yet, the first branches point towards the sample center, as expected. But the last avalanches do deviate and propagate towards the thicker region of the film. A possible explanation would rely on the fact that avalanches usually avoid each other and there is still flux-free area in the thicker regions, while the thinner region is already plenty of flux.

One can also discuss these results using the H-J_C diagram presented in Figure 22, in Chapter 2. Figures 92(a) and (b) show a schematic representations of the last results. Panel (a) shows the situation at higher temperature presented in Figures 89(a)-(j). All edges of the rectangular sample have no avalanches and their $H(J_C)$ curves do not cross the instability region for any magnetic field. Notice that each edge has a different value of H_{C2}, what is indicated: the dashed line crosses the y axis at different values of the vertical coordinate. Panel (b) describes what occurs in Figures 91(a)-(e). The top-half of the sample, , represented by the blue dashed line at left, exhibits no flux avalanches. The bottom-half, close to the thinner edge, is represented by the red dashed line, and the lower threshold field (H_1^{th}) for avalanche triggering is indicated by a red dot, where the critical current crosses the threshold field curve (H^{th}). Even increasing the applied field up to 150 Oe, we were not able to reach H_2^{th} at that nominal temperature for the bottom edge. In this diagram, H_2^{th} is the point where the red dashed line would cross the instability border at higher applied fields. In both cases, low and high temperatures, $H(J_C)$ curves for any point at the lateral edges with varying thicknesses would be between the curves for the thinner and the thicker edges.

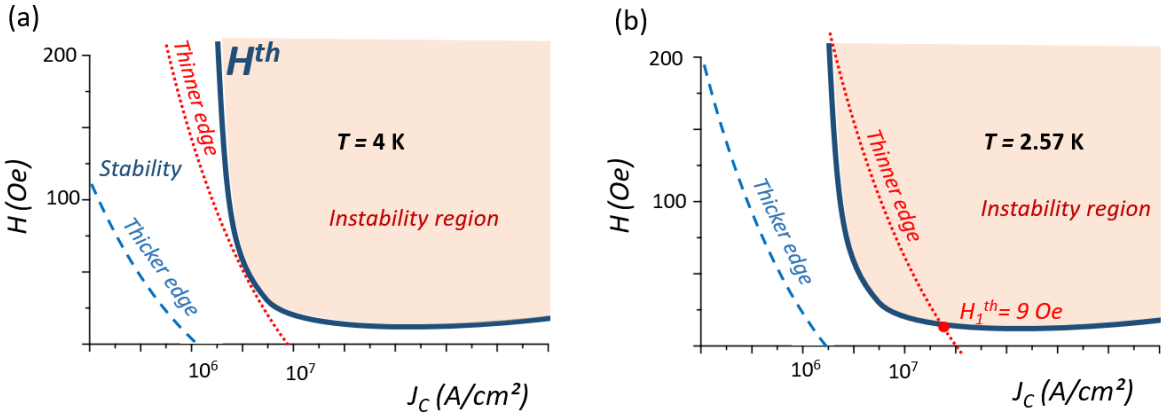

Figure 92: Schematic representation of a H-J_C diagram for the wedge-shaped Pb thin film, at $T = 4$ K (a) and $T = 2.57$ K (b), based on Yurchenko *et al.* [153]. The blue dashed line represents the increasing field experiment at constant temperature for the thicker edge of the rectangular sample, whereas the red dashed line represents the same experiment, but for the thinner edge.

By analyzing this rectangular wedge-shaped sample made intentionally, one can

answer the two main questions introduced in the beginning of this Chapter: **(1)** *can we change the smooth penetration regime by varying the sample thickness along one of its dimensions?* The answer is **yes**, we can, and we were able to change the J_C by one order of magnitude in the same sample. **(2)** *Will the avalanche regime be affected by this variation?* The answer is also **yes**, it will, as we discussed above. Nonetheless, to have a more systematic view of the wedge-shaped Pb films, we also prepared square samples in two different wedge setups: the first one, presented in the next section, is the square sample whose thickness variation is aligned to the sample edge. The second setup is a squared wedge-shaped film whose thickness variation is aligned to the diagonal of the sample.

7.6 Square samples - wedge aligned to the sample edge

In this section we will present and discuss results for square samples prepared on the same batch of the rectangular sample treated in the previous section. We assume that, as for the rectangular film, the thickness of the Ge layer is constant, and so one can make estimations of the thickness variation based on the EDS results. Figure 93 shows the location of the samples during the deposition and spots were the EDS measurements were performed. The samples were labeled S1, S2, and S3.

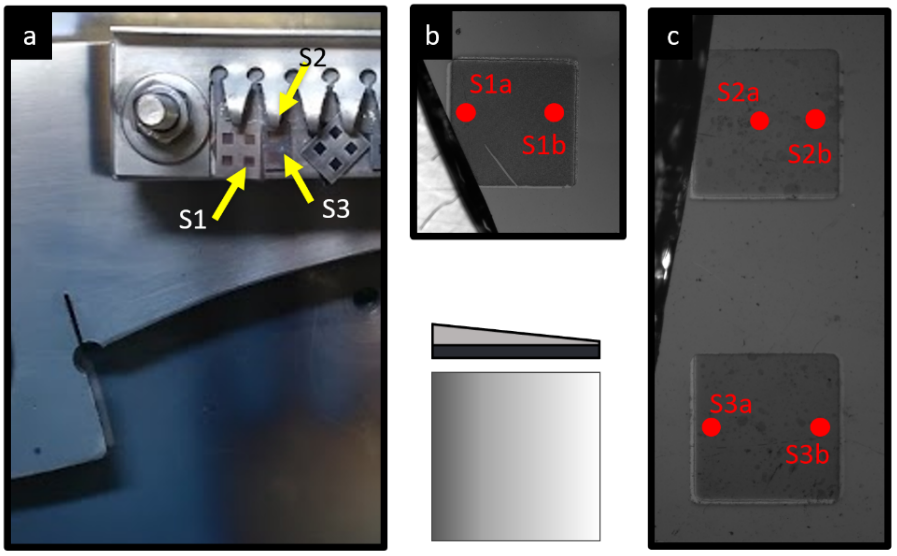

Figure 93: (a) Location of the three squared samples in the substrate-holder just after the deposition. The wedge was planned to be aligned to the edges of the squares by positioning properly the shadow masks. Detail of the sample S1 (b), S2 and S3 (c) and the places where the EDS spectra were taken. The thickness variation is illustrated in panel (b) for all the three squared samples. The sample S1 (b) is upside-down compared to its position in (a), to make the thinner edge points to the right side.

Although one cannot ascribe a numerical value for the thickness precisely, the Pb/Ge ratio indicates thicknesses values below 100 nm. The main results from EDS in the indicated locations are organized in Table 3. Not only the Pb/Ge ratio should be taken into account when evaluating the direction of the thickness variation, but also the sample position during the deposition, relative to the diffuse shadow, and also the absolute content of Pb and Si - the larger is the Si count, the thinner is the film.

Table 3: Summary of the EDS results at the locations indicated in Figure 93.

Sample	Atomic %			Pb/Ge ratio
	Ge	**Pb**	**Si**	
S1a	23.43	49.75	16.7	2.12
S1b	21.8	43.46	24.43	1.99
S2a	22.2	55.68	11.71	2.51
S2b	22.2	54.66	13.02	2.46
S3a	24.9	53.70	8.70	2.16
S3b	24.3	51.31	12.06	2.11

Figures 94 and 95 show the smooth penetration for the square samples. The defect caused while cleaving the film, at the bottom-left corner of S1 and the damages

(scratch-like) make it difficult a direct interpretation of the thickness variation effects in the smooth penetration regime. Nevertheless, the two remaining 90 degrees corners in the right-hand side of S1 show d-lines at 45° from the edges, indicating no sudden change in J_C between the vertical and the horizontal edges.

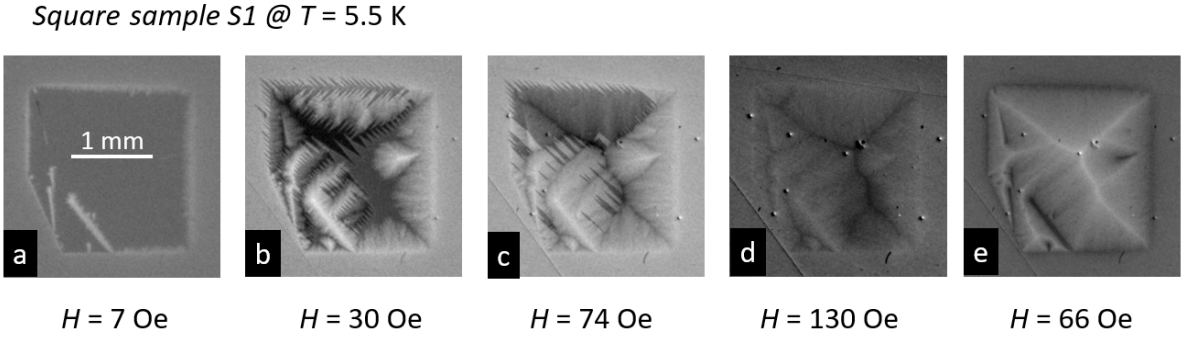

Figure 94: MO images of the wedge-shaped thin film of square borders, S1, at $T = 5.5$ K and increasing field (a-d), after a ZFC. Decreasing H after reaching 150 Oe, panel (e) shows the image at $H = 66$ Oe. The critical temperature obtained at the MOI setup is 6.5 K.

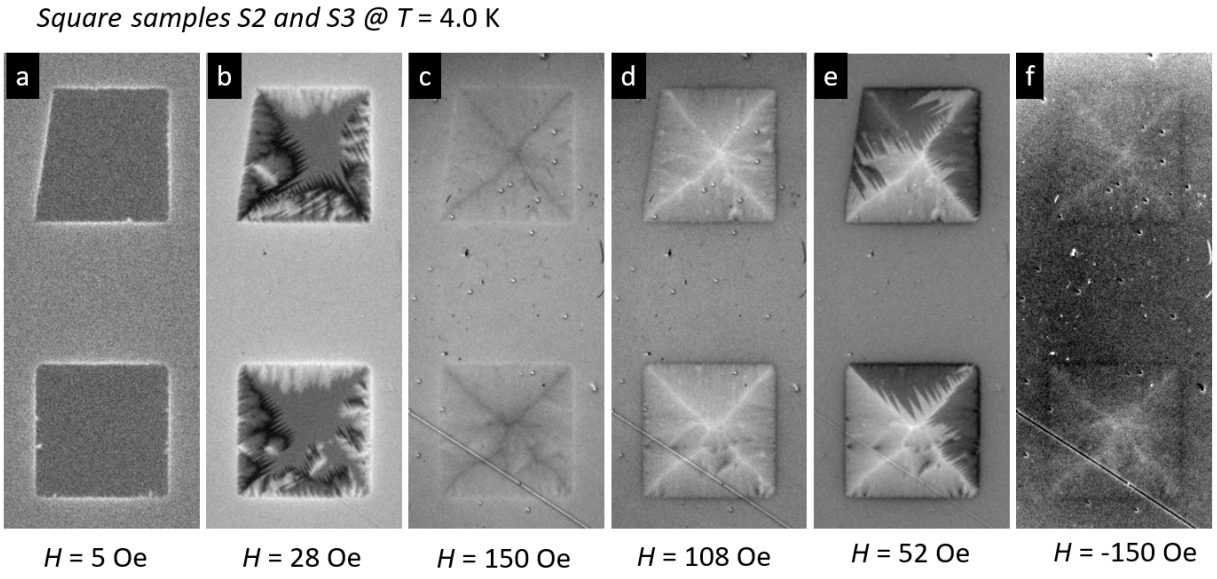

Figure 95: MO images of sampels S2 and S3, for increasing field (a-c) and decreasing field (d-f), after a ZFC. The critical temperature obtained at the MOI setup is 5.6 K.

Based on EDS data, the thickness variation on samples S1 and S2 is approximately 10 nm, while on sample S3 is smaller than ≈ 5 nm. This feature has no clear

effect on the smooth penetration, but it does affect the instability regime. Figure 96 and 97 show the avalanche regime for the three square specimens. The thinner edge, on the right-hand side of S1, shows more avalanches than the left-hand side, the thicker one. At $T = 2.42$ K, the left and the top edges show smooth penetration for higher fields, while the left edge is still triggering flux avalanches. Moreover, S1 is thinner than S2 and S3, as one can evaluate from the Si and Pb atomic % in Table 3, which allows one to expect a larger instability region for S1 - with more numerous and larger avalanches.

All the square samples corroborate the expectation that J_C is higher for thinner edges: the avalanche regime is larger in all thinner edges, and the smooth penetration goes deeper from the thicker edges. Another important issue in the lack of Ge in two edges of each presented sample: Does the unprotected Pb in two of the sample's edges play an important role in avalanche triggering? The first answer to this question comes from a careful look into the sample's position in Figure 93. In panel (a), the thinner edge of S1 comes from the left, while the thinner edge for S2 and S3 comes from the right. This is important because the unprotected Pb lies on the right borders of these three samples. To make all the thinner edges point towards right, we turned the S1 180°, and so the bare Pb for S1 is in the opposite direction of S2 and S3. With the orientation of the gradient properly identified for each sample, the experimental data show that avalanche triggering is predominant in the thinner edge for all samples.

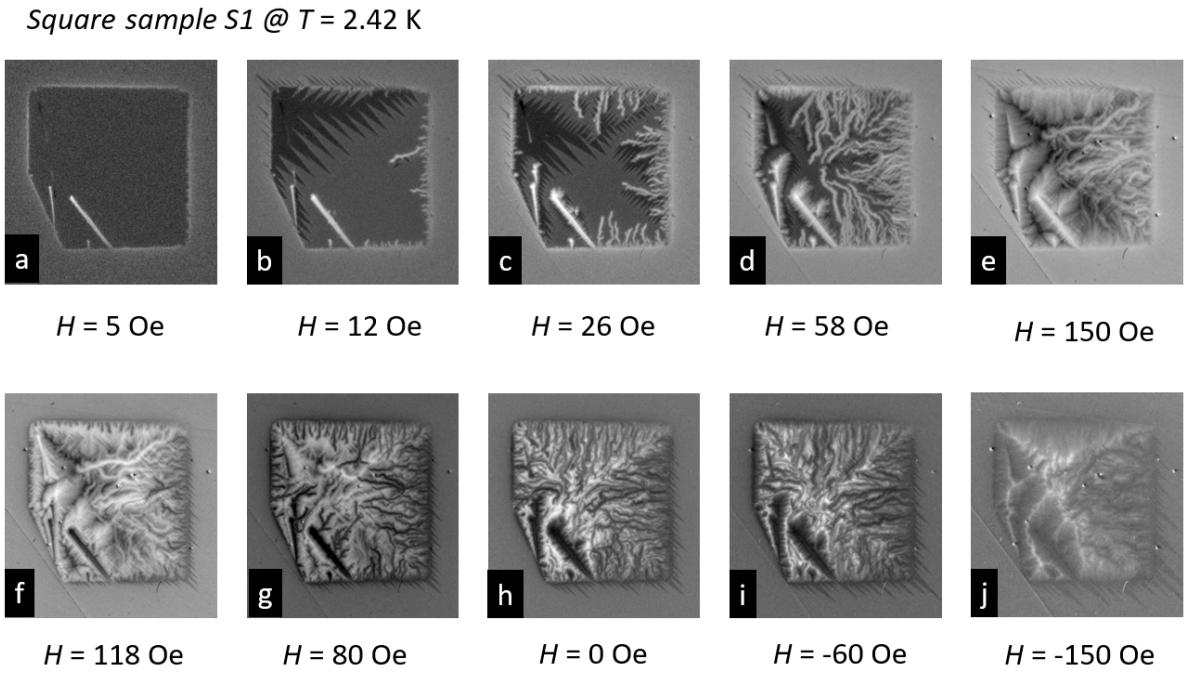

Figure 96: MO images of the avalanche regime in sample S1. The sequence begun after a ZFC at $T = 2.42$ K.

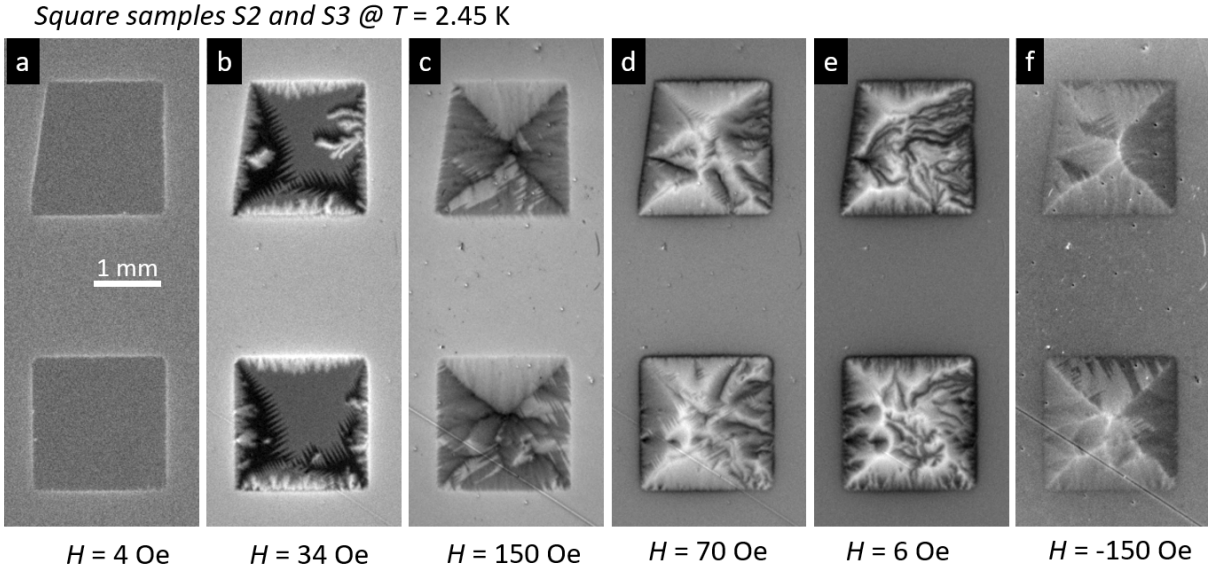

Figure 97: MO images of samples S2 and S3, both at the same temperature $T = 2.45$ K. S3 has less thickness variation than S2, but both show more anti-avalanches on their right edges for decreasing field.

7.7 Square samples - wedge aligned to the sample diagonal

In a further deposition, we changed the diffuse shutter distance, letting it closer to the substrate holder. Furthermore, the following set of samples also has a different feature: the thickness variation is along the sample diagonal, i.e., rotated by 45 degrees as compared to samples S1, S2, and S3. Figure 98 shows optical images of the samples DS1, DS2, DS3, and DS4. Panel (b) is a schematic view of the Pb and Ge mismatch, while (c) indicates the direction of the thickness variation for sample DS4.

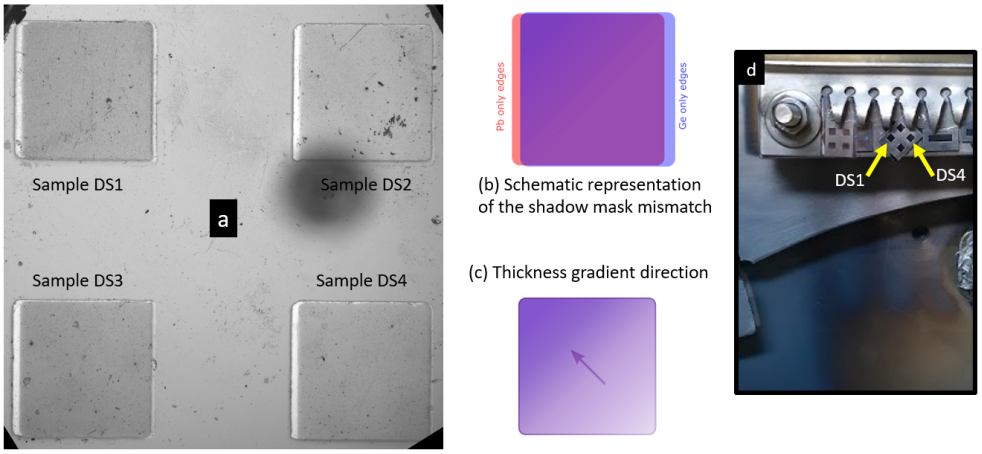

Figure 98: (a) Optical images of the four samples with the wedge aligned to the square's diagonal. (b) Schematic representation of the sample edges. (c) The direction of the thickness gradient in the sample DS4. (d) Shadow mask position and location at the chamber during the deposition. All the squares have nominal area $\approx 2 \times 2$ mm^2.

7.7.1 Smooth penetration

Figure 99 shows quantitative MO images of the samples DS1-DS4, at $T = 5$ K after a ZFC procedure, with the applied field ranging from zero to 150 Oe. The flux density scale is indicated above the panels. The samples DS1 and DS2 have some small scratches and punctual defects that difficult the visualization of the d-lines. Sample DS3 is expected to have uniform thickness due to its position in the sample holder, while DS4 has its smaller thickness at the bottom-right corner, and its maximum thickness at its

top-left corner. The d-line angles in sample DS3 are, indeed, 45°.

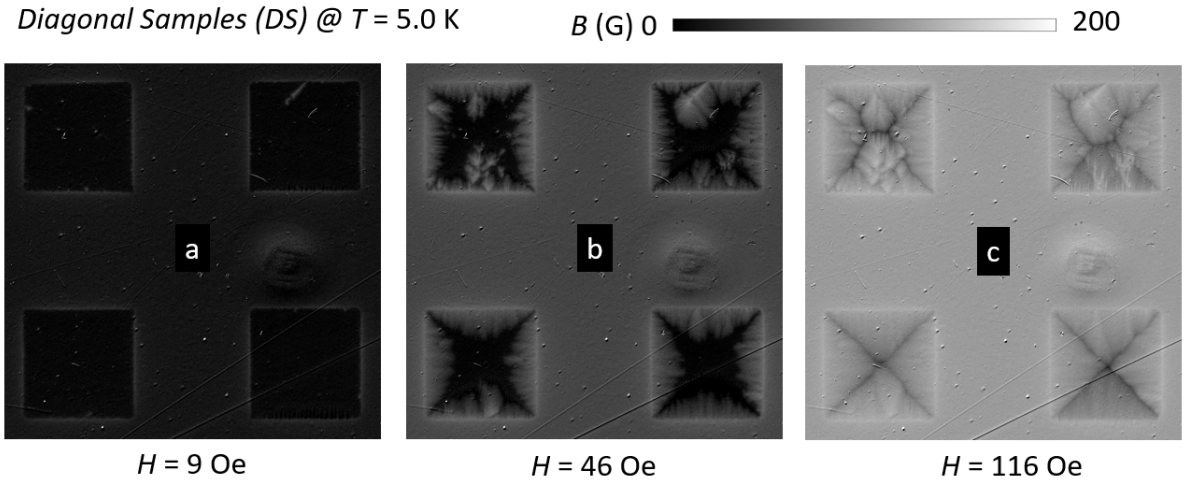

Figure 99: Quantitative MO images of samples DS1-DS4, after a ZFC procedure down to $T = 5$ K. The applied field is indicated below each panel. The critical temperature obtained at the MOI setup is 6.8 K.

Sample DS4 shows a small asymmetry with respect to its d-lines and in the position where the d-lines encounter each other at the central portion of the sample. Figures 100(a) and (b) show details of this asymmetry. Labeling the d-lines based on its quadrants in the image, taking the central point as the origin of coordinates, D_1 and D_3 are equal in length (1.36 mm), whereas D_2 is the longer d-line, with 1.40 mm, and D_4 is the shortest, with 1.24 mm. Using the horizontal edge as a reference for angular measurement, the D_3 angle is shown in Figure 100(c).

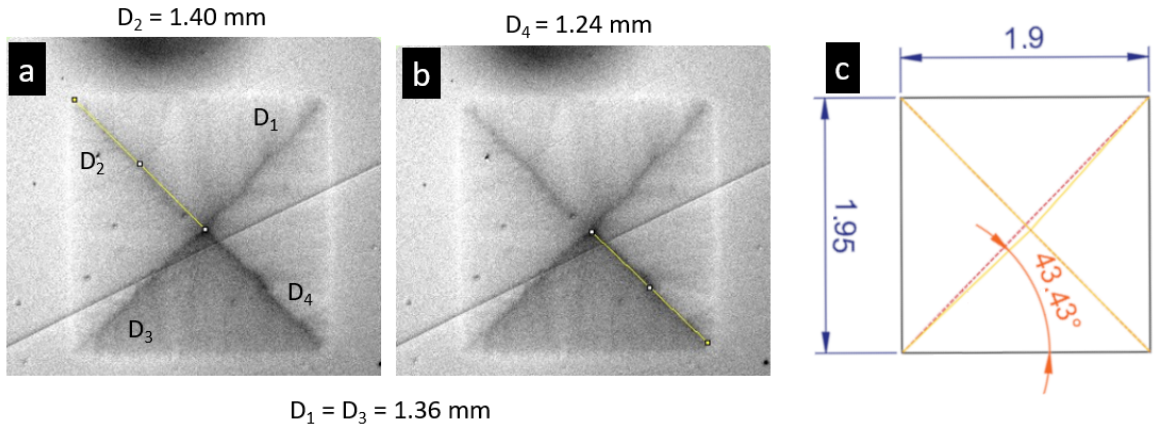

Figure 100: Geometrical parameters of the d-lines (labeled D_1 to D_4 of the DS4 sample. Panel (a) shows the longer d-line, while (b) the shortest one. (c) Geometrical reconstruction of the DS4 with real sides (it is not a perfect square) and the angle between the d-lines. The red dashed line in (c) shows the d-line position for a uniform sample, while the orange line shows the measured data.

As occurs to the DS3 sample, DS4 is not exactly squared, but its dimensions are 1.90×1.95 mm^2. If the J_C in this sample were uniform, one would expect for the d-lines D_3 and D_1 to be 45° from their horizontal reference, shown as red dashed lines in panel (c). Nonetheless, their angle are both 43.43°. Using the Equation 2.25 from Chapter 2, the J_C on the vertical edge is 94.6 % of the J_C at the bottom edge. Recalling that J_C is a function of the position in the sample, and that the d-lines are created where the current lines have to bend, the difference of 5.4 % between the J_C values is similar to the difference between the current starting point and the curve ending point, as illustrated in Figure 15. An important remark is that the d-lines D_2 and D_4 are both 45°. To explain better what is happening in these diagonal-aligned wedge-shaped samples, Figure 101 shows schemes of an exaggerated thick film. The colored circular points on the surface of the film illustration mean the height of the point, concerning the thickness of the film - the thicker the point more red it is. Thinner points are in blue. In panel (a), representing both the d-lines D_1 and D_3, the current curves towards a site with different height - this is illustrated by color changing arrows. That is the reason why the angles are different from 45° in these two d-lines. Panel (b) shows what occurs to d-line D_4, in which the

current goes back to its same height after bending at the corner of the sample. This is why the angles for d-lines D_4 and D_2 are at 45°.

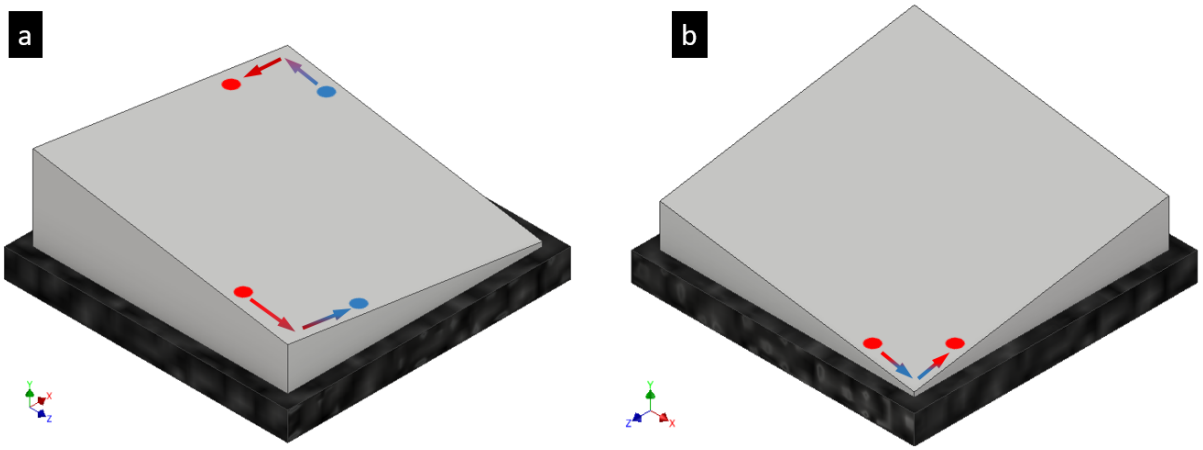

Figure 101: Schematic representation of a wedge-shaped thin film with the thickness variation aligned to the sample diagonal. The colored circles mean the film thickness: the highest points are in red, and the lower points are in blue. (a) Representation of the two symmetric diagonals, in which a current line changes its height as it needs to bend in the two highlighted corners. (b) The thinner corner of the sample, at which the current finds a symmetric track during its bending.

7.7.2 Avalanche regime

Figure 102 shows MO images taken for increasing fields after a ZFC procedure at 2.44 K. Panels (a) and (b) present the well defined edges of all samples. As observed in the rectangular and in the square samples S1, S2, and S3, the avalanche triggering is much more numerous in the thinner edges, as shown in Figure 102 (c) and (d). For sample DS1, the thinner edge is the top left one, whereas for the sample DS4 is at the bottom right edge. Panel (e) shows smooth penetration in both. Sample DS2 was scratched during the removal of the deposition chamber. Sample DS3 is a uniform film, in which the avalanche triggering has no preferential side to take place. Panel (f) illustrated the thickness distribution among these four samples: the uniform purple in DS2 and DS3 indicates their thickness uniformity, whereas the direction of the thickness variation for samples DS1 and DS4 are different, and so is the slope. Performing the same experiment but at $T = 3$ K, one is closer to H_2^{th} for some edges. Figure 103 shows MO images after

ZFC for an increasing field, up to 150 Oe in panels (a), (b) and (c), and also for decreasing field in panels (d), (e), and (f).

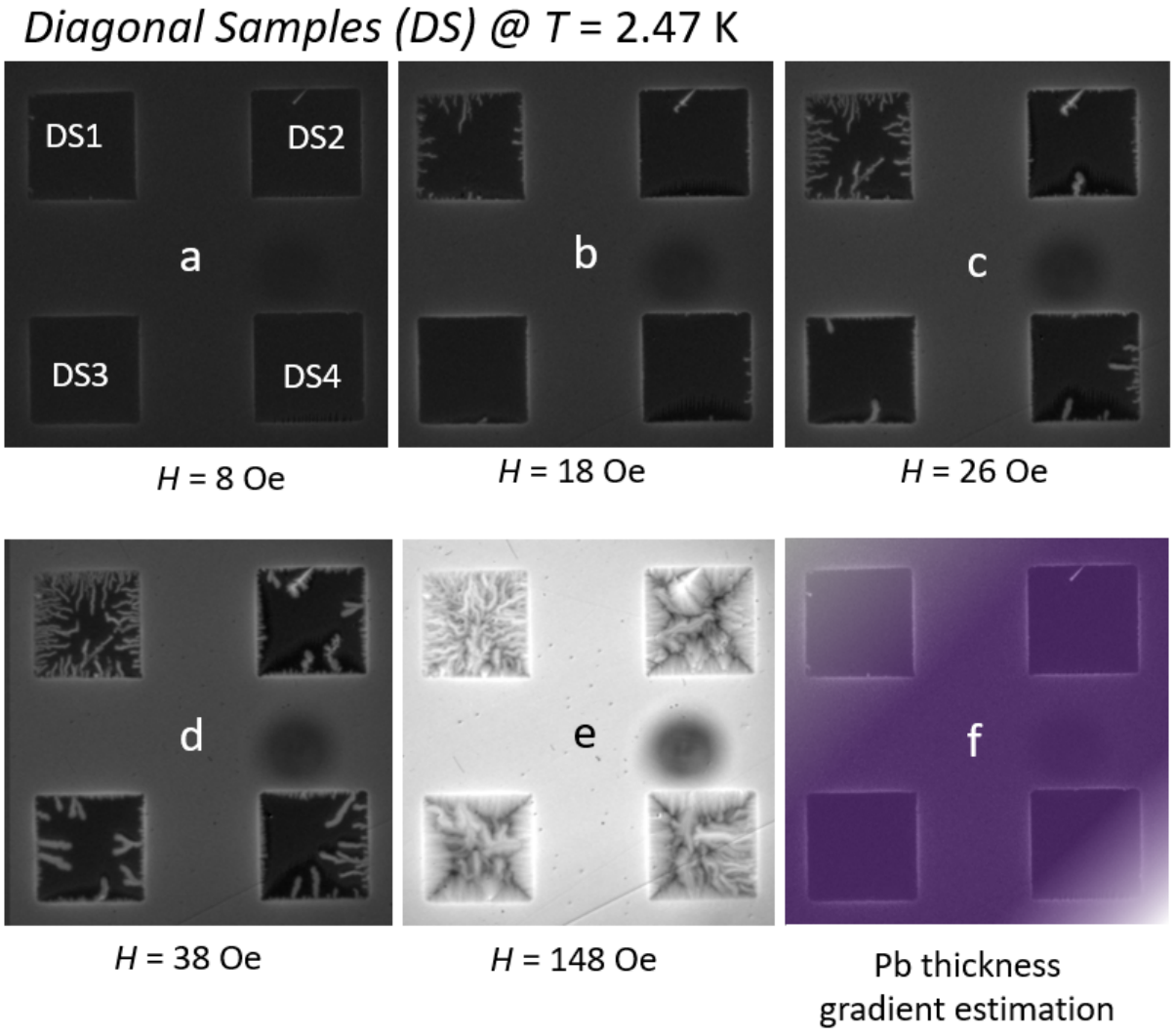

Figure 102: Panels (a) through (e), MO images after a ZFC procedure at 2.47 K of samples DS1, DS2, DS3, and DS4, in which there is a thickness gradient aligned to the square diagonal in samples DS1 and DS4 (f). The black smudge close to sample DS4 is due to dust in the optical window of the cryostat during the experiment.

In Figure 103(b), the smooth penetration in sample DS3 confirms its thickness uniformity. The flux penetration is not uniform in sample DS4. In panel (c), at 150 Oe, sample DS1 shows smooth penetration only in its thicker edges. An interesting feature of this set of samples is their diversity regarding anti-avalanches. Taking DS3 as a reference in Figure 103(d), the anti-avalanches are all diffuse and not so much branched. Sample

DS4 shows different dendritic morphology for its anti-avalanches, depending on the edge it is triggered. The anti-avalanches from the thinner edges are smaller and less blurred than those starting at the thicker edges. These blurred anti-avalanches in DS4 are similar to the dendrites in DS3. Decreasing the field further, which implies a more intense inverse field in the edges of the sample, panel (e) shows larger and more branched anti-avalanches in samples DS3 and DS4, but the morphology diversity in the later is still evident. Finally, in panel (f) one can still see the last anti-avalanche that started from the right thinner edge in DS4 - a large and quite branched avalanche. Furthermore, the top and left edges of the sample DS1 also show anti-avalanches, whereas their opposite borders show smooth penetration.

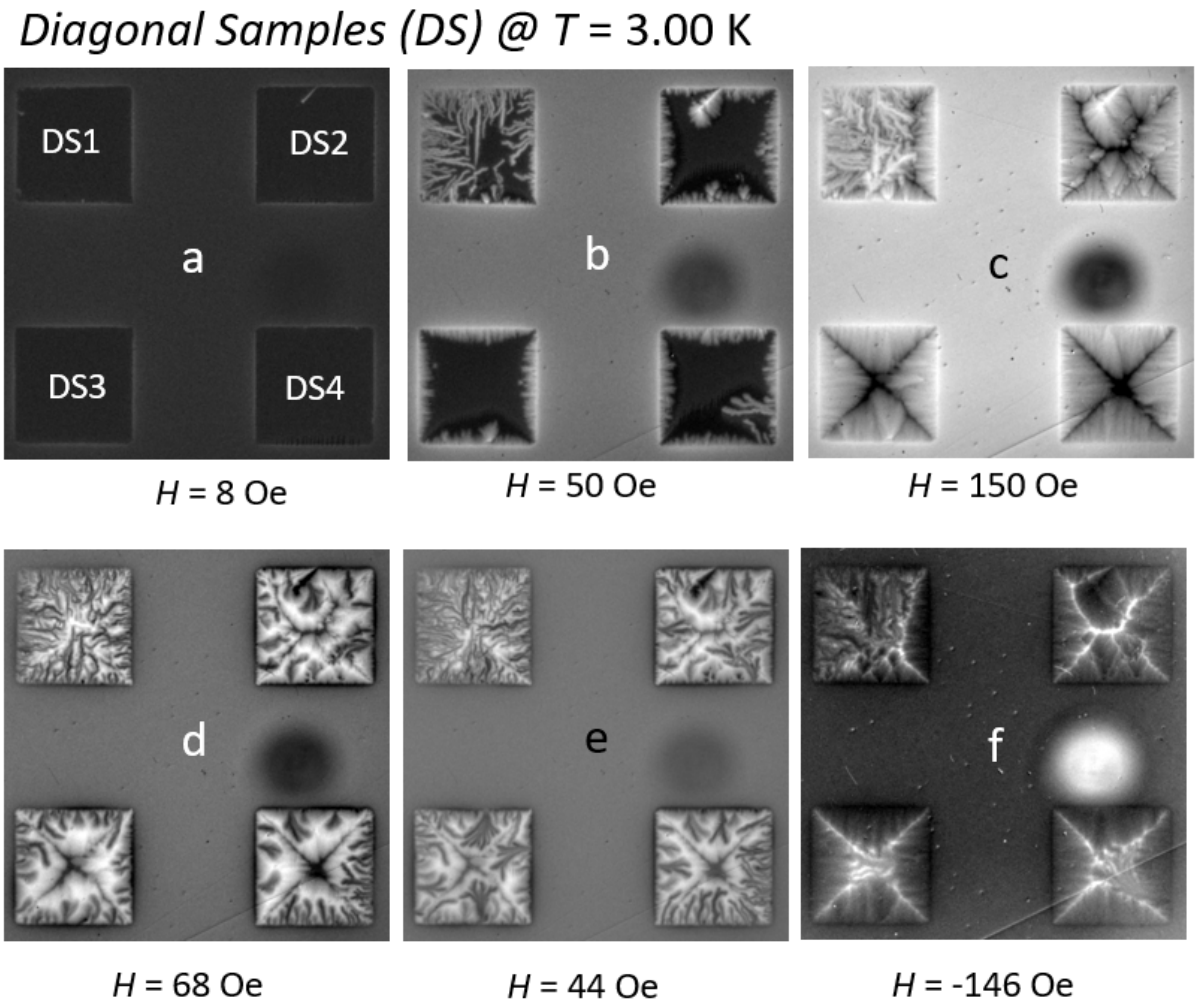

Figure 103: Panels (a) through (f), MO images as a function of applied field after a ZFC procedure at $T = 3$ K of samples DS1, DS2, DS3, and DS4. The smudge close to sample DS4 is due to dust in the optical window of the cryostat during the experiment.

Once the edges show different behavior as the temperature is increased, we built a HT diagram for each edge of the DS1 and DS4 samples. Figure 104(a) displays the data collected from the MO images for sample DS1. Avalanches are stochastic, and one would need a big number of repetitions to draw a more delimited edge for the instability region in the graph. This is the reason why we illustrated it blurred. The colors are the opposite in panel (b) to reinforce the idea that the thinner edges are in opposite directions, when one compares samples DS1 and DS4.

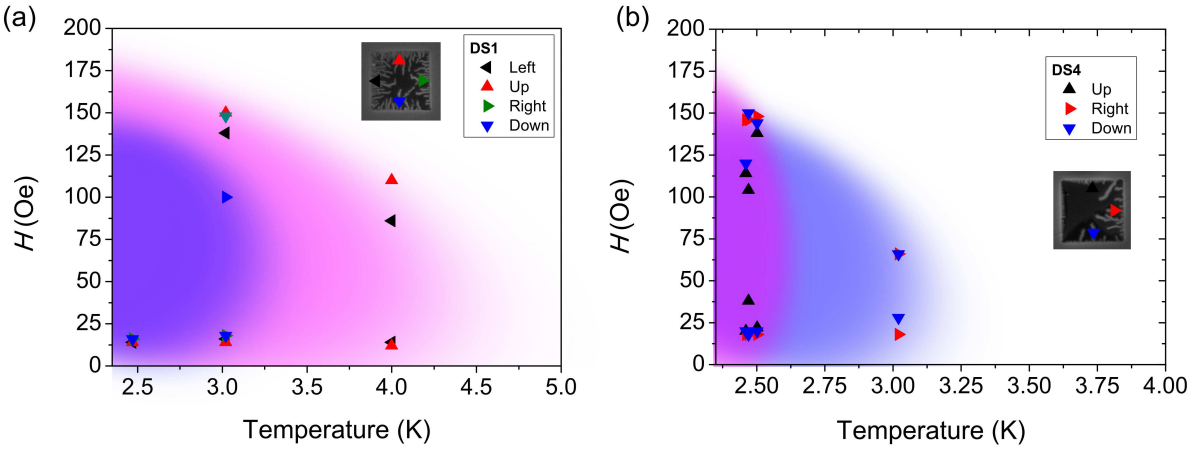

Figure 104: HT diagram for the sample DS1 (a), and DS4 (b). The edges in which each point belongs are indicated by the point: the top edge has triangles pointing up, and so on. For both graphs, the instability region for the top-left edges is represented in magenta, while the bottom-right edges are represented in blue.

A natural question arises: may these results be ascribed to a thermal gradient along the samples during the MOI measurements? Once one knows that the lower the temperature, the higher is the possibility that avalanches occur, could we certify that there is no appreciable thermal gradient? To address these questions we performed a T_C measurement in the MOI setup by making a Field-Cooling (FC) with $H = 20$ Oe down to $T = 2.47$ K, then $H = 0$ and increasing the temperature, observing the trapped flux in the film. Figure 105 displays three MO images of such measurement. In its panel (a), one can easily identify all the four samples at $T = 6.7$ K. In (b), $T = 6.8$ K, the contrast is smaller, and at $T = 6.9$ K, one can not see any of the samples. If there were an important thermal gradient, we expected to see the samples vanishing at different temperatures, but what the experiment shows is that the four samples were at the same temperature, within an error bar smaller than 0.1 K.

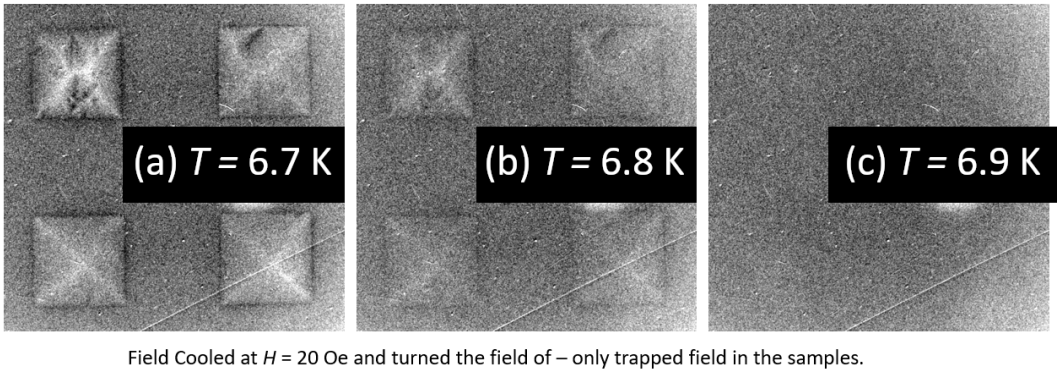

Figure 105: Critical temperature measurement in the MOI experiment for the samples DS1, DS2, DS3, and DS4. Images taken after a field cooling at $H = 20$ Oe, down to $T = 2.47$ K, followed by a slow increase in temperature. The temperature values as indicated, (a) $T = 6.7$ K, (b) $T = 6.8$ K, and (c) $T = 6.9$ K.

7.8 Conclusions

In summary, we successfully prepared wedge-shaped superconducting Pb thin films with apparent well-defined borders and with thickness variation of approximately 10 nm/mm, an achievement with no similar report in the literature. In these samples, we observed a strong dependence of J_C with the film thickness d, with the values approximately changing one order of magnitude from an edge to the other in the same sample. Moreover, this critical current density variation promotes a rich flux avalanche regime, in which one is able to observe different dendritic morphologies at the same temperature and field, but at edges with different thickness. The work described in this chapter opens the gate for new and deeper studies on wedge-shaped superconducting thin films, for example, with stronger thickness variation or different thicknesses range for films which can also behave as a type-I superconductor for larger values of the thickness.

8 Final Remarks and Perspectives

In summary, in this thesis we believe there are four main contributions: **(i)** a detailed explanation about the numerical methods for the magneto-optical images, showing more clearly some features of the MOI, such as an adequate experimental approach to study situations with both polarities of the magnetic field (positive and negative), a richer description of the flux avalanches, and the discussion about some important artifacts; **(ii)** the study of the bi-layered superconducting system where we realize the existence of crossing anti-avalanches and the halo-like structure surrounding the anti-avalanches; **(iii)** the development of thermal evaporation facility and deposition apparatus focused on low melting points materials, where one can produce superconducting thin films with defined borders projected to fit in the characterization facilities of the lab, and so promoting the dawning of the superconducting thin film deposition in the Superconductivity and Magnetism Group at UFSCar; **(iv)** the development of a method and its utilization to make nanoscaled wedge-shaped superconducting thin films, which allowed us to answer some essential initial questions about this subject and also to formulate a somewhat larger number of new questions. These new questions are not only about this subject, but includes the nature of the intriguing phenomena of flux avalanches in superconductors.

This page is intentionally left blank.

9 Appendix A - Thermal evaporator conception & design

This thermal evaporator project was identified E01 and relies on the necessities to prepare superconducting metallic films with either uniform or wedge-shaped which can oxidize in a short period of time. It allows us to begin the thin film preparation, a new line of research in GSM. We will organize the thermal evaporator E01 development in three parts: (1) vacuum system; (2) electrical system, and (3) measuring systems.

A thermal evaporator is a facility where one can evaporate metals and condensate the vapor of them on the suitable substrates, in order to achieve metallic films on the surface of these substrates. Such metallic vapors are usually very reactive to the atmosphere gases, and most of the metals of interest in our case have a low melting point. One cannot make films in the standard conditions of pressure and temperature, and so a vacuum chamber is currently used to achieve the low pressure needed (at least 10^{-4} torr), and we pass high current through a tungsten boat to achieve the melting temperature of the metal.

In order to clarify the functionality of the hundred of parts used to compose this equipment, we describe the thermal evaporator as illustrated in Figure 106:

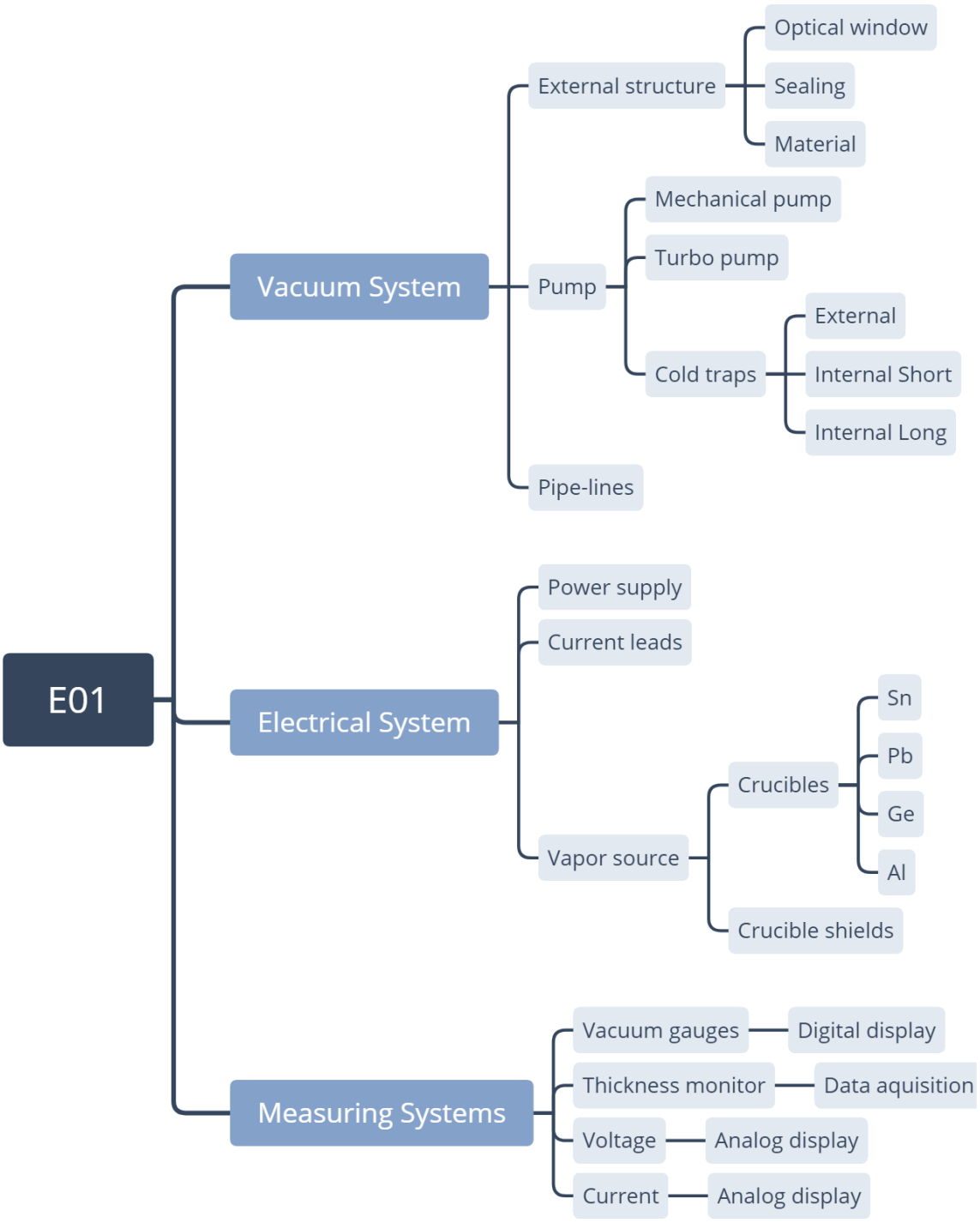

Figure 106: Schematic representation of the E01 subsystems and components.

9.1 Vacuum system

The external structure of the E01 should be mechanically stable to support the outside atmospheric pressure and chemically stable to avoid reaction with the metallic

vapors from inside. The best choice for the chamber walls, base, and cover, was stainless steel. Once most of its constituents are welded, we choose a well weldable alloy of stainless steel. The optical windows are made by soda-lime glass. All other parts and the subsystem are, somehow, directly linked to the external structure of the chamber. Figure 107 shows one of the blueprints of the vacuum chamber in panel (a), and a photograph of the chamber in use in panel (b).

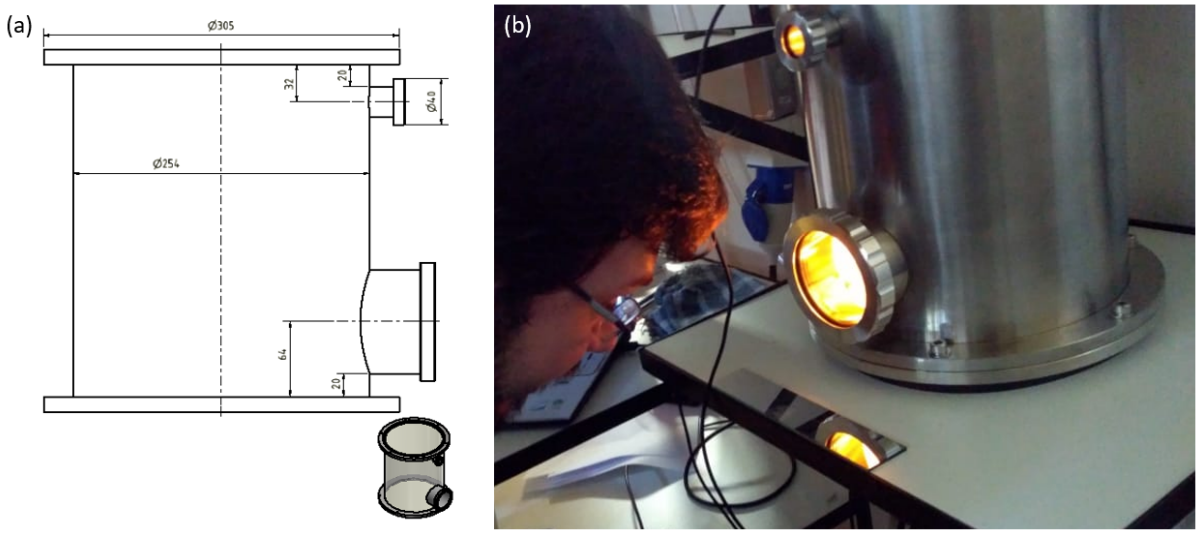

Figure 107: (a) Blueprint of the external structure of the vacuum chamber, and (b) a photograph of the chamber during a deposition process.

The vacuum system is illustrated in Figure 36. First, the pumping system, consisting of a mechanical pump (down to 10^{-3} torr), works as a backing pump for the turbo-molecular pump (down to 10^{-7} torr). To enhance vacuum stability and its base pressure, there is also a cold trap, cooled using liquid nitrogen. This cold trap is placed between the chamber and the pumping system. As all the pumping system is used in other experimental setups in the laboratory, it was kept on the trolley. An interesting feature of this design of cold-trap[1] is its performance: in less than 15 min it was able to change the base pressure of the chamber by one order of magnitude. The system can reach the base pressure of about $2 \cdot 10^{-6}$ torr without the cold trap, but it takes at least 10

[1]The authors are working in parallel to patent the design of this cold-trap.

hours. Both the two vacuum gauges, Pirani and Penning models, are attached directly to the chamber. We proposed a labyrinth-like structure linking the chamber to the gauges to avoid metallic vapors in the sensors.

We classify as 'internal structure' all components that are not permanently linked to the chamber and are inside of it. The labyrinth-like assembly used to protect the vacuum gauges is an example. Figure 35 illustrates the main parts of this subsystem. Nevertheless, the more critical assembly of this subsystem is the substrate holder, detailed in Figure 108. For either protect the substrate entirely or partially, we used fixed and movable shutters, illustrated in Figure 109.

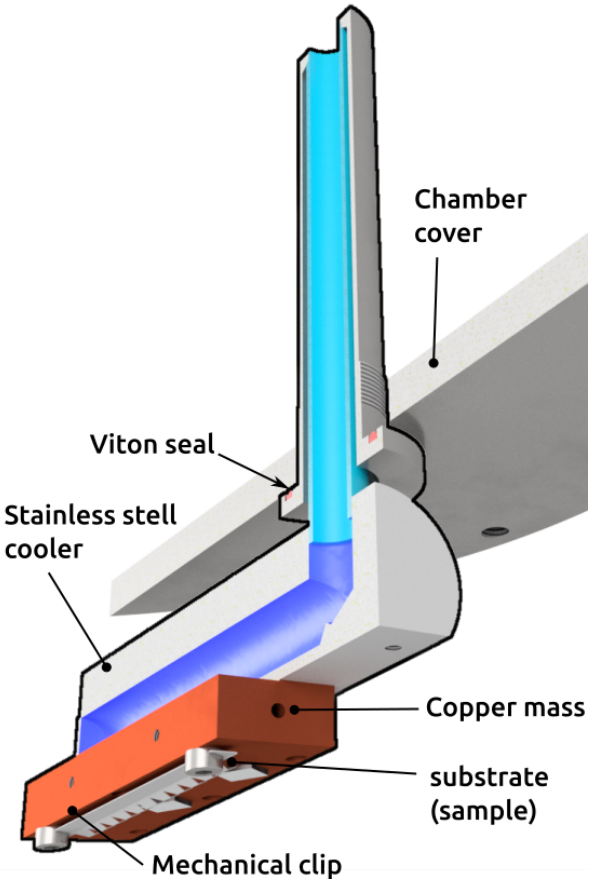

Figure 108: Illustration of the substrate holder. The substrates are in mechanical contact with the copper mass by the clip tip. A cross-section of the cooling system is also shown.

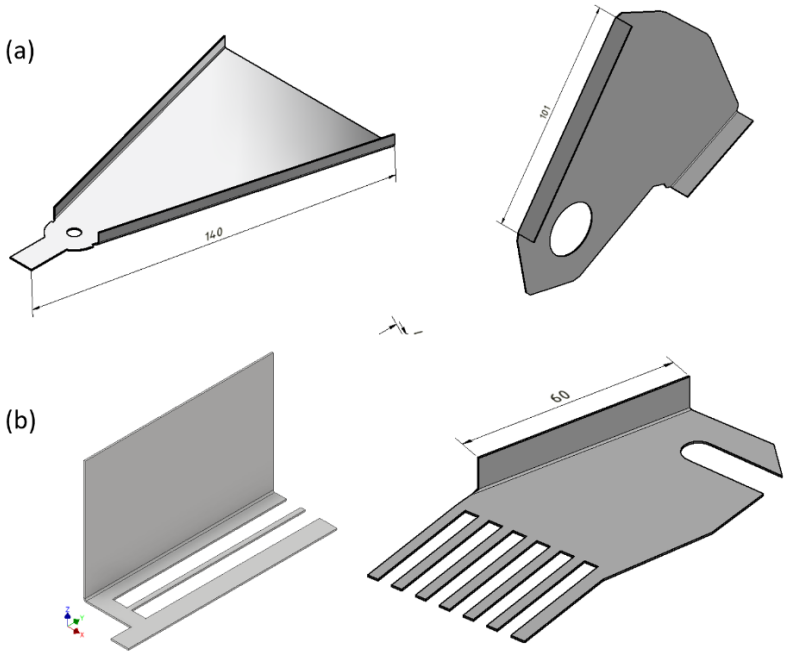

Figure 109: 3D representations of the shutters used in the thermal evaporator.

9.2 Electrical system

The electrical system is the one used to drive electrical current through the boats and heat them by Joule effect. Currents up to 100 A were applied by a Tecktrol current supply. Figure 110 shows some of the electric components of the thermal evaporator, while Figure 111 shows pictures of this system.

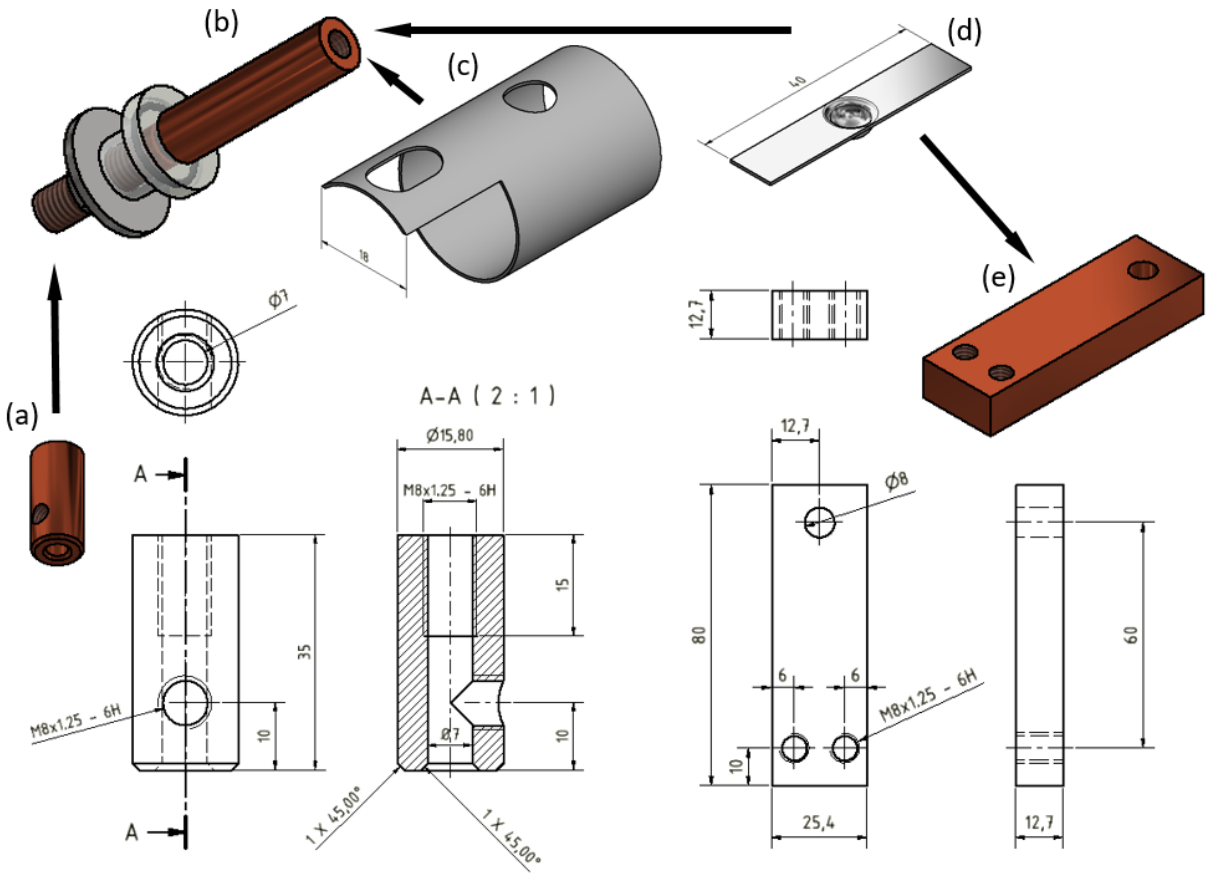

Figure 110: Illustration of the electrical system in the vacuum chamber. Cables connect the power supply to the external connector (a), which is bolted to the positive current lead (b). The crucible shield (c) and the crucible (d) are connected to one of the current leads. The crucible is also connected to the negative current lead (e). Screws, nuts, and washers are not shown. The blueprints at the bottom stand for (a) and (e) components.

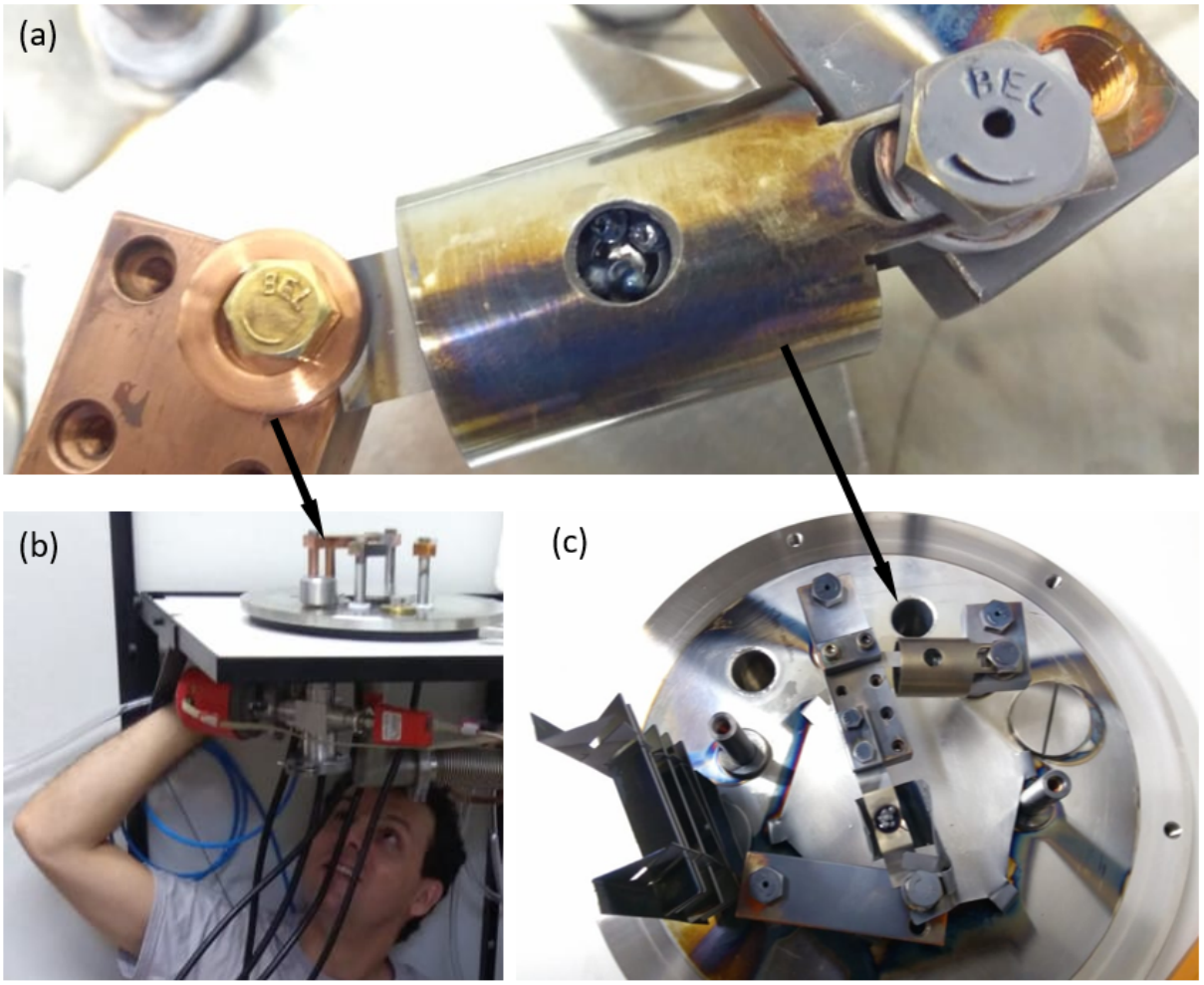

Figure 111: (a) Photograph of the Pb crucible inside the shield and the current leads. (b) Me adjusting the external connector showed in Figure 110(a). (c) An overview of the evaporator base, showing both the Ge and the Pb crucibles at the center, and the optical window protection at left.

9.3 Measuring systems

The most important sensor in the chamber is the thickness monitor - a quartz crystal microbalance, adapted from a open-source project Open-QCM [2]. The signal to and from the QCM passes through the chamber walls by a electrical feed-through, whose main part is illustrated in Figure 112(a).

[2]The original setup of this project focus on liquid applications of this quartz crystal microblance.

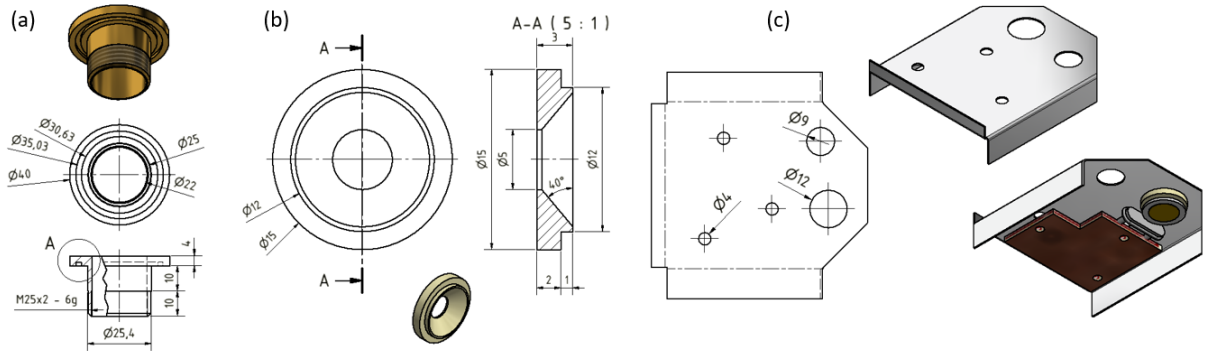

Figure 112: (a) Blueprint of the electrical feed-through for the data cables of the QCM and the thermometer. (b) Protection ring for the crystal, and (c) the QCM case.

9.4 Thermal evaporator Fabrication

The vacuum chamber must avoid any kind of leaks once it is supposed to achieve the vacuum limit of the rubber used to connect the parts (typically 10^{-7} *torr*). Once we used stainless steel to build the chamber's external structure, we needed to weld most of its parts. The optical windows and the connection to the vacuum pump had to be welded directly to the chamber, and we used tungsten inert gas welding (TIG) and an experienced welder, namely, the mechanical engineer Araldo Luiz Isaias de Moraes, who has experience welding parts for high vacuum. Most of the machined parts were produced in the workshop of the cryogenic lab in the Department of Physics at UFSCar, by the technician Cláudio Márcio Raffa. Figures 113, 114, and 115 show blueprints used during the manufacturing of the thermal evaporator. All of them have passed through revision several times, as indicated in the bottom of each page.

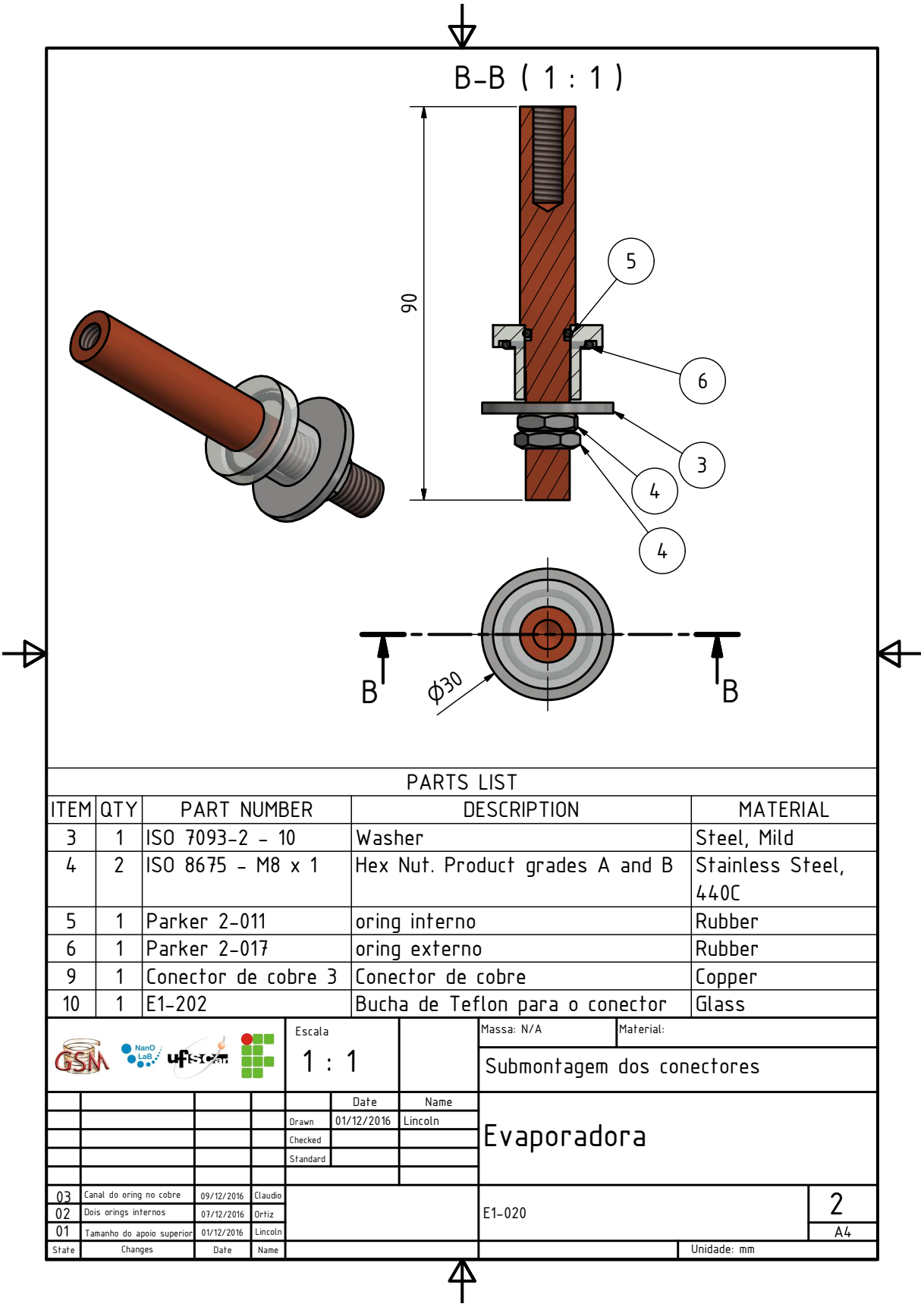

PARTS LIST

ITEM	QTY	PART NUMBER	DESCRIPTION	MATERIAL
3	1	ISO 7093-2 - 10	Washer	Steel, Mild
4	2	ISO 8675 - M8 x 1	Hex Nut. Product grades A and B	Stainless Steel, 440C
5	1	Parker 2-011	oring interno	Rubber
6	1	Parker 2-017	oring externo	Rubber
9	1	Conector de cobre 3	Conector de cobre	Copper
10	1	E1-202	Bucha de Teflon para o conector	Glass

Escala 1 : 1

Massa: N/A

Material:

Submontagem dos conectores

	Date	Name
Drawn	01/12/2016	Lincoln
Checked		
Standard		

Evaporadora

State	Changes	Date	Name
03	Canal do oring no cobre	09/12/2016	Claudio
02	Dois orings internos	07/12/2016	Ortiz
01	Tamanho do apoio superior	01/12/2016	Lincoln

E1-020

2

A4

Unidade: mm

Figure 113: Blueprint of the sub-assembly for the electrical current connection in the vacuum chamber.

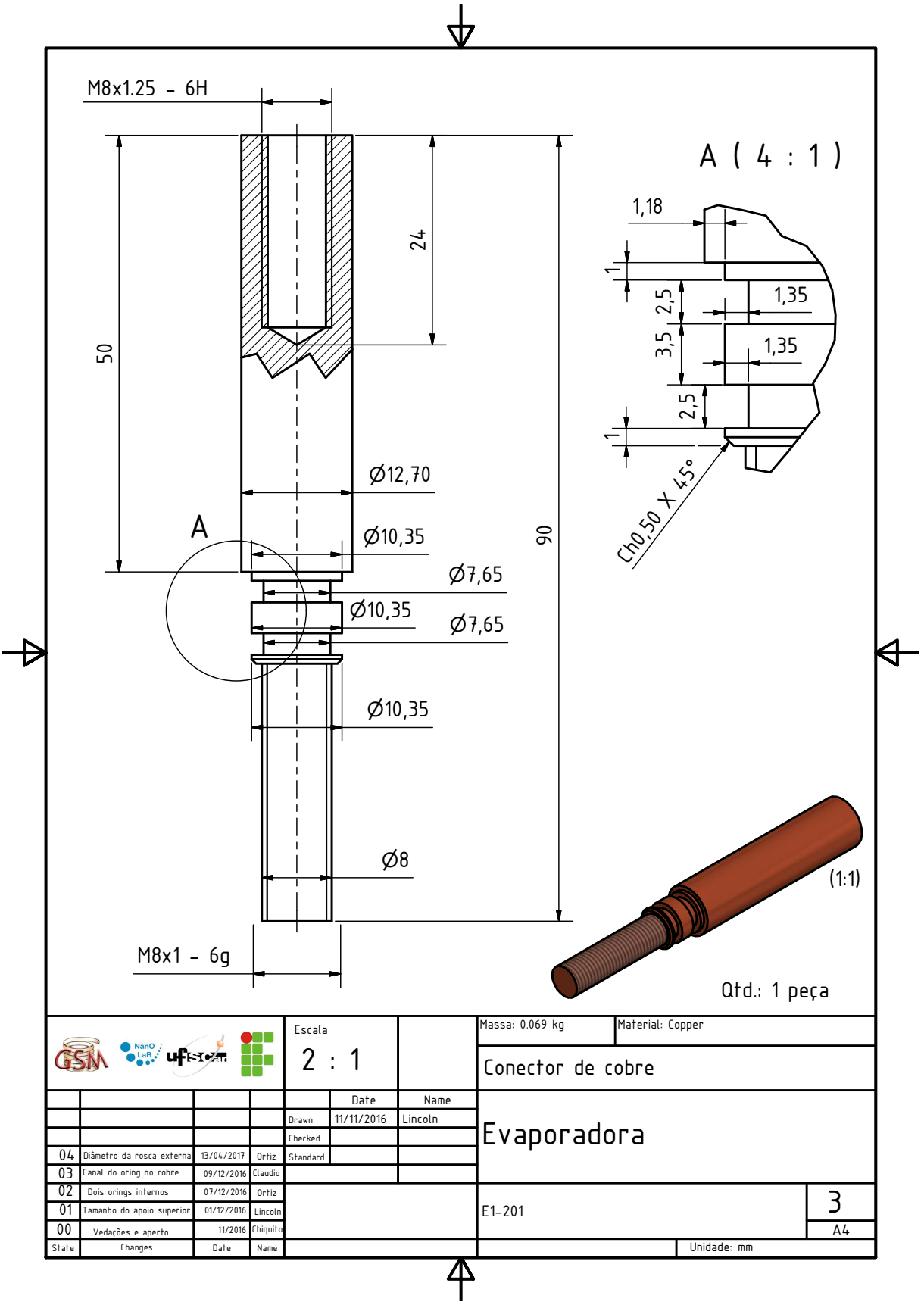

Figure 114: Blueprint of the internal current lead.

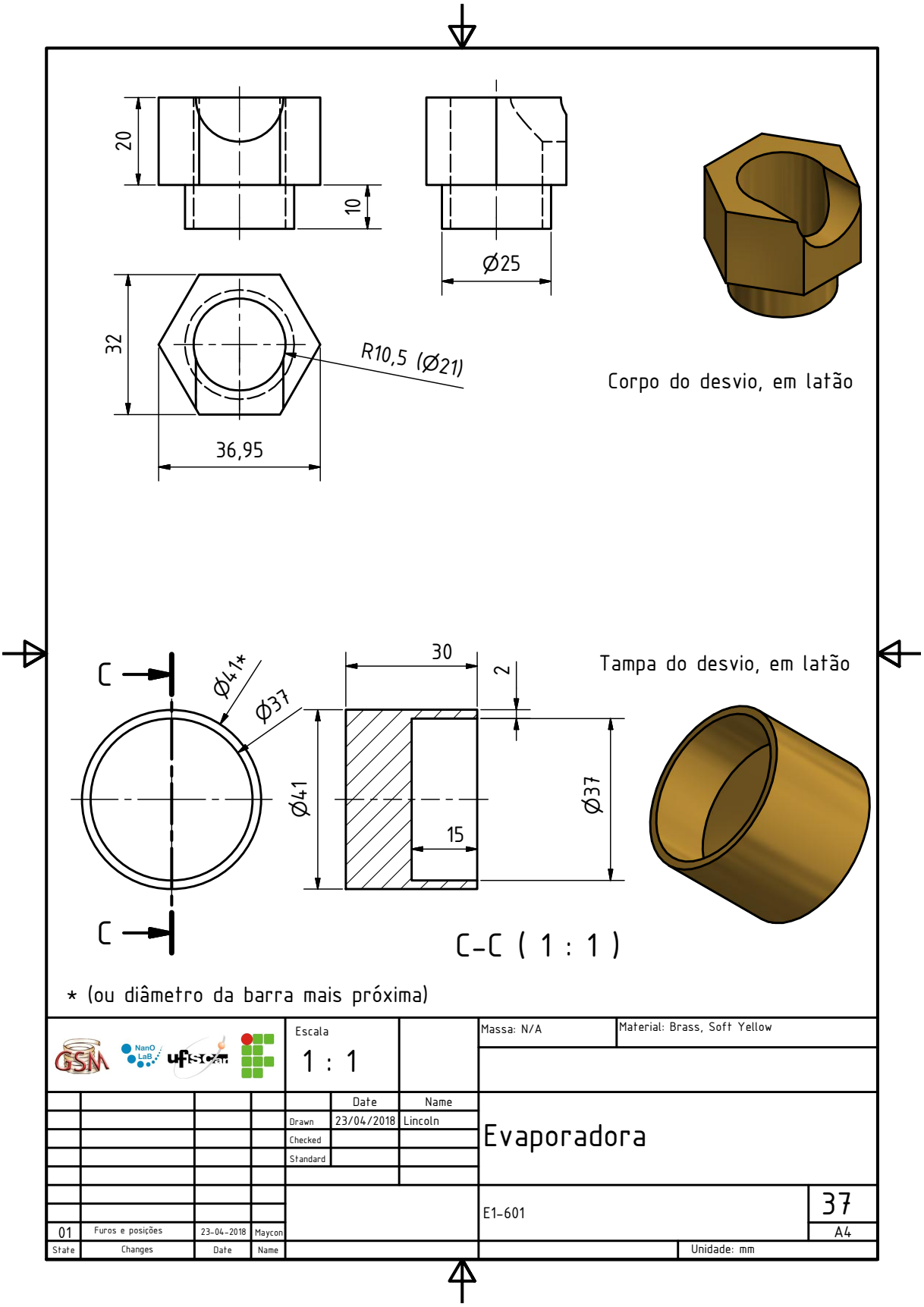

Figure 115: Brass parts for protection of the vacuum gauges.

Index

List of publications

- G. Shaw, J. Brisbois, L. B.G.L. Pinheiro, J. Müller, S. Blanco Alvarez, T. Devillers, N. M. Dempsey, J. E. Scheerder, J. Van De Vondel, S. Melinte, P. Vanderbemden, M. Motta, W. A. Ortiz, K. Hasselbach, R. B.G. Kramer, and A. V. Silhanek. Quantitative magneto-optical investigation of superconductor/ferromagnet hybrid structures. **Review of Scientific Instruments**, 89(2), 2018. ISSN 10897623. doi: 10.1063/1.5016293.

- L. B. L. G. Pinheiro, M. Motta, F. Colauto, T. Johansen, E. Bellingeri, C. Bernini, C. Ferdeghini, and W. Ortiz. Imaging flux avalanches in V_3Si superconducting thin films. **IEEE Transactions on Applied Superconductivity**, 2019. ISSN 1051-8223. doi: 10.1109/TASC.2019.2902788.

- L. B. L. G. Pinheiro, M. Caputo, C. Cirillo, C. Attanasio, T.H. Johansen, W.A. Ortiz, A.V. Silhanek, and M. Motta. Magnetic flux avalanches in Nb/NbN thin films. **Low Temperature Physics**/Fizika Nizkikh Temperatur, 2020, v. 46, No. 4, pp. doi: 10.1063/10.0000868.

Bibliography

[1] H. K. Onnes. Sur les résistances électriques. In *Rapports et discussions de la réunion tenue a Bruxelles du 30 Octobre au 3 Novembre 1911*, pages 133–144. Eduard IJdo, Leiden, 1911.

[2] P. Brown, K. Semeniuk, D. Wang, B. Monserrat, C. J Pickard, and F. M. Grosche. Strong coupling superconductivity in a quasiperiodic host-guest structure. *Science Advances*, 4(April):1–6, 2018.

[3] J. G. Bednorz and K. A. Müller. Possible hightc superconductivity in the ba-la-cu-o system. *Zeitschrift für Physik B Condensed Matter*, 64(2):189–193, Jun 1986. ISSN 1431-584X. doi: 10.1007/BF01303701. URL `https://doi.org/10.1007/BF01303701`.

[4] P. H. Hor, R. L. Meng, Y. Q. Wang, L. Gao, Z. J. Huang, J. Bechtold, K. Forster, and C. W. Chu. Superconductivity above 90 K in the square-planar compound system ABa2Cu3O6+x with A=Y, La, Nd, Sm, Eu, Gd, Ho, Er and Lu. *Physical Review Letters*, 58(18):1891–1894, 1987. ISSN 00319007. doi: 10.1103/PhysRevLett.58.1891.

[5] A. P. Drozdov, M. I. Eremets, I. A. Troyan, V. Ksenofontov, and S. I. Shylin. Conventional superconductivity at 203 kelvin at high pressures in the sulfur hydride system. *Nature*, 525(7567):73–76, 2015. ISSN 14764687. doi: 10.1038/nature14964.

[6] M. Somayazulu, M. Ahart, A. K. Mishra, Z. M. Geballe, M. Baldini, Y. Meng, V. V. Struzhkin, and R. J. Hemley. Evidence for Superconductivity above 260 K in Lanthanum Superhydride at Megabar Pressures. *Physical Review Letters*, 122 (2):27001, 2019. ISSN 10797114. doi: 10.1103/PhysRevLett.122.027001. URL `https://doi.org/10.1103/PhysRevLett.122.027001`.

[7] Serway. Modern physics downloads, web essays and appendices, 2019. URL `http://www.cengage.com/resource_uploads/static_resources/0534493394/4891/SerwayCh12-Superconductivity.pdf`.

[8] J. Bardeen, L. N. Cooper, and J. R. Schrieffer. Microscopic theory of Superconductivity. *Physical Review*, 106(1):1689–1699, 1957. doi: 10.1103/PhysRev.106.162.

[9] J. Bardeen, L. N. Cooper, and J. R. Schrieffer. The microscopic theory of superconductivity. *Physical Review*, 108(5):549–564, 1957. doi: 10.1103/PhysRev.108.1175.

[10] L. N. Cooper. Bound electron pairs in a degenerate fermi gas. *Physical Review*, 104 (4):1189–1190, 1956. ISSN 0031899X. doi: 10.1103/PhysRev.104.1189.

[11] B. D. Josephson. Possible new effects in superconductive tunnelling. *Physics Letters*, 1(7):251–253, 1962. doi: 10.1016/0031-9163(62)91369-0.

[12] C. Monroe. Quantum computers ready to leap out of the lab. *Nature*, 541, 2017.

[13] W. Meissner and R. Ochsenfeld. Ein neuer Effekt bei Eintritt der Supraleitfähigkeit. *Die Naturwissenschaften*, 21(44):787–788, 1933. ISSN 00281042. doi: 10.1007/BF01504252.

[14] A.C. Rose-Innes. *Introduction to Superconductivity*. International Series in Solid State Physics. Elsevier Science, 2012. ISBN 9780323161923.

[15] F. London and H. London. Supraleitung und diamagnetismus. *Physica*, 2(1-12): 341–354, 1935. ISSN 00318914. doi: 10.1016/S0031-8914(35)90097-0.

[16] A. B. Pippard. The surface energies of superconductors. *Mathematical Proceedings of the Cambridge Philosophical Society*, 47(3):617–625, 1951. ISSN 14698064. doi: 10.1017/S0305004100027018.

[17] V. Ginzburg and L. D. Landau. On the theory of superconductivity. In D. TER HAAR, editor, *COLLECTED PAPERS OF L. D. LANDAU*, volume 1064, chapter 73, pages 546–568. Elsevier, London, 1950. ISBN 978-0-08-010586-4. doi: 10.1016/B978-0-08-010586-4.50078-X. URL `https://www.sciencedirect.com/book/9780080105864/collected-papers-of-ld-landau{#}book-description`.

[18] A. B. Pippard and F. R. S. Sir Lawrence Bragg. An experimental and theoretical study of the relation between magnetic field and current in a superconductor. *Proceedings of the Royal Society A: Mathematical, Physical and Engineering Sciences*, 216(A):547–568, 1953. doi: 10.1098/rspa.1953.0040. URL `http://rspa.royalsocietypublishing.org/content/216/1127/547`.

[19] M. Cyrot and D. Pavuna. *Introduction to Superconductivity and High-Tc Materials*. World Scientific, 1992. ISBN 9789810201449. URL `https://books.google.com.br/books?id=ZKaemvYLVegC`.

[20] M. Tinkham. *Introduction to Superconductivity*. Dover Books on Physics Series. Dover Publications, 2004. ISBN 9780486134727. URL `https://books.google.com.br/books?id=VpUk3NfwDIkC`.

[21] K. Fossheim and A. Sudboe. *Superconductivity: Physics and Applications*. Wiley, 2004. ISBN 9780470844526. URL `https://books.google.com.br/books?id=HyZvZLLQBwEC`.

[22] R. Prozorov, A. F. Fidler, J. R. Hoberg, and P. C. Canfield. Suprafroth in type-I superconductors. *Nature Physics*, 4(4):327–332, 2008. ISSN 17452473. doi: 10.1038/nphys888.

[23] R. Prozorov and J. R. Hoberg. Dynamic formation of metastable intermediate state patterns in type-I superconductors. *Journal of Physics: Conference Series*, 150(5): 1–4, 2009. ISSN 17426596. doi: 10.1088/1742-6596/150/5/052217.

[24] J. R. Hoberg and R. Prozorov. Current-driven transformations of the intermediate-state patterns in type-I superconductors. *Physical Review B - Condensed Matter and Materials Physics*, 78(10):1–5, 2008. ISSN 10980121. doi: 10.1103/PhysRevB.78.104511.

[25] A. Mughal, S. J. Cox, D. Weaire, S. R. Burke, and S. Hutzler. Demonstration and interpretation of scutoid cells in a quasi-2D soap froth. *Philosophical Magazine Letters*, 98(8):358–364, 2018. ISSN 0950-0839. doi: 10.1080/09500839.2018.1552806. URL `http://arxiv.org/abs/1809.08421`.

[26] R. Gabbrielli, A. J. Meagher, D. Weaire, K. A. Brakke, and S. Hutzler. An experimental realization of the Weaire-Phelan structure in monodisperse liquid foam. *Philosophical Magazine Letters*, 92(1):1–6, 2012. ISSN 09500839. doi: 10.1080/09500839.2011.645898.

[27] B. Macias Rodriguez and A. G. Marangoni. The fat in a perfect croissant. *Physics Today*, 71(1):70–71, 2018. ISSN 00319228. doi: 10.1063/PT.3.3828.

[28] A.A. Abrikosov. The magnetic properties of superconducting alloys. *Journal of Physics and Chemistry of Solids*, 2(3):199 – 208, 1957. ISSN 0022-3697. doi: https://doi.org/10.1016/0022-3697(57)90083-5. URL `http://www.sciencedirect.com/science/article/pii/0022369757900835`.

[29] T. K. Hunt. Critical-Current Behavior in Narrow Thin-Film Superconductors. *Physical Review*, 151(1):325–327, 1966.

[30] D. Dew-Hughes. The critical current of superconductors: An historical review. *Low Temperature Physics*, 27(9-10):713–722, 2001. ISSN 1063777X. doi: 10.1063/1.1401180.

[31] C. P. Bean. Magnetization of hard superconductors. *Physical Review Letters*, 8(6): 250–253, 1962. doi: https://doi.org/10.1103/PhysRevLett.8.250.

[32] C. P. Bean. Magnetization of High-Field Superconductors. *Review of Modern Physics*, 36(1):31–39, 1964.

[33] E. Altshuler and T. H. Johansen. Colloquium: Experiments in vortex avalanches. *Reviews of Modern Physics*, 76(2):471–487, 2004. ISSN 00346861. doi: 10.1103/RevModPhys.76.471.

[34] A. Shalnikov. Superconducting Thin Films. *Nature*, 142(July):74, 1938.

[35] Y. Guo, Y. Zhang, X. Bao, T. Han, Z. Tang, L. Zhang, W. Zhu, E. G. Wang, Q. Niu, Z. Q. Qiu, J. Jia, Z. Zhao, and Q. Xue. Superconductivity modulated by quantum size effects. *Science (New York, N.Y.)*, 306(5703):1915–1917, 2004. ISSN 0036-8075. doi: 10.1126/science.1105130.

[36] G. J. Dolan and J. Silcox. Critical thicknesses in superconducting thin films. *Physical Review Letters*, 30(13):603–606, 1973. ISSN 00319007. doi: 10.1103/PhysRevLett.30.603.

[37] J. Pearl. Current distribution in superconducting films carrying quantized fluxoids. *Applied Physics Letters*, 5(4):65–66, 1964. ISSN 00036951. doi: 10.1063/1.1754056.

[38] C. P. Poole, R. Prozorov, H. A. Farach, and R. J. Creswick. *Superconductivity (Third Edition)*. Elsevier, London, third edition edition, 2014. ISBN 978-0-12-409509-0. doi: https://doi.org/10.1016/B978-0-12-409509-0.00008-1.

[39] E. H. Brandt. Superconductors and vortices at radio frequency magnetic fields, at max planck institute for metals research - d-70506 stuttgart - germany, 4-6 october, 2010. URL `https://surfacetreatments.infn.it/`.

[40] E. H. Brandt and M. Indenbom. Type-II-superconductor strip with current in a perpendicular magnetic field. *Physical Review B*, 48(17):12893–12906, 1993. ISSN 01631829. doi: 10.1103/PhysRevB.48.12893.

[41] E. Zeldov, John R. Clem, M. McElfresh, and M. Darwin. Magnetization and transport currents in thin superconducting films. *Physical Review B*, 49(14):9802–9822, 1994. ISSN 01631829. doi: 10.1103/PhysRevB.49.9802.

[42] T. H. Johansen, M. Baziljevich, H. Bratsberg, Y. Galperin, P. Lindelof, Y. Shen, and P. Vase. Direct observation of the current distribution in thin superconducting strips using magneto-optic imaging. *Physical Review B*, 54(22):16264–16269, 1996. ISSN 0163-1829. doi: 10.1103/PhysRevB.54.16264.

[43] Th. Schuster, M.V. Indenbom, M.R. Koblischka, H. Kuhn, and H. Kronmüller. Observation of current-discontinuity lines in type-II superconductors. *Phys. Rev. B*, 49(5):3443–3452, 1994.

[44] Ch. Jooss, J. Albrecht, H. Kuhn, S. Leonhardt, and H. Kronmüller. Magneto-optical studies of current distributions in high-Tc superconductors. *Reports on Progress in Physics*, 65(5):651–788, 2002. ISSN 00344885. doi: 10.1088/0034-4885/65/5/202. URL `http://iopscience.iop.org/0034-4885/65/5/202`.

[45] Th. Schuster, H. Kuhn, and E. Brandt. Flux penetration into flat superconductors of arbitrary shape: Patterns of magnetic and electric fields and current. *Physical Review B - Condensed Matter and Materials Physics*, 54(5):3514–3524, 1996. ISSN 1550235X. doi: 10.1103/PhysRevB.54.3514.

[46] J. Albrecht, A. T. Matveev, J. Strempfer, H. U. Habermeier, D. V. Shantsev, Y. M. Galperin, and T. H. Johansen. Dramatic role of critical current anisotropy on flux avalanches in MgB2 films. *Physical Review Letters*, 98(11):2–5, 2007. ISSN 00319007. doi: 10.1103/PhysRevLett.98.117001.

[47] Pierre-Gilles de Gennes. *Superconductivity of Metals and Alloys*. Advanced book classics. Advanced Book Program, Perseus Books, 1999. ISBN 9780738201016. URL `https://books.google.com.br/books?id=xacsAAAAYAAJ`.

[48] T. H. Johansen, M. Baziljevich, D. V. Shantsev, P. E. Goa, Y. M. Galperin, W. N. Kang, H. J. Kim, E. M. Choi, M-S. Kim, and S. I. Lee. Dendritic flux patterns in MgB2 films. *Superconductor Science and Technology Dendritic*, 14:726–728, 2001.

[49] A. J. Qviller, V. V. Yurchenko, K. Eliassen, J. I. Vestgrden, T. H. Johansen, M. R. Nevala, I. J. Maasilta, K. Senapati, and R. C. Budhani. Irreversibility of the threshold field for dendritic flux avalanches in superconductors. *Physica C: Superconductivity and its Applications*, 470(19):897–900, 2010. ISSN 09214534. doi: 10.1016/j.physc.2010.02.066. URL `http://dx.doi.org/10.1016/j.physc.2010.02.066`.

[50] T. Frello, M. Baziljevich, T. H. Johansen, N. H. Andersen, Th. Wolf, and M. R. Koblischka. Flux turbulence in NdBa2Cu3O6+x and underdoped YBa2Cu3O6+x single crystals. *Physical Review B*, 59(10):6639–6642, 1999.

[51] E. Baruch-El, M. Baziljevich, T. H. Johansen, and Y. Yeshurun. Substrate Influence on Dendritic Flux Instability in YBCO Thin Films. *Journal of Superconductivity and Novel Magnetism*, 28:379–382, 2015. doi: 10.1007/s10948-014-2723-9.

[52] J. I. Vestgården, D. V. Shantsev, Y. M. Galperin, and T. H. Johansen. Dynamics and morphology of dendritic flux avalanches in superconducting films. *Phys. Rev. B*, 84:054537, Aug 2011. doi: 10.1103/PhysRevB.84.054537. URL `https://link.aps.org/doi/10.1103/PhysRevB.84.054537`.

[53] R. G. Mints and A. L. Rakhmanov. Critical state stability in type-II superconductors and superconducting-normal-metal composites. *Reviews of Modern Physics*, 53(3):551–592, 1981. ISSN 00346861. doi: 10.1103/RevModPhys.53.551.

[54] S.L. Wipf. Review of stability in high temperature superconductors with emphasis on flux jumping. *Cryogenics*, 31(11):936–948, nov 1991. ISSN 0011-2275. doi: 10.1016/0011-2275(91)90217-K. URL `https://www.sciencedirect.com/science/article/abs/pii/001122759190217K`.

[55] D. V. Denisov, D. V. Shantsev, Y. M. Galperin, Eun-Mi Choi, Hyun-Sook Lee, Sung-Ik Lee, A. V. Bobyl, P. E. Goa, A. A. F. Olsen, and T. H. Johansen. Onset of dendritic flux avalanches in superconducting films. *Phys. Rev. Lett.*, 97:077002, Aug 2006. doi: 10.1103/PhysRevLett.97.077002. URL `https://link.aps.org/doi/10.1103/PhysRevLett.97.077002`.

[56] J. I. Vestgården, D. V. Shantsev, Y. M. Galperin, and T. H. Johansen. Lightning in superconductors. *Scientific Reports*, 2:1–8, 2012. ISSN 20452322. doi: 10.1038/srep00886.

[57] S. Blanco Alvarez, J. Brisbois, S. Melinte, R. B.G. Kramer, and A. V. Silhanek. Statistics of thermomagnetic breakdown in Nb superconducting films. *Scientific Reports*, 9(1):1–9, 2019. ISSN 20452322. doi: 10.1038/s41598-019-39337-5.

[58] Jérémy Brisbois. *Magneto-optical investigation of superconducting hybrid structures.* Phd thesis, Université de Liège, 2017.

[59] Danusa do Carmo. *Manipulação da penetração regular de uxo magnético e avalanches termomagnéticas em filmes supercondutores.* Tese de doutorado, Universidade Federal de São Carlos, 2017.

[60] M. Motta, F. Colauto, J. I. Vestgården, J. Fritzsche, M. Timmermans, J. Cuppens, C. Attanasio, C. Cirillo, V. V. Moshchalkov, J. Van de Vondel, T. H. Johansen, W. a. Ortiz, and a. V. Silhanek. Controllable morphology of flux avalanches in microstructured superconductors. *Physical Review B*, 89(13):134508, apr 2014. ISSN 1098-0121. doi: 10.1103/PhysRevB.89.134508. URL `http://link.aps.org/doi/10.1103/PhysRevB.89.134508`.

[61] M. Motta. *Flux avalanches in patterned superconducting thin films: ac susceptibility, morphology and related studies*. PhD thesis, UFSCar, 2013.

[62] Y. Lu, Z. Jing, H. Yong, and Y. Zhou. Flux avalanche in a superconducting film with non-uniform critical current density Subject Areas :. *Proc. R. Soc. A*, 472: 20160469, 2016. doi: 10.1098/rspa.2016.0469.

[63] I. Giaever and K. Megerle. Study of superconductors by electron tunneling. *Physical Review*, 122(4):1101–1111, 1961. ISSN 0031899X. doi: 10.1103/PhysRev.122.1101.

[64] J. J. Hauser and H. C. Theuerer. Superconductivity in Pb-Al superimposed films. *Physics Letters*, 14(4):14–15, 1965.

[65] Ivar Giaever. Magnetic coupling between two adjacent type-ii superconductors. *Physical Review Letters*, 15(21):0–2, 1965.

[66] I. Giaever. Flux pinning and flux-flow resistivity in magnetically coupled superconducting films. *Physical Review Letters*, 16(11):460–462, 1966. ISSN 00319007. doi: 10.1103/PhysRevLett.16.460.

[67] S Lacroix. Superconductor data storage device, 1970. URL `http://www.google.tl/patents/US3500344`.

[68] T. Tamegai, A. Mine, Y. Tsuchiya, S. Miyano, S. Pyon, Y. Mawatari, and S. Nagasawa. Physica C : Superconductivity and its applications Critical states and thermomagnetic instabilities in three-dimensional nanostructured superconductors. *Physica C: Superconductivity and its applications*, 533:74–79, 2017. ISSN 0921-4534. doi: 10.1016/j.physc.2016.07.009. URL `http://dx.doi.org/10.1016/j.physc.2016.07.009`.

[69] R. Holm and W. Meissner. Messungen mit Hilfe von flüssigem Helium. XIII. *Zeitschrift für Physik*, 74(11-12):715–735, 1932. ISSN 1434-6001. doi: 10.1007/BF01340420. URL `http://www.springerlink.com/content/h871763031j18137/`.

[70] S Franssila. *Shadow Masks*. Wiley, Singapore, first edition edition, 2010. ISBN 9781119991892. URL `https://books.google.com.br/books?id=cvoR9vmDJIQC`.

[71] A. Ludwig, J. Cao, J. Brugger, and I. Takeuchi. MEMS tools for combinatorial materials processing and high-throughput characterization. *Measurement Science and Technology*, 16(1):111–118, 2005. ISSN 09570233. doi: 10.1088/0957-0233/16/1/015.

[72] Alfred Ludwig. Discovery of new materials using combinatorial synthesis and high-throughput characterization of thin- fi lm materials libraries combined with computational methods. *npj Computational Materials*, 70(February), 2019. ISSN 2057-3960. doi: 10.1038/s41524-019-0205-0. URL `http://dx.doi.org/10.1038/s41524-019-0205-0`.

[73] V. Palmisano, M. Filippi, A. Baldi, M. Slaman, H. Schreuders, and B. Dam. An optical hydrogen sensor based on a Pd-capped Mg thin film wedge. *International Journal of Hydrogen Energy*, 35(22):12574–12578, 2010. ISSN 03603199. doi: 10.1016/j.ijhydene.2010.09.001. URL `http://dx.doi.org/10.1016/j.ijhydene.2010.09.001`.

[74] C. Zhang, Y. Zhang, X. Yuan, S. Lu, J. Zhang, A. Narayan, Y. Liu, H. Zhang, Z. Ni, R. Liu, E. S. Choi, A. Suslov, S. Sanvito, L. Pi, H. Z. Lu, A. C. Potter, and F. Xiu. Quantum Hall effect based on Weyl orbits in Cd 3 As 2. *Nature*, 565(7739): 331–336, 2019. ISSN 14764687. doi: 10.1038/s41586-018-0798-3.

[75] J. P. Prineas, W. J. Johnston, M. Yildirim, J. Zhao, and Arthur L. Smirl. Tunable slow light in Bragg-spaced quantum wells. *Applied Physics Letters*, 89(24):1–4, 2006. ISSN 00036951. doi: 10.1063/1.2403927.

[76] Alfred Ludwig. Combinatorial fabrication of magnetic multilayer films. *Applied Surface Science*, 223:78–83, 2004. doi: 10.1016/S0169-4332(03)00910-3.

[77] P. Sabatino, G. Carapella, and M. Gombos. Preferentially directed flux motion in a very thin superconducting strip with nanostructured profile. *Journal of Applied Physics*, 112(October):article number 089309, 2012. doi: 10.1063/1.4759206.

[78] E. Sardella and E. H. Brandt. Vortices in a mesoscopic superconducting disk of variable thickness. *Superconductor Science and Technology*, 23(2):025015, 2009. ISSN 0953-2048. doi: 10.1088/0953-2048/23/2/025015.

[79] Q. Du, M. D. Gunzburger, and J. S. Peterson. Computational simulation of type-II superconductivity including pinning phenomena. *Physical Review B*, 51(22):1–7, 1995. doi: 10.1057/978-1-349-94848-2_707-1.

[80] S. J. Chapman and M. D. Gunzburger. A model for superconducting thin films having variable thickness. *Z angew Math Phys*, 47:410–431, 1996. ISSN 01672789. doi: 10.1016/0167-2789(93)90089-J.

[81] V. N. Gladilin, J. Ge, J. Gutierrez, M. Timmermans, J. Van De Vondel, J. Tempere, J. T. Devreese, and V. V. Moshchalkov. Vortices in a wedge made of a type-I superconductor. *New Journal of Physics*, 17(6), 2015. ISSN 13672630. doi: 10.1088/1367-2630/17/6/063032.

[82] S. Gražulis, D. Chateigner, R. T. Downs, A. F. T. Yokochi, M. Quirós, L. Lutterotti, E. Manakova, J. Butkus, P. Moeck, and A. Le Bail. Crystallography Open Database – an open-access collection of crystal structures. *Journal of Applied Crystallography*, 42(4):726–729, Aug 2009. doi: 10.1107/S0021889809016690. URL `http://dx.doi.org/10.1107/S0021889809016690`.

[83] K. Momma and F. Izumi. *VESTA3* for three-dimensional visualization of crystal, volumetric and morphology data. *Journal of Applied Crystallography*, 44(6):1272–1276, Dec 2011. doi: 10.1107/S0021889811038970. URL https://doi.org/10.1107/S0021889811038970.

[84] W.D. Callister. *Materials Science and Engineering: An Introduction*. Wiley international edition. Wiley, 1994. ISBN 9780471581284. URL https://books.google.com.br/books?id=FpxRAAAAMAAJ.

[85] C. Xu, Y. Chan, Y. Chen, P. Chen, X. Wang, C. Dejoie, M. Wong, J. A. Hlevyack, H. Ryu, H. Kee, N. Tamura, M. Chou, Z. Hussain, S. Mo, and T. Chiang. Elemental topological dirac semimetal: α-sn on insb(111). *Phys. Rev. Lett.*, 118:146402, Apr 2017. doi: 10.1103/PhysRevLett.118.146402. URL https://link.aps.org/doi/10.1103/PhysRevLett.118.146402.

[86] M. Liao, Y. Zang, Z. Guan, H. Li, Y. Gong, K. Zhu, X. P. Hu, D. Zhang, Y. Xu, Y. Y. Wang, K. He, X. C. Ma, S. C. Zhang, and Q. K. Xue. Superconductivity in few-layer stanene. *Nature Physics*, 14(4):344–348, 2018. ISSN 17452481. doi: 10.1038/s41567-017-0031-6.

[87] M. P. Nutley, A. T. Boothroyd, C. R. Staddon, D. MK. Paul, and J. Penfold. Magnetic-induction profile in a type-i superconductor by polarized-neutron reflectometry. *Phys. Rev. B*, 49:15789–15798, Jun 1994. doi: 10.1103/PhysRevB.49.15789. URL https://link.aps.org/doi/10.1103/PhysRevB.49.15789.

[88] J. Brisbois, B. Raes, J. Van de Vondel, V. V. Moshchalkov, and A. V. Silhanek. Determination of the magnetic penetration depth in a superconducting pb film. *Journal of Applied Physics*, 115(10):103906, 2014. doi: 10.1063/1.4868298. URL https://doi.org/10.1063/1.4868298.

[89] Juris Meija, Tyler B. Coplen, Michael Berglund, Willi A. Brand, Paul De Bièvre, Manfred Gröning, Norman E. Holden, Johanna Irrgeher, Robert D. Loss, Thomas Walczyk, and Thomas Prohaska. Atomic weights of the elements 2013 (IUPAC technical report). *Pure and Applied Chemistry*, 88(3):265–291, March 2016. doi: 10.1515/pac-2015-0305. URL https://doi.org/10.1515/pac-2015-0305.

[90] Haijiang Hu, Guang Xu, Li Wang, Zhengliang Xue, Yulong Zhang, and Guanghui Liu. The effects of nb and mo addition on transformation and properties in low carbon bainitic steels. *Materials & Design*, 84:95–99, November 2015. doi: 10.1016/j.matdes.2015.06.133. URL https://doi.org/10.1016/j.matdes.2015.06.133.

[91] G. Ghosh and G.B. Olson. Integrated design of nb-based superalloys: Ab initio calculations, computational thermodynamics and kinetics, and experimental results. *Acta Materialia*, 55(10):3281–3303, June 2007. doi: 10.1016/j.actamat.2007.01.036. URL https://doi.org/10.1016/j.actamat.2007.01.036.

[92] M. Ashkin, J. R. Gavaler, J. Greggi, and M. Decroux. The upper critical field of nbn films. ii. *Journal of Applied Physics*, 55(4):1044–1048, 1984. doi: 10.1063/1.333185. URL https://doi.org/10.1063/1.333185.

[93] D. Hazra, N. Tsavdaris, S. Jebari, A. Grimm, F. Blanchet, F. Mercier, E. Blanquet, C. Chapelier, and M. Hofheinz. Superconducting properties of very high quality NbN thin films grown by high temperature chemical vapor deposition. *Superconductor Science and Technology*, 29(10):105011, sep 2016. doi: 10.1088/0953-2048/29/10/105011. URL `https://doi.org/10.1088%2F0953-2048%2F29%2F10%2F105011`.

[94] I. Tretyakov, S. Ryabchun, M. Finkel, A. Maslennikova, K. Natalia, A. Lobastova, B. Voronov, and G. Gol'tsman. Low noise and wide bandwidth of NbN hot-electron bolometer mixers. *Applied Physics Letters*, 98(3):033507, January 2011. doi: 10.1063/1.3544050. URL `https://doi.org/10.1063/1.3544050`.

[95] V. Michal, S. Bouat, J. Villegier, and J. Sedlacek. Superconducting NbN band-pass filter and matching circuit for 30 ghz rsfq data converter. In *2009 19th International Conference Radioelektronika*, pages 161–164, April 2009. doi: 10.1109/RADIOELEK.2009.5158787.

[96] V. Larrey, J. . Villegier, M. Salez, F. Miletto-Granozio, and A. Karpov. Processing and characterization of high jc NbN superconducting tunnel junctions for thz analog circuits and RSFQ. *IEEE Transactions on Applied Superconductivity*, 9(2):3216–3219, June 1999. doi: 10.1109/77.783713.

[97] R. Cheng, C.-L. Zou, X. Guo, S. Wang, X. Han, and H. X. Tang. Broadband on-chip single-photon spectrometer. *Nature Communications*, 10(1), September 2019. doi: 10.1038/s41467-019-12149-x. URL `https://doi.org/10.1038/s41467-019-12149-x`.

[98] W. Qiu, K. Makise, H. Terai, Y. Nakamura, and Z. Wang. Measurement of quality factor and losses in superconducting microwave resonator integrated with NbN/AlN/NbN qubit circuit. *Journal of Physics: Conference Series*, 507(PART 4), 2014. ISSN 17426596. doi: 10.1088/1742-6596/507/4/042032.

[99] J. M. Murduck, J. Vicent, I. K. Schuller, and J. B. Ketterson. Fabrication of NbNI AIN superconducting. *Journal of Applied Physics*, 62(10):4216–4219, 1987. doi: 10.1063/1.339836.

[100] I. A. Rudnev, D. V. Shantsev, T. H. Johansen, and A. E. Primenko. Avalanche-driven fractal flux distributions in NbN superconducting films. *Applied Physics Letters*, 87(4):1–4, 2005. ISSN 00036951. doi: 10.1063/1.1992673.

[101] G.F. Hardy and J.K. Hulm. The Superconductivity of Some Transition Metal Compounds. *Physical Review*, 93(1949):1004, 1954. ISSN 0031-899X. doi: 10.1103/PhysRev.93.1004.

[102] S. Tanaka, A. Miyake, B. Salce, D. Braithwaite, T. Kagayama, and K. Shimizu. Pressure Investigation of Superconductivity of V_3Si. *Journal of Physics: Conference Series*, 200:012202, 2010. doi: 10.1088/1742-6596/200/1/012202.

[103] C. W. Chu and V. Diatschenko. Study of Transforming and Nontransforming V3Si up to 29 kbar. *Physical Review Letters*, 41(8):572–575, 1978.

[104] M. Pulver. Anisotropy of the critical data of superconducting V3Si-single crystals. *Zeitschrift fur Physik*, 257:22–28, 1972. ISSN 14346001. doi: 10.1007/BF01398194.

[105] B. W. Batterman and C. S. Barrett. Crystal Structure of Superconducting V_3Si. *Physical Review Letters*, 13(13):390–393, 1964.

[106] R. Brand and W.W. Webb. Effects of stress and structure on critical current densities of superconducting V_3Si. *Solid State Communications*, 7:19–21, 1969.

[107] D. Kim, D. Uk Lee, E. Kyu Kim, and W.-J. Cho. Charge loss mechanism of nonvolatile v_3si nano-particles memory device. *Applied Physics Letters*, 101(23), 2012. doi: 10.1063/1.4770060. cited By 4.

[108] D.U.K. Lee, D. Kim, K.S. Lee, and E.K. Kim. Memory effect by carrier trapping into v3si nanocrystals among $Si0_2$ layers on multi-layered graphene layer. *Journal of Nanoscience and Nanotechnology*, 14(11):8654–8658, 2014. doi: 10.1166/jnn.2014.9985.

[109] C. Ferdeghini, E. Bellingeri, C. Fanciulli, M. Ferretti, P. Manfrinetti, I. Pallecchi, M. Putti, C. Tarantini, M. Tropeano, A. Andreone, G. Lamura, and Ruggero V. Superconducting Properties of V3Si Thin Films Grown by Pulsed Laser Ablation. *IEEE Transactions on Applied Superconductivity*, 19(3):2682–2685, 2009.

[110] M. Zehetmayer and J. Hecher. Testing V_3Si for two-band superconductivity. *Superconductor Science and Technology*, 27(4):6, 2014. ISSN 0953-2048. doi: 10.1088/0953-2048/27/4/044006. URL `http://stacks.iop.org/0953-2048/27/i=4/a=044006?key=crossref.d2fb5d6894c8991a9258fafca769de14`.

[111] P. K. Sinha and L. K. Mishra. An Evaluation of Super Fluid Density as a Function of Reduced Temperature (T / T C) for Multi Gap Superconductors. *Journal of Pure Applied and Industrial Physics*, 7(February):45–55, 2017.

[112] Inc. Ted Pella. Vacuum deposition techniques and tables, 2018. URL `www.tedpella.com/company_html/Vacuum-Deposition-Techniques-and-Tables.htm`.

[113] P. Walker and W.H. Tarn. *CRC Handbook of Metal Etchants*. CRC Press, 1991. ISBN 0-8493-3623-6.

[114] Department of Physics - Brown University - Professor Gang Xiao's research group. Magnetron sputtering technology summary, 2019. URL `https://www.brown.edu/research/labs/xiao/magnetic-sputtering-technology-summary`.

[115] M. Z. Khan, E. Rivasto, J. Tikkanen, H. Rijckaert, M. Malmivirta, M. O.r Liedke, M. Butterling, A. Wagner, H. Huhtinen, I. Van Driessche, and P. Paturi. Enhanced flux pinning isotropy by tuned nanosized defect network in superconducting YBa2Cu3O6+x films. *Scientific Reports*, 9(1):1–12, 2019. ISSN 20452322. doi: 10.1038/s41598-019-51978-0. URL `http://dx.doi.org/10.1038/s41598-019-51978-0`.

[116] P.W. Hawkes and L. Reimer. *Scanning Electron Microscopy: Physics of Image Formation and Microanalysis*. Springer Series in Optical Sciences. Springer Berlin Heidelberg, 2013. ISBN 9783540389675. URL https://books.google.com.br/books?id=ulrvCAAAQBAJ.

[117] L. Zhuang, S. Bao, R. Wang, S. Li, L. Ma, and Dechun Lv. Thin film thickness measurement using electron probe microanalyzer. In *2009 International Conference on Applied Superconductivity and Electromagnetic Devices*. IEEE, sep 2009. doi: 10.1109/asemd.2009.5306671. URL https://doi.org/10.1109/asemd.2009.5306671.

[118] F.L. Ng, J. Wei, F.K. Lai, and K.L. Goh. Metallic thin film depth measurements by x-ray microanalysis. *Applied Surface Science*, 252(11):3972–3976, mar 2006. doi: 10.1016/j.apsusc.2005.09.038. URL https://doi.org/10.1016/j.apsusc.2005.09.038.

[119] R. Pascual, L.R. Cruz, C.L. Ferreira, and D.T. Gomes. Thin film thickness measurement using the energy-dispersive spectroscopy technique in a scanning electron microscope. *Thin Solid Films*, 185(2):279–286, mar 1990. doi: 10.1016/0040-6090(90)90092-r. URL https://doi.org/10.1016/0040-6090(90)90092-r.

[120] LCE. Equipamentos do lce, ufscar, 2019. URL http://www.lce.dema.ufscar.br/cursos/esc_equip.html.

[121] Myscope, Training for advanced research, 2019. URL http://www.ammrf.org.au/myscope/common/images.php?module=sem.

[122] Physical electronics, inc. (phi) techiniques, 2019. URL https://www.phi.com/surface-analysis-techniques/aes.html.

[123] Hooke College of Applied Sciences. Atomic force microscopy (afm) for polymer characterization and analysis, 2017. URL https://www.youtube.com/watch?v=Flg3N86qKSU.

[124] R L Fagaly. Superconducting quantum interference device instruments and applications. *Review of Scientific Instruments*, 77(101101):45, 2006. doi: 10.1063/1.2354545.

[125] Hanns-Ulrich Habermeier. *Paving the Way for the Success of Magneto-Optics*, chapter 1, pages 1–10. Nato Science Series II:. Springer Netherlands, 2012. ISBN 9789400710078. URL https://books.google.com.br/books?id=nJxrCQAAQBAJ.

[126] L. E. Helseth, R. W. Hansen, E. I. Il'yashenko, M. Baziljevich, and T. H. Johansen. Faraday rotation spectra of bismuth-substituted ferrite garnet films with in-plane magnetization. *Phys. Rev. B*, 64:174406, Oct 2001. doi: 10.1103/PhysRevB.64.174406. URL https://link.aps.org/doi/10.1103/PhysRevB.64.174406.

[127] L. E. Helseth, A. G. Solovyev, R. W. Hansen, E. I. Il'yashenko, M. Baziljevich, and T. H. Johansen. Faraday rotation and sensitivity of (100) bismuth-substituted ferrite garnet films. *Phys. Rev. B*, 66:064405, Aug 2002. doi: 10.1103/PhysRevB.66.064405. URL https://link.aps.org/doi/10.1103/PhysRevB.66.064405.

[128] F. Colauto, M. Motta, A. Palau, M. G. Blamire, T. H. Johansen, and W. A. Ortiz. First observation of flux avalanches in a-MoSi superconducting thin films. *IEEE Transactions on Applied Superconductivity*, 25(3), 2015. ISSN 10518223. doi: 10.1109/TASC.2014.2376183.

[129] Montana Instruments. Cryostation, 2019. URL `https://www.montanainstruments.com/Products/Cryostation/`.

[130] G. Shaw, J. Brisbois, L. B.G.L. Pinheiro, J. Müller, S. Blanco Alvarez, T. Devillers, N. M. Dempsey, J. E. Scheerder, J. Van De Vondel, S. Melinte, P. Vanderbemden, M. Motta, W. A. Ortiz, K. Hasselbach, R. B.G. Kramer, and A. V. Silhanek. Quantitative magneto-optical investigation of superconductor/ferromagnet hybrid structures. *Review of Scientific Instruments*, 89(2), 2018. ISSN 10897623. doi: 10.1063/1.5016293.

[131] C. A. Schneider, W. S. Rasband, and K. W. Eliceiri. NIH image to ImageJ: 25 years of image analysis. *Nature Methods*, 9(7):671–675, June 2012. doi: 10.1038/nmeth.2089. URL `https://doi.org/10.1038/nmeth.2089`.

[132] M. Faucher, T. Fournier, B. Pannetier, C. Thirion, W. Wernsdorfer, J. C. Villegier, and V. Bouchiat. Niobium and niobium nitride SQUIDs based on anodized nanobridges made with an atomic force microscope. *Physica C: Superconductivity*, 368(1):211 – 217, 2002. ISSN 0921-4534. doi: https://doi.org/10.1016/S0921-4534(01)01168-6. URL `http://www.sciencedirect.com/science/article/pii/S0921453401011686`.

[133] J. R. Gavaler, M. A. Janocko, A. Patterson, and C. K. Jones. Very High Critical Current and Field Characteristics of Niobium Nitride Thin Films. *Journal of Applied Physics*, 42(1):54–57, 1971. doi: 10.1063/1.1659649.

[134] J. H. Tyan and J. T. Lue. Grain boundary scattering in the normal state resistivity of superconducting NbN thin films. *Journal of Applied Physics*, 75(1):325–331, 1994. ISSN 00218979. doi: 10.1063/1.355853.

[135] A. V. Silhanek, S. Raedts, and V. V. Moshchalkov. Paramagnetic reentrance of ac screening: Evidence of vortex avalanches in Pb thin films. *Physical Review B - Condensed Matter and Materials Physics*, 70(14):5–7, 2004. ISSN 01631829. doi: 10.1103/PhysRevB.70.144504.

[136] M. Motta, F. Colauto, R. Zadorosny, T. H. Johansen, R. B. Dinner, M. G. Blamire, G. W. Ataklti, V. V. Moshchalkov, a. V. Silhanek, and W. a. Ortiz. Visualizing the ac magnetic susceptibility of superconducting films via magneto-optical imaging. *Physical Review B*, 84(21):214529, dec 2011. ISSN 1098-0121. doi: 10.1103/PhysRevB.84.214529. URL `http://link.aps.org/doi/10.1103/PhysRevB.84.214529`.

[137] A. Soibel, E. Zeldov, M. Rappaport, Y. Myasoedov, T. Tamegai, S. Ool, M. Konczykowskl, and V. B. Geshkenbein. Imaging the vortex-lattice melting process in the presence of disorder. *Nature*, 406(6793):282–287, 2000. ISSN 00280836. doi: 10.1038/35018532.

[138] L. B. L. G. Pinheiro, M. Motta, F. Colauto, T. Johansen, E. Bellingeri, C. Bernini, C. Ferdeghini, and W. Ortiz. Imaging flux avalanches in V_3Si superconducting thin films. *IEEE Transactions on Applied Superconductivity*, pages 1–1, 2019. ISSN 1051-8223. doi: 10.1109/TASC.2019.2902788.

[139] G. Ravikumar, M. R. Singh, and H. Küpfer. Measurement of magnetic relaxation in the peak regime of V3Si. *Physica C: Superconductivity and its Applications*, 403 (1-2):25–31, 2004. ISSN 09214534. doi: 10.1016/j.physc.2003.11.004.

[140] A. Nabialek, V. Chabanenko, S. Vasiliev, G. Shushmakova, H. Szymczak, and B. Kodess. Two components of the magnetostriction of the crystalline metallic V3Si superconductor. *Journal of Applied Physics*, 105(6):063918, 2009. ISSN 0021-8979. doi: 10.1063/1.3093696. URL `http://aip.scitation.org/doi/10.1063/1.3093696`.

[141] V. V. Chabanenko, B. N. Kodess, S. V. Vasiliev, A. Nabiałek, N. V. Kuzovoi, E. Kuchuk, S. A. Kononogov, and H. Szymczak. Fine structure of thermal runaway process in the V3Si singlecrystal superconductor as a result of pinning center response. *Physics Procedia*, 36:634–637, 2012. ISSN 18753892. doi: 10.1016/j.phpro.2012.06.181.

[142] J. Brisbois, O. A. Adami, J. I. Avila, M. Motta, W. A. Ortiz, N. D. Nguyen, P. Vanderbemden, B. Vanderheyden, R. B G Kramer, and A. V. Silhanek. Magnetic flux penetration in Nb superconducting films with lithographically defined microindentations. *Physical Review B - Condensed Matter and Materials Physics*, 93(5):1–13, 2016. ISSN 1550235X. doi: 10.1103/PhysRevB.93.054521.

[143] M. Roussel, a V. Pan, a V. Bobyl, Y. Zhao, S. X. Dou, and T. H. Johansen. Magnetic flux penetration in MgB 2 thin films produced by pulsed laser deposition. *Superconductor Science and Technology*, 18(10):1391–1395, 2005. ISSN 0953-2048. doi: 10.1088/0953-2048/18/10/025.

[144] A. E. Pashitski, A. Gurevich, A. A. Polyanskii, D. C. Larbalestier, A. Goyal, E. D. Specht, D. M. Kroeger, J. A. DeLuca, and J. E. Tkaczyk. Reconstruction of Current Flow and Imaging of Current-Limiting Defects in Polycrystalline Superconducting Films. *Science (New York, N.Y.)*, 275(5298):367–9, 1997. ISSN 1095-9203. doi: 10.1126/science.275.5298.367. URL `http://www.ncbi.nlm.nih.gov/pubmed/8994028`.

[145] A. M. Toxen. Critical Fields of Thin Superconducting Films. I. Thickness Effects. *Physical Review*, 127(2):382–386, 1962.

[146] E. F. Talantsev and J. L. Tallon. Universal self-field critical current for thin-film superconductors. *Nature Communications*, 6:7820, 2015. ISSN 2041-1723. doi: 10.1038/ncomms8820. URL `http://www.nature.com/doifinder/10.1038/ncomms8820`.

[147] K. Il'in, D. Rall, M. Siegel, A. Engel, A. Schilling, A. Semenov, and H. W. Huebers. Influence of thickness, width and temperature on critical current density of Nb thin film structures. *Physica C: Superconductivity and its Applications*, 470(19):953–956, 2010. ISSN 09214534. doi: 10.1016/j.physc.2010.02.042.

[148] R. D. Chaudhari and J. B. Brown. Critical currents in superconducting films of indium. *Phys. Rev.*, 139:A1482–A1488, Aug 1965. doi: 10.1103/PhysRev.139.A1482. URL https://link.aps.org/doi/10.1103/PhysRev.139.A1482.

[149] S. Onori and A. Rogani. Thickness dependence of perpendicular critical fields in superconducting films of in, pb and sn. *Physica B+C*, 132(2):217 – 222, 1985. ISSN 0378-4363. doi: https://doi.org/10.1016/0378-4363(85)90067-1. URL http://www.sciencedirect.com/science/article/pii/0378436385900671.

[150] Leonardo Rodrigues Cadorim, Thiago de Oliveira Calsolari, Rafael Zadorosny, and Edson Sardella. Crossover from type I to type II regime of mesoscopic superconductors of the first group. *Journal of Physics: Condensed Matter*, 32(9):095304, dec 2019. doi: 10.1088/1361-648x/ab4a4a.

[151] Autodesk. *Inventor^{TM} 2018*. Autodesk Inc., 111 McInnis Parkway San Rafael, CA 94903 USA, 2019. URL https://www.autodesk.com/education/free-software/inventor-professional.

[152] Blender Online Community. *Blender - a 3D modelling and rendering package*. Blender Foundation, Stichting Blender Foundation, Amsterdam, 2019. URL http://www.blender.org.

[153] V. V. Yurchenko, D. V. Shantsev, T. H. Johansen, M. R. Nevala, I. J. Maasilta, K. Senapati, and R. C. Budhani. Reentrant stability of superconducting films and the vanishing of dendritic flux instability. *Physical Review B - Condensed Matter and Materials Physics*, 76(9):092504, 2007. ISSN 10980121. doi: 10.1103/PhysRevB.76.092504.